THE UNIVERSITY OF CHICAGO

PARAMETRIC CONTROL OF FLUX-TUNABLE SUPERCONDUCTING CIRCUITS

A DISSERTATION SUBMITTED TO
THE FACULTY OF THE DIVISION OF THE PHYSICAL SCIENCES
IN CANDIDACY FOR THE DEGREE OF
DOCTORATE

DEPARTMENT OF PHYSICS

BY
YAO LU

CHICAGO, ILLINOIS
MARCH 2019

To Mom, Dad, Bo and Sofia

TABLE OF CONTENTS

LIST OF FIGURES

LIST OF TABLES

ACKNOWLEDGMENTS

The last six years have been truly an incredible journey, with so many beautiful memories to be deeply cherished for the rest of my life. This could have been a very different experience without all the support from my colleagues and my family.

First and foremost, I need to thank my advisor David Schuster, who has given me so much to be thankful for that I don't even know where to begin. It was Dave who introduced me to circuit QED that opens the door to an amazing new world for me. It goes without saying how much I have learned throughout my PhD life from his deep knowledge and sharp intuition of superconducting circuits. More importantly, his kind personality, open-mindedness, and enthusiasm for new ideas have made working in the Schuster lab both enjoyable and exciting. As one of the early generations, I had a lot of fun growing with the lab and watching her prosper over the years, which is reflected as a growing number of dilution refrigerators, as well as an increasing population of smart minds in the lab.

Indeed, most of my thesis work would have been impossible, if I had not had the opportunity to work with such a wonderful crew.

Among them, I am obliged to Nelson Leung for the comradeship on the remote quantum module experiment. It would be hard to imagine having the whole experiment done in such an efficient way without Nelson's brilliant set of skills, especially the coding part which still benefits the lab till today. I am also thankful to Vatsan Chakram for the many stimulating discussions we have had for various projects. Being deeply occupied himself by the "grand project" as a postdoc, Vatsan is always ready and able to provide help to other folks with a warm heart, from which the whole lab including myself has been immensely benefited. I want to thank David Mckay, aka "Dr. Dave", who was the first to lead me into the lab as well as the beginning of my research. From his comprehensive mentorship I have gained a lot, from circuit QED theory to fabrication skills. It was a short but memorable experience working with him, till today his late-night howls of fury from dropping a sample to the ground still echoes in my ears. What will also be unforgettable is the many rides to CNM with Nate Earnest - driving to one day worth of fabrication will surely be less

fun without our interesting conversations on the road. Thanks also go to Helin, Alex, Brendan, Andrew, Gerwin, Gabrielle, Kevin, Akash, Ankur, Sasha, Ge and the rest of the Schuster lab team: it has been a great pleasure and a privilege of mine to work alongside with you guys.

Outside the Schuster lab, I am indebted to many physicists who enlightened me with their wisdom, including Eliot Kapit, Jens Koch, Jay Walter, Aash Clerk, Jon Simon, Guilu Long, Luyan Sun, Siyuan Han, Ray Simmonds and Joe Aumentado. Many thanks to David Czaplewski at ANL, Peter Duda at PNF and Wook Jun Nam at Searle cleanroom for their help and guidance on the fabrication of the circuit devices. I sincerely appreciate the communications with Peter Groszkowski, Ziwen Huang, Xinyuan You and Youpeng Zhong, who inspired me to look at my research from different perspectives, from which I always end up learning something new.

Finally, I must also thank Sofia Lu for her particularly enjoyable company in the last 18 months. It was such a pleasure to meet you, and I am looking forward to all the fun we are going to have together for many years to come. To Mom and Dad, thank you for raising me up to where I want to be today. I always feel extremely lucky to have you as my parents. To my wife Bo, thank you for always believing in me and being there for me whenever I need - this journey would have been unthinkable without your unconditional love and support.

ABSTRACT

Quantum computing is at an exciting time, with practical quantum processors coming closer to experimental realization. Yet a major challenge in building a practical quantum computer is to generate and manipulate interactions between its many components. Superconducting (SC) qubits are promising candidates not only because they have strong coupling and high-fidelity readout, but also for allowing versatile parametric control that can realize different effective interactions at will, which might be difficult to achieve through other means. In this thesis, we start from the simple example of parametrically flux modulated SC qubit and demonstrate its application towards quantum communication between remote SC modules. We then move on to discuss the parametric modulation of the light-matter interaction strength, where we introduce a novel SC tunable coupler device that allows for the direct dc-flux control of qubit-qubit or qubit-cavity coupling strength without sacrificing qubit coherence, as well as the convenient realization of blue- and red-sideband interactions through appropriate choice of parametric flux-modulation frequency. By engineering the dissipative system-environment interactions through sophisticated parametric control of this tunable coupler device, we achieve the autonomous stabilization of arbitrary qubit states, in a manner akin to laser cooling in atomic physics. Finally, we present our on-going experimental effort of extending the idea of autonomous stabilization to autonomous quantum error correction, an important step towards the ultimate realization of the universal quantum computer.

CHAPTER 1

INTRODUCTION TO SUPERCONDUCTING QUBITS

To begin our story with the beginning of our story, we record that the theory of quantum mechanics was born almost one hundred years ago. Ever since its inception, quantum mechanics has revolutionized our understanding of the fundamental principles of nature. While quantum mechanics governs the way how microscopic particles behave, in our everyday life, macroscopic objects that are composed of these particles rarely display quantum effects for direct observation, making the study and control of individual quantum systems inherently exciting and challenging. Tremendous effort has been devoted to the deeper understanding and practical application of quantum mechanics over the years. The first generation of quantum technology has seen the invention of transistors and laser, yet they are still "classical machines" that behave and are used in classical ways on the macroscopic level (as all classical machines do). It was not until the early 1980s that, based upon earlier theoretical developments and experimental progress, more and more people started to realize the value of building "quantum machines" that are operated fundamentally through quantum mechanical principles - by leveraging the unique quantum features these machines exhibits, they can easily outperform their classical counterparts. New seeds, such as quantum computing, quantum communication, and quantum cryptography, begin to grow and prosper from the cross-pollination of quantum mechanics and other disciplines including computer science and information theory, and matures into the booming field of quantum information science as we know it today.

The introduction, like the remaining part of this dissertation, will focus on quantum computation and its physical realization via superconducting qubits. We aim to provide high-level descriptions for these basic concepts, leaving more detailed discussions for the following chapters.

1.1 Basic Idea of Quantum Computing

As Richard Feynman famously noted [1], "If you want to make a simulation of nature, you'd better make it quantum mechanical, and by golly it's a wonderful problem, because it doesn't look so easy." The bizarre quantum natures, such as entanglement and superposition of quantum states, impedes the efficient simulation of quantum many-body systems through classical means. This is both a curse and a blessing because in return it provides powerful computational resources, such as qubits and quantum algorithms, for the simulation of such systems and beyond. This is known as the art of quantum computing [2, 3, 4].

1.1.1 Qubit: quantum bit

Akin to the classical bit that carries the minimum amount of classical information, the quantum bit, commonly referred to as "qubit", is the basic unit of quantum information. A classical bit can be represented by a binary digit with two states 0 and 1. The state of a classical bit is deterministic - it is either 0 or 1. On the contrary, a qubit can be in a coherent superposition of both 0 and 1, a striking feature unique to quantum states. The general state of a qubit can be written as

$$|\psi\rangle = \alpha\,|0\rangle + \beta\,|1\rangle\,, \tag{1.1}$$

where α and β are normalized complex numbers, $|\alpha|^2 + |\beta|^2 = 1$. Here, $|0\rangle$ and $|1\rangle$ are orthogonal basis vectors in the 2-dimensional Hilbert space, $\langle i|j\rangle = \delta_{ij}$.

There are various physical implementations of a qubit, from the polarization of a photon to the angular moment of spin-half particles and so on. In principle, any two-level quantum-mechanical system can be used as a qubit, even multilevel systems too as long as the addressability of an individual two-level subspace is guaranteed, as we will see later in the example of superconducting qubits. However, this does not necessarily suggest that all qubits are created equal, as there are significant variances among different realizations in terms of their quality, measured by the coherence properties and the feasibility of control, readout, storage, etc.

1.1.2 The Bloch sphere representation of qubit

The state of a single qubit can be better visualized by recasting Eq. 1.1 into the following form,

$$|\psi\rangle = \cos\frac{\theta}{2}|0\rangle + e^{i\phi}\sin\frac{\theta}{2}|1\rangle, \tag{1.2}$$

which immediately acquires a geometrical meaning as the two parameters, $0 \leq \theta \leq \pi$ and $0 \leq \phi \leq 2\pi$, can be directly related to the polar and azimuthal angles of a sphere, known as the Bloch sphere, shown in Fig. 1.1(a). The red arrow, a.k.a the Bloch vector, stands for a single qubit with its information stored in its orientation. It is easy to verify that the north and south pole of the Bloch sphere represent $|0\rangle$ and $|1\rangle$ states, while along the equator are the equal superpositions of the basis states with different phases.

Pure states described by Eq. 1.1 and 1.2 are represented by Bloch vectors of unit length. Bloch vectors shorter than unity, on the other hand, represent "mixed states" that are inside of the Bloch sphere and are comprised of a statistical ensemble of pure states $|\psi_i\rangle$ with classical probabilities p_i,

$$\rho = \sum_i p_i |\psi_i\rangle\langle\psi_i|, \quad \sum_i p_i = 1. \tag{1.3}$$

As Fig. 1.1(b) shows, the decomposition of a given mixed state into pure states is, generally speaking, not unique, except for the eigen-decomposition where the pure state components are the eigenstates at the crossing between the Bloch sphere and the Bloch vector. In reality, almost every quantum state that we can create is a mixed state no matter how close it is to a pure state, because of the inevitable loss of quantum information within the state preparation process. The most extreme case is the "maximally mixed state" at the center of the Bloch sphere which is an even mixture of two bases states, and is mathematically equivalent to the identity matrix. In this case, all the quantum information is completely lost and the state becomes classical again.

Using the density matrix ρ appearing in Eq. 1.3, we can conveniently express an arbitrary state

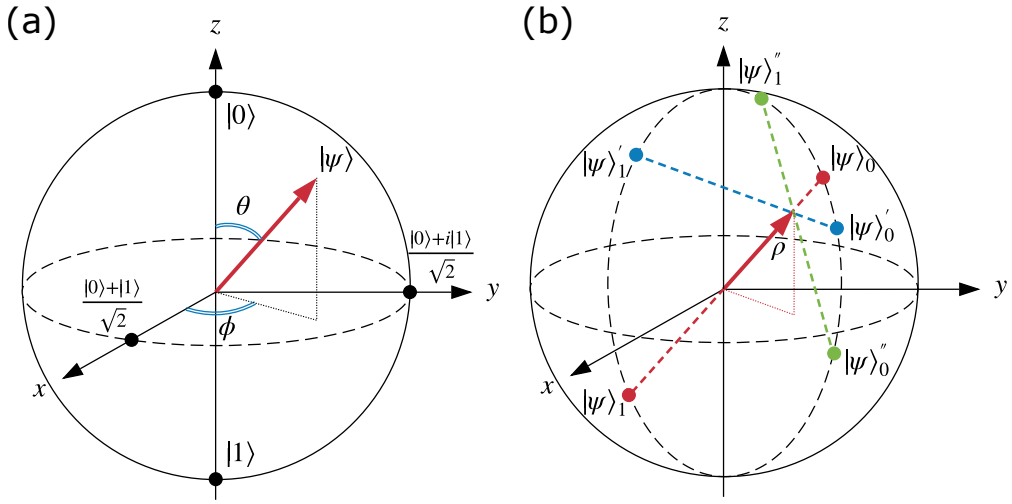

Figure 1.1: The Bloch sphere representation of a qubit state.(a) The pure state is represented by the Bloch vector of unit length. (b) Non-uniqueness of the decomposition of a mixed state.

of the qubit, whether it be pure or mixed, as a function of the Bloch vector in the following way:

$$\rho = \frac{1}{2}\left(I + \vec{n}\cdot\vec{\sigma}\right), \tag{1.4}$$

where I is the identity matrix, $\vec{n} = \left(n_x, n_y, n_z\right)$ is the Bloch vector, and $\vec{\sigma} = \left(\sigma_x, \sigma_y, \sigma_z\right)$ is the Pauli vector with the Pauli matrices defined by

$$\sigma_x = \begin{pmatrix} 0 & 1 \\ 1 & 0 \end{pmatrix}, \quad \sigma_y = \begin{pmatrix} 0 & -i \\ i & 0 \end{pmatrix}, \quad \sigma_z = \begin{pmatrix} 1 & 0 \\ 0 & -1 \end{pmatrix}. \tag{1.5}$$

1.1.3 Quantum entanglement

Entanglement is yet another profound or even spooky (in Einstein's words) phenomenon exclusively found in the quantum world. Entanglement occurs for a multi-body quantum system when correlation exists among its local constituents so that the overall state ρ CANNOT be written as a product of each individual state ρ_i as below,

$$\rho = \rho_1 \otimes \rho_2 \otimes \cdots \otimes \rho_n = \otimes_i^n \rho_i, \tag{1.6}$$

nor, in a broader sense, a "separable state" in the form of

$$\rho = \sum_k p_k \rho_{k1} \otimes \rho_{k2} \otimes \cdots \otimes \rho_{kn} = \sum_k p_k \otimes_{ki}^{n} \rho_i, \quad \sum_k p_k = 1. \tag{1.7}$$

The product state in Eq. 1.6 is obviously a special case of the separable state in Eq. 1.7. If a density matrix cannot be written in the form of a separable state, it is called an "entangled state". One class of the most important entangled states are the following "Bell states" [5],

$$\left|\psi^{\pm}\right\rangle = \frac{1}{\sqrt{2}} \left(|01\rangle \pm |10\rangle\right), \quad \left|\phi^{\pm}\right\rangle = \frac{1}{\sqrt{2}} \left(|00\rangle \pm |11\rangle\right), \tag{1.8}$$

which are the necessary ingredients in various quantum communication protocols. A common misbelief about entanglement is that information can be communicated faster-than-light (FTL) through measurement of the Bell state: suppose Alice and Bob each hold a particle of Bell state $\left|\psi^{+}\right\rangle$ and they separate far away from each other. A paradox then arises that if Bob measures his particle (particle B) and finds it to be in the $|0\rangle$ ($|1\rangle$) state, then instantaneously the particle that Alice holds (particle A) will collapse into the state of $|1\rangle$ ($|0\rangle$), which "violates" the special relativity - except this is no true. In fact, Alice would not notice any difference in her particle regardless of the outcome of Bob's measurement, without classical communication between the two parties. This is known as the "no-communication theorem" [6, 7] - no FTL communication allowed after all, there is nothing spooky about entanglement!

Nonetheless, the study of quantum entanglement, such as understanding its classification and detection [8, 9, 10, 11, 12, 13], is rightfully one of the most interesting topics in the field of quantum information theory, which is well-motivated by the fact that entanglement is exploited as a key resource in every aspect of quantum computation and quantum communication. Perhaps it is not an exaggeration to say that entanglement is what makes the quantum speedup possible - quantum parallelism residing in superposition alone is not enough, as Scott Aaronson put it "quantum computers would not solve hard search problems instantaneously by simply trying all the possible solutions at once", but one needs to employ entanglement to interfere the unwanted

paths away, leaving only the desired answer.

1.1.4 Analog and digital quantum simulation

Suppose we want to simulate a system with initial state $|\psi\rangle$ evolving under some Hamiltonian $\hat{\mathcal{H}}$,

$$|\psi(t)\rangle = e^{-i\hat{\mathcal{H}}t/\hbar}|\psi(0)\rangle, \tag{1.9}$$

for the sake of brevity here we assume a time-independent Hamiltonian and a closed system without any loss. One may be tempted to calculate the propagator $U(t) = e^{-i\hat{\mathcal{H}}t/\hbar}$ for each t, but will soon be stuck in the same conundrum as the Indian King in the wheat and chessboard problem - the resource for such an operation quickly explodes when the size of the system n becomes large, as the complexity of this calculation scales exponentially as $O\left(2^{3n}\right)$. While exact calculations based on first principles are only possible for small Hilbert spaces, approximation methods such as mean-field theory, tensor network theory, density functional theory and quantum Monte Carlo algorithms all have their limitations [14]. As the most "original" application of quantum computation, quantum simulation [15, 16, 17], which aims to mimic the dynamical or static behavior of the quantum system of interest via another more controllable quantum platform (the quantum simulator), is perhaps by far the most realistic path to achieving quantum advantage for practical subjects such as the simulation of high-Tc superconductivity [18, 19], quantum phase transitions [20, 21, 22, 23, 16], quantum chemistry [24, 25, 26], etc.

Quantum simulation can be loosely classified into digital and analog quantum simulation. In digital quantum simulation, the continuous time-space of the evolution is discretized (digitized) so that the evolution operator can be decomposed and implemented through the application of a sequence of single- and two-qubit gates from a universal quantum gate set [27, 28, 29, 30, 31]. Digital quantum simulation is especially helpful when the system Hamiltonian can be written as a sum of subsystem Hamiltonians,

$$\hat{\mathcal{H}} = \sum_k \hat{\mathcal{H}}_k, \tag{1.10}$$

where the subsystems do not commute with each other, while each being easier to compute than the overall Hamiltonian. Then, according to the first-order Trotter formula [32]

$$e^{A+B} = \lim_{n\to\infty} \left(e^{A/n} e^{B/n}\right)^n, \tag{1.11}$$

the evolution operator can be rewritten as

$$U(t) = e^{-\frac{i}{\hbar}\sum_k \hat{\mathcal{H}}_k t} \approx \left(\prod_k e^{-\frac{i}{\hbar}\hat{\mathcal{H}}_k \frac{t}{N}}\right)^N, \tag{1.12}$$

when $\frac{t}{N} \to 0$. Each term in the product can be decomposed into single- and two-qubit gates, while the product forms a gate sequence and the evolution operator is implemented through applying the sequence N times. Because of this, digital quantum simulation is a highly universal approach that can be reprogrammed to simulate any local quantum system within its computational capacity. On the downside, how to efficiently scale up such as digital quantum simulator while maintaining its efficiency in performing the universal gate set is a difficult open problem.

In contrast, the idea of analog quantum simulation is to construct another system that bears a Hamiltonian $\hat{\mathcal{H}}_{\text{sim}}$ closely resembling $\hat{\mathcal{H}}$ so that its evolution of state, which we can better control and measure, can be mapped back to the original system to accomplish the simulation of it in different parameter regimes and conditions. Such analog simulators are single-purpose devices that trade in universality for lower errors and higher scalability for particular problems, but in return they become less versatile than digital quantum simulators for simulating various other systems with different Hamiltonians. One such example of the analog quantum simulator is the recent work on the simulation of the Mott insulator of microwave photons with superconducting qubits [33].

Illustrated in Fig. 1.2, eight tunable superconducting qubits with nearest-neighboring couplings

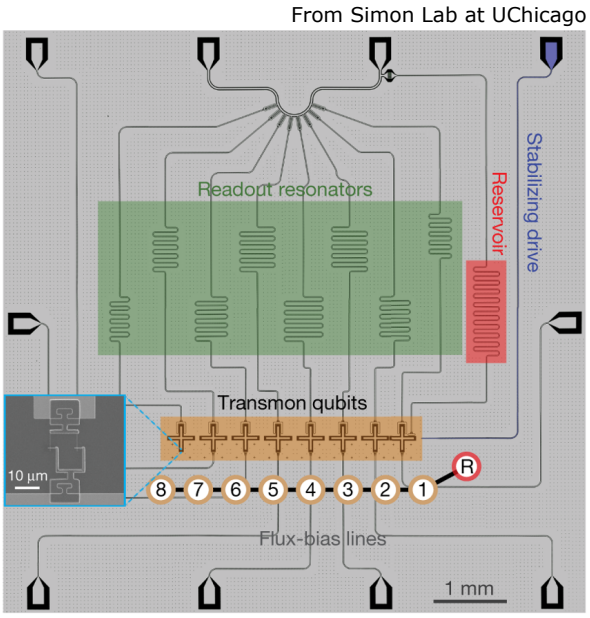

Figure 1.2: Building a Bose Hubbard lattice with a superconducting circuit.

constitute a one-dimensional lattice, with a Hamiltonian given by

$$\hat{\mathcal{H}}/\hbar = -\sum_{\langle ij \rangle} J_{ij} \hat{a}_i^\dagger \hat{a}_j + \frac{U}{2} \sum_i \hat{n}_i \left(\hat{n}_i - 1\right) + \sum_i \epsilon_i \hat{n}_i. \tag{1.13}$$

This is none other than the well-known Bose-Hubbard Hamiltonian, a paradigm for strongly interacting bosons. Hence the usefulness of the simulator for the exploration of Bose Hubbard physics such as phase transition and in this particular case, the stabilization of Mott insulator phase.

We need to point out that, while in this case the natural Hamiltonian of the simulator coincides with the simulated system, in general this is not a requirement for analog quantum simulations, provided that the simulator possesses enough tunability to support the engineering of its Hamiltonian to better accommodates the goal of the simulation. We will demonstrate how this can be achieved through the parametric control of superconducting circuits, with more concrete examples in the following chapters .

1.2 Quantum Computing with Superconducting Qubit

As alluded to earlier, most qubit proposals are built upon microscopic systems that naturally exhibit quantum effects, such as atoms [34, 35, 36, 37], ions [38, 39, 40, 41], electron or nuclei spin [42, 43, 44, 45], etc. While they are reasonable candidates as microscopic particles are intrinsically quantum coherent once carefully isolated from the environment, the microscopic nature of these systems also put constraints on their usage as qubits. For instance, while a very well-isolated two-level atom seems to be an excellent choice for quantum information storage, it does not interact very strongly with a propagating photon so that it is difficult to control its state with a shining laser. This can be partially resolved by placing the atom into a high-finesse optical cavity, where photons can bounce back and forth between the walls of the cavity and interact with the atom for an effectively much longer time, with a Hamiltonian described by the quantum Rabi model in cavity quantum electrodynamics[1] (cavity QED):

$$H/\hbar = \omega_r a^\dagger a + \frac{\omega_a}{2}\sigma_z + g\left(a^\dagger + a\right)\sigma_x. \tag{1.14}$$

The first two terms represent the energies of cavity mode (standing wave as a result of photon interference) and the atom, whereas the last term is the coupling between the cavity and the atom. The study of cavity QED with natural atoms embedded in optical cavities is fundamentally interesting and lays a solid groundwork as a prototype quantum computing system for many other possible candidates. In the meantime, a considerable amount of effort in the optimization of the system is required for compensating the tiny dipole moment of natural atoms and the weak inter-atom interaction strength, potentially limiting its scalability for quantum computation purposes.

An alternative to the natural, microscopic systems is the artificial atom made with superconducting circuits [46, 47, 48, 49, 50]. While being a macroscopic system formed by hundreds of billions of atoms, the collective electrodynamical modes within the circuit still exhibit quan-

1. From this point forward we will use a convention that σ_z is the atomic inversion operator defined as the negative Pauli-Z operator.

tum behavior, much like natural atoms. Thanks to its macroscopic size, the dipole moment of a superconducting qubit can be engineered many orders of magnitude larger than a natural atom, engendering the relatively easy attainment of strong couplings between different modes, as well as more efficient control and readout schemes. Further, superconducting qubits are highly scalable as they can be fabricated with standard lithography techniques for making computer chips. Unlike in cavity QED where trapping the atoms takes additional experimental overhead, superconducting qubits will stably stay at precisely the same locations without ever being lost due to inelastic collisions. Finally, as an artificial atom, the parameters influencing its quantum behavior can be fine-tuned either in the design or even in situ after it is made, allowing for extremely versatile manipulations at a level difficult or impossible with natural atoms.

1.2.1 Quantum LC oscillator

In principle, being macroscopic per se does not prohibit an object from being quantum, but its interaction with the environment will. The reason why quantum effects are not common to see in everyday life is not only because we are too big, but more importantly because we are too hot (thermally populated) and too messy (disordered)! For any classical mode, mechanical or electrical, it is just a matter of proper isolation and cooling before we can witness its quantum properties. Take the simplest case of a pendulum as an example (Fig. 1.3(a)). Under small angles ($\theta \sim 0$), the Lagrangian is readily written

$$\mathcal{L} = T - V = \frac{1}{2}ml^2\dot{\theta}^2 - \frac{1}{2}mgl\theta^2, \tag{1.15}$$

which yields the Euler-Lagrangian equation of motion

$$\ddot{\theta} + \frac{g}{l}\theta = 0, \tag{1.16}$$

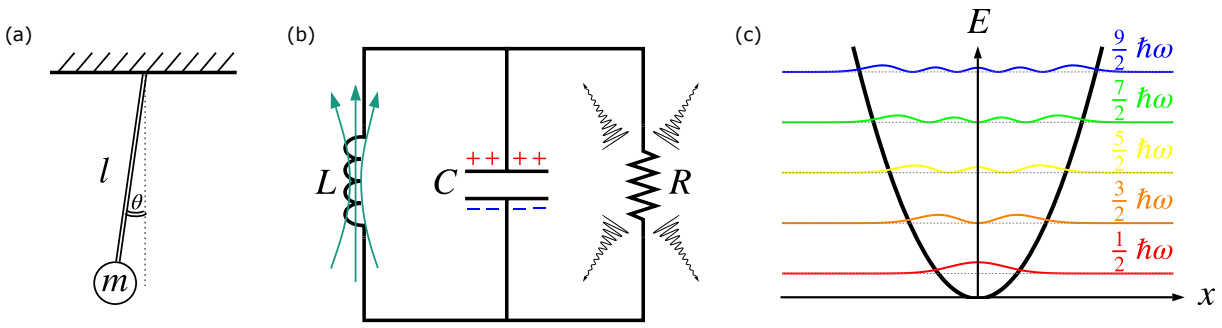

Figure 1.3: The analogy between a classical pendulum and a quantum LC oscillator. (a) The pendulum, although macroscopic, can still be thought of as a quantum object, but does not typically reveal its quantum nature due to its poor isolation from the environment. (b) The collective motion of electrons (or Cooper pairs) in a microwave LC oscillator possesses quantum coherence when the circuit is cooled down to 20 mK. (c) Both the pendulum and the microwave LC oscillator can be quantized into quantum harmonic oscillators, with linear energy levels evenly spaced by their oscillation frequency $\hbar\omega$.

where we can find the oscillation frequency to be

$$\omega = \sqrt{\frac{g}{l}}. \tag{1.17}$$

So far we have applied a completely classical-mechanical treatment of the pendulum, but there is nothing to stop us from quantizing the pendulum into a quantum mode. To this end, we find the "momentum" variable conjugate to the angle,

$$L = \frac{\partial \mathcal{L}}{\partial \dot{\theta}} = ml^2\theta = mlv, \tag{1.18}$$

which has a physical interpretation of angular momentum. Now, the angle and angular momentum can be promoted to quantum operators following canonical quantization,

$$\left[\hat{\theta}, \hat{L}\right] = \hat{\theta}\hat{L} - \hat{L}\hat{\theta} = i\hbar, \tag{1.19}$$

so that the classical Hamiltonian

$$\mathcal{H} = L\dot{\theta} - \mathcal{L} = \frac{L^2}{2ml^2} + \frac{1}{2}mgl\theta^2 \tag{1.20}$$

can be rewritten using the ladder operators as

$$\hat{\mathcal{H}}/\hbar = \omega\left(\hat{a}^\dagger\hat{a} + \frac{1}{2}\right), \tag{1.21}$$

with

$$\hat{a} = \sqrt{\frac{m\omega l^2}{2\hbar}}\left(\hat{\theta} + \frac{i}{m\omega l^2}\hat{L}\right), \quad \hat{a}^\dagger = \sqrt{\frac{m\omega l^2}{2\hbar}}\left(\hat{\theta} - \frac{i}{m\omega l^2}\hat{L}\right). \tag{1.22}$$

In an ideal world where the pendulum is perfectly isolated from the environment, it should just act like a quantum harmonic oscillator dictated by Eq. 1.21, with equidistant energy levels shown in Fig 1.3(c). In reality, the pendulum will interact with the environment until it reaches thermal equilibrium at temperature T, and falls into a thermal mixed state

$$\rho = \sum_n P_n \left|n\right\rangle \left\langle n\right|, \tag{1.23}$$

with the population of its n-th level following the Maxwell-Boltzmann distribution:

$$P_n = \frac{1}{Z}g_n e^{-n\hbar\omega/k_B T}, \tag{1.24}$$

where Z is the partition function, g_n is the degeneracy of the n-th level, k_B is the Boltzmann constant. Suppose the macroscopic pendulum has an oscillation frequency of $2\pi \times 10$ Hz, then according to Eq. 1.24, at room temperature $T \approx 300$K, the pendulum has a mean excitation number as high as 6.25×10^{11}! This corresponds to a highly classical state that resembles a maximally mixed state in the low energy space. Equivalently, in order to achieve a pure quantum state with 99% population in the ground state $|0\rangle$, the pendulum will have to be cooled down to a ridiculously low temperature of 0.1 nK. A more practical solution relies on modifying the mode frequency

instead, either by making the pendulum much smaller or the effective g much larger. The same calculation shows that with mode frequency higher than 2 GHz, it only takes 20 mK to ensure 99% fidelity for the ground state, well within the reach of modern dilution refrigerators.

While in theory it is possible to build such a "macroscopic quantum coherence" with a pendulum (in fact, it has already been realized in the forms of quantum drum [51] and other optomechanical devices), it is much easier to use microwave LC oscillators as artificial quantum modes. A standard oscillator circuit, as demonstrated in Fig. 1.3(b), is formed by an inductor L and a capacitor C, which together give rise to the oscillation of the collective motion of electrons at frequency $\omega = 1/\sqrt{LC}$. Following the same quantization procedure but with the "position" and "momentum" operators being the inductor flux Φ and the capacitor charge Q[1],

$$\left[\hat{\Phi}, \hat{Q}\right] = i\hbar, \tag{1.25}$$

the Hamiltonian of the LC oscillator in the second quantization form is found to be

$$\hat{\mathcal{H}}/\hbar = \omega\left(\hat{a}^\dagger \hat{a} + \frac{1}{2}\right), \tag{1.26}$$

and the flux and charge operators can also be expressed in ladder operators as

$$\hat{\Phi} = \sqrt{\frac{\hbar Z_c}{2}}\left(a^\dagger + a\right), \quad \hat{Q} = i\sqrt{\frac{\hbar}{2Z_c}}\left(a^\dagger - a\right), \tag{1.27}$$

where $Z_c = \sqrt{L/C}$ is the characteristic impedance of the oscillator.

According to our previous discussion, once the oscillation frequency is in the GHz level, the quantum feature of the LC oscillator can become accessible at experimentally feasible low temperatures. This can be readily realized by simply making the size of the circuit smaller such that it resonates with microwaves at micrometer wavelength. Unfortunately this is not quite enough

1. The subtlety here is that the sign of the commutation relationship actually depends on which variable is treated as the "position" or "momentum". While this doesn't affect the final quantization result, it can simplify further calculations for certain regimes.

to make a good quantum LC oscillator yet, because typically an LC oscillator is damped from coupling to a dissipative environment represented by the resistor R in the circuit diagram, which can significantly degrade its quantum coherence properties. Luckily, as another crucial benefit of operating the circuit at few tens of milli-Kelvin, if we make the microwave LC circuit out of superconducting material such as Aluminum or Niobium with critical temperatures higher than the operating temperature, electrons will be bounded into a coherent condensate of bosons (Cooper pairs) and the circuit will transition into a resistance-free superconducting phase, eliminating the most serious source of dissipation and noise.

1.2.2 Josephson junction

Superconducting LC oscillators are quantum harmonic oscillators in the microwave domain, replicating the role of the optical cavities in cavity QED systems. However, just like natural atoms are a necessity in cavity QED, harmonic oscillators alone are not sufficient for circuit QED because their linear energy levels prevent their usage as two-level atoms. In order to selectively address a specific pair of levels with a single photon, we need to introduce non-linearity (anharmonicity) into the system in a non-dissipative manner. Amazingly, this is made possible by a superconducting device called the Josephson junction [52, 53]. Pictured in Fig. 1.4(b), the most common method to create a Josephson junction is via two superconducting electrodes separated by a thin insulating oxide, through which the coherent tunneling of Cooper pairs may occur and give rise to a supercurrent of

$$I = I_c \sin\theta, \tag{1.28}$$

where the critical current I_c is the maximum current that the junction can sustain and θ is the superconducting phase difference between the two sides of the dioxide barrier. This phase also evolves in time in the presence of a potential difference V across the junction according to

$$V = \phi_0 \frac{\partial\theta}{\partial t}, \tag{1.29}$$

where $\phi_0 = \hbar/2e$ is the reduced flux quantum. From the above Josephson equations we find

$$V = \frac{\phi_0}{I_c \cos\theta} \frac{dI}{dt}, \tag{1.30}$$

which suggests that the Josephson inductance can be defined as

$$L_J = \frac{\phi_0}{I_c \cos\theta}. \tag{1.31}$$

Recall from Eq. 1.29 that the superconducting phase difference θ is related to the flux through

$$\Phi = \phi_0 \theta, \tag{1.32}$$

we can conclude that the Josephson junction is equivalent to a nonlinear inductor whose inductance is a function of its flux, with an inductive energy given by

$$E = \int IV dt = \phi_0 I_c \sin\theta \frac{\partial\theta}{\partial t} dt = -E_J \cos\theta, \tag{1.33}$$

where $E_J = \phi_0 I_c$ is called the Josephson energy.

So far we have been only considering the energy of the junction arising from the Josephson effect. If the junction were only inductive, then Eq. 1.33 would fully describe the Josephson junction. The superconducting phase would be perfectly quantized, represented by a continuous basis vector $|\theta\rangle$ with eigenenergy $-E_J \cos\theta$, but there would be no way of changing the phase state, a rather uninteresting quantum circuit. However, we also need to take the capacitive energy into account, which emerges from the Coulomb charging energy of the parallel plate capacitor C_J naturally embedded in the S-I-S architecture. The Lagrangian of the Josephson junction then becomes

$$\mathcal{L} = \frac{1}{2} C_J \phi_0^2 \dot{\theta}^2 + E_J \cos\theta, \tag{1.34}$$

in which Eq. 1.29 is used again. Then, the classical equation of motion can be acquired from the

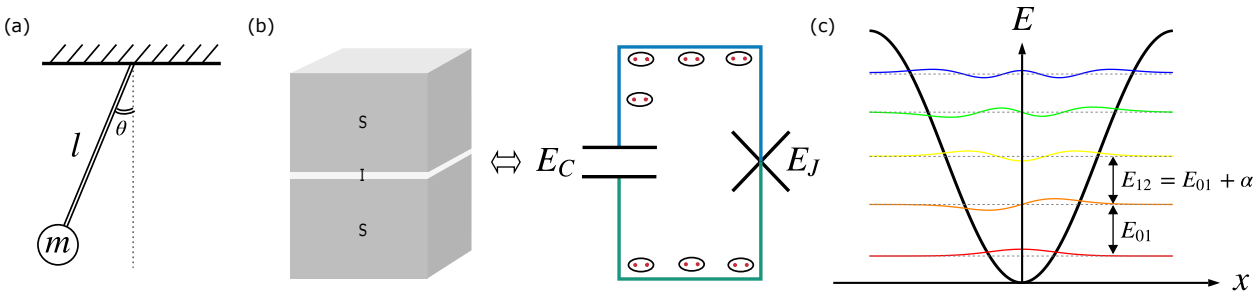

Figure 1.4: The analogy between a nonlinear pendulum and a Josephson junction. (a) The motion of the pendulum becomes nonlinear when it is allowed to make large angular excursions. (b) The tunneling of the Cooper pairs through the barrier, along with the electrostatic charging of the parallel superconducting plates, underlies the nonlinear dynamics of the Josephson junction characterized by the charging energy E_c and the Josephson energy E_J. (c) The nonlinear pendulum and the Josephson junction share the same cosine potential energy which gives rise to unevenly-spaced energy levels.

Euler-Lagrangian equation,

$$C_J\phi_0^2\ddot{\theta} + E_J \sin\theta = 0, \tag{1.35}$$

which is mathematically equivalent to the oscillation of a nonlinear pendulum at large angle (Fig. 1.4 (a)).

More interestingly, we obtain the Hamiltonian from Legendre transformation,

$$\hat{\mathcal{H}} = \frac{\hat{P}^2}{2C_J\phi_0^2} - E_J \cos\hat{\theta}, \tag{1.36}$$

where $\hat{P} = C_J\phi_0^2\dot{\theta}$ is the momentum operator that obeys the commutation relationship with $\hat{\theta}$,

$$\left[\hat{\theta}, \hat{P}\right] = i\hbar. \tag{1.37}$$

As $\hat{P}$ is related to the charge stored in the capacitor through $\hat{P} = \phi_0\hat{Q}$, Eq. 1.36 can be written in a more meaning way as

$$\hat{\mathcal{H}} = 4E_c\hat{n}^2 - E_J \cos\hat{\theta}, \tag{1.38}$$

in terms of the number of Cooper pairs $\hat{n}$ charging the capacitor. Here, $E_c = e^2/2C_J$ is the

charging energy, and the two operators follow the commutation relationship

$$\left[\hat{\theta}, \hat{n}\right] = i. \tag{1.39}$$

Thus, we may write out the Schrödinger equation in the phase basis

$$-4E_c \frac{\partial^2 \psi(\theta)}{\partial \theta^2} - E_J \cos\theta \psi(\theta) = E\psi(\theta). \tag{1.40}$$

by making use of $\hat{n} = -i\partial/\partial\theta$. This is equivalent to a single particle in a 1D cosine potential, see Fig. 1.4(c). Due to the nonlinearity of the cosine potential, the eigenenergies of the Josephson junction are no longer evenly-spaced like the quantum harmonic oscillator, but exhibit an anharmonicity $\alpha = E_{21} - E_{10}$ critical for its control as a qubit. The calculation of the individual eigenenergy and the wavefunction can be executed either by numerically solving the 2nd order ODE, or computing from the analytical Mathieu's functions [54, 48].

It is vital to note that here the Cooper pair number operator has integer eigenvalues, while the phase operator is defined within $[-\pi, \pi]$, similar to the angle of the nonlinear pendulum. Because θ and $\theta + 2\pi$ physically correspond to the same state, the wavefunction must also follow the 2π-periodicity as $\psi(\theta) = \psi(\theta + 2\pi)$, which is not always the case for periodic lattice according to the Bloch theorem. This periodic boundary condition is lifted, however, if the Josephson junction is shunted by a linear inductance that breaks the periodicity of the potential energy.

The Hamiltonian in Eq. 1.38 can also be written in the charge basis[1],

$$\hat{\mathcal{H}} = 4E_c \sum_n n^2 |n\rangle\langle n| - \frac{E_J}{2} \sum_n \left(|n\rangle\langle n+1| + |n+1\rangle\langle n|\right), \tag{1.41}$$

which is recognized as a 1D tight-binding model, with the on-site energy being the charging energy, and the tunneling energy of the Cooper pair equal to the Josephson energy. When $E_c \gg E_J$, dubbed as the charge qubit regime, intuitively the low-energy manifold is confined within a small

1. See Appendix. 6.1 for detailed derivation.

$\langle n \rangle$ range, and can be directly found through the diagonalization of the Hamiltonian by keeping enough $|n\rangle$ levels greater than the spread of the wavefunction. In the opposite "transmon regime" where $E_c \ll E_J$, charge basis will no longer be a good representation because the wavefunction is widely dispersed across many charge basis, making the diagonalization more susceptible to truncation errors. In either case, with properly designed circuit parameters, the Josephson junction can provide enough nonlinearity suitable for quantum operations as a "superconducting qubit".

1.2.3 Superconducting Quantum Interference Devices

Another important superconducting element is the Superconducting Quantum Interference Device (SQuID) [55, 56], which is a crucial building block for flux-tunable superconducting circuits in particular relevance to this thesis. Here and in the following, SQuID will mostly refer to dc-SQuIDs made of split Josephson junctions presented in Fig. 1.5, but it should be noted that rf-SQuID composed of a Josephson junction shunted by a linear inductance is also of great interest as a potential candidate of superconducting qubits [57, 58].

The dc-SQuID is essentially a superconducting loop formed by two Josephson junctions that is threaded by an external flux, creating a difference between the two superconducting phases proportional to the penetrating flux of Φ_{ext} within a single period of flux quantum Φ_0,

$$\theta_2 - \theta_1 = 2\pi n + 2\pi \frac{\Phi_{ext}}{\Phi_0}. \tag{1.42}$$

Assuming the Josephson energies of the two junctions are $E_{J1,2}$, and the charging energies $E_{c1,2}$, we write out the Lagrangian of the split junction as

$$\mathcal{L} = \frac{1}{2} C_1 \dot{\Phi}_1^2 + \frac{1}{2} C_2 \dot{\Phi}_2^2 + E_{J1} \cos\theta_1 + E_{J2} \cos\theta_2 \tag{1.43}$$

where the flux variables $\Phi_{1,2}$ are related to the phase variables $\theta_{1,2}$ through

$$\theta_{1,2} = 2\pi \Phi_{1,2} / \Phi_0. \tag{1.44}$$

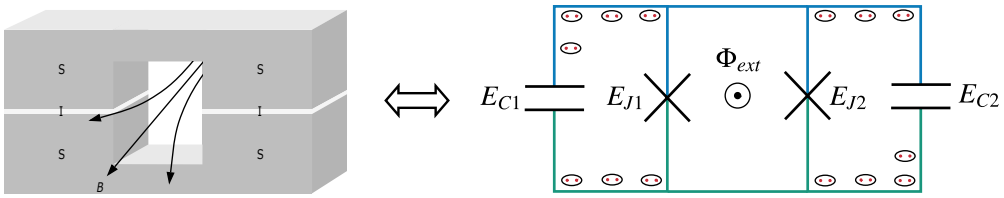

Figure 1.5: The sketch of a split Josephson junction and its circuit model. The superconducting loop formed by the two junctions allows for external flux control of the circuit.

Eq. 1.42 to 1.44 combine to a new Lagrangian

$$\mathcal{L} = \frac{1}{2}\left(C_1 + C_2\right)\dot{\Phi}_1^2 + C_2\dot{\Phi}_{ext}\dot{\Phi}_1 + E_{J1}\cos\theta_1 + E_{J2}\cos\left(\theta_1 + 2\pi\frac{\Phi_{ext}}{\Phi_0}\right), \tag{1.45}$$

which finally leads to a Hamiltonian

$$\hat{\mathcal{H}} = \frac{\left(4e^2\hat{n}_1 - C_2\dot{\Phi}_{ext}\right)^2}{2\left(C_1 + C_2\right)} - E_{J1}\cos\hat{\theta}_1 - E_{J2}\cos\left(\hat{\theta}_1 + 2\pi\frac{\Phi_{ext}}{\Phi_0}\right), \tag{1.46}$$

with the same commutation relationship between $\hat{n}_1$ and $\hat{\theta}_1$ as Eq. 1.39. Further assuming the external flux to be quasi-static[1], i.e. $\dot{\Phi}_{ext} \approx 0$, Eq. 1.46 is reduced to the formed of a single Josephson junction Hamiltonian,

$$\hat{\mathcal{H}} = 4E_c\hat{n}^2 - E_J^{\text{eff}}\cos\left(\hat{\theta} + \theta_0\right), \tag{1.47}$$

where $E_c = e^2/2\left(C_1 + C_2\right)$, E_J^{eff} is the effective Josephson energy modified by the external flux,

$$E_J^{\text{eff}} = \left(E_{J1} + E_{J2}\right)\sqrt{\cos\left(\pi\frac{\Phi_{ext}}{\Phi_0}\right)^2 + \left(\frac{E_{J1} - E_{J2}}{E_{J1} + E_{J2}}\right)^2\sin\left(\pi\frac{\Phi_{ext}}{\Phi_0}\right)^2}, \tag{1.48}$$

and θ_0 is the phase offset

$$\theta_0 = \pi\frac{\Phi_{ext}}{\Phi_0} - \arctan\left[\frac{E_{J1} - E_{J2}}{E_{J1} + E_{J2}}\tan\left(\pi\frac{\Phi_{ext}}{\Phi_0}\right)\right]. \tag{1.49}$$

1. The case with time-dependent external flux will be discussed in Chapter 2.

When the flux is quasi-static, the phase offset can be eliminated by the phase displacement transformation $\hat{U}_{\theta_0} = \exp(i\theta_0\hat{n})$,

$$\hat{\mathcal{H}}_{\text{new}} = \hat{U}_{\theta_0}\mathcal{H}\hat{U}_{\theta_0}^{\dagger} = 4E_c\hat{n}^2 - E_J^{\text{eff}}\cos\hat{\theta}, \tag{1.50}$$

without affecting the boundary condition of the wavefunction[1]. Observe that the detailed form of θ_0 is dependent on our definition of the charge/phase variable in Eq. 1.45. In the static flux scenario, the Hamiltonian is invariant under any normalized linear combination of θ_1 and θ_2 as the phase offset can always be gauged away. We may approximate the dc-SQuID as a single Josephson junction with flux-tunable Josephson energy.

1.2.4 Control, readout and storage

Before we have seen how the superconducting LC circuit can act like a quantum harmonic oscillator and the Josephson junction as a nonlinear artificial atom. By integrating these two critical components together, we can replicate the same light-matter interaction between the optical cavity and natural atoms as in the cavity QED system. The laser drives in cavity QED is then replaced by dc or microwave pulses for the control and readout of the circuit QED system, represented by the conceptual circuit diagram in Fig. 1.6 with a driven Hamiltonian (with $\hbar = 1$)

$$\hat{\mathcal{H}} = \tilde{\omega}_r\hat{a}^{\dagger}\hat{a} + \frac{\tilde{\omega}_q}{2}\sigma_z + \chi\hat{a}^{\dagger}\hat{a}\sigma_z + \hat{\mathcal{H}}_{\text{drive}}(t), \tag{1.51}$$

where $\tilde{\omega}_{r,q}$ are the dressed frequencies of the qubit and the cavity different from their bare frequencies $\omega_{r,q}$, χ is a qubit-state-dependent shift to the cavity (or a photon-number-dependent shift to the qubit, depending on which mode one looks at), and $\hat{\mathcal{H}}_{\text{drive}}(t)$ stands for the time-dependent external drive that brings about all kinds of interesting dynamics. Some may even argue that it is the

1. This is because there is no real boundary for the charge basis as it can go to $\pm\infty$, to be contrasted with the phase variable which is compact so that a charge displacement transformation can indeed alter the boundary condition. This is why the charge offset (see more discussions in Chapter 2) generally affects the energy spectrum unless the compactness of θ is removed by, say, the shunting inductor in the fluxonium's case.

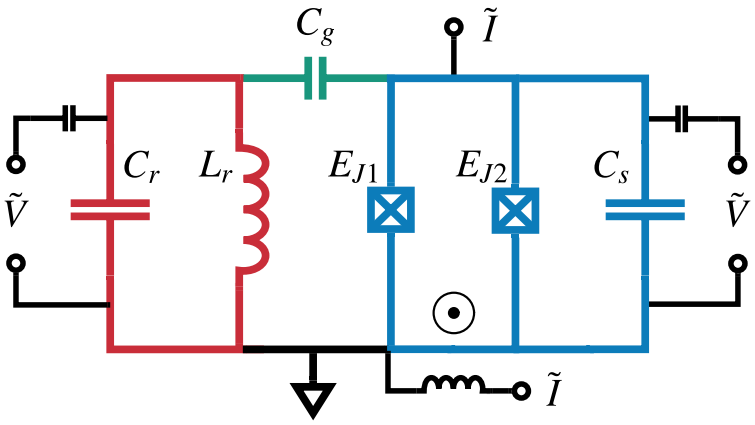

Figure 1.6: A generalized superconducting circuit model with all the control knobs such as voltage, current and flux controls.

$\hat{\mathcal{H}}_{\text{drive}}(t)$ that makes superconducting circuit such an amazing tool for probing quantum physics, as it can be flexibly engineered to possess a wealth of interaction terms with decent amplitudes, through quasi-static or dynamic modulations of the circuit control knobs involving voltage, current and flux. Qubit states can be flipped and multiple qubits can simultaneously interact with each, fulfilling the requirement for universal quantum operations. Circuit QED features substantially larger coupling strength that facilitates the high-fidelity dispersive readout of the qubit state from the χ term, which is a quantum non-demolition measurement[1] of σ_z that can be applied either repetitively or in a single-shot fashion with the aid of parametric amplifiers [59].

Aside from nice control and readout properties, superconducting qubits in different parameter regimes are optimized over the years to achieve long coherence times for storing quantum information. From the prototype qubit of Cooper-pair box which only has nanosecond level coherence time barely enough for the observation of coherent oscillation [60], to the modern transmon and fluxonium qubit that approach millisecond lifetime [61, 62], it only takes three years on average for a 10-fold improvement of the coherence time, a phenomenon nicknamed "Schoelkopf's law" as the quantum computing version of the "Moore's law". In this process, a variety of useful qubit concepts have been demonstrated, including the quantronium [63], the phase qubit [64], the flux

1. This is only true in a perturbation sense as the electric-dipole coupling doesn't commute with σ_z.

qubit [46], tunable coupling circuits [65, 66, 67, 68, 69, 70, 71, 72], etc, accompanied by scientific and technological breakthroughs within and beyond circuit QED. Superconducting quantum circuits are now being scaled up experimentally to systems with several tens of qubits [73, 74, 75], capable of performing a large number of high-fidelity quantum gates with control and readout operations.

1.3 Thesis Overview

We intend to put the experiment and theory on equal footing in this dissertation. Chapter 2 introduces some frequently used analytical and numerical methods for circuit QED calculation, crucial for the understanding and the design of superconducting circuits. Their applications are demonstrated with concrete examples for more intuition comprehension of each case. Mathematical descriptions of the driven Hamiltonians are found for superconducting circuits subject to different parametric modulations, namely the modulation of voltage, current and flux as the focus of this thesis. Discussion is also made for the correct quantization scheme of flux-driven circuits. Chapter 3 analyzes how "sidebands", i.e. the quasi-energy levels of the qubit, can be generated when the qubit frequency is parametrically modulated, useful for the creation of the stimulated Vacuum Rabi oscillation that is vital to scalable circuit QED architecture. The data begins to flow in this chapter where the multimode circuit and the quantum communication circuits are experimentally tested under qubit frequency modulation, with a pursuit of achieving higher connectivity and scalability in superconducting circuits. The investigation of parametric flux modulation continues in Chapter 4, but with a different focus on the modulation of the coupling strength, which calls for more dedicated tunable coupling circuit devices. Based on a solid theoretical ground, We explore how sideband interactions come into play through the parametric control of our tunable coupling circuit, and how they can be manipulated in the experiment to our advantage for parametric amplification, photon swapping operation and most interestingly, the universal stabilization of a single qubit state as well as two qubit Bell states. This sets a firm foundation for Chapter 5, where all the previous knowledge of driven superconducting circuits are combined to achieve the ultimate

goal of autonomous quantum error correction (AQEC), a prerequisite for the realization of universal quantum computation. We demonstrate our experimental implementation of AQEC with the specially designed VSLQ circuit, and provide a thorough explanation of its working mechanism built on top of driven dissipation processes. Rather than a report of separated experiments, this thesis aims to present a dynamic collection of several published works as well as newly-made unpublished observations, both in theory and in experiment, that are organically interlinked by the theme line of parametric flux control of superconducting circuits, testifying its full power as an indispensable resource of circuit QED that is worth further explorations.

CHAPTER 2

CIRCUIT QUANTUM ELECTRODYNAMICS

In the previous chapter, we introduced some background knowledge about quantum computation and set up the basic framework of quantum computing with superconducting circuits, where we have seen how the individual components of a circuit, such as the LC oscillator and the Josephson junction, can be treated as linear and nonlinear quantum modes. In practice, a useful superconducting circuit possessing adequate functionalities is almost always a multiplex system containing several or even tens of quantum modes coupled to each other. It is therefore of vital importance to develop a quantum description for such integrated quantum circuits as well as for the external drives they are subject to. In this chapter, we first briefly review the circuit quantization technique capable of systematically finding static and driven circuit Hamiltonians, then proceed to establish the Hamiltonian model for different types of parametric modulations. Important canonical transformations and useful numerical simulation methods are also covered, aiming to provide further insights to the reader. Throughout this chapter, for better concreteness and consistency, we base all our discussions on one particular circuit example depicted in Fig. 1.6, which is a hypothetical circuit model containing all the circuit elements and control knobs well-suited for pedagogical purpose.

2.1 Quantization of Superconducting Circuits

In this section we restrict our discussions to the circuits with physical sizes much smaller than their characteristic wavelengths, allowing for a lumped element interpretation decomposing the circuit into separate inductors and capacitors. The central idea of circuit quantization can be condensed into the following procedures [76, 77]: first find the energy for all inductive elements based on their flux (phase) drops, which is $\Phi^2/2L$ for a linear inductor and $-E_J \cos(2\pi\Phi/\Phi_0)$ for a Josephson junction, then the voltage V_i at each node i of the circuit network is determined by circuit geometry and Kirchhoff's law as a linear combination of all voltage drops $\dot{\Phi}$, enabling the rest capacitive

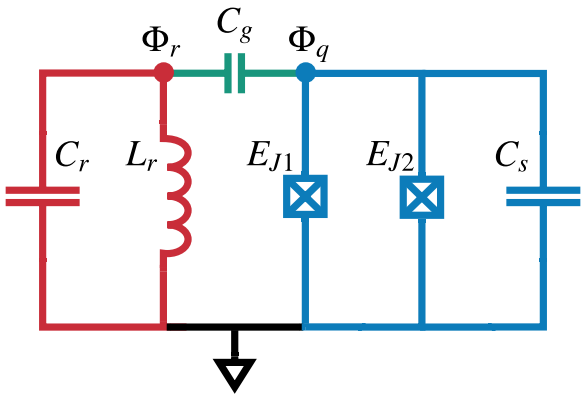

Figure 2.1: Circuit quantization using node flux variables, Φ_r and Φ_q.

energy, $\frac{1}{2}CV^2$, to be expressed as a function of $\dot{\Phi}$, which can be thought of as the kinetic part of the circuit Lagrangian while inductive energy the potential part. The circuit Hamiltonian is then constructed, and the circuit quantization is completed through the canonical quantization process introduced in Chapter 1.

In actual calculations, it is usually much more convenient to use the "node flux" Φ_i for each node i, than the flux drop $\Phi_{ij} = \Phi_i - \Phi_j$ as circuit variables. As a concrete example, let us consider the quantization of the circuit in Fig. 2.1. Among all the nodes in a circuit, one can always be chosen as the "reference node" where the node flux is simply set to zero. We set the node where the circuit is electrically grounded as the reference node, leaving the other two "active nodes" labeled as Φ_r and Φ_q. The circuit Lagrangian is straightforwardly represented by

$$\mathcal{L} = T - V = \frac{1}{2}C_r\dot{\Phi}_r^2 + \frac{1}{2}C_s\dot{\Phi}_q^2 + \frac{1}{2}C_g\left(\dot{\Phi}_r - \dot{\Phi}_q\right)^2 - \frac{\Phi_r^2}{2L_r} + E_{J\Sigma}\cos\left(2\pi\frac{\Phi_q}{\Phi_0}\right), \tag{2.1}$$

where $E_{J\Sigma}$ is the effective Josephson energy of the SQuID given by Eq. 1.48. The charge variables are

$$\begin{aligned} Q_r &= \frac{\partial\mathcal{L}}{\partial\dot{\Phi}_r} = \left(C_r + C_g\right)\dot{\Phi}_r - C_g\dot{\Phi}_q, \\ Q_q &= \frac{\partial\mathcal{L}}{\partial\dot{\Phi}_q} = \left(C_s + C_g\right)\dot{\Phi}_q - C_g\dot{\Phi}_r, \end{aligned} \tag{2.2}$$

which can be written in the matrix representation as

$$\mathbf{Q} = \mathbf{C}\dot{\mathbf{\Phi}}. \tag{2.3}$$

Recall that the kinetic energy is actually from $\frac{1}{2}C\dot{\Phi}^2$ which also has a matrix form of

$$T = \frac{1}{2}\dot{\mathbf{\Phi}}^T\mathbf{C}\dot{\mathbf{\Phi}} = \frac{1}{2}\mathbf{Q}^T\mathbf{C}^{-1}\mathbf{Q}, \tag{2.4}$$

so the circuit Lagrangian may finally be written in terms of the conjugate variables, Q and Φ:

$$\mathcal{L} = T - V = \frac{1}{2}\mathbf{Q}^T\mathbf{C}^{-1}\mathbf{Q} - \frac{\Phi_r^2}{2L_r} + E_{J\Sigma}\cos\left(2\pi\frac{\Phi_q}{\Phi_0}\right), \tag{2.5}$$

and the quantum Hamiltonian after the canonical quantization is

$$\hat{\mathcal{H}} = \frac{1}{2}\hat{\mathbf{Q}}^T\mathbf{C}^{-1}\hat{\mathbf{Q}} + \frac{\hat{\Phi}_r^2}{2L_r} - E_{J\Sigma}\cos\left(2\pi\frac{\hat{\Phi}_q}{\Phi_0}\right). \tag{2.6}$$

Expanding the kinetic energy and translating everything into the number and phase basis give

$$\hat{\mathcal{H}} = 4E_{cr}\hat{n}_r^2 + \frac{1}{2}E_l\hat{\theta}_q^2 + 4E_{cq}\hat{n}_q^2 - E_{J\Sigma}\cos\hat{\theta}_q + 4E_{cg}\hat{n}_r\hat{n}_q, \tag{2.7}$$

which is clearly constituted of a linear oscillator mode and a nonlinear Josephson junction mode, coupled to each other via the "dipole-dipole" interaction induced by the coupling capacitor. In this particular case, we can readily transform the basis of the circuit Hamiltonian into the tensor product of harmonic oscillator basis and the Mathieu's function, so that the overall wavefunction of the coupled system can be easily obtained from matrix rediagonalization. For more general cases, one can typically follow the same principle of first finding out the spectrum for each mode, either numerically or analytically, and then combining and diagonalizing the joint Hamiltonian. One caveat should be noticed when the modes are coupled through nonlinear interactions such as a Josephson energy, where this modular approach becomes ineffective and one needs to numerically solve the

Schrödinger equation for the complete circuit wavefunction in the multidimensional Hilbert space, which is of course much more computationally expensive.

2.2 Parametric Modulation of Superconducting Circuits

Parametric modulation is not a new concept in mechanics and electronics, and is usually associated with frequency conversion and amplification process. The most canonical example of parametric modulation is perhaps a child on a swing, where modulating frequency at twice the resonance frequency results in an amplification of the oscillation. In this section and in the rest of the thesis, parametric control of superconducting circuits is defined, in a more general sense, as the engineering of circuit Hamiltonian with time-dependent circuit parameters, by coupling the circuit to different control knobs. Roughly speaking, superconducting circuits have three typical control knobs, namely the voltage, current and flux control, which we will describe in the following subsections.

2.2.1 Modulation of gate voltage

The charge control of a superconducting circuit is enabled by coupling a voltage source to an active node of the circuit, illustrated in Fig. 2.2. For simplicity, we ignore the resonator part of the circuit for this discussion. The voltage then induces a polarization charge $C_g V_g$ on the Josephson capacitor[1], which modifies the energy of the Josephson nonlinear mode as[2]

$$\hat{\mathcal{H}} = 4E_c \left(\hat{n} - n_g\right)^2 - E_J \cos\hat{\theta}, \tag{2.8}$$

where $n_g = C_g V_g / 2e$ is called the charge offset. We ignore the voltage division of $C_g V_g / \left(C_g + C_r\right)$ on the resonator for simplicity. Note that the charge offset is a classical quantity as the measurement of the applied external voltage and hence a continuous variable. Microscopically it corre-

1. C_g here is the gate capacitor not to be confused with the coupling capacitor in the previous subsection. The name "gate" is merely a historical convention originating from the way gates were performed for a Cooper-pair box.

2. See Appendix. 6.2 for its derivation.

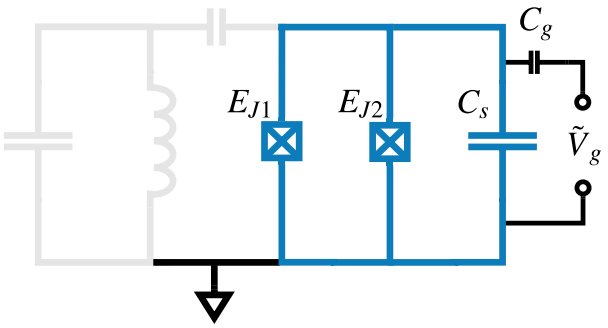

Figure 2.2: Modulation of the gate voltage V_g of a Josephson junction. The resonator part is grayed out for being irrelevant to the discussion.

sponds to a "bodily displacement of the electron fluid in the electrodes with respect to the ion lattice" [78]. We may be tempted to formally cancel out the charge offset through a gauge transformation $\hat{n} \to \hat{n} + n_g$, but only at the expense of altering the boundary condition of the Josephson junction wavefunction in the phase basis, which will no longer be perfectly 2π-periodic but up to a phase, much like a Bloch wave in the 1D periodic lattice with a wave vector $k = n_g$. Similar to the band structure exhibited by the solid-state system, the Josephson junction also has an energy-charge dispersion relation [48],

$$E_m\left(n_g\right) = E_c a_{2[n_g + k(m,n_g)]}\left(-E_J/2E_c\right), \tag{2.9}$$

where $a_\nu\left(q\right)$ denotes Mathieu's characteristic value, and $k\left(m, n_g\right)$ is a eigenvalue-sorting function defined as

$$k\left(m, n_g\right) = \sum_{l=\pm 1}\left[\text{int}\left(2n_g + \frac{l}{2}\right) \bmod 2\right]\left\{\text{int}\left(n_g\right) + l\left(-1\right)^m\left[\left(m+1\right) \text{div } 2\right]\right\}. \tag{2.10}$$

We plot the dispersion relation for $0 < n_g < 0.5$ under different E_J/E_c ratios 1.0, 10.0 and 50.0, in Fig. 2.3. Noticeably, in the two different regimes where $E_J \leq E_c$ and $E_J \gg E_c$, the Josephson mode has drastically different properties. The first regime is like a insulator phase where localization of Cooper pairs prevails, manifested by the strong dependence of the energy

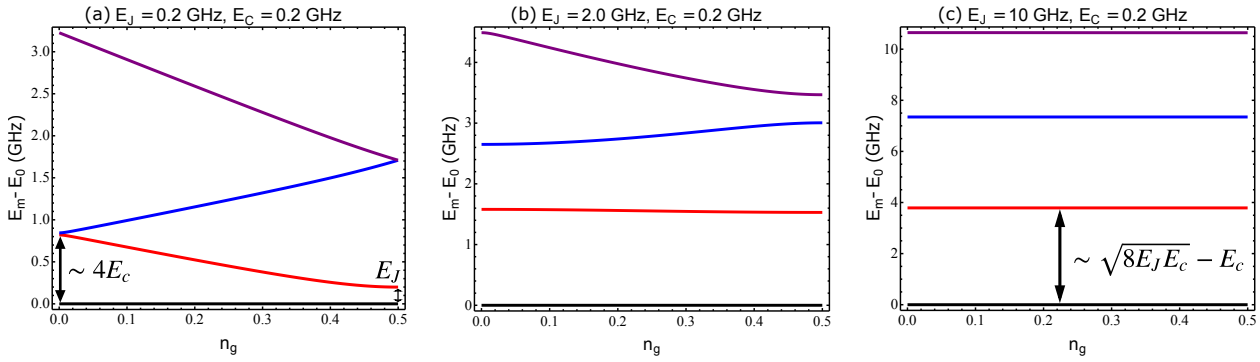

Figure 2.3: Energy bands of the Josephson nonlinear mode at different E_J/E_c ratios, with E_c fixed at 0.2 GHz. As the ratio is increased the charge dispersion becomes exponentially suppressed, making the mode highly immune to charge noise.

spectrum against the perturbation of the charge offset. The lowest two energies have a charge-tunable spacing of

$$E_{01} = \sqrt{E_J^2 + \left[4E_c\left(1 - 2n_g\right)\right]^2}, \tag{2.11}$$

which is suitable as a qubit given its large anharmonicity. Indeed, this is the well-known Cooper-pair box (CPB) [60, 79], one of the early generations of superconducting qubit.

When the E_J/E_c ratio increases, the energy bands begin to lose their dependence on the bias charge, as the tunneling of Cooper pairs becomes more and more energetically favorable, and the system settles on a "superfluid" phase insensitive to low energy charge fluctuations. In the extreme case of $E_J \gg E_c$, the system is equivalent to a 1D tight-binding model with nearest-neighbor hopping, giving rise to a dispersion relation as a cosine function of the wave vector (charge offset),

$$E_m\left(n_g\right) = \bar{E}_m + \epsilon_m \cos\left(n_g 2\pi\right), \tag{2.12}$$

with charge dispersion ϵ_m being

$$\epsilon_m \sim (-1)^{m+1} E_c \frac{2^{4(m+1)}}{m!}\sqrt{\frac{2}{\pi}}\left(\frac{E_J}{2E_c}\right)^{\frac{m}{2}+\frac{3}{4}} e^{-\sqrt{8E_J/E_c}}. \tag{2.13}$$

The exponential insensitivity of the energy levels to charge fluctuation endows substantially longer

coherence time to the so-called transmon qubit, who possesses an offset-charge-free transition energy between the ground and the first excited state,

$$E_{01} = \sqrt{8E_J E_c} - E_c, \tag{2.14}$$

with anharmonicity $\alpha \sim E_c$.

When the gate voltage becomes time-dependent, so will be the charge offset and Eq. 2.8 becomes

$$\hat{\mathcal{H}}(t) = 4E_c\hat{n}^2 - E_J \cos\hat{\theta} - 8E_c n_g(t)\,\hat{n}. \tag{2.15}$$

In the weak interaction limit, assuming the energy scale of the drive term is much less than the static Hamiltonian, we can safely approximate the drive term as a perturbation which doesn't affect the wavefunctions, and can therefore be expressed in the same basis as the static Hamiltonian[1],

$$\hat{\mathcal{H}}(t) = \left(\sqrt{8E_c E_J} - E_c\right)\hat{a}^\dagger\hat{a} - \frac{E_c}{2}\hat{a}^{\dagger 2}\hat{a}^2 - 8n_g(t)\,E_c\left(\frac{E_J}{8E_c}\right)^{1/4}\frac{i\left(\hat{a}-\hat{a}^\dagger\right)}{\sqrt{2}}, \tag{2.16}$$

where we have assumed the transmon regime, and kept the leading order perturbation in the expansion of ladder operators. We see that the voltage modulation is essentially arising from the coupling between the external field coupled to the dipole moment of the artificial atom, akin to the interaction between the laser and natural atoms. Just like laser driving in cavity QED, voltage modulation is the most elementary yet important control scheme in circuit QED that leads to fascinating dynamics such as Rabi oscillation and four-wave mixing that we will further explore in section 2.3.

1. When the drive term becomes comparable to the static part of the Hamiltonian, a re-quantization of the circuit at each n_g is necessary to find out the correct wavefunctions in either phase or charge basis, which can then be used for the calculation of the evolution.

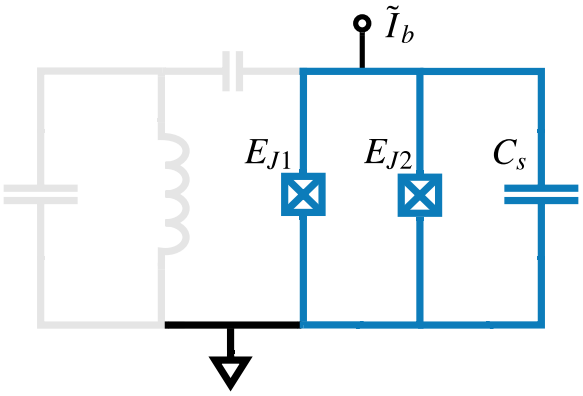

Figure 2.4: Modulation of the bias current I_b of a Josephson junction. The resonator part is grayed out for being irrelevant to the discussion.

2.2.2 *Modulation of bias current*

We include the modulation of bias current into our discussion for the sake of completeness and generality, although this scheme is very rarely practiced outside the field of phase qubits [64]. Shown in Fig. 2.4, a Josephson junction (for simplicity we take the split junction as one, assuming zero penetrating flux) is biased by an external current I_b from coupling to a current source. The external current and the Josephson voltage together give rise to a coupling energy of

$$E = \int I_b V dt = I_b \Phi_0 \theta, \tag{2.17}$$

leading to a circuit Hamiltonian (again neglecting the resonator part) of

$$\hat{\mathcal{H}} = 4E_c \hat{n}^2 - E_J \cos\hat{\theta} + I_b \Phi_0 \hat{\theta}, \tag{2.18}$$

with a potential energy resembling a "tilted washboard". Phase qubits are typically operated at strong biasing current approaching the critical current of junction, leading to a cubic well that traps three levels at the local minimum of the potential, with the lowest two being the qubit and the top one for readout. Instead, we consider a time-dependent small current $I_b(t)$ modulating a

transmon qubit at the "current sweetspot", where the driven Hamiltonian can be written as

$$\hat{\mathcal{H}}(t) = \left(\sqrt{8E_cE_J} - E_c\right)\hat{a}^\dagger\hat{a} - \frac{E_c}{2}\hat{a}^{\dagger 2}\hat{a}^2 - I_b(t)\,\Phi_0\left(\frac{8E_c}{E_J}\right)^{1/4}\frac{\hat{a}+\hat{a}^\dagger}{\sqrt{2}}, \tag{2.19}$$

which has similar effects to the voltage modulation in Eq. 2.16 as they are off by merely a phase difference.

2.2.3 Modulation of SQuID flux

In section 1.2.3, we have demonstrated the static tuning of the effective Josephson energy from flux biasing a dc-SQuID. Here we extend our investigation to the dynamic modulation of the SQuID flux shown in Fig 2.5, where $\Phi_{ext} = 0$ is time-dependent and $\dot{\Phi}_{ext} = 0$ no longer holds true for Eq. 1.46,

$$\hat{\mathcal{H}} = \frac{\left(4e^2\hat{n}_1 - C_2\dot{\Phi}_{ext}(t)\right)^2}{2(C_1+C_2)} - E_{J1}\cos\hat{\theta}_1 - E_{J2}\cos\left(\hat{\theta}_1 + 2\pi\frac{\Phi_{ext}(t)}{\Phi_0}\right), \tag{2.20}$$

Recall that there is a "freedom" in choosing the phase variable - we can parameterize the two phases in the follow way without violating the flux quantization relation:

$$\Phi_1 = \Phi_0 + r_1\Phi_{ext}, \quad \Phi_2 = \Phi_0 + r_2\Phi_{ext} \tag{2.21}$$

with $r_2 - r_1 = 1$. Plugging them back to the SQuID Lagrangian yields

$$\mathcal{L} = \frac{1}{2}(C_1+C_2)\dot{\Phi}_0^2 + (C_1r_1 + C_2r_2)\dot{\Phi}_0\dot{\Phi}_{ext} + E_{J1}\cos(\theta_0 + r_1\theta_{ext}) + E_{J2}\cos(\theta_0 + r_2\theta_{ext}), \tag{2.22}$$

and

$$\hat{\mathcal{H}} = \frac{\hat{Q}_0^2}{2(C_1+C_2)} + \frac{(C_1r_1 + C_2r_2)\hat{Q}_0\dot{\Phi}_{ext}}{2(C_1+C_2)} - E_{J1}\cos\left(\hat{\theta}_0 + r_1\theta_{ext}\right) - E_{J2}\cos\left(\hat{\theta}_0 + r_2\theta_{ext}\right), \tag{2.23}$$

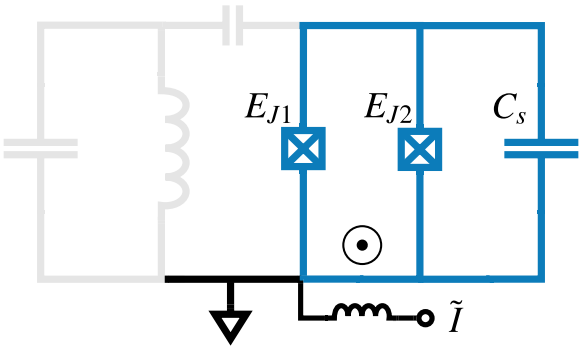

Figure 2.5: Modulation of the SQuID flux Φ_{ext} with time-dependent current signal. The resonator part is grayed out for being irrelevant to the discussion.

where the $\dot{\Phi}_{ext}$ terms in the kinetic energy can be removed from setting

$$r_1 = -\frac{C_2}{C_1 + C_2}, \quad r_2 = \frac{C_1}{C_1 + C_2}, \tag{2.24}$$

resulting in a simplified Hamiltonian of

$$\hat{\mathcal{H}} = \frac{\hat{Q}_0^2}{2\left(C_1 + C_2\right)} - E_{J1}\cos\left(\hat{\theta}_0 - \frac{C_2\theta_{ext}}{C_1 + C_2}\right) - E_{J2}\cos\left(\hat{\theta}_0 + \frac{C_1\theta_{ext}}{C_1 + C_2}\right). \tag{2.25}$$

Remarkably, it has been proved that the particular gauge choice in Eq. 2.24 is more than a personal preference for the sake of Hamiltonian simplification - it is, in fact, the only correct way of quantizing the circuit under time-dependent external flux[1], while all the other choices cause inconsistency issues for the calculation of flux-driven transition rates [80]. Using trigonometry relationships Eq. 2.25 can be compactly written as

$$\hat{\mathcal{H}}\left(t\right) = 4E_c\hat{n}^2 - E_J^{\text{eff}}\left(t\right)\cos\left[\hat{\theta} + \theta_0\left(t\right)\right], \tag{2.26}$$

1. See Appendix. 6.3 for the general quantization procedure incorporating dynamic flux modulations.

where $E_c = e^2/2\,(C_1 + C_2)$, $E_J^{\text{eff}}(t)$ is the time-dependent effective Josephson energy,

$$E_J^{\text{eff}}(t) = (E_{J1} + E_{J2}) \cos\left[\pi \frac{\Phi_{ext}(t)}{\Phi_0}\right] \sqrt{1 + \left(\frac{E_{J1} - E_{J2}}{E_{J1} + E_{J2}}\right)^2 \tan\left[\pi \frac{\Phi_{ext}(t)}{\Phi_0}\right]^2}, \tag{2.27}$$

and $\theta_0(t)$ is the time-dependent phase offset

$$\theta_0(t) = \frac{2\pi C_1}{C_1 + C_2} \frac{\Phi_{ext}(t)}{\Phi_0} - \arctan\left\{\frac{E_{J1} - E_{J2}}{E_{J1} + E_{J2}} \tan\left[\pi \frac{\Phi_{ext}(t)}{\Phi_0}\right]\right\}. \tag{2.28}$$

Finally, Eq. 2.26 can be regrouped in static and dynamic terms,

$$\begin{aligned} \hat{\mathcal{H}}(t) &= 4E_c\hat{n}^2 - \overline{f_c(t)} \cos\hat{\theta} + \overline{f_s(t)} \sin\hat{\theta} \\ &- \left\{f_c(t) - \overline{f_c(t)}\right\} \cos\hat{\theta} + \left(f_s(t) - \overline{f_s(t)}\right) \sin\hat{\theta}, \end{aligned} \tag{2.29}$$

where

$$f_c(t) = E_J^{\text{eff}}[\Phi_{ext}(t)] \cos[\theta_0(t)], \quad f_s(t) = E_J^{\text{eff}}[\Phi_{ext}(t)] \sin[\theta_0(t)], \tag{2.30}$$

and the bar represents time-averaged value. We rewrite Eq. 2.29 as

$$\hat{\mathcal{H}}(t) = 4E_c\hat{n}^2 - \overline{E_J} \cos\hat{\theta} - F_c(t) \cos\hat{\theta} + F_s(t) \sin\hat{\theta}, \tag{2.31}$$

where we have already gauged away the static offset from merging the cosine and sine potential. For a transmon, this driven Hamiltonian can be expressed in terms of the ladder operators as

$$\begin{aligned} \mathcal{H}(t) &= \left(\sqrt{8E_c\overline{E_J}} - E_c\right) \hat{a}^\dagger\hat{a} - \frac{E_c}{2}\hat{a}^{\dagger 2}\hat{a}^2 \\ &+ \frac{F_c(t)}{2}\sqrt{\frac{2E_c}{\overline{E_J}}}\left(\hat{a}^\dagger + a\right)^2 + F_s(t)\left(\frac{8E_c}{\overline{E_J}}\right)^{1/4} \frac{\hat{a} + \hat{a}^\dagger}{\sqrt{2}}. \end{aligned} \tag{2.32}$$

This reveals that the transmon frequency could be shifted by the flux modulation due to the non-linearity $E_J^{\text{eff}}(t)$, which is known as the dc-offset observed in our experiment.

2.3 Important Canonical Transformations in Circuit-QED

In this section we discuss some of the most important canonical transformations that have been frequently and widely applied in the field of circuit-QED. These analytical methods are not only great at reducing the computation complexity mathematical wise, but also immensely helpful for acquiring physical insight of the quantum system we are working with. We base our discussion on a detailed problem for the first three transformations, and practice all four on a "grand example" in the finale subsection.

2.3.1 Bogoliubov-Valatin transformation

The Bogoliubov-Valatin (B-V) transformation was initially developed for finding solutions of BCS theory in the context of superfluidity, and soon became a successful effective theories for quantum many-body systems. Here we introduce it, pertinent to our discussions, as a diagonalization technique for bosonic quadratic Hamiltonians. To get a flavor, let's take a moment to look at the original Bogoliubov theory with a Hamiltonian that describes the weakly interacting Bose gas [81],

$$\hat{\mathcal{H}} = \sum_{p\neq 0} \frac{p^2}{2m} \hat{a}_p^\dagger \hat{a}_p + \frac{1}{2} gn \sum_{p\neq 0} \left(2\hat{a}_p^\dagger \hat{a}_p + \hat{a}_p^\dagger \hat{a}_{-p}^\dagger + \hat{a}_p \hat{a}_{-p} \right), \tag{2.33}$$

where $\hat{a}_p$ is the annihilation operator for a single particle state of a plane wave with momentum p. Then the spectral properties of this Hamiltonian can be found from the following transformation,

$$\hat{a}_p = u b_p + v b_{-p}^\dagger, \quad \hat{a}_p^\dagger = u b_p^\dagger + v b_{-p}. \tag{2.34}$$

The commutation relationship between a_p and $a_p^\dagger$ imposes a constraint for parameters u and v,

$$u^2 - v^2 = 1. \tag{2.35}$$

Plugging Eq. 2.34 into Eq. 2.33, we find that the non-diagonal terms disappears at

$$\frac{gn}{2}\left(u^2+v^2\right)+\left(\frac{p^2}{2m}+gn\right)uv=0, \tag{2.36}$$

which, along with Eq. 2.35 ,uniquely determines u and v as

$$u,\ v=\pm\sqrt{\frac{p^2/2m+gn}{2\epsilon\left(p\right)}\pm\frac{1}{2}}, \tag{2.37}$$

where

$$\epsilon\left(p\right)=\sqrt{\frac{gn}{m}p^2+\left(\frac{p^2}{2m}\right)^2} \tag{2.38}$$

gives the famous Bogoliubov dispersion relation. The Hamiltonian is finally diagonalized by the transformation as

$$\hat{\mathcal{H}}=E_0+\sum_{p\neq 0}\epsilon\left(p\right)\hat{b}_p^\dagger\hat{b}_p. \tag{2.39}$$

The above Hamiltonian can be taken as a special case of bosonic quadratic Hamiltonians, which has a more general form of [82, 83]

$$\hat{\mathcal{H}}=\sum_{i,j=1}^{n}\left(m_{ij}\hat{a}_i^\dagger\hat{a}_j+k_{ij}\hat{a}_i^\dagger\hat{a}_j^\dagger+k_{ij}^*\hat{a}_i\hat{a}_j\right). \tag{2.40}$$

For simplicity we limit ourselves to the "normal Hamiltonian",

$$\hat{\mathcal{H}}=\sum_{i,j=1}^{n}m_{ij}\hat{a}_i^\dagger\hat{a}_j, \tag{2.41}$$

with $m_{ij}=m_{ji}^*$. This Hamiltonian only contains the "energy-conserving" terms which is typically a good approximation in circuit-QED. It can be compactly written in a matrix form,

$$\hat{\mathcal{H}}=\frac{1}{2}\mathbf{\Psi}^\dagger\mathbf{M}\mathbf{\Psi}, \tag{2.42}$$

where $\mathbf{\Psi}$ is the bare-mode vector with the annihilation operator with its i-th element being $\hat{a}_i$, and $\mathbf{M}$ is the coefficient matrix with m_{ij} being its entries. $\mathbf{M}$ is obviously Hermitian and can be diagonalized by a unitary matrix $\mathbf{U}$, $\mathbf{UMU}^\dagger = \mathbf{\Omega}$ with the diagonal matrix $\mathbf{\Omega}$ carrying the normal-mode energies ω_i, which also diagonalize the Hamiltonian into

$$\hat{\mathcal{H}} = \frac{1}{2}\mathbf{\Phi}^\dagger \mathbf{\Omega} \mathbf{\Phi} = \sum_i \omega_i \hat{b}_i^\dagger \hat{b}_i, \tag{2.43}$$

where the $\mathbf{\Phi} = \left(\hat{b}_1, \hat{b}_2, \cdots\right)^{\mathrm{T}}$ is the normal-mode vector connecting to the bare modes through

$$\mathbf{\Phi} = \mathbf{U}^\dagger \mathbf{\Psi}. \tag{2.44}$$

Such transformation becomes handy when we encounter coupled linear modes in superconducting circuits, such as the one demonstrated in Fig. 2.6(a) where a transmon is capacitively coupled to a "multimode circuit" consisting of a pair of coupled resonator modes. Skipping the circuit quantization procedure, we empirically write down the circuit Hamiltonian,

$$\hat{\mathcal{H}}/\hbar = \omega_q \hat{a}^\dagger \hat{a} + \frac{\alpha}{2}\hat{a}^{\dagger 2}\hat{a}^2 + g_q\left(\hat{a}^\dagger \hat{b}_1 + \hat{a}\hat{b}_1^\dagger\right) + \omega_{r1}\hat{b}_1^\dagger \hat{b}_1 + \omega_{r2}\hat{b}_2^\dagger \hat{b}_2 + g_r\left(\hat{b}_1^\dagger \hat{b}_2 + \hat{b}_1 \hat{b}_2^\dagger\right), \tag{2.45}$$

where the coefficient of the multimode Hamiltonian is simply

$$\hat{\mathbf{M}} = \begin{pmatrix} \omega_1 & g_r \\ g_r & \omega_2 \end{pmatrix}, \tag{2.46}$$

which can be diagonalized as

$$\hat{\mathbf{M}} = \mathbf{U}^\dagger \mathbf{\Omega} \mathbf{U} = \begin{pmatrix} \cos\theta & -\sin\theta \\ \sin\theta & \cos\theta \end{pmatrix} \cdot \begin{pmatrix} \omega_1' & 0 \\ 0 & \omega_2' \end{pmatrix} \cdot \begin{pmatrix} \cos\theta & \sin\theta \\ -\sin\theta & \cos\theta \end{pmatrix}, \tag{2.47}$$

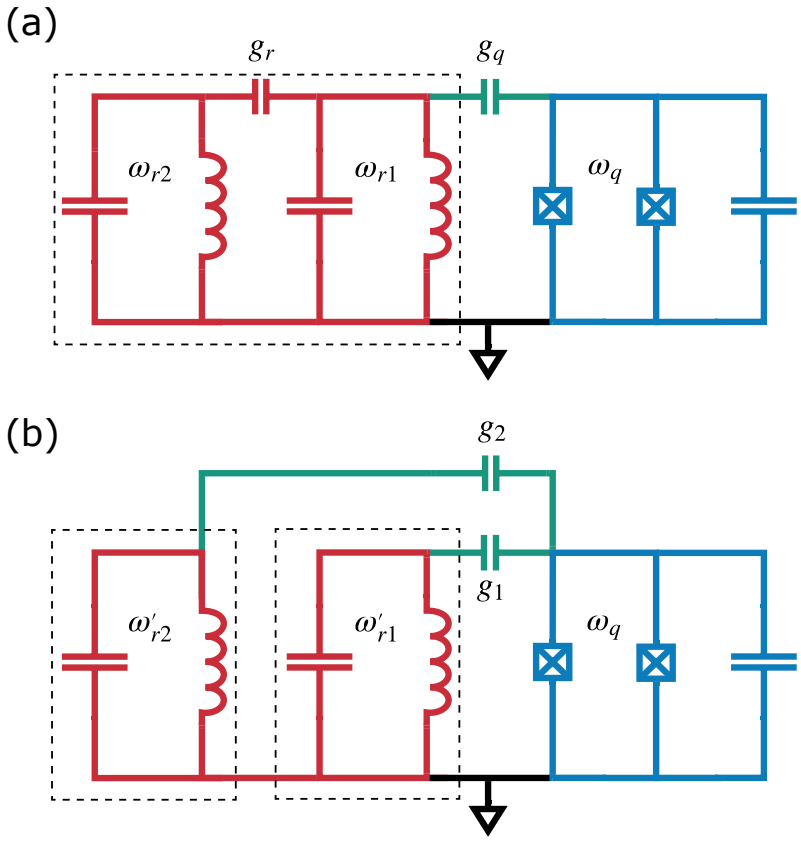

Figure 2.6: The Bogoliubov-Valatin transformation of the multimode circuit. (a) A transmon is capacitively coupled to the multimode within the dashed box that is composed of two coupled LC oscillators. (b) The effective circuit after the Bogoliubov-Valatin transformation, showing that the two bare resonator modes hybridize into two uncoupled normal modes (circled by dashed boxes), which are simultaneously coupled to the transmon with renormalized coupling strengths.

where θ is the mixing angle defined as

$$\theta = \frac{1}{2} \arctan\left(\frac{2g}{\omega_{r2} - \omega_{r1}}\right). \tag{2.48}$$

Under the unitary transformation U the bare resonator mode $\hat{b}_i$ becomes dressed mode $\hat{c}_i$,

$$\begin{pmatrix} \hat{b}_1 \\ \hat{b}_2 \end{pmatrix} = \begin{pmatrix} \cos\theta & \sin\theta \\ -\sin\theta & \cos\theta \end{pmatrix} \cdot \begin{pmatrix} \hat{c}_1 \\ \hat{c}_2 \end{pmatrix}, \tag{2.49}$$

and the circuit Hamiltonian in Eq. 2.45 becomes

$$\hat{\mathcal{H}}/\hbar = \omega_q \hat{a}^\dagger \hat{a} + \frac{\alpha}{2}\hat{a}^{\dagger 2}\hat{a}^2 + g_1\left(\hat{a}^\dagger \hat{c}_1 + \hat{a}\hat{c}_1^\dagger\right) + g_2\left(\hat{a}^\dagger \hat{c}_2 + \hat{a}\hat{c}_2^\dagger\right) + \omega'_{r1}\hat{c}_1^\dagger \hat{c}_1 + \omega'_{r2}\hat{c}_2^\dagger \hat{c}_2. \quad (2.50)$$

We immediately see the two effects of the BV transformation: it not only diagonalizes the multimode circuit into two decoupled normal modes with dressed frequencies $\omega'_{r1,2}$, but also effectively couples the transmon to all the normal modes, with renormalized coupling strength g_i, as shown in Fig. 2.6(b). For the special case of two identical resonators, both effective coupling strengths become $g_q/\sqrt{2}$ regardless of the coupling between the bare modes. A similar result can be obtained for a multimode chain architecture, where the transmon can get full connectivity to all normal modes by only physically coupling to a single bare mode, an extremely important feature for the random access circuit [84, 85, 86] we will discuss in Chapter 3.

2.3.2 Schrieffer-Wolff transformation

Schrieffer-Wolff (S-W) transformation [87, 88, 89] is another important Hamiltonian diagonalization technique. Unlike the B-V transformation where linear modes are precisely diagonalized into normal modes, the S-W transformation is a perturbation theory that can block-diagonalize Hamiltonians with nonlinear modes up to any desired order, given that the block off-diagonal terms can be treated as perturbations. Such Hamiltonians can in general be written as

$$\hat{\mathcal{H}} = \hat{\mathcal{H}}_0 + \epsilon\hat{\mathcal{V}} \quad (2.51)$$

where $\hat{\mathcal{H}}_0$ is block diagonal and $\hat{\mathcal{V}}$ is block off-diagonal, with ϵ being a small quantity representing the energy ratio between the two parts. The goal is to find a unitary transformation such that the transformed Hamiltonian,

$$\overline{\hat{\mathcal{H}}} = e^{\hat{\mathcal{S}}}\hat{\mathcal{H}}e^{-\hat{\mathcal{S}}} \quad (2.52)$$

is block diagonal up to the desired order in ϵ, where $\hat{\mathcal{S}}$ is the generator of the S-W transformation, which is obviously anti-Hermitian.

Eq. 2.52 can be expanded using the Campbell-Baker-Hausdorff formula

$$\overline{\hat{\mathcal{H}}} = \hat{\mathcal{H}}_0 + \epsilon\hat{\mathcal{V}} + \left[\hat{\mathcal{S}}, \hat{\mathcal{H}}_0\right] + \left[\hat{\mathcal{S}}, \hat{\mathcal{V}}\right] + \frac{1}{2!}\left[\hat{\mathcal{S}}, \left[\hat{\mathcal{S}}, \hat{\mathcal{H}}_0\right]\right] + \frac{\epsilon}{2!}\left[\hat{\mathcal{S}}, \left[\hat{\mathcal{S}}, \hat{\mathcal{V}}\right]\right] + \cdots, \tag{2.53}$$

from which we may speculate that the generator $\hat{\mathcal{S}}$ has to be block off-diagonal too (or rather, any block diagonal component of $\hat{\mathcal{S}}$ would be useless for the block diagonalization of $\hat{\mathcal{H}}$), so that all the even order $\left[\hat{\mathcal{S}}, \hat{\mathcal{H}}\right]$ commutators and odd order $\left[\hat{\mathcal{S}}, \hat{\mathcal{V}}\right]$ have to be block off-diagonal, while all the rest terms are block diagonal and have to be zero:

$$\epsilon\hat{\mathcal{V}} + \left[\hat{\mathcal{S}}, \hat{\mathcal{H}}_0\right] + \frac{\epsilon}{2!}\left[\hat{\mathcal{S}}, \left[\hat{\mathcal{S}}, \hat{\mathcal{V}}\right]\right] + \frac{1}{3!}\left[\hat{\mathcal{S}}, \left[\hat{\mathcal{S}}, \left[\hat{\mathcal{S}}, \hat{\mathcal{H}}_0\right]\right]\right] + \frac{\epsilon}{4!}\left[\left[\hat{\mathcal{S}}, \left[\hat{\mathcal{S}}, \left[\hat{\mathcal{S}}, \left[\hat{\mathcal{S}}, \hat{\mathcal{V}}\right]\right]\right]\right]\right] + \cdots = 0, \tag{2.54}$$

Now we are ready to set off a perturbation calculation where we assume $\hat{\mathcal{S}}$ as a power series of ϵ[1],

$$\hat{\mathcal{S}} = \epsilon\hat{\mathcal{S}}_1 + \epsilon^2\hat{\mathcal{S}}_2 + \epsilon^3\hat{\mathcal{S}}_3 + \cdots. \tag{2.55}$$

Plugging this back into Eq. 2.54, we solve $\hat{\mathcal{S}}_i$ iteratively from each order of ϵ,

$$\begin{aligned}
\epsilon &: \quad \hat{\mathcal{V}} + \left[\hat{\mathcal{S}}_1, \hat{\mathcal{H}}_0\right] = 0 && (2.56)\\
\epsilon^3 &: \quad \left[\hat{\mathcal{S}}_3, \hat{\mathcal{H}}_0\right] + \frac{1}{2!}\left[\hat{\mathcal{S}}_1, \left[\hat{\mathcal{S}}_1, \hat{\mathcal{V}}\right]\right] + \frac{1}{3!}\left[\hat{\mathcal{S}}_1, \left[\hat{\mathcal{S}}_1, \left[\hat{\mathcal{S}}_1, \hat{\mathcal{H}}_0\right]\right]\right] = 0 && (2.57)\\
&\vdots
\end{aligned}$$

where all the even order $\hat{\mathcal{S}}_i$ terms are zero[2]. The approximately diagonalized Hamiltonian is thus

$$\overline{\hat{\mathcal{H}}} = \hat{\mathcal{H}}_0 + \left[\hat{\mathcal{S}}_1, \hat{\mathcal{V}}\right] + \frac{1}{2!}\left[\hat{\mathcal{S}}_1, \left[\hat{\mathcal{S}}_1, \hat{\mathcal{H}}_0\right]\right] = \hat{\mathcal{H}}_0 + \frac{1}{2}\left[\hat{\mathcal{S}}_1, \hat{\mathcal{V}}\right] \tag{2.58}$$

1. The zeroth order term is missing because the diagonalization is a small rotation in the Hilbert space.

2. This is only true when the perturbation is purely block off-diagonal, otherwise both even and odd terms should exist.

up to second order in ϵ.

The power of the S-W transformation can be seen in two aspects. First, it is a perturbation theory on quantum operators, returning the diagonalized Hamiltonian in an analytical form that promises intuitive understandings of the system on a quantum physics level. One good example may be the diagonalization of the quantum Rabi model that describes the light-matter interaction in circuit- and cavity-QED,

$$\hat{\mathcal{H}}/\hbar = \hat{\mathcal{H}}_0/\hbar + \hat{\mathcal{V}}/\hbar = \omega_r \hat{a}^\dagger \hat{a} + \frac{\omega_a}{2}\hat{\sigma}_z + g\left(\hat{a}^\dagger + \hat{a}\right)\hat{\sigma}_x, \tag{2.59}$$

which is typically in the dispersive regime where $g \ll \omega_r, \omega_q, \Delta$, so that the coupling term can be treated as an block off-diagonal perturbation, with the ratio g/Δ being "the ϵ". To apply the S-W transformation, we make an reasonable initial guess of the generator $\hat{\mathcal{S}}$ to share the same form of $\hat{\mathcal{V}}/\hbar = g\left(\hat{a}^\dagger\hat{\sigma}^- + \hat{a}^\dagger\hat{\sigma}^+ + h.c.\right)$ except being anti-Hermitian,

$$\hat{\mathcal{S}} = \left(\alpha\hat{a}^\dagger\hat{\sigma}^- - \alpha^*\hat{a}\hat{\sigma}^+\right) + \left(\beta\hat{a}^\dagger\hat{\sigma}^+ - \beta^*\hat{a}\hat{\sigma}^-\right), \tag{2.60}$$

with α and β being the undetermined parameters. Plugging it back to Eq. 2.56, and making use of the commutator relationships in Appendix. 6.4, we obtain the first order perturbation generator as

$$\hat{\mathcal{S}} = \frac{g}{\Delta}\left(\hat{a}^\dagger\hat{\sigma}^- - \hat{a}\hat{\sigma}^+\right) + \frac{g}{\Sigma}\left(\hat{a}^\dagger\hat{\sigma}^+ - \hat{a}\hat{\sigma}^-\right), \tag{2.61}$$

where Δ and Σ are the cavity-qubit detuning and sum frequency, respectively. Combining this with Eq. 2.58 one finds the diagonalized Hamiltonian in the analytical form[1],

$$\overline{\hat{\mathcal{H}}}/\hbar = \tilde{\omega}_r\hat{a}^\dagger\hat{a} + \frac{1}{2}\left(\tilde{\omega}_q - \frac{g^2}{\Delta} + \frac{g^2}{\Sigma}\right)\hat{\sigma}_z - \left(\frac{g^2}{\Delta} - \frac{g^2}{\Sigma}\right)\hat{a}^\dagger\hat{a}\hat{\sigma}_z. \tag{2.62}$$

Here, the g^2/Δ and the g^2/Σ in the qubit frequency term are named "Lamb shift" and "Bloch-Siegert shift", while the last term is the dispersive shift (Stark shift) that can interpreted as qubit-

1. We have abandoned the two-photon terms here because they are higher-order perturbations.

state-dependent cavity shift or vice versa. In the typical regime where $\Sigma \gg \Delta$, this Hamiltonian is further reduced to the textbook dispersive Hamiltonian,

$$\overline{\hat{\mathcal{H}}}/\hbar = \tilde{\omega}_r \hat{a}^\dagger \hat{a} + \frac{1}{2}\left(\tilde{\omega}_q - \frac{g^2}{\Delta}\right)\hat{\sigma}_z - \frac{g^2}{\Delta}\hat{a}^\dagger \hat{a}\hat{\sigma}_z, \tag{2.63}$$

which we have seen as the static part in Eq. 1.51.

The second nice feature of the S-W transformation arises from the fact that it is a block diagonalization technique capable of decoupling any two orthogonal subspaces in a many-body system, as long as their gap is sufficiently larger than their coupling strength. Indeed, the initial invention of the S-W transformation was with the intention of obtaining an effective low energy model for a quantum many-body system by decoupling it from the high energy manifold. As such, we can selectively decouple any m modes from another n modes in a l-mode ($l \leq m+n$) superconducting circuit using the S-W transformation with generator

$$\hat{\mathcal{S}} = \sum_{i=1,j=1}^{m,n} \hat{\mathcal{S}}_{i,j}, \tag{2.64}$$

where $\hat{\mathcal{S}}_{i,j}$ is the S-W transformation generator for decoupling the i-th and j-th mode belonging to the m- and n-mode subgroup, respectively. The simplest circuit example can be found in Fig 2.7(a), where two resonator modes are simultaneously coupled to a flux-tunable transmon, a geometry that can be obtained from the multimode architecture as we have discussed in the previous section. Within the two-level approximation, the circuit Hamiltonian is

$$\hat{\mathcal{H}}/\hbar = \frac{\omega_q}{2}\hat{\sigma}_z + \omega_{r1}\hat{a}_1^\dagger \hat{a}_1 + \omega_{r2}\hat{a}_2^\dagger \hat{a}_2 + g_1\left(\hat{a}_1\hat{\sigma}^+ + \hat{a}_1^\dagger \hat{\sigma}^-\right) + g_2\left(\hat{a}_2\hat{\sigma}^+ + \hat{a}_2^\dagger \hat{\sigma}^-\right). \tag{2.65}$$

According to Eq. 2.61 and Eq. 2.64, the generator of the S-W transformation that decouples the qubit from the resonator manifold reads

$$\hat{\mathcal{S}} = \frac{g_1}{\Delta_1}\left(\hat{a}_1^\dagger \hat{\sigma}^- - \hat{a}_1\hat{\sigma}^+\right) + \frac{g_2}{\Delta_2}\left(\hat{a}_2^\dagger \hat{\sigma}^+ - \hat{a}_2\hat{\sigma}^-\right), \tag{2.66}$$

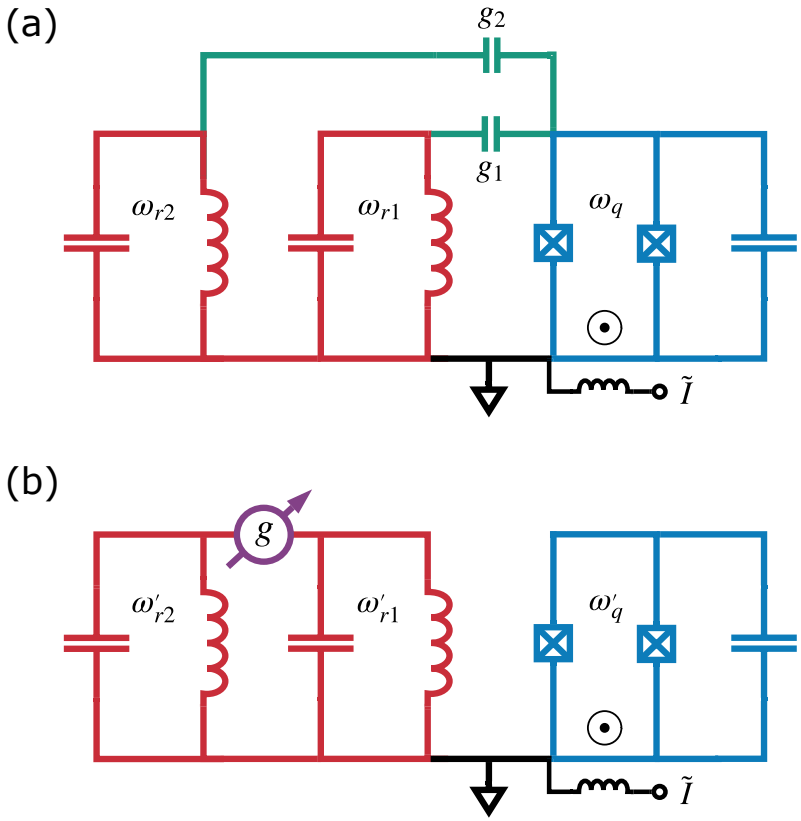

Figure 2.7: The Schrieffer-Wolff transformation of a superconducting circuit. (a) A flux-tunable transmon is coupled to two resonators. (b) The Schrieffer-Wolff transformation decouples the transmon simultaneously from both resonator modes, while creating a flux-tunable coupling strength between the resonators.

and to the leading order in g/Δ the circuit Hamiltonian is S-W transformed to

$$\begin{aligned}\overline{\hat{\mathcal{H}}}/\hbar &= \hat{\mathcal{H}}_0/\hbar + \frac{1}{2}\left[\hat{\mathcal{S}}_1, \hat{\mathcal{V}}\right]/\hbar \\ &= \frac{1}{2}\sum_{i=1}^{2}\left(\omega_q - \frac{g_i^2}{\Delta_i}\right)\hat{\sigma}_z \\ &\quad + \sum_{i=1}^{2}\left(\omega_{ri} - \frac{g_i^2}{\Delta_i}\hat{\sigma}_z\right)\hat{a}_i^\dagger\hat{a}_i + \frac{g_1 g_2}{2}\left(\frac{1}{\Delta_1} + \frac{1}{\Delta_2}\right)\left(\hat{a}_1^\dagger\hat{a}_2 + \hat{a}_1\hat{a}_2^\dagger\right)\hat{\sigma}_z.\end{aligned} \tag{2.67}$$

As expected we see that the qubit is decoupled from the resonator space now. The last line in

Eq. 2.67 is the effective mean-field Hamiltonian of the resonators

$$\hat{\mathcal{H}}/\hbar = \omega'_{r1}\hat{a}_1^\dagger\hat{a}_1 + \omega'_{r2}\hat{a}_2^\dagger\hat{a}_2 + g\left(\Phi_{ext}\right)\left(\hat{a}_1^\dagger\hat{a}_2 + \hat{a}_1\hat{a}_2^\dagger\right) \tag{2.68}$$

with dressed frequencies

$$\omega'_{ri} = \omega_{ri} - \frac{g_i^2}{\Delta_i}\langle\hat{\sigma}_z\rangle, \tag{2.69}$$

and a flux-tunable coupling strength

$$g\left(\Phi_{ext}\right) = \frac{g_1 g_2\langle\hat{\sigma}_z\rangle}{2}\left(\frac{1}{\omega_{r1} - \omega_q\left(\Phi_{ext}\right)} + \frac{1}{\omega_{r2} - \omega_q\left(\Phi_{ext}\right)}\right). \tag{2.70}$$

A truly beautiful piece of physics has emerged here: the originally uncoupled modes start to interact with each other via a virtual process mediated by the transmon mode, at a strength that is sensitive to the fluctuation or modulation of the transmon energy. In fact, this is what inspired the invention of many tunable coupling circuits where the control of the coupling strength is achieved through the modulation of the coupler frequency [65], as we shall see in Chapter 4.

2.3.3 Rotating frame transformation

Controlling a qubit state on demand is at the heart of quantum computation. The central question to ask for a driven superconducting circuit is how its quantum state evolves under the time-dependent Hamiltonian,

$$\hat{\mathcal{H}}\left(t\right) = \hat{\mathcal{H}}_0 + \hat{\mathcal{H}}_d\left(t\right). \tag{2.71}$$

As we have seen before, normally the driven Hamiltonian does not commute with itself at different moments of time, making the state evolution difficult to calculate as it can no longer be compactly written in the form of a time integral. Without loss of generality, let us write Eq. 2.71 in the energy

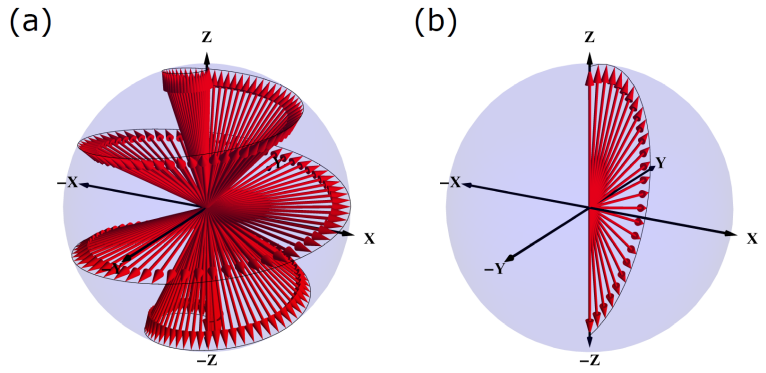

Figure 2.8: Rotating frame transformation in the Bloch sphere. (a) In the lab frame, a qubit driven along the X-axis rotates from -Z to Z at the Rabi frequency, while precessing around Z at the qubit frequency. (b) Transforming to the rotating frame, the precession along the Z-axis disappears, leaving only the Rabi oscillation along X.

eigenbasis of $\hat{\mathcal{H}}_0$,

$$\hat{\mathcal{H}}(t) = \sum_i E_i |i\rangle \langle i| + \sum_i f_i(t) |i\rangle \langle i| + \sum_{i \neq j} g_{i,j}(t) |i\rangle \langle j| , \tag{2.72}$$

where $g_{ij}(t) = g_{ij}^*(t)$ holds for Hermiticity. For now let us temporarily ignore the last term that gives rise to finite transition rates between different levels, but focus on the first two terms which cause the phases of the superposition to advance,

$$|\psi(t)\rangle = \sum_i c_i e^{-\frac{i}{\hbar}\left(E_i t + \int_0^t f_i(t)dt\right)} |i\rangle . \tag{2.73}$$

Geometrically this can be seen as a rotation of the state vector in time, which can obviously be eliminated by a time-reversal evolution operator,

$$U(t) = e^{\frac{i}{\hbar}\left(E_i t + \int_0^t f_i(t)dt\right)|i\rangle\langle i|} \tag{2.74}$$

that defines a "rotating frame" where the state vector keeps still. It is straightforward to check from the Schrödinger equation that in the rotating frame the "lab frame" Hamiltonian is transformed into

$$\hat{\mathcal{H}}_{\text{rot}} = U(t)\,\hat{\mathcal{H}}(t)\,U^{\dagger}(t) + i\hbar\dot{U}(t)\,U^{\dagger}(t), \tag{2.75}$$

hence the name "rotating frame transformation". From Eq. 2.72 and Eq. 2.75 we have

$$\hat{\mathcal{H}}_{\text{rot}} = \sum_{i\neq j} g_{i,j}(t)\, e^{\frac{i}{\hbar}\left[(E_i-E_j)t+\int_0^t (f_i(t)-f_j(t))dt\right]} |i\rangle\langle j|. \tag{2.76}$$

While in the most general sense this Hamiltonian still doesn't commute with itself at different times, special cases do exist where its complexity can be greatly reduced. For the most naive example where

$$g_{i,j}(t) = g_{i,j}(0)\, e^{-\frac{i}{\hbar}\left[(E_i-E_j)t+\int_0^t (f_i(t)-f_j(t))dt\right]}, \tag{2.77}$$

the time-dependency is completely removed, albeit an rather idealized scenario. More realistically, we may expect there to be slow-rotating terms where

$$\left|\omega_{i,j} - \left|\frac{i}{\hbar}\left[\left(E_i - E_j\right)t + \int_0^t \left(f_i(t) - f_j(t)\right)dt\right]\right|\right| \sim 0, \tag{2.78}$$

as well as fast-oscillating terms where

$$\left|\omega_{i,j} - \left|\frac{i}{\hbar}\left[\left(E_i - E_j\right)t + \int_0^t \left(f_i(t) - f_j(t)\right)dt\right]\right|\right| \gg 0, \tag{2.79}$$

with $\omega_{i,j}$ with dominant Fourier component of $g_{i,j}(t)$. Thus, we can make the "rotating wave approximation" (RWA) and keep only the slow-rotating terms in Eq. 2.76 as the effective Hamiltonian, while abandoning the fast-oscillating terms that are averaged out in the time integration. Subtleties arise when such a clear slow/fast boundary is absent, or when multi-photon processes may be present, the RWA becomes ineffective or needs to be applied with great caution [90].

To put the theory to test, we study the evolution of a voltage-driven transmon, with a Hamiltonian introduced in Eq. 2.15 that can be rewritten as

$$\hat{\mathcal{H}}(t)/\hbar = \omega_q \hat{a}^{\dagger}\hat{a} + \alpha \hat{a}^{\dagger 2}\hat{a}^2 + i\epsilon(t)\left(\hat{a}^{\dagger} - \hat{a}\right). \tag{2.80}$$

In a frame rotating at ω_q, the operator $\hat{a}$ is phase shifted to $\hat{a}e^{-i\omega_q t}$, so the rotating frame Hamiltonian is

$$\hat{\mathcal{H}}_{\text{rot}}/\hbar = \alpha\hat{a}^{\dagger 2}\hat{a}^2 + i\epsilon\left(t\right)\left(\hat{a}^\dagger e^{i\omega_q t} - \hat{a}e^{-i\omega_q t}\right). \tag{2.81}$$

Keeping the lowest three levels,

$$\hat{\mathcal{H}}_{\text{rot}}/\hbar = \alpha\left|2\right\rangle\left\langle 2\right| + \epsilon\left(t\right)\left[i\left(\left|1\right\rangle\left\langle 0\right| + \sqrt{2}\left|2\right\rangle\left\langle 1\right|\right)e^{i\omega_q t} + h.c.\right]. \tag{2.82}$$

We go into a second rotating frame where the $|2\rangle$ rotates at α, and assume $\epsilon\left(t\right) = \epsilon_0 \sin\omega_d t$, Eq. 2.82 becomes

$$\hat{\mathcal{H}}_{\text{rot}}/\hbar = -\frac{\epsilon_0}{2}\left\{\left|1\right\rangle\left\langle 0\right|\left[e^{i(\omega_q-\omega_d)t} - e^{i(\omega_q+\omega_d)t}\right] + \sqrt{2}\left|2\right\rangle\left\langle 1\right|\left[e^{i(\omega_q+\alpha-\omega_d)t} - e^{i(\omega_q+\alpha+\omega_d)t}\right]\right\} + h.c. \tag{2.83}$$

When $\delta_q = \omega_q - \omega_d \approx 0$ and $\epsilon_0 \ll \alpha$, we apply the RWA and get

$$\hat{\mathcal{H}}_{\text{rot}}/\hbar = -\frac{\epsilon_0}{2}\left(\left|1\right\rangle\left\langle 0\right| e^{i\delta_q t} + \left|0\right\rangle\left\langle 1\right| e^{-i\delta_q t}\right), \tag{2.84}$$

which finally transforms to a Hamiltonian analogous to a spin in the magnetic field $\vec{B} = -\epsilon_0\vec{x} + \delta_q\vec{z}$,

$$\hat{\mathcal{H}}_{\text{rot}}/\hbar = \frac{\delta_q}{2}\hat{\sigma}_z - \frac{\epsilon_0}{2}\hat{\sigma}_x, \tag{2.85}$$

so that the state vector will rotate along the "B field" in the rotating frame, while in the lab frame the trajectory is convoluted with a precession along the Z-axis. This explains why a multilevel artificial atom, such as a transmon, can be used as a two-level qubit, as long as the anharmonicity far exceeds the drive amplitude.

While the fast-oscillating terms do not directly participate in the dynamic evolution of states, they manifest their effects through off-resonantly dressing the energy levels, giving rise to AC Stark shifts. One particular example is the counter-rotating terms that we have dropped off in Eq. 2.83.

When driving on resonance, in the lowest two levels we have

$$\hat{\mathcal{H}}_{\text{rot}}/\hbar = -\frac{\epsilon_0}{2}\left(|1\rangle\langle 0| - |1\rangle\langle 0| e^{i2\omega_q t} + h.c.\right). \tag{2.86}$$

Reverting to the frame counter-rotating at ω_q against qubit's precession, the Hamiltonian changes to

$$\hat{\mathcal{H}}_{\text{rot}}/\hbar = 2\omega_q |1\rangle\langle 1| - \frac{\epsilon_0}{2}\left(|1\rangle\langle 0| e^{-i2\omega_q t} - |1\rangle\langle 0| + h.c.\right). \tag{2.87}$$

where the $|0\rangle$ and $|1\rangle$ state are dressed by the counter-rotating term. In the dressed-state basis the Hamiltonian is

$$\hat{\mathcal{H}}_{\text{rot}}/\hbar = \sqrt{\epsilon_0^2 + 4\omega_q^2}\,|1\rangle\langle 1| - \frac{\epsilon_0}{2}|1\rangle\langle 0| e^{-i2\omega_q t} + h.c.. \tag{2.88}$$

Now, transforming back to the original rotating frame, we find the qubit no longer being driven on resonance,

$$\hat{\mathcal{H}}_{\text{rot}}/\hbar = -\frac{\epsilon_0}{2}\left(|1\rangle\langle 0| e^{i\chi_q t} + |0\rangle\langle 1| e^{-i\chi_q t}\right), \tag{2.89}$$

but with a small detuning denoted by

$$\chi = \sqrt{\epsilon_0^2 + 4\omega_q^2} - 2\omega_q \approx \frac{\epsilon_0^2}{4\omega_q}, \tag{2.90}$$

which is essentially the same Bloch-Siegert shift we saw in the last subsection, but created through external drives as opposed to coupling to a static mode.

2.3.4 Displacement transformation

We have learned in subsection 2.3.1 how the B-V transformation diagonalizes coupled harmonic oscillator modes. Here we demonstrate how to diagonalize a single mode whose dipole moment is coupled to a static field,

$$\hat{\mathcal{H}}/\hbar = \omega\hat{a}^\dagger\hat{a} + \epsilon\hat{a}^\dagger + \epsilon^*\hat{a}, \tag{2.91}$$

through the displacement transformation,

$$D(\alpha) = e^{\alpha\hat{a}^\dagger - \alpha^*\hat{a}}, \tag{2.92}$$

with α being a complex number. Physically, this is known as the Glauber displacement operator [91] that displaces a coherent state by α in the phase space. Using the Campbell-Baker-Hausdorff formula we can easily verify that it also displaces the ladder operators as[1] $\hat{a} \to \hat{a} + \alpha$, $\hat{a}^\dagger \to \hat{a}^\dagger + \alpha^*$. The displaced Hamiltonian is then

$$\hat{\mathcal{H}}_{\text{disp}}/\hbar = D^\dagger(\alpha)\,\hat{\mathcal{H}}D(\alpha)/\hbar = \omega\hat{a}^\dagger\hat{a} + (\epsilon + \omega\alpha)\,\hat{a}^\dagger + (\epsilon^* + \omega\alpha^*)\,\hat{a}, \tag{2.93}$$

which is diagonal under the choice of[2] $\alpha = -\epsilon/\omega$. Like in the rotating frame where the transitions are unveiled by removing the precessing of the qubit, the displacement transformation moves to the frame of the driven cavity where the induced interactions are more easily seen. In the following we apply the displacement transformation to the circuit-QED model shown in Fig. 2.9, where we also make use of the other three canonical transformations as a review of the whole section. In the circuit, a transmon is coupled to a multimode of resonators, with its bias charge dynamically modulated by an external voltage drive. In the charge and phase operator representation, the circuit Hamiltonian is given by

$$\begin{aligned}\hat{\mathcal{H}}(t) &= 4E_{cq}\hat{n}_q^2 - E_J\cos\hat{\theta}_q + 4E_{cg}\hat{n}_q\hat{n}_{r1} - 8E_{cq}n_g(t)\,\hat{n}_q \\ &+ 4E_{cr1}\hat{n}_{r1}^2 + \frac{E_{L1}}{2}\theta_{r1}^2 + 4E_{cr2}\hat{n}_{r2}^2 + \frac{E_{L2}}{2}\theta_{r2}^2 + 4E_{cgr}\hat{n}_{r1}\hat{n}_{r2}.\end{aligned} \tag{2.94}$$

1. See Appendix. 6.1 for its derivation.

2. Strictly speaking, this expression should be written as $\alpha = \epsilon/(i\kappa - \omega)$ with the photon loss rate κ taken into account. Here and in the following we assume negligible photon loss rate within the context of displacement transformation.

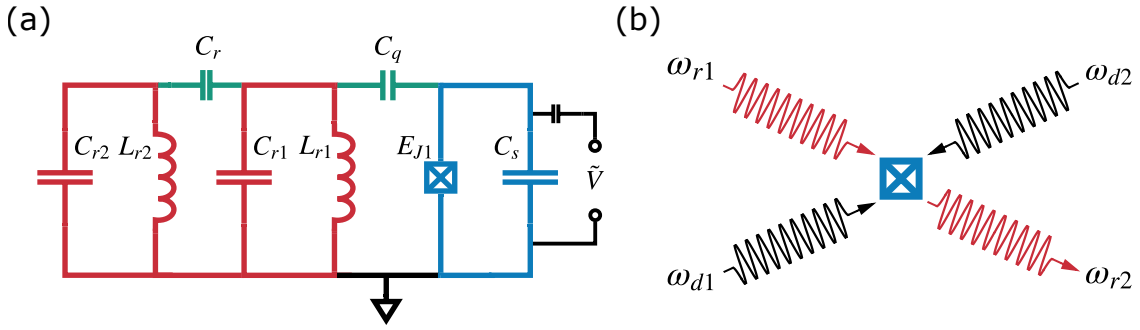

Figure 2.9: Application of all four transformations in a superconducting circuit. (a) A voltage-driven transmon is statically coupled to a multimode circuit. The transformation techniques allow us to analytically study the circuit dynamics, where we find driven at half the detuning of the two normal modes leads to a photon-swapping interaction between them. (b) In the nonlinear optics point of view, this is equivalent to the four-wave mixing process where interactions between three wavelengths produce a new wavelength.

In the second quantization form, with qubit approximated by a two-level qubit, we have

$$\begin{aligned}\hat{\mathcal{H}}/\hbar &= \frac{\omega_q}{2}\sigma_z + g_q\left(\hat{a}_1^\dagger\hat{\sigma}^- + \hat{a}_1\hat{\sigma}^+\right) + \epsilon\left(t\right)\hat{\sigma}_x \\ &+ \omega_{r1}\hat{a}_1^\dagger\hat{a}_1 + \omega_{r2}\hat{a}_2^\dagger\hat{a}_2 + g_r\left(\hat{a}_1^\dagger\hat{a}_2 + \hat{a}_1\hat{a}_2^\dagger\right),\end{aligned} \tag{2.95}$$

which can be followed by a B-V transformation that turns bare modes $\hat{a}_i$ into normal modes $\hat{b}_i$,

$$\hat{\mathcal{H}}/\hbar = \frac{\omega_q}{2}\sigma_z + \omega_{r1}\hat{b}_1^\dagger\hat{b}_1 + \omega_{r2}\hat{b}_2^\dagger\hat{b}_2 + g_1\left(\hat{b}_1^\dagger\hat{\sigma}^- + \hat{b}_1\hat{\sigma}^+\right) + g_2\left(\hat{b}_2^\dagger\hat{\sigma}^- + \hat{b}_2\hat{\sigma}^+\right) + \epsilon\left(t\right)\hat{\sigma}_x. \tag{2.96}$$

Here and in the following, we keep the same notation for the mode frequencies although they are shifted as dressed frequencies. Using first order S-W transformation we may decouple the qubit from the normal modes like we did in Eq. 2.67. Here we go beyond the first order to the third order perturbation in g/Δ, where the S-W generator is

$$\hat{\mathcal{S}} = \sum_{i=1}^{2}\frac{g_i}{\Delta_i}\left[\hat{b}_i^\dagger\hat{\sigma}^- - \hat{b}_i\hat{\sigma}^+ - \frac{4g_i^2}{3\Delta_i^2}\hat{b}_i^\dagger\hat{b}_i\left(\hat{b}_i^\dagger\hat{\sigma}^+ - \hat{b}_i\hat{\sigma}^-\right)\right]. \tag{2.97}$$

For simplicity we keep only the relevant terms in the effective Hamiltonian after the S-W transfor-

mation,

$$e^{\hat{\mathcal{S}}}\hat{\mathcal{H}}e^{-\hat{\mathcal{S}}}/\hbar \approx \frac{\omega_q}{2}\hat{\sigma}_z+\sum_{i=1}^{2}\omega_{ri}\hat{b}_i^\dagger\hat{b}_i+\sum_{i=1}^{2}\chi_i\hat{b}_i^\dagger\hat{b}_i\hat{\sigma}_z+\chi_{12}\hat{b}_1^\dagger\hat{b}_1\hat{b}_2^\dagger\hat{b}_2\hat{\sigma}_z+\epsilon\left(t\right)\left[\hat{\sigma}_x+\sum_{i=1}^{2}\frac{g_i}{\Delta_i}\left(\hat{b}_1^\dagger+\hat{b}_1\right)\right].$$

Assuming the voltage drive a monochromatic cosine signal at frequency ω_d with amplitude ϵ_0, and suppose $\omega_{r2} > \omega_{r1}$, we then apply a rotating frame transformation

$$U\left(t\right) = e^{i\omega_d t\left(\frac{\hat{\sigma}_z}{2}-\hat{b}_1^\dagger\hat{b}_1+\hat{b}_2^\dagger\hat{b}_2\right)} \tag{2.98}$$

that transforms the Hamiltonian to

$$\hat{\mathcal{H}} = \frac{\Delta_q}{2}\hat{\sigma}_z+\sum_{i=1}^{2}\Delta_{ri}\hat{b}_i^\dagger\hat{b}_i+\sum_{i=1}^{2}\chi_i\hat{b}_i^\dagger\hat{b}_i\hat{\sigma}_z+\chi_{12}\hat{b}_1^\dagger\hat{b}_1\hat{b}_2^\dagger\hat{b}_2\hat{\sigma}_z+\sum_{i=1}^{2}\frac{g_i\epsilon_0}{2\Delta_i}\left(\hat{b}_i^\dagger+\hat{b}_i\right), \tag{2.99}$$

where $\Delta_q = \omega_q - \omega_d$, $\Delta_{r1} = \omega_{r1} + \omega_d$ and $\Delta_{r2} = \omega_{r2} - \omega_d$. Here we have tilted the qubit eigenbasis to align with the fictitious B field axis $\vec{B} = -\epsilon_0\vec{x} + \delta_q\vec{z}$, under the assumption that $\epsilon_0 \ll \Delta_q$. We now apply the displacement transformation

$$D\left(\alpha_1,\alpha_2\right) = e^{\sum_{i=1}^{2}\left(\alpha_i\hat{a}_i^\dagger-\alpha_i^*\hat{a}_i\right)}, \tag{2.100}$$

with $\alpha_i \approx g_i\epsilon_0/\left(2\Delta_{ri}\Delta_i\right)$, to the Hamiltonian, cancelling the drive term while creating new terms in addition to the ones in Eq. 2.99,

$$\begin{aligned}\hat{\mathcal{H}}/\hbar &= \frac{\Delta_q}{2}\hat{\sigma}_z+\sum_{i=1}^{2}\Delta_{ri}\hat{b}_i^\dagger\hat{b}_i+\sum_{i=1}^{2}\chi_i\left(\hat{b}_i^\dagger\hat{b}_i+\alpha_i\hat{b}_i^\dagger+\alpha_i^*\hat{b}_i+|\alpha|^2\right)\hat{\sigma}_z \\ &+ \chi_{12}\left(\hat{b}_1^\dagger\hat{b}_1+\alpha_1\hat{b}_1^\dagger+\alpha_1^*\hat{b}_1+|\alpha|^2\right)\left(\hat{b}_2^\dagger\hat{b}_2+\alpha_2\hat{b}_2^\dagger+\alpha_2^*\hat{b}_2+|\alpha|^2\right)\hat{\sigma}_z. \end{aligned} \tag{2.101}$$

Finally, moving to the rotating frame corresponding to the first two terms, one finds

$$\begin{aligned}\hat{\mathcal{H}}/\hbar &= \sum_{i=1}^{2}\chi_i\left(\hat{b}_i^\dagger\hat{b}_i+\alpha_i\hat{b}_i^\dagger e^{i\Delta_{ri}t}+\alpha_i^*\hat{b}_i e^{-i\Delta_{ri}t}+|\alpha_i|^2\right)\hat{\sigma}_z \\ &+ \chi_{12}\left(\hat{b}_1^\dagger\hat{b}_1+\alpha_1\hat{b}_1^\dagger e^{i\Delta_{r1}t}+\alpha_1^*\hat{b}_1 e^{-i\Delta_{r1}t}+|\alpha_1|^2\right)\left(\hat{b}_2^\dagger\hat{b}_2+\alpha_2\hat{b}_2^\dagger e^{i\Delta_{r2}t}+\alpha_2^*\hat{b}_2 e^{-i\Delta_{r2}t}+|\alpha_2|^2\right)\hat{\sigma}_z.\end{aligned} \tag{2.102}$$

The interference between the rotating operators in the last line leads to a truly interesting effect: when we set $\Delta_{r1}=\Delta_{r2}$, i.e. when $\omega_d=(\omega_{r2}-\omega_{r1})/2$, the only non-fast-oscillating term is

$$\hat{\mathcal{H}}/\hbar=\chi_{12}\left(\alpha_1\alpha_2^*\hat{b}_1^\dagger\hat{b}_2+\alpha_1^*\alpha_2\hat{b}_1\hat{b}_2^\dagger\right) \tag{2.103}$$

which represents a photon-swapping interaction between the two normal modes. This result can be more extended to the bichromatic drive tone case by time-dependent displacement transformation, where the same interaction is induced by two photons of different frequencies, as long as they bridge the gap between the normal modes. This phenomenon is known as the "four-wave mixing" [92, 93] in nonlinear optics illustrated by the cartoon in Fig. 2.9, which can be thought of as the conversion of three photons (waves) into a fourth one.

The calculation above serves well for our purposes of demonstrating all the transformations and nicely grasps the core feature of the four-wave mixing effect. However, it imposes a two-level approximation on the transmon which is arguably an over-simplification. In the next section, miraculously, we will see how a complete analysis for the full transmon case is made possible by looking at the same problem from a different angle.

2.4 Numerical Simulations of Superconducting Circuits

While these analytical treatments offer great insights for understanding circuit-QED on the physical level, they may not be suitable for the exact calculation of superconducting circuits with high precision demands. First of all, the modeling of a real-life superconducting circuit with Hamilto-

nian parameters alone is no easy task, especially for large distributed circuits that cannot be well approximated by the lumped-element model. Secondly, as we have seen in the four-wave mixing example in the last section, theoretical analysis of driven circuits may require complicated calculations involving high-order perturbation theory. Finally, dissipation is universally present in superconducting circuits and must be taken into account, yet the numerical evaluation of effects exerted on the qubit by the open system it is coupled to is beyond the reach of aforementioned analytical solutions. In this section, we overcome these difficulties with theories and methods that are directly applicable to the numerical simulation of superconducting circuits.

2.4.1 Black-box quantization and ABCD matrix

Previously we have seen that the Hamiltonian of a transmon is given with ladder operators by

$$\hat{\mathcal{H}} = \omega_q \hat{a}^\dagger \hat{a} + \alpha \hat{a}^{\dagger 2} \hat{a}^2, \tag{2.104}$$

which originates from the harmonic oscillator basis defined by the quadratic terms, expanding the nonlinearity up to θ^4 and keeping only its leading order contribution to the transmon energy. One then typically approximates the charge operator as a harmonic oscillator field operator and further formulates the Hamiltonian of a transmon-cavity system. Then one faces two options in the subsequent calculation: one can either take the nonlinear term into the diagonalization for a precise solution of the spectrum in nonlinear basis, at the cost of obscuring the high order interactions from the nonlinearity, or one can choose to only diagonalize the linear part that elucidates nonlinearity-induced interaction at all levels, which may compromise the accuracy of the spectrum but only slightly so for the low-energy manifold of transmon of our interest. As a concrete example of the latter approach, let's revisit the four-wave mixing problem starting from rewriting Eq. 2.94 as,

$$\begin{aligned} \hat{\mathcal{H}}(t) \;\approx\; & 4E_{cq}\hat{n}_q^2 + \frac{E_J}{2}\hat{\theta}_q^2 + \sum_{i=1}^{2}\left(4E_{cri}\hat{n}_{ri}^2 + \frac{E_{Li}}{2}\theta_{ri}^2\right) + 4E_{cg}\hat{n}_q\hat{n}_{r1} + 4E_{cgr}\hat{n}_{r1}\hat{n}_{r2} \\ - \;& \frac{E_J}{24}\hat{\theta}_q^4 - 8E_{cq}n_g(t)\,\hat{n}_q. \end{aligned} \tag{2.105}$$

As opposed to expressing every term with ladder operators, this time we leave the θ^4 alone,

$$\begin{aligned}\hat{\mathcal{H}}(t) &= \omega_q \hat{a}_q^\dagger \hat{a}_q + g_q\left(\hat{a}_{r1}^\dagger \hat{a}_q + \hat{a}_{r1}\hat{a}_q^\dagger\right) + \omega_{r1}\hat{a}_{r1}^\dagger \hat{a}_{r1} + \omega_{r2}\hat{a}_{r2}^\dagger \hat{a}_{r2} + g_r\left(\hat{a}_{r1}^\dagger \hat{a}_{r2} + \hat{a}_{r1}\hat{a}_{r2}^\dagger\right) \\ &- \frac{E_J}{24}\hat{\theta}_q^4 + \epsilon(t)\,\hat{a}_q^\dagger + \epsilon^*(t)\,\hat{a}_q, \end{aligned} \tag{2.106}$$

which is simplified by a B-V transformation,

$$\begin{aligned}\hat{\mathcal{H}}(t) &= \omega_q \hat{b}_q^\dagger \hat{b}_q + \omega_{r1}\hat{b}_{r1}^\dagger \hat{b}_{r1} + \omega_{r2}\hat{b}_{r2}^\dagger \hat{b}_{r2} \\ &- \frac{E_J}{24}\left[\theta_q^0\left(\hat{b}_q^\dagger + \hat{b}_q\right) + \sum_{i=1}^{2}\beta_i\theta_{ri}^0\left(\hat{b}_{ri}^\dagger + \hat{b}_{ri}\right)\right]^4 + \epsilon(t)\,\hat{b}_q^\dagger + \epsilon^*(t)\,\hat{b}_q, \end{aligned} \tag{2.107}$$

where θ^0 stands for the zero-point fluctuation of the phase, and $\beta_{1,2}$ are the wavefunction participation of the two normal modes in the transmon that scales as g/Δ assuming strong hybridization of the multimode. Like before we kept the same frequency notations for simplicity. Going to a frame rotating with the drive term as well as the two normal modes, we have

$$\begin{aligned}\hat{\mathcal{H}}(t) &= \Delta_q \hat{b}_q^\dagger \hat{b}_q + \epsilon_0 \hat{b}_q^\dagger + \epsilon_0^* \hat{b}_q \\ &- \frac{E_J}{24}\left[\theta_q^0\left(\hat{b}_q^\dagger e^{i\omega_d t} + \hat{b}_q e^{-i\omega_d t}\right) + \sum_{i=1}^{2}\beta_i\theta_{ri}^0\left(\hat{b}_{ri}^\dagger e^{i\omega_{ri} t} + \hat{b}_{ri} e^{-i\omega_{ri} t}\right)\right]^4, \end{aligned} \tag{2.108}$$

and finally, we displace the transmon field and then move to the frame rotating with the transmon,

$$\hat{\mathcal{H}}(t) = -\frac{E_J}{24}\left[\theta_q^0\left(\hat{b}_q^\dagger e^{i\omega_d t} + \hat{b}_q e^{-i\omega_d t}\right) + \theta_q^0\left(\alpha^* e^{i\omega_d t} + \alpha e^{-i\omega_d t}\right) + \sum_{i=1}^{2}\beta_i\theta_{ri}^0\left(\hat{b}_{ri}^\dagger e^{i\omega_{ri} t} + \hat{b}_{ri} e^{-i\omega_{ri} t}\right)\right]^4, \tag{2.109}$$

with $\alpha = -\epsilon_0/\Delta_q$. Now we can conveniently find out all the slow-oscillating terms from the expansion under a certain drive frequency ω_d, such as the four-wave mixing terms at $\omega_d = (\omega_{r1} + \omega_{r2})/2$.

The advantage of such a quantization technique becomes more prominent for larger circuits where the transmon is coupled to a complicated two-port linear network. Standard circuit quan-

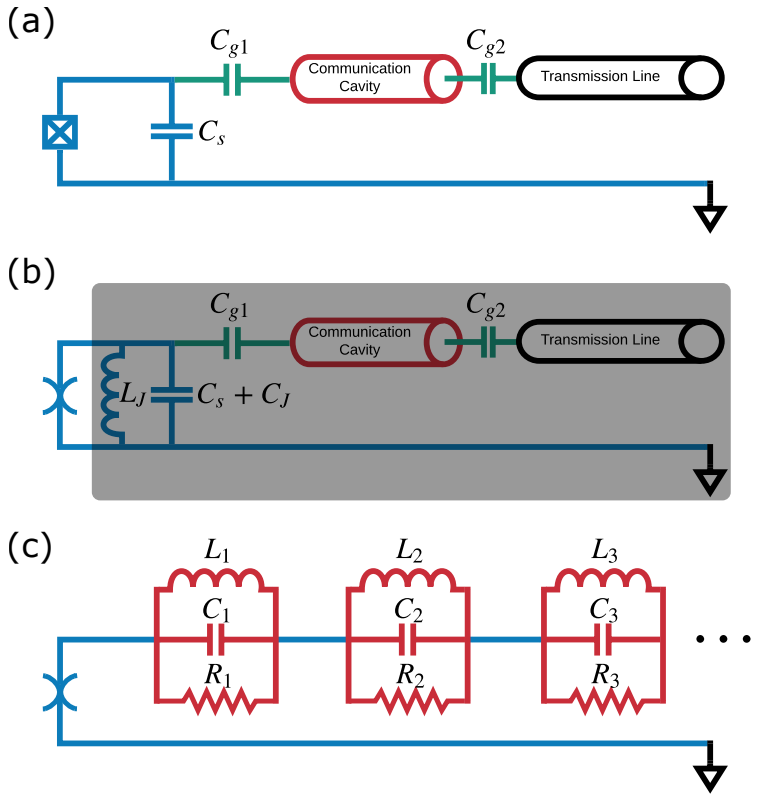

Figure 2.10: Black-box quantization of the communication circuit. (a) In the communication circuit, a transmon is coupled to a coplanar waveguide (CPW) cavity as the "communication cavity", which is further coupled to the transmission line/coaxial cable. (b) The linear part of the Josephson energy is extracted and merged with other linear part of the circuit, forming a black-box of RLC network. (c) Equivalent circuit of the black box consisting of a series of parallel RLC oscillators, whose information can be extracted from the ABCD matrix calculation.

tization procedure in section 2.1 more or less fails on such large scale circuit either when the analytical model is unavailable, or because of the divergence and renormalization issues in calculating the multimode Purcell effect. In contrast, following the spirit of the above analysis, one may circumvent these issues by grouping all the linear circuit components into a black box and routinely solve the mode properties through circuit network theory, which are then fed into the θ^4 nonlinearity for gaining more sophisticated information such as the self-Kerr and cross-Kerr between the modes. This is exactly how the BBQ - "Black-box quantization" [94] - works, shown in Fig. 2.10 by the particular "communication circuit" as an example. The communication circuit, which will be the topic of Chapter 3, is made of two transmons each coupled to an on-chip copla-

nar waveguide (CPW) cavity, and a one-meter-long transmission line (TL) coupling the two CPW cavities together. Of particular interest is how the lifetime of the transmon is affected by the lossy TL, and the coupling strength between the transmon and the hybridized CPW-TL modes. We first decompose the transmon Josephson energy into a linear inductive energy defined by the Josephson inductance plus the Josephson nonlinearity. According to the Foster theorem, the black-box network can be synthesized by a series of parallel RLC oscillators, with an input admittance of

$$Y(\omega) = \left[\sum_{i=1}^{N}\left(j\omega C_i + \frac{1}{j\omega L_i} + \frac{1}{R_i}\right)^{-1}\right]^{-1}. \tag{2.110}$$

The resonances of the RLC oscillators can be found from solving $Y(\omega) = 0$, with the i-th mode frequency and lifetime being

$$\omega_i = \mathrm{Re}\left(\frac{j}{2R_iC_i} + \sqrt{\frac{1}{L_iC_i} - \frac{1}{4R_i^2C_i^2}}\right) \approx \frac{1}{\sqrt{L_iC_i}}, \tag{2.111}$$

$$\tau_i = \frac{1}{2}\left[\mathrm{Im}\left(\frac{j}{2R_iC_i} + \sqrt{\frac{1}{L_iC_i} - \frac{1}{4R_i^2C_i^2}}\right)\right]^{-1} \approx R_iC_i, \tag{2.112}$$

assuming weak dissipation limit $R_i \gg \sqrt{L_i/C_i}/2$. Then it is easy to verify that R_i, L_i and C_i are given by

$$R_i = \frac{1}{\mathrm{Re}Y(\omega_i)}, C_i = \frac{1}{2}\mathrm{Im}\frac{dY(\omega)}{d\omega}\bigg|_{\omega=\omega_i}, L_i = \left[\frac{\omega_i^2}{2}\mathrm{Im}\frac{dY(\omega)}{d\omega}\bigg|_{\omega=\omega_i}\right]^{-1}, Z_i = \left[\frac{\omega_i}{2}\mathrm{Im}\frac{dY(\omega)}{d\omega}\bigg|_{\omega=\omega_i}\right]^{-1}, \tag{2.113}$$

The admittance function of any linear microwave circuit can be obtained from finite element numerical simulation like HFSS. For the communication circuit where the circuit model is well established, a semi-analytical solution with the ABCD matrix is possible. Appendix. 6.5 offers more detail on the ABCD matrix calculation of $Y(\omega)$, here we will jump to the result plotted in Fig. 2.11. As our actual device is a flux-tunable transmon, we would like to know the frequency dependence of the transmon coherence. In the simulation we sweep L_J to mimic the flux tuning

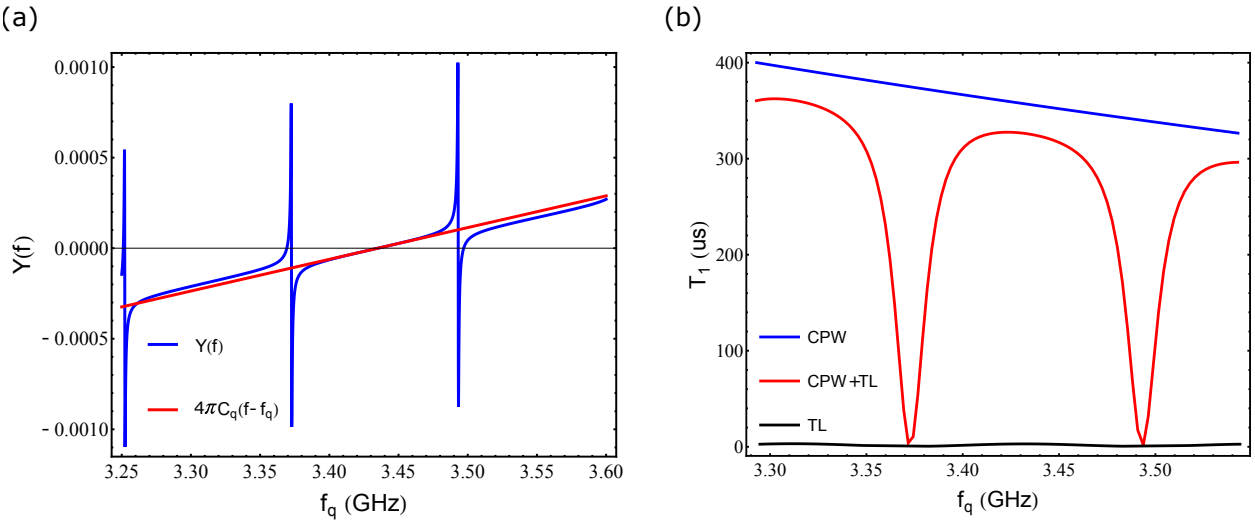

Figure 2.11: Numerical simulation of the transmon lifetime in the communication circuit. (a) For comparison we compare the three cases where either the CPW or the TL is absent, or they are both present. The admittance matrix is obtained from the ABCD matrix of the "black-box" network in Fig. 2.10, and the spectrum of Im$Y(\omega)$ provides useful information about each normal mode in the equivalent Foster circuit. Depicted here is the when the CPW is missing, and Im$Y(\omega)$ crosses zero at the transmon frequency and the TL multimode frequencies. (b) Plotting transmon lifetime for the three situations as a function of its frequency, by varying L_J. We see the huge difference between the baseline coherence with and without the CPW, showing the Multimode Purcell effect as well as the protection of the CPW as a filter. The Purcell limit placed by the CPW is much higher than the transmon intrinsic coherence and can be safely ignored.

effect. At each L_J value, the crossing between zero and Im$Y(\omega)$ is found around the expected transmon frequency, from which the resistance, capacitance and further the lifetime of the transmon are determined according to Eq. 2.112 and Eq. 2.113. Repeating the same procedure for different L_J results in the curves shown in Fig. 2.11(b), where we find clear evidence for the Purcell limit the TL multimode exerts to the transmon that periodically brings down its lifetime (with a period equal to the free spectral range of the TL), as well as for the protection of the transmon coherence the communication cavity provides as a Purcell filter.

The RLC oscillators can be thought of as the normal modes after the Bogoliubov transformation, whose phases add up to be the Josephson phase according to Kirchhoff's law,

$$\hat{\theta} = \sum_{i=1}^{N} \sqrt{\frac{\hbar}{2} Z_i} \left(\hat{a}_i^\dagger + \hat{a}_i \right), \tag{2.114}$$

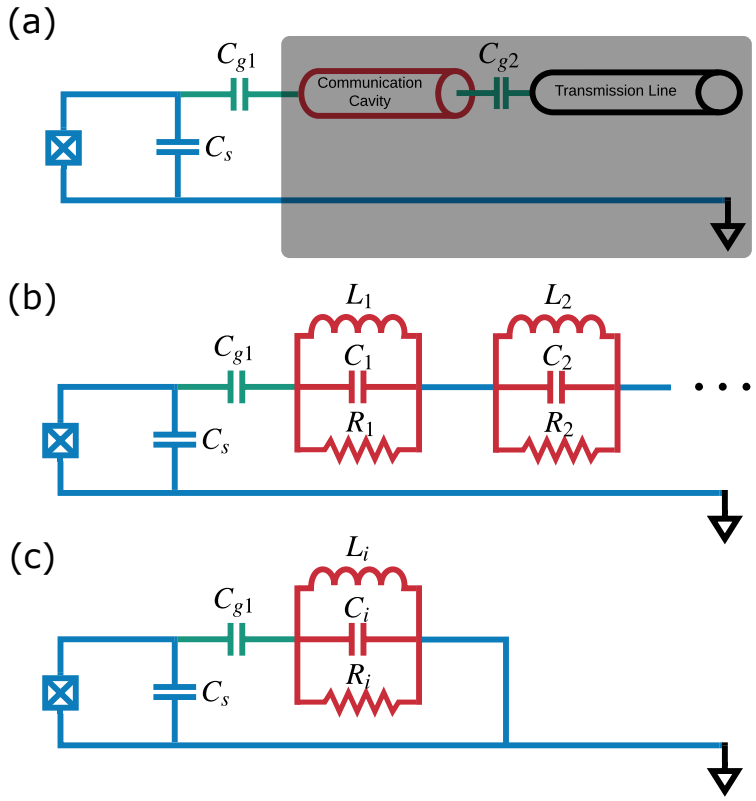

Figure 2.12: An alternative approach for the calculation of coupling strength between the transmon and the normal modes. (a) In this scheme, the black box only extends to the right side of the coupling capacitor C_{g1}. (b) The black box is transformed into an equivalent RLC circuit like before, allowing for a subsequent standard circuit quantization treatment. (c) Under the weak coupling condition and large normal mode detunings, the coupling strength between the transmon and the i-th mode can be obtained from this effective circuit model.

assuming no flux penetrating the loop. Now we have numerically obtained an Eq. 2.107-like Hamiltonian for the communication circuit, and from this point on we can expand the Josephson nonlinearity up to any order we want and find the energy corrections with perturbation theory. In this basis, the transmon-cavity interactions appear in the form of cross-Kerr terms, where the bare transmon-cavity coupling strength can be indirectly inferred. Here we present a variation of the black-box quantization directly offering the bare coupling strengths, again using the example of the communication circuit. Instead of wrapping everything into the black box including the linear part of the JJ , we choose to only diagonalize the part beyond the coupling capacitance of the transmon, illustrated in Fig. 2.12. Similarly we can reconstruct the normal modes as equivalent

RLC oscillators, which then allows for a standard circuit quantization calculation for the coupling strength, by selecting a few oscillators of interest and group them with the transmon, shown in Fig. 2.12(b). Demonstrated in Appendix. 6.6, this protocol works under the condition that the gap between the selected and the remaining normal modes Δ be much larger than their coupling energy induced by the transmon coupling capacitor C_g, which is often met by the real circuit when the coupling is small.

2.4.2 Master equation and Monte Carlo wavefunction method

So far we have restricted our investigation to unitary evolution of closed systems, where the state vector and the density matrix are determined by the Schrödinger equation and the von Neumann equation,

$$|\dot{\Psi}\rangle = -\frac{i}{\hbar}\hat{\mathcal{H}}\,|\Psi\rangle\,, \tag{2.115}$$

$$\dot{\rho_s} = -\frac{i}{\hbar}\left[\hat{\mathcal{H}}, \rho_s\right]. \tag{2.116}$$

In the physical world, systems are never really closed but are coupled to each other, however weak the coupling strength is. Such interactions are accompanied by the transferring of energy and entanglement between the subsystems, which appear as dissipation/excitation and decoherence processes to an individual subsystem. Within a two-level density matrix model, these processes are described by

$$\rho_s\left(t\right) = \begin{pmatrix} \frac{\gamma_\downarrow}{\gamma_\uparrow+\gamma_\downarrow} + \left[P_g\left(0\right) - \frac{\gamma_\downarrow}{\gamma_\uparrow+\gamma_\downarrow}\right] e^{-\left(\gamma_\uparrow+\gamma_\downarrow\right)t} & P_\phi\left(0\right) e^{-\gamma_\phi t - \frac{\gamma_\uparrow+\gamma_\downarrow}{2}t} \\ P_\phi^*\left(0\right) e^{-\gamma_\phi t - \frac{\gamma_\uparrow+\gamma_\downarrow}{2}t} & \frac{\gamma_\uparrow}{\gamma_\uparrow+\gamma_\downarrow} - \left[P_g\left(0\right) - \frac{\gamma_\downarrow}{\gamma_\uparrow+\gamma_\downarrow}\right] e^{-\left(\gamma_\uparrow+\gamma_\downarrow\right)t} \end{pmatrix}, \tag{2.117}$$

where $\gamma_{\downarrow,\uparrow}$, γ_ϕ stand for the decay, excitation and dephasing rate, respectively, and $P_g\left(0\right)$ and $P_\phi\left(0\right)$ are the ground state population and the phase amplitude at $t = 0$. Based on these values we may further define the "relaxation time" T_1, "decoherence time" T_2^* and the "pure dephasing

time" T_ϕ,

$$T_\phi = \frac{1}{\gamma_\phi}, \quad T_1 = \frac{1}{\gamma_\uparrow + \gamma_\downarrow}, \quad T_2^* = \left(\frac{1}{T_\phi} + \frac{1}{2T_1}\right)^{-1}, \tag{2.118}$$

which form the standard characterization of quantum coherence. Note that $T_2^* \leq 2T_1$ always holds true, and typically a qubit system is operated at low enough temperature where the excitation rate can be ignored, $T_1 \approx \gamma_\downarrow^{-1}$. As Eq. 2.117 only applies to open two-level systems without external control Hamiltonian, its generalization to controlled higher dimensional systems is highly desirable. Such generalization can be achieved by the aid of the quantum master equation,

$$\dot{\rho_s} = -\frac{i}{\hbar}\left[\hat{\mathcal{H}}, \rho_s\right] + \sum_i \gamma_i \mathcal{D}\left[\hat{L}_i\right]\rho_s, \tag{2.119}$$

where $\mathcal{D}\left[\hat{L}_i\right]$ is the Lindblad superoperator with jump operator $\hat{L}_i$ acting on the density matrix as

$$\mathcal{D}\left[\hat{L}_i\right]\rho = \hat{L}_i \rho \hat{L}_i^\dagger - \frac{1}{2}\left\{\hat{L}_i^\dagger \hat{L}_i, \rho\right\}. \tag{2.120}$$

The mathematical details for deriving the master equation are very nicely covered by many references [95, 96] and we refrain from further discussions, except emphasizing the two approximations made herein: the Born approximation that assumes the sufficiently weak interaction between the subsystem and its environment so that the state of the environment is unaffected by the subsystem, and the Markov approximation stating the memoryless property of the environment, that it has a very short correlation time and thus never returns past information back to the subsystem. The jump operators corresponding to the relaxation process are $\hat{\sigma}_\pm$ that flip the ground and excited state population for a qubit, or the ladder operators $\hat{a}^\dagger$ and $\hat{a}$ that climb up and down in the Fock state basis, while the pure dephasing is represented by $\hat{\sigma}_z/\sqrt{2}$ or $\hat{a}^\dagger\hat{a}$, representing the fluctuation of photon energies. For multilevel artificial atoms, it is also possible to include jump operators between higher levels, with modified amplitudes according to their physical sources [97].

The relaxation and dephasing mechanism can also be understood from the prospective of noise series, resulting either from the classical fluctuation of circuit parameters or control signals, or the

circuit degrees of freedom coupling to quantum fluctuations [98, 99]. In the light of this theory, the relaxation and the dephasing process of a qubit can be pictured as $\hat{\sigma}_{x,y}$ and $\hat{\sigma}_z/\sqrt{2}$ operators coupled to classical or quantum fluctuators, $f_{xy}(t)$ and $f_z(t)$, which carry different power spectral densities (PSD) as the Fourier transformation of their autocorrelation functions,

$$S_{xy,z}[\omega] = \int_{-\infty}^{\infty} d\tau e^{i\omega\tau} \langle f_{xy,z}(t) f_{xy,z}(0) \rangle, \tag{2.121}$$

which is related to the bare qubit decay and dephasing times through

$$\gamma_\phi = S_{zz}[0], \quad \gamma_\downarrow = S_{xy}[\omega_q], \quad \gamma_\uparrow = S_{xy}[-\omega_q], \tag{2.122}$$

with $S_{xy}[-\omega_q] = e^{-\beta\hbar\omega_q} S_{xy}[\omega_q]$ restricting the last two under thermal equilibrium.

As a practical application, let us consider the simple case where qubit is driven off-resonantly by a Rabi drive, namely

$$\hat{\mathcal{H}}(t) = \frac{\omega_q}{2}\hat{\sigma}_z + \Omega_x \hat{\sigma}_x \cos(\omega_d t), \tag{2.123}$$

and we want to find out how the lab-frame noises (neglecting the fluctuation of the drive tone) affect the driven qubit in the dressed basis along the Rabi drive axis. Combining rotating frame transformation, qubit basis transformation and Eq. 2.121, one finds the "dressed" relaxation rate and dephasing rate as

$$\begin{aligned}
\widetilde{\gamma}_\phi &= S_{zz}[0]\cos^2\theta + \left\{S_{xy}[\omega_d] + S_{xy}[-\omega_d]\right\}\frac{\sin^2\theta}{2}, \\
\widetilde{\gamma}_\downarrow &= S_{zz}[\Omega_R]\frac{\sin^2\theta}{2} + S_{xy}[\Omega_R - \omega_d]\sin^4\frac{\theta}{2} + S_{xy}[\Omega_R + \omega_d]\cos^4\frac{\theta}{2}, \\
\widetilde{\gamma}_\uparrow &= S_{zz}[-\Omega_R]\frac{\sin^2\theta}{2} + S_{xy}[-\Omega_R - \omega_d]\cos^4\frac{\theta}{2} + S_{xy}[-\Omega_R + \omega_d]\sin^4\frac{\theta}{2},
\end{aligned} \tag{2.124}$$

under the weak dissipation approximation where $\Omega_R = \sqrt{\Delta^2 + \omega_x^2} \gg \gamma_\phi, \gamma_{\uparrow\downarrow}$, with $\Delta_q = \omega_q - \omega_d$. Further assuming the near-resonance and weak-drive condition $\omega_d \sim \omega_q \gg \Omega_R$, as well as low qubit temperature $k_B T \ll \hbar\omega_q$, we have $S_{xy}[-\omega_d] \approx S_{xy}[\Omega_R - \omega_d] \approx S_{xy}[-\Omega_R - \omega_d] \approx 0$.

Then Eq. 2.124 simplifies to

$$\begin{aligned}
\widetilde{\gamma}_{\phi} &= S_{zz}[0]\cos^2\theta + S_{xy}[\omega_d]\frac{\sin^2\theta}{2}, \\
\widetilde{\gamma}_{\downarrow} &= S_{zz}[\Omega_R]\frac{\sin^2\theta}{2} + S_{xy}[\omega_d+\Omega_R]\cos^4\frac{\theta}{2}, \\
\widetilde{\gamma}_{\uparrow} &= S_{zz}[-\Omega_R]\frac{\sin^2\theta}{2} + S_{xy}[\omega_d-\Omega_R]\sin^4\frac{\theta}{2}.
\end{aligned} \tag{2.125}$$

This suggests that the driven qubit can be used as a noise spectrum analyzer to characterize noise PSDs with coherence measurements [100]. If all the noise channels were white noise, i.e. their PSD are uniform and the dissipation parameters are frequency independent, Eq. 2.125 would reduce to Eq. 4.30-4.32 in subsection 4.3.1 and evolution of the qubit can be perfectly solved from master equation. However, realistic noise sources especially dephasing noise usually exhibit a colored power spectrum such as 1/f type, which necessitates a more rigorous quantum noise analysis beyond the capability of ordinary master equation simulations. We hereby introduce an efficient numerical method that accommodates 1/f dephasing noise in the simulation, which is known as the Monte Carlo wavefunction method or the quantum jump approach [101, 102, 103, 104]. Unlike the master equation that solves the whole density matrix, the Monte Carlo simulation deals with state vectors and stochastic jump operators for a single trajectory each time, then averages over all the trajectories in the end. Technically, this may allow for a computational speed-up under certain scenarios [105]. Physically this may be closer an approximation to reality because trajectories and quantum jumps are actually observable in experiments, via high fidelity quantum non-demolition readout [106, 107, 108, 109]. The procedure of the Monte Carlo wavefunction method is outlined as follows:

1. Define the "effective Hamiltonian" as

$$\hat{\mathcal{H}}_{\text{eff}}(t) = \hat{\mathcal{H}}(t) - \frac{i\hbar}{2}\sum_i \gamma_i \hat{L}_i^{\dagger}\hat{L}_i, \tag{2.126}$$

which is non-Hermitian. Here $\hat{\mathcal{H}}(t)$ carries a time-sequence generated from the 1/f noise

PDF of interest. Choose a small time step δt such that the evolution operator can be well-approximated by terms linear to δt,

$$|\psi(t+\delta t)\rangle = \left[1 - i\hat{\mathcal{H}}_{\text{eff}}(t)\,\delta t\right]|\psi(t)\rangle\,. \tag{2.127}$$

One can check that the new state is no longer normalized,

$$P = \langle\psi(t+\delta t)\,|\psi(t+\delta t)\rangle = 1 - \sum_i p_i < 1, \tag{2.128}$$

where $p_i = \gamma_i \delta t\,\langle\psi(t)|\,\hat{L}_i^\dagger \hat{L}_i\,|\psi(t)\rangle$. This results from the non-Hermitian term in Eq. 2.126, which can be intuitively thought of as a damping term that evacuates the population from the excited state manifold.

2. Compare P with a random number R drawn from $[0,1]$. If $P > R$, intuitively it is more probable for no quantum jump to happen, so the final state is just a properly normalized $|\psi(t+\delta t)\rangle$,

$$|\psi(t+\delta t)\rangle' = |\psi(t+\delta t)\rangle\,/\sqrt{P}. \tag{2.129}$$

Note that even if no quantum jumps have occurred, they still impose a "back-action" effect on the final state, in the sense that for a superposition of the ground and excited state, no-jump is saying that the state was more likely to be a ground state.

On the other hand, if $P < R$, then a quantum jump $\hat{L}_i$ has happened among all the jump operators, with a probability of $\widetilde{p_i} = p_i / \sum_i p_i$, and the final state is

$$|\psi(t+\delta t)\rangle' = \frac{\hat{L}_i\,|\psi(t)\rangle}{\sqrt{\langle\psi(t)|\,\hat{L}_i^\dagger \hat{L}_i\,|\psi(t)\rangle}}. \tag{2.130}$$

3. Iterate on δt until a single trajectory is completed, then construct many trajectories by repeating the same procedure. Averaging over these trajectories yields the density state as a function of time.

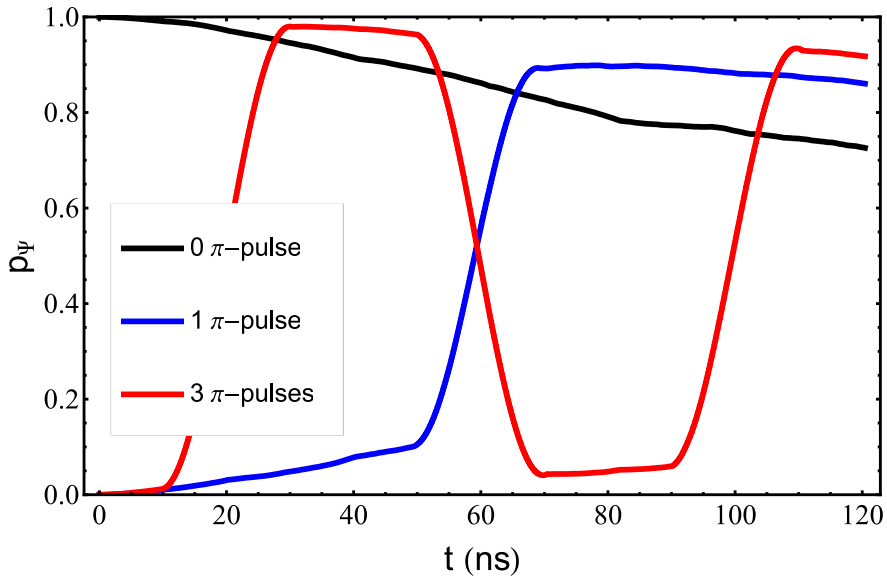

Figure 2.13: Monte Carlo wavefunction simulation of spin echo sequence under 1/f dephasing noise. Qubit is initialized at the equal superposition of the ground and excited state at the beginning of time. Under free evolution without spin echo, qubit decoheres according to the black line. A π pulse inserted in the middle of time flips the qubit, causing the phase to refocus under the autocorrelated 1/f noise and the increase of the decoherence time shown by the blue curve. Inserting more π pulses further suppresses the 1/f noise and leads to $T_2 \rightarrow 2T_1$, shown by the red curve. The Gaussian rather than exponential decay envelope is indicative of the 1/f spectrum.

The definitions of T_1 and T_2^* we have seen earlier are from NMR conventions, where there is another characteristic time T_2, defined as the transverse relaxation time with the inhomogeneity of the magnetic field (partially) removed by spin echos. The same concept can be borrowed for removing the temporal inhomogeneity (long correlation time) of single atom frequency in cavity or circuit-QED. As a demonstration of the Monte Carlo approach, we show in Fig. 2.13 how the 1/f noise is suppressed by a single spin echo, i.e. a π pulse inserted in the middle of x-y plane free rotation. The PSD of the 1/f dephasing noise can be more strongly filtered by applying echo pulses repetitively, where T_2 will approach the $2T_1$ limit under zero white noise component.

2.4.3 *Quantum input-output theory*

In many scenarios, it is more natural and convenient to move to the Heisenberg picture for analyzing the dynamics of a quantum system, where the time-dependency of the system is folded to the operator side as opposed to the state. The Heisenberg equation which is the equivalence of the Schrödinger equation in the Heisenberg picture is given by

$$\dot{\hat{A}} = \frac{i}{\hbar}\left[\hat{\mathcal{H}}, \hat{A}\right] + \left(\frac{\partial \hat{A}}{\partial t}\right)_H, \tag{2.131}$$

where $\hat{A}$ is an arbitrary operator and $\hat{\mathcal{H}}$ is the system Hamiltonian in the Heisenberg picture, and the last term is present when the operator $\hat{A}$ has explicit time-dependence. Mimicking the Lindblad master equation in the Schrödinger picture, we have for the Heisenberg picture

$$\dot{\hat{A}} = \frac{i}{\hbar}\left[\hat{\mathcal{H}}, \hat{A}\right] + \sum_i \hat{L}_i^\dagger \hat{A} \hat{L}_i - \frac{1}{2}\left\{\hat{L}_i^\dagger \hat{L}_i, \hat{A}\right\} + \left(\frac{\partial \hat{A}}{\partial t}\right)_H, \tag{2.132}$$

that describes the evolution of the operator for an open system. For the special case when the operator is the annihilation operator of a lossy cavity, it is easy to check that Eq. 2.132 produces

$$\dot{\hat{a}} = \frac{i}{\hbar}\left[\hat{\mathcal{H}}, \hat{a}\right] - \frac{\kappa}{2}\hat{a} + \left(\frac{\partial \hat{a}}{\partial t}\right)_H, \tag{2.133}$$

where κ is the photon loss rate of the cavity. To model a driven cavity under a coherent drive field $\hat{\mathcal{H}}_{\text{drive}} = \epsilon \cos\omega_d t \left(\hat{a}^\dagger + \hat{a}\right)$, strictly speaking, one cannot directly substitute the Hamiltonian in Eq. 2.133 by the time-dependent Hamiltonian in the Schrödinger picture, as it typically does not commute with the propagator. However, by applying a rotating frame transformation that cancels out the time-dependency as well as moving the operator to the interaction picture, one can obtain the Heisenberg equation for a driven damped cavity as

$$\dot{\hat{a}} = -\left(i\omega_c + \frac{\kappa}{2}\right)\hat{a} - \frac{i\epsilon}{2}e^{-i\omega_d t}. \tag{2.134}$$

The frequency spectrum of the cavity field is easily found from the Fourier transformation of Eq. 2.134 to be[1]

$$\hat{a}\left[\omega\right] = -\frac{i\pi\epsilon}{i\left(\omega_c - \omega\right) + \frac{\kappa}{2}}, \tag{2.135}$$

with the time-evolution of the cavity population being (assuming Fock initial state)

$$\langle \hat{a}^\dagger\left(t\right)\hat{a}\left(t\right)\rangle = e^{-\kappa t}\langle \hat{a}^\dagger\left(0\right)\hat{a}\left(0\right)\rangle + \frac{\epsilon^2}{4\left(\omega_c - \omega_d\right)^2 + \kappa^2}\left[1 - 2e^{-\frac{\kappa t}{2}}\cos\left(\omega_c - \omega_d\right)t + e^{-\kappa t}\right], \tag{2.136}$$

which saturates at the well-known $\bar{n} = \epsilon^2/\kappa^2$ steady state.

The classical drive field can be extended to a quantum model as an ensemble of bath modes, useful for describing the interaction between the cavity and propagating photons in a transmission line. Under the rotating wave approximation and Markov approximation, the equation of motion for the cavity driven by the bath modes can be derived as a quantum Langevin equation,

$$\dot{\hat{a}} = \frac{i}{\hbar}\left[\hat{\mathcal{H}}, \hat{a}\right] - \frac{\kappa_c + \kappa_i}{2}\hat{a} + \sqrt{\kappa_c}\hat{b}_{\text{in}}, \tag{2.137}$$

where κ_c and κ_i stands for the coupling and the internal decay rate of the cavity, and $\hat{b}_{\text{in}}$ is the input field that is defined as

$$\hat{b}_{\text{in}} = -\frac{1}{\sqrt{2\pi}}\int_{-\infty}^{\infty}\hat{b}\left(\omega\right)e^{-i\omega(t-t_0)}d\omega, \tag{2.138}$$

which is a propagating wave towards the cavity with t_0 being the initial moment when the wave packet is away from the cavity. The coupling between the cavity and the bath modes and the coupling decay rate are connected by Fermi's golden rule,

$$\kappa_c = 2\pi g^2, \tag{2.139}$$

1. The exponent of the Fourier transformation applied to the annihilation operator here and in the following has opposite sign to the conventional mathematical definition.

where we have made the Markov approximation. One can equally find the time-reversed equation with an output field $\hat{b}_{\text{out}}$,

$$\dot{\hat{a}} = \frac{i}{\hbar}\left[\hat{\mathcal{H}}, \hat{a}\right] + \frac{\kappa_c + \kappa_i}{2}\hat{a} - \sqrt{\kappa_c}\hat{b}_{\text{out}}, \tag{2.140}$$

so that the boundary condition between the input, output and the intra-cavity field is found from Eq. 2.137 and Eq. 2.140 as

$$\hat{b}_{\text{in}} + \hat{b}_{\text{out}} = \sqrt{\kappa_c}\hat{a}, \tag{2.141}$$

which is the so-called input-output relation. This formalism forms the basic framework of the input-output theory (IOT) [110, 111, 112, 113] as a powerful tool for solving a variety of problems including parametric conversion, amplification and quantum communication etc. Here we review a few applications of the IOT that are particularly relevant to our experiments. First of all, we notice that for the coherently driven cavity, the input field can be replaced by its mean value, $\langle \hat{b}_{\text{in}} \rangle = \beta e^{-i\omega_d t}$, so Eq. 2.140 becomes completely equivalent to Eq. 2.134. More generally, IOT allows one to find out the reflection and transmission coefficients of the cavity. As an example we consider a cavity coupled to a "hanger line" shown in Fig. 2.14, which is one of the most popular coupling scheme for readout cavities. Assuming balanced input and output impedance, we can use network analysis technique such as the ABCD matrix method to find out the transmission coefficient S_{21} as [114, 115, 116]

$$S_{21}(\omega) = 1 - \frac{Q_l}{Q_c}\frac{1}{1 - 2iQ_l(\omega - \omega_c)}, \tag{2.142}$$

where Q_l and Q_c are the loaded quality factor and the coupling quality factor connected to the circuit parameters via

$$Q_c = \frac{2\omega_c C}{Z_0 \omega_c^2 C_g^2}, \quad Q_l = \frac{2\omega_c C}{Z_0 \omega_c^2 C_g^2 + 2/R}, \tag{2.143}$$

and $\omega_c = 1/\sqrt{LC}$ is the cavity resonance frequency. From the IOT prospective, the quantum

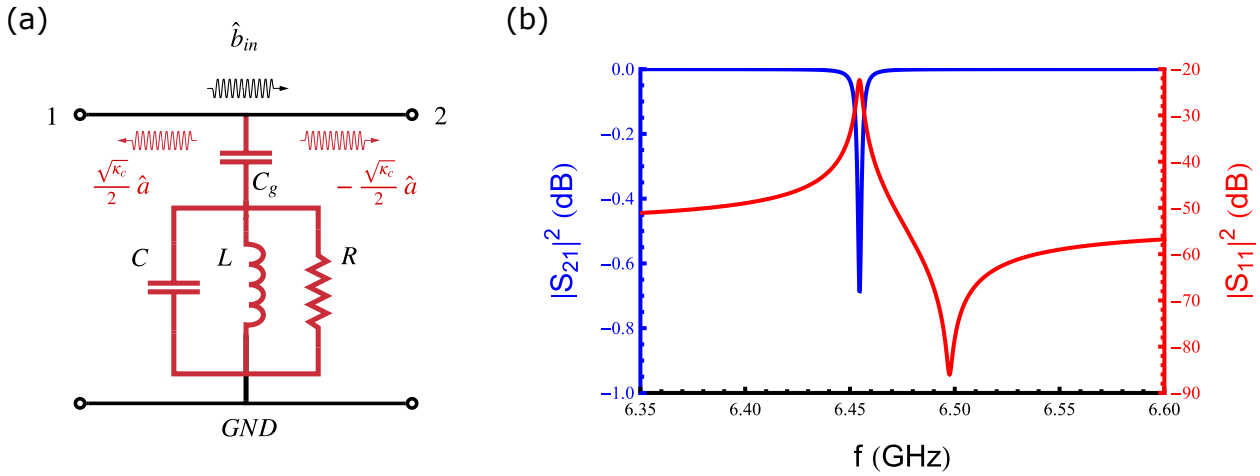

Figure 2.14: Quantum input-output theory of an RLC oscillator coupled to a "hanger" transmission line. (a) The cavity is driven by an input field $\hat{b}_{\text{in}}$ propagating from port 1 to port 2, while the intra-cavity field $\hat{a}$ leaks into the transmission line and propagates along both directions. The output fields detected at port 1 and port 2 are from the mixing between the input field and the intra-cavity field. (b) The transmission and the reflection coefficient as functions of the drive frequency. Hanger line readout allows the determination of the internal and coupling quality factors of the cavity from fitting the line-shapes with Eq. 2.142.

Langevin equation of the driven cavity is

$$\dot{\hat{a}} = -\left(i\omega_c + \frac{\kappa_i + \kappa_c}{2}\right)\hat{a} + \sqrt{\kappa_c}\hat{b}_{\text{in}}, \tag{2.144}$$

with boundary conditions

$$\hat{b}_{\text{out},1} = \frac{\sqrt{\kappa_c}}{2}\hat{a}, \quad \hat{b}_{\text{out},2} = -\frac{\sqrt{\kappa_c}}{2}\hat{a} + \hat{b}_{\text{in}}, \tag{2.145}$$

for the two ports. Note that the factor of 1/2 of the intra-cavity field amplitude is from the fact that emitted photons can travel in both directions of the hanger line. The transmission coefficient is obtained by solving the quantum Langevin equation in the frequency domain,

$$S_{21}(\omega) = \frac{\hat{b}_{\text{out},2}(\omega)}{\hat{b}_{\text{out},1}(\omega)} = \frac{\kappa_i - 2i(\omega - \omega_c)}{\kappa_i + \kappa_c - 2i(\omega - \omega_c)}. \tag{2.146}$$

Making use of the relations between the decay rates and the quality factors,

$$\kappa_i = \omega_c/Q_i, \quad \kappa_c = \omega_c/Q_c, \quad Q_l^{-1} = Q_i^{-1} + Q_c^{-1}, \tag{2.147}$$

one can be easily verify that Eq. 2.142 and Eq. 2.146 are identical.

The IOT is also useful for studying active networks containing non-reciprocal elements such as parametric amplifiers [111, 112, 99, 117, 118]. In the case of the non-degenerate parametric amplifier depicted in Fig 2.15a, the Hamiltonian is generally given by

$$\hat{\mathcal{H}}/\hbar = \omega_1 \hat{a}_1^\dagger \hat{a}_1 + \omega_2 \hat{a}_2^\dagger \hat{a}_2 + g\left(e^{-i\omega_p t + i\phi}\hat{a}_1^\dagger \hat{a}_2^\dagger + e^{i\omega_p t - i\phi}\hat{a}_1 \hat{a}_2\right), \tag{2.148}$$

where the pump frequency is close to the sum frequency of the two modes, $\omega_p \approx \omega_1 + \omega_2$. Moving to the rotating frame where $\hat{a}_1 \to \hat{a}_1 e^{-i\omega_p t}$, the Hamiltonian transforms to be time-independent,

$$\hat{\mathcal{H}}/\hbar = \delta_1 \hat{a}_1^\dagger \hat{a}_1 + \omega_2 \hat{a}_2^\dagger \hat{a}_2 + g\left(e^{i\phi}\hat{a}_1^\dagger \hat{a}_2^\dagger + e^{-i\phi}\hat{a}_1 \hat{a}_2\right) \tag{2.149}$$

with $\delta_1 = \omega_1 - \omega_p$. Substituting this into Eq. 2.133 and in the rotating basis, we have

$$\dot{\hat{a}}_1 = -\left(i\omega_1 + \frac{\kappa_1}{2}\right)\hat{a}_1 - ige^{-i\omega_p t + i\phi}\hat{a}_2^\dagger + \sqrt{\kappa_1}\hat{b}_{\text{in},1}, \tag{2.150}$$

$$\dot{\hat{a}}_2 = -\left(i\omega_2 + \frac{\kappa_2}{2}\right)\hat{a}_2 - ige^{-i\omega_p t + i\phi}\hat{a}_1^\dagger + \sqrt{\kappa_2}\hat{b}_{\text{in},2}, \tag{2.151}$$

which can be Fourier transformed into the frequency domain,

$$\left[i\left(\omega - \omega_1\right) - \frac{\kappa_1}{2}\right]\hat{a}_1\left(\omega\right) = ige^{i\phi}\hat{a}_2^\dagger\left(\omega_p - \omega\right) - \sqrt{\kappa_1}\hat{b}_{\text{in},1}\left(\omega\right), \tag{2.152}$$

$$\left[i\left(\omega - \omega_2\right) - \frac{\kappa_2}{2}\right]\hat{a}_2\left(\omega\right) = ige^{i\phi}\hat{a}_1^\dagger\left(\omega_p - \omega\right) - \sqrt{\kappa_2}\hat{b}_{\text{in},2}\left(\omega\right). \tag{2.153}$$

Plugging the boundary conditions Eq. 2.141 into these equations, we obtain

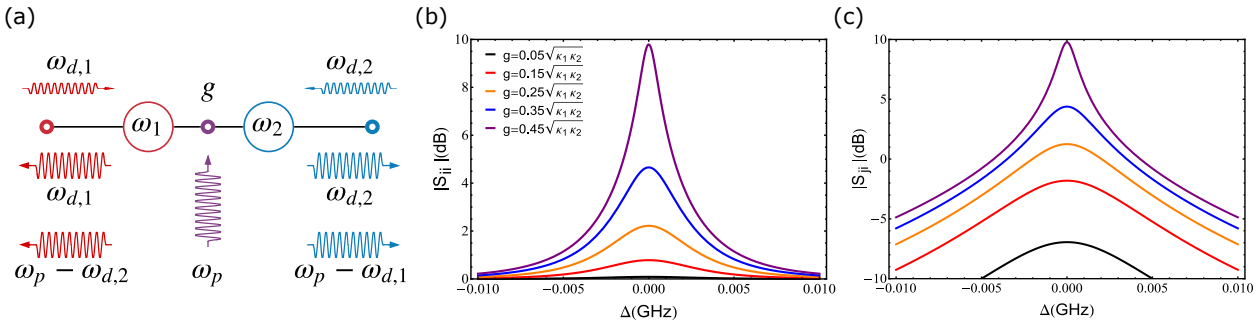

Figure 2.15: Input-output theory of a non-degenerate parametric amplifier. (a) The sketch of the non-degenerate paramp where the incident tone at frequency $\omega_{d,i}$ on the i-th mode is amplified by the pump signal at $\omega_p \approx \omega_1 + \omega_2$, giving rise to the reflected tone at $\omega_{d,i}$ and a transmitted tone converted to $\omega_p - \omega_{d,i}$. (b) Reflection spectrum of the i-th mode centered at the mode frequency, under different coupling strength g. The gain increases with g and explodes at $g = \sqrt{\kappa_1\kappa_2}/2$. (c) Transmission spectrum of the non-degenerate paramp under different coupling strengths. The transmitted signal acquires a similar gain to the reflected tone at $g \approx \sqrt{\kappa_1\kappa_2}/2$.

$$\left(i\Delta_1 + \frac{\kappa_1}{2}\right)\frac{\hat{b}_{\text{in},1}(\omega)}{\sqrt{\kappa_1}} + \left(i\Delta_1 - \frac{\kappa_1}{2}\right)\frac{\hat{b}_{\text{out},1}(\omega)}{\sqrt{\kappa_1}} = \frac{ige^{i\phi}}{\sqrt{\kappa_2}}\left[\hat{b}^\dagger_{\text{in},2}(\omega_p - \omega) + \hat{b}^\dagger_{\text{out},2}(\omega_p - \omega)\right], \tag{2.154}$$

$$\left(i\Delta_2 + \frac{\kappa_2}{2}\right)\frac{\hat{b}_{\text{in},2}(\omega)}{\sqrt{\kappa_2}} + \left(i\Delta_2 - \frac{\kappa_2}{2}\right)\frac{\hat{b}_{\text{out},2}(\omega)}{\sqrt{\kappa_2}} = \frac{ige^{i\phi}}{\sqrt{\kappa_1}}\left[\hat{b}^\dagger_{\text{in},1}(\omega_p - \omega) + \hat{b}^\dagger_{\text{out},1}(\omega_p - \omega)\right], \tag{2.155}$$

from which we can finally solve for the output fields

$$\hat{b}_{\text{out},1}(\omega) = \frac{\left\{\left[i(\omega - \omega_1) + \frac{\kappa_1}{2}\right]\left[i(\omega_p - \omega - \omega_2) + \frac{\kappa_2}{2}\right] + g^2\right\}\hat{b}_{\text{in},1}(\omega) + i\sqrt{\kappa_1\kappa_2}ge^{i\phi}\hat{b}^\dagger_{\text{in},2}(\omega_p - \omega)}{\left[-i(\omega - \omega_1) + \frac{\kappa_1}{2}\right]\left[i(\omega_p - \omega - \omega_2) + \frac{\kappa_2}{2}\right] - g^2}, \tag{2.156}$$

$$\hat{b}_{\text{out},2}(\omega) = \frac{\left\{\left[i(\omega - \omega_2) + \frac{\kappa_2}{2}\right]\left[i(\omega_p - \omega - \omega_1) + \frac{\kappa_1}{2}\right] + g^2\right\}\hat{b}_{\text{in},2}(\omega) + i\sqrt{\kappa_1\kappa_2}ge^{i\phi}\hat{b}^\dagger_{\text{in},1}(\omega_p - \omega)}{\left[-i(\omega - \omega_2) + \frac{\kappa_2}{2}\right]\left[i(\omega_p - \omega - \omega_1) + \frac{\kappa_1}{2}\right] - g^2}. \tag{2.157}$$

We see that the output field is a combination of its reflected input field and the converted input field of the other mode, both acquiring a gain through the parametric amplification. For resonant pumping and driving conditions, Eq. 2.156 and 2.157 further reduce to

$$\hat{b}_{\text{out},1}(\omega_1) = \frac{\left(\kappa_1\kappa_2 + 4g^2\right)\hat{b}_{\text{in},1}(\omega_1) + 4i\sqrt{\kappa_1\kappa_2}ge^{i\phi}\hat{b}_{\text{in},2}(\omega_2)}{\kappa_1\kappa_2 - 4g^2}, \tag{2.158}$$

$$\hat{b}_{\text{out,2}}(\omega_2) = \frac{\left(\kappa_1\kappa_2 + 4g^2\right)\hat{b}_{\text{in,2}}(\omega_2) + 4i\sqrt{\kappa_1\kappa_2}ge^{i\phi}\hat{b}_{\text{in,1}}(\omega_1)}{\kappa_1\kappa_2 - 4g^2} \tag{2.159}$$

where the amplification of the input fields is reflected as the increasing gain of the Lorentzian-shaped reflection and transmission spectrum as the coupling strength g approaches $\sqrt{\kappa_1\kappa_2}/2$, illustrated in Fig. 2.15b and c.

Finally, the IOT can also be solved in the time domain to investigate the dynamic process of photon emission and absorption [119, 120]. One particularly interesting example would be the release and catch of a single photon between two remote atom-cavity systems useful for quantum communication tasks. Specifically, the system to our interest is the communication device that will be more formally introduced in Chapter 3, which is composed of two identical microwave cavities connected by a coaxial cable, while each resonantly coupled to a superconducting qubit with tunable strengths. Assuming qubit 1 is initially excited, the single-photon transferring process between the two qubits is well-described by the quantum Langevin equations,

$$\dot{\hat{a}}_1 = -\frac{\kappa_1}{2}\hat{a}_1 - ig_1(t)\hat{\sigma}_1^- + \sqrt{\kappa_1}\hat{b}_{\text{in,1}}, \tag{2.160}$$

$$\dot{\hat{\sigma}}_1^- = -\frac{\gamma_1}{2}\hat{\sigma}_1^- - ig_1(t)\hat{a}_1, \tag{2.161}$$

$$\dot{\hat{a}}_2 = -\frac{\kappa_2}{2}\hat{a}_2 - ig_2(t)\hat{\sigma}_2^- + \sqrt{\kappa_2}\hat{b}_{\text{in,2}}, \tag{2.162}$$

$$\dot{\hat{\sigma}}_2^- = -\frac{\gamma_2}{2}\hat{\sigma}_2^- - ig_2(t)\hat{a}_2, \tag{2.163}$$

with boundary conditions

$$\hat{b}_{\text{in,i}} + \hat{b}_{\text{out,i}} = \sqrt{\kappa_i}\hat{a}_i, \tag{2.164}$$

$$\hat{b}_{\text{in,i}}(t) = e^{-\kappa_0 T_s}\hat{b}_{\text{out,j}}(t - T_s). \tag{2.165}$$

Here κ_i, γ_i and g_i stand for the cavity and qubit decay rate and the coupling strength of the i-th module, while κ_0 and T_s are the internal loss rate and the single-passage time of the cable. When the cable is nearly lossless, it is an easy exercise to prove the relation between its free spectral range $\Delta\nu_{\text{FSR}}$ and the single-passage time T_s, $\Delta\nu_{\text{FSR}} = (2T_s)^{-1}$. Two important regimes are

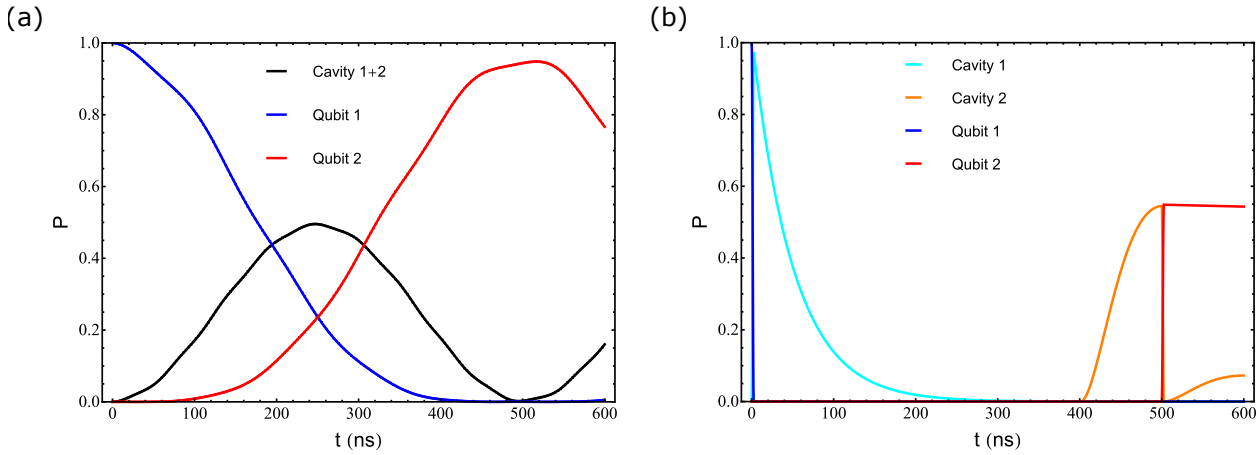

Figure 2.16: Time-domain input-output simulation of the single-photon transfer process between two remote quantum modules. Each module consists a superconducting qubit parametrically coupled to a microwave cavity that is connected to a coaxial cable, forming a quantum communication network. (a) In the "weak coupling regime" where $\Delta\nu_{\mathrm{FSR}} = 166\,\mathrm{MHz}$, $\kappa = 10\,\mathrm{MHz}$, $\gamma = 0.1\,\mathrm{MHz}$ and $g = 2\pi \times 1\,\mathrm{MHz}$, photon transferring is accomplished by simultaneously turning on the parametric qubit-cavity coupling for both modules, giving rise to a Lambda system that allows for qubit population swapping in a holonomic-gate fashion [121, 122]. The transfer fidelity in this case is mostly limited by qubit loss and systematic leakage into off-resonant cable modes. (b) In the "strong coupling regime" where $\Delta\nu_{\mathrm{FSR}} = 1.25\,\mathrm{MHz}$, $\kappa = 20\,\mathrm{MHz}$, $\gamma = 0.1\,\mathrm{MHz}$ and $g = 2\pi \times 100\,\mathrm{MHz}$, photon transfer can be achieved by first applying a qubit-cavity swapping operation, followed by the release, propagation and re-absorption of the photon between the cavities. Finally a qubit-cavity swapping is applied when the receiver cavity reaches maximum population and completes the transfer process. With fast swap gates and uncontrolled emission rate, the envelope of the wave packet is time-reversal-asymmetric and can only results in a fidelity of 54% as is shown in the simulation, which is dominantly limited by the reflection of the photon and can be substantially improved by engineering the swapping pulse shape or the emission rate. Qubit dephasing and cable loss also contribute to the infidelity but are neglected for both simulations for simplicity.

worth noting here:

1. The "weak coupling regime" where $\Delta\nu_{\mathrm{FSR}} \gg \kappa \gtrapprox g$, corresponding to what we have experimentally achieved in Chapter 3 where the two cavities hybridize into two normal modes[1] that are simultaneously coupled to both qubits, allowing the normal modes to be employed as a quantum bus to coherently swap the photon between the qubits, as demonstrated in Fig. 2.16a. The IOT simulation in this regime nicely reproduces the trajectories we have

1. Three normal modes will appear in the case where the cavity modes are degenerate with one of the cable modes.

observed in the communication experiment as well as the master equation simulation in Fig. 3.8c. The cable modes in this case are only "virtually" participating the transfer process as the free spectral range is far larger than all the coupling strengths, making the cable loss only weakly reduce the transfer fidelity through the Purcell effect.

2. The "strong coupling regime" where $\Delta\nu_{\mathrm{FSR}} \ll \kappa \lessapprox g$. In this regime, the cavity modes hybridize with an ensemble of cable modes with different wave vectors, a result of either a long coaxial cable or strong coupling between the cavity and the cable. The transmitted photon simultaneously occupies all these cable modes, rendering the full master equation simulation computationally challenging. In contrast, the IOT represented by Eq. 2.160 to 2.165 nicely produces the real-time propagation of the wave packet that can be thought of as a collective excitation of the cable modes. In this regime, photon transferring is achieved by the "pitch and catch" of the propagating photon (aka the "flying qubit") illustrated in Fig. 2.16b, where the time-reversal symmetry of the photon envelope is critical for yielding a high transfer fidelity [123, 124, 125, 126, 127].

2.4.4 Floquet method

According to the Bloch theorem, the wavefunction of single electron moving in a periodic 1D lattice can be written in the form

$$\hat{\psi}_k(x) = e^{ikx}\hat{u}_k(x), \tag{2.166}$$

with $\hat{u}_k(x)$ having the same periodicity as the lattice. The wavefunction is also invariant under displacement of the quasimomentum by integer numbers of the reciprocal lattice vector K,

$$\hat{\psi}_k(x) = \hat{\psi}_{k+nK}(x), \tag{2.167}$$

so that we can fold all the non-degenerate quasimomentum into the first Brillouin zone of $[-K/2, K/2]$. Mathematically, the structure outlined by Eq. 2.166 and 2.167 is well explained by the Floquet

theory [128] which predicts it to be a common feature of periodic linear differential equations, including of course Schrödinger equations with spatial or temporal periodicity. The latter can be thought of as the dual of the Bloch theorem that describes a periodically-driven quantum system, such as a superconducting circuit parametrically driven by a coherent field at frequency Ω with a period of $T = 2\pi/\Omega$,

$$i\hbar\frac{\partial\hat{\psi}}{\partial t} = \left[\hat{\mathcal{H}}_0 + \hat{\mathcal{H}}_d \cos\Omega t\right]\hat{\psi}. \tag{2.168}$$

Mapping the variables $k \leftrightarrow \omega$ and $x \leftrightarrow t$, we can *a priori* write out its solution mimicking Eq. 2.166 and 2.167 as [129]

$$\hat{\psi}_\omega(t) = e^{-i\omega t}\hat{u}_\omega(t), \tag{2.169}$$

where $\hat{u}_\omega(t) = \hat{u}_\omega(t+T)$ is called the "Floquet mode" with respect to the quasi-energy $\hbar\omega$, which is equivalent to all quasi-energies differing by an integer number of Ω,

$$\hat{\psi}_\omega(t) = \hat{\psi}_{\omega+n\Omega}(t), \tag{2.170}$$

so that the wavefunctions are only uniquely defined within the "first Brillouin zone", $[-\hbar\Omega/2, \hbar\Omega/2]$.

In order to actually use Eq. 2.169 for computation, we first need to obtain for all the allowed ω and their corresponding Floquet modes. Except for a few special cases where analytical solutions are present, in general finding them require numerical calculations. One way is to perform an *ab initio* calculation of the time-dependent Schrödinger equation for the propagator $U(T, 0)$, and make use the following relationship [130],

$$U(T)\,\hat{\psi}_\omega(0) = e^{-i\omega T}\hat{\psi}_\omega(0), \tag{2.171}$$

which is saying that the initial Floquet modes are eigenvectors of $U(T)$ with quasienergies directly determined by its eigenvalues. Once the propagator is numerically obtained for $[0, T]$, the Floquet

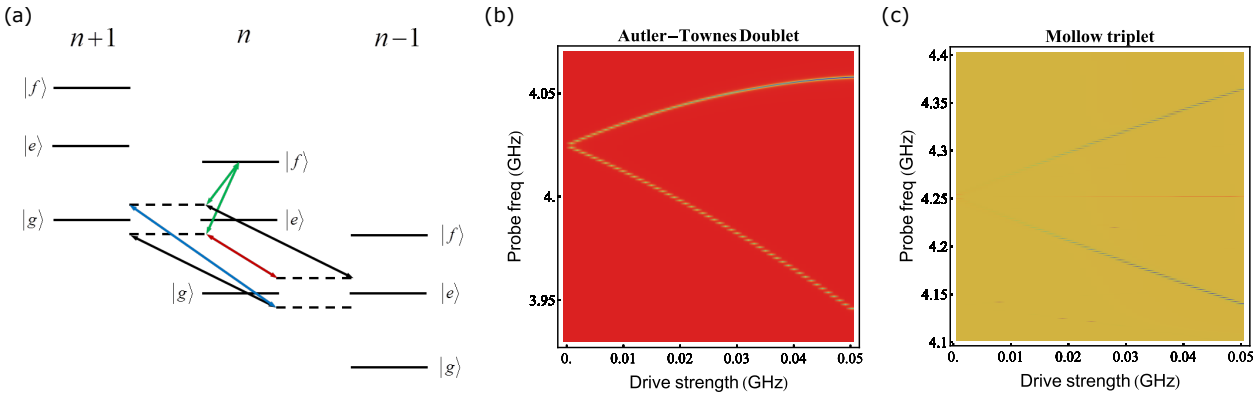

Figure 2.17: Floquet simulation of the Autler-Townes doublet and the Mollow triplet. The simulation is done for a transmon qubit coupled to a readout resonator, and measuring the cavity transmission amplitude at different probe frequencies and drive strengths. (a) Quasienergy spectrum of the driven transmon up to the $|f\rangle$ level. Under resonant driving, $|g\rangle$ and $|e\rangle$ hybridize into equal superposition states between different Floquet bands. The dressed states are dressed again by another probe tone, giving rise to finite transition rates between different quasienergy levels. The green arrows represent the Autler-Townes transition, while the blue, black and red arrows correspond to the Mollow triplet. (b) The Autler-Townes 2D spectrum against the probe frequency and the drive strength. The upper and lower branch are transitions from $|f, n\rangle$ to $|g, n+1\rangle \pm |e, n\rangle$. The center of the doublet is shifted down with increased drive strength due to the Bloch-Siegert Shift and the $|f\rangle$-level-induced AC Stark shift. (c) The Mollow triplet manifesting the couplings between the dressed state manifolds. The upper and the lower branch are from transitions between dressed levels of opposite parity, while the center one between the same parity appears as a weak signal from the $|f\rangle$ level hybridization. Unlike the Autler-Townes transition, the center frequency of the Mollow triplet is fixed by the energy of the drive field and remains unshifted w.r.t the drive strength.

state up to an arbitrary time t can be calculated through

$$\hat{\psi}_\omega(t) = e^{-i\omega t} U(t \bmod T)\, U(T)^{\lfloor t/T \rfloor}\, \hat{\psi}_\omega(0)\,, \tag{2.172}$$

and the overall state evolves as the superposition of all Floquet states with weights determined by the initial condition.

More intuition can be gained by approaching the Floquet formalism from a slightly different prospective [129, 131], where one expresses the T-periodic Floquet mode as a Fourier series,

$$\hat{\psi}_\omega(t) = \sum_\sigma \sum_{n=-\infty}^{\infty} c_{\sigma,n} e^{-in\Omega t} |\sigma\rangle\,, \tag{2.173}$$

in any orthogonal basis $|\sigma\rangle$ of the driven system. Substituting this into Eq. 2.168 and 2.169, and after some rearrangements, we arrive to

$$\sum_{\sigma'}\sum_{n'=-\infty}^{\infty} c_{\sigma',n}\left[n\hbar\omega\delta_{\sigma,\sigma'}\delta_{n,n'}+\frac{1}{T}\int_0^T dt\,\langle\sigma|\,\hat{\mathcal{H}}_0+\hat{\mathcal{H}}_d\cos\Omega t\,\left|\sigma'\right\rangle e^{-i(n'-n)\Omega t}\right]=\omega c_{\sigma,n}. \tag{2.174}$$

The above equation can be understood as a secular equation of the time-independent "Floquet Hamiltonian", which is an infinite Hermitian matrix defined by

$$\langle\sigma,n|\,\hat{\mathcal{H}}_F\left|\sigma',n'\right\rangle=\left(\hat{\mathcal{H}}_0+n\hbar\Omega\hat{I}\right)\delta_{n,n'}+\frac{\hat{\mathcal{H}}_d}{2}\delta_{n,n'\pm1}, \tag{2.175}$$

where H_0 and H_d are already in the $|\sigma\rangle$ basis. The quasienergies can be immediately obtained from diagonalizing $\hat{\mathcal{H}}_F$ with a proper truncation. This approach not only has the key advantage of reducing time-dependent problems into time-independent eigenvalue problems, but is also more physically meaningful as it is equivalent to treating the classical coherent drive as a quantum harmonic oscillator in a highly-excited coherent state. Correspondingly, the quasienergy levels are "real" in the sense that the spectroscopy of a periodically driven system under another weak probe tone exhibits discrete transition signals where selection rules are met, much like that of real energy levels. As an example, we plot the Floquet simulation of the Autler-Townes doublet and the Mollow triplet spectrum in Fig. 2.17, where the quantum nature of the drive field is reflected as a splitting of the transition signal on the probe tone spectroscopy. In the simulation, the strength of the drive tone resonant with the qubit $|g\rangle$ to $|e\rangle$ transition frequency, f_{ge}, is tuned between 0 and $2\pi\times50$ MHz, while the frequency of a separate probe tone sweeps across f_{ge} or f_{ef} with a fixed strength $2\pi\times0.1$ MHz.

CHAPTER 3

PARAMETRIC MODULATION OF QUBIT FREQUENCY

This chapter begins the presentation of our experimental results realizing the parametric control of flux-tunable superconducting circuits. Well-equipped with necessary theoretical knowledge after all the previous discussions, we now focus our analysis on the flux-driven circuits where the qubit frequency is dynamically modulated by one or a few coherent drive fields. This gives rise to the generation of "sidebands" of the qubit mode that can selectively couple to multiple other modes, a critical resource of connectivity and scalability exploited for the multimode quantum processor and the remote quantum module network, as we will see in the following sections.

3.1 Generation of Sidebands

In radio broadcasting, a carrier wave that is modulated produces sidebands besides its basic frequency. A frequency modulated (FM) signal with basic frequency ω_0 and modulation frequency ω_d has Fourier components at $\omega_0 \pm n\omega_d$ that appear as "sideband" signals, i.e.

$$f(t) = A_0 \cos(\omega_0 t + A_d \sin \omega_d t) = \sum_{n=-\infty}^{\infty} J_n(A_d) \cos(\omega_0 + n\omega_d) t. \tag{3.1}$$

where the amplitude of the m-th sideband is the m-th order Bessel function of the first kind of the modulation strength. Analogous to the FM signal is a FM qubit with a Hamiltonian

$$\hat{\mathcal{H}}_q/\hbar = (\omega_0 + \epsilon_d \cos \omega_d t) \frac{\hat{\sigma}_z}{2}, \tag{3.2}$$

whose propagator is given by

$$U_q = e^{-\frac{i}{\hbar}\int \hat{\mathcal{H}}_q dt} = e^{-i\left(\omega_0 t + \frac{\epsilon_d}{\omega_d}\sin\omega_d t\right)\frac{\hat{\sigma}_z}{2}} = \sum_{n=-\infty}^{\infty} J_n\left(\frac{\epsilon_d}{\omega_d}\right) e^{-\frac{i(\omega_0+n\omega_d)t}{2}\hat{\sigma}_z}. \tag{3.3}$$

Here we have made use of the Jacobi-Anger identity,

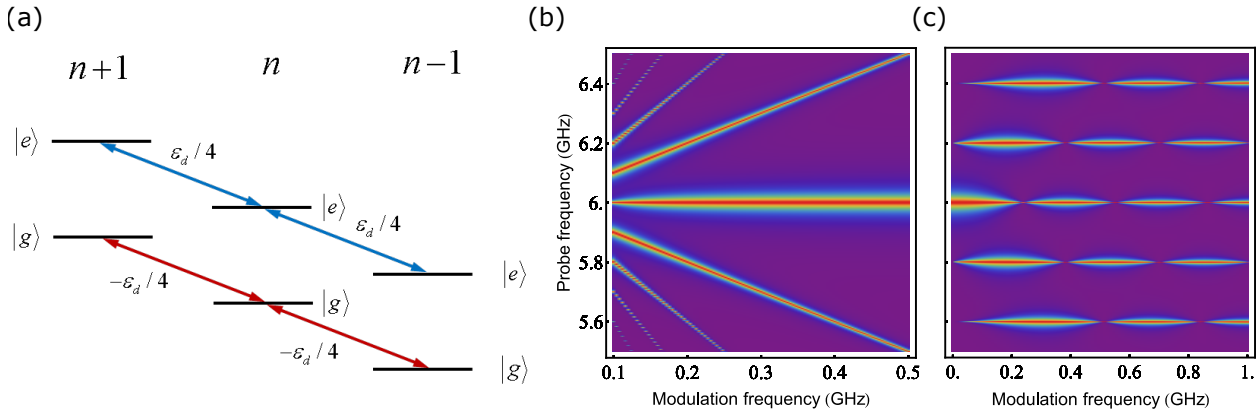

Figure 3.1: Floquet picture of the qubit frequency modulation and the generation of sidebands. (a) Quasienergy spectrum of the "FM qubit" where the modulation is effectively coupling all $|g\rangle$ and $|e\rangle$ levels between different Floquet bands with nearest neighbour coupling. (b) Spectroscopy of the FM qubit under a weak probe tone, where transitions between quasienergy levels show linear dependency on the modulation frequency. (c) The modulation frequency is fixed at 0.2 GHz while the modulation amplitude is swept from 0 to 1 GHz, resulting in the oscillation of the effective coupling strength between the sidebands and the probe field as a Bessel function of the modulation strength, which closely matches the theoretical prediction in Eq. 3.8.

$$e^{iz\sin\theta} = \sum_{n=-\infty}^{\infty} J_n(z)\, e^{in\theta}. \tag{3.4}$$

Already we see the generation of sidebands in Eq. 3.3, as the evolution of the FM qubit consists an infinite number of qubit evolution operators at all the sideband frequencies with different amplitudes. From the Floquet theory point of view, these sidebands are real spectral lines that can be observed with a probe tone. Depicted in Fig. 3.1a, the modulation can be thought of as creating a tight-binding lattice for the ground and the excited state manifold in the Floquet basis, with hopping parameters of opposite phases:

$$\hat{\mathcal{H}}^{(g)}_{\text{Floquet}}/\hbar = \sum_{n=-\infty}^{\infty} (\omega_0 - n\omega_d)\,|g,n\rangle\langle g,n| - \frac{\epsilon_d}{4}\left(|g,n\rangle\langle g,n+1| + h.c.\right), \tag{3.5}$$

$$\hat{\mathcal{H}}^{(e)}_{\text{Floquet}}/\hbar = \sum_{n=-\infty}^{\infty} (\omega_0 - n\omega_d)\,|e,n\rangle\langle e,n| + \frac{\epsilon_d}{4}\left(|e,n\rangle\langle e,n+1| + h.c.\right). \tag{3.6}$$

Diagonalization of these lattices gives rise to the dressed states for the n-th Floquet band,

$$\widetilde{|g,n\rangle} = \sum_{k=-\infty}^{\infty} J_k\left(\frac{\epsilon_d}{2\omega_d}\right)|g,n+k\rangle\,, \quad \widetilde{|e,n\rangle} = \sum_{k=-\infty}^{\infty} J_{-k}\left(\frac{\epsilon_d}{2\omega_d}\right)|e,n+k\rangle\,, \tag{3.7}$$

so the effective coupling strength between the quasienergy levels $\widetilde{|g,n\rangle}$ and $\widetilde{|e,n+k\rangle}$ with transition frequency $\omega_0 + k\omega_d$ is

$$g_k = A_p J_k\left(\frac{\epsilon_d}{\omega_d}\right), \tag{3.8}$$

where A_p is the amplitude of the probe tone, and we have used the identity

$$\sum_{k=-\infty}^{\infty} J_{-k}(x)\, J_{k+l}(y) = J_l(x+y)\,. \tag{3.9}$$

The modulation frequency and amplitude dependence of the sideband signals are well captured by the Floquet simulation, shown in Fig. 3.1b and c. Remarkably, when the ratio between the amplitude and frequency of the modulation reaches one of the zero points of the Bessel function, the qubit becomes "invisible" to the probe tone, which can be understood as a dynamical decoupling mechanism and has important applications as a hopping-energy tuning technique in many-body physics.

3.2 Stimulated Vacuum Rabi Interaction

Much like how the FM qubit responds to the probe tone at all sideband frequencies, a FM qubit can resonantly interact with the cavity mode it is coupled to when the detuning frequency matches one of the sidebands [132, 133]. Consider the Rabi model with a FM qubit,

$$\hat{\mathcal{H}}(t)/\hbar = \omega_c \hat{a}^\dagger \hat{a} + \frac{\omega_q + \epsilon_d \cos\omega_d t}{2}\hat{\sigma}_z + g\left(\hat{a}^\dagger + \hat{a}\right)\hat{\sigma}_x. \tag{3.10}$$

Rewriting it in the dressed basis with a leading-order S-W transformation and with all the static terms cancelled out by a rotating frame transformation, we have an effective Hamiltonian,

$$\hat{\mathcal{H}}_{\text{eff}}(t)/\hbar = \epsilon_d \cos\omega_d t \left(\frac{\hat{\sigma}_z}{2} + \frac{g}{\Delta}\hat{a}\hat{\sigma}^+ e^{i\Delta t} + \frac{g}{\Sigma}\hat{a}^\dagger\hat{\sigma}^+ e^{i\Sigma t} + h.c. \right), \tag{3.11}$$

where $\Delta = \omega_q - \omega_c$ and $\Delta = \omega_q + \omega_c$. Keep moving to the rotating frame by applying the transformation $U = e^{i\hat{\sigma}_z \int \epsilon_d \cos\omega_d t/2}$, we arrive to

$$\hat{\mathcal{H}}_{\text{eff}}(t)/\hbar = \epsilon_d \cos\omega_d t \left[\frac{g}{\Delta}\hat{a}\hat{\sigma}^+ e^{i\left(\Delta t + \frac{\epsilon_d}{\omega_d}\sin\omega_d t\right)} + \frac{g}{\Sigma}\hat{a}^\dagger\hat{\sigma}^+ e^{i\left(\Sigma t + \frac{\epsilon_d}{\omega_d}\sin\omega_d t\right)} + h.c. \right]. \tag{3.12}$$

According to the Jacobi-Anger identity in Eq. 3.4, when $\omega_d = \Delta/n$, the effective Hamiltonian under the RWA is

$$\hat{\mathcal{H}}_{\text{eff}}/\hbar = g J_n\left(\frac{n\epsilon_d}{\Delta}\right)\left(\hat{a}^\dagger\hat{\sigma}^- + \hat{a}\hat{\sigma}^+\right), \tag{3.13}$$

where we have used the recurrence relation,

$$2kJ_k(x) = x\left[J_{k-1}(x) + J_{k+1}(x)\right]. \tag{3.14}$$

We immediately see that the effective coupling strength is exactly the same as what we obtained in Eq. 3.8, which is not surprising as the probe field is essentially a mode in a highly-excited coherent state. Eq. 3.13 describes a single-photon exchange interaction between the qubit and the cavity mode, which is dubbed the "stimulated vacuum Rabi interaction" due to its resemblance of the vacuum-Rabi Hamiltonian for the static case. Similarly, when $\omega_d = \Sigma/n$, a two-photon pumping term is generated,

$$\hat{\mathcal{H}}_{\text{eff}}/\hbar = g J_n\left(\frac{n\epsilon_d}{\Sigma}\right)\left(\hat{a}^\dagger\hat{\sigma}^+ + \hat{a}\hat{\sigma}^-\right), \tag{3.15}$$

which can be used for squeezing, amplification and stabilization etc. In practice, the modulation frequency is usually set to the (absolute) detuning frequency, where the strength of these interactions becomes the 1st order Bessel function that has the largest maximum value of all orders $n \leq 1$,

$g_{\max} \approx 0.58g$, reached at $\epsilon_d \approx 1.84\Delta$ or $\epsilon_d \approx 1.84\Sigma$. The latter typically corresponds to a very large modulation amplitude and is usually hard to actually achieve.

Such sideband interactions obtained from FM qubits possess various advantages over traditional dc-flux controlled qubit. Under dc-flux tuning, the qubit can only be brought into resonance with an individual mode within its tunable range. Excitations are loaded into the modes by adiabatically tuning the qubit frequency through or near a mode resonance, which may suffer from stray Landau-Zener transition to all other modes in its path that leaves residual excitations in the manifold. Also, the qubit must be returned to the far-dispersive regime to minimize spurious unwanted interactions, requiring longer gate durations. In contrast, the parametric flux modulation can directly target the mode of interest with controllable interaction strength and phase, even if the mode is out of the dc-flux tuning range. By simultaneously modulating the qubit at multiple frequencies, it is possible to entangle the qubit with multiple modes at the same time, either for swapping population or for more complicated quantum operations. These nice properties, along with the multimode architecture that solves the connectivity issue, paves the road towards the building of random access quantum processor and remote quantum modules, which will be demonstrated in the following sections.

3.3 Random Access Quantum Information Processors

A practical quantum computer requires a large number of qubits working in cooperation, a challenging task for any quantum hardware platform. For superconducting qubits, there is an ongoing effort to integrate increasing numbers of qubits on a single chip [134, 135, 136, 137, 138, 139, 140]. This typically involves coupling many Josephson junction qubits into a lattice structure with nearest-neighbor interactions. While in ion trap quantum computers an all-to-all connectivity can be easily attained and exploited to its advantage [141, 142, 143], superconducting chip devices are constrained by circuit geometry that prevents high connectivity to be achieved. Classical computation architectures typically address this challenge by using a central processor which can randomly access a large memory, with the two elements often comprising distinct physical systems. We

implement a quantum analog of this architecture, realizing a random access quantum information processor using circuit QED.

As in the classical case, quantum logic elements, such as superconducting qubits, are expensive in terms of control resources and have limited coherence times. Quantum memories based on harmonic oscillators, instead, can have coherence times two orders of magnitude longer than the best qubits [144, 145], but are incapable of logic operations on their own. This observation suggests supporting each logic-capable processor qubit with many harmonic oscillator modes as "memory qubits". In the near term, this architecture provides a means of controlling tens of highly coherent qubits with minimal cryogenic and electronic-control overhead. To build larger systems compatible with existing quantum error correction architectures, one can connect individual modules consisting of a single processor qubit and a number of bits of memory while still accessing each module in parallel.

In this section, as the first important application of qubit frequency modulation we have achieved, we describe how to make use of a single non-linear element to enable universal quantum logic with random access on a collection of harmonic oscillators. Information is stored in distributed, readily accessible, and spectrally distinct resonator modes, while single qubit gates can be performed on arbitrary modes through frequency-selective parametric control to exchange information between the transmon and individual resonator modes. Making use of higher levels of the transmon, controlled-phase (CZ) and controlled-NOT (CX) gates on arbitrary pairs of modes can be realized, completing all the ingredients necessary for universal quantum computation with harmonic modes.

3.3.1 Multimode quantum memory

The multimode quantum memory circuit consists of a transmon coupled to a linear array of identical, strongly coupled superconducting resonators [84], shown in Fig. 3.2, with a circuit Hamiltonian of

$$\hat{\mathcal{H}}/\hbar = \omega_q \hat{a}^\dagger \hat{a} + \frac{\alpha}{2}\hat{a}^{\dagger 2}\hat{a}^2 + g_q\left(\hat{a}^\dagger \hat{b}_1 + \hat{a}\hat{b}_1^\dagger\right) + g_r \sum_{k=1}^{n-1}\left(\hat{b}_k^\dagger \hat{b}_{k+1} + \hat{b}_k \hat{b}_{k+1}^\dagger\right) + \omega_r \sum_{k=1}^{n} \hat{b}_k^\dagger \hat{b}_k. \quad (3.16)$$

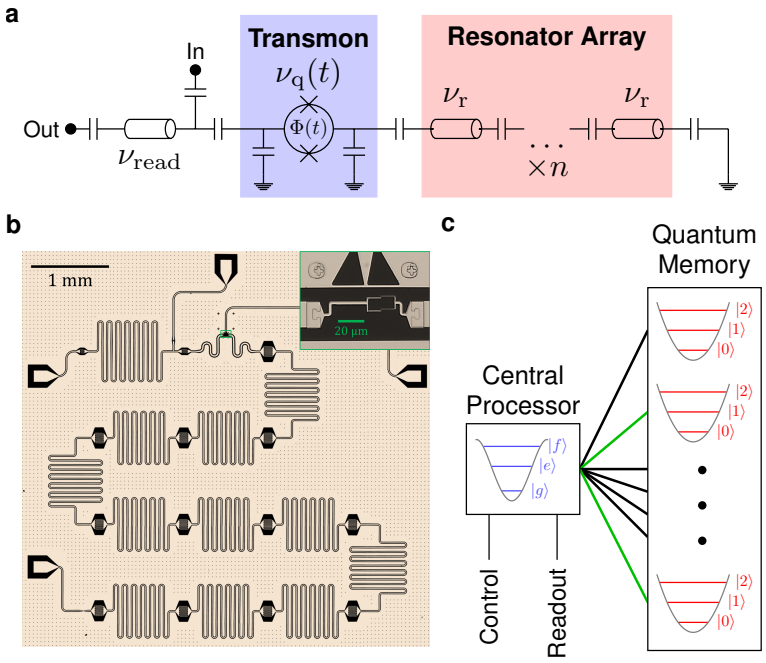

Figure 3.2: Random access superconducting quantum information processor. (a) and (b), Schematic and optical image, respectively, of the superconducting microwave circuit. The circuit comprises an array of 11 identically designed, coplanar waveguide (CPW) half-wave resonators, capacitively coupled strongly to each other. The top end of the array is capacitively coupled to a tunable transmon qubit. The transmon is measured with a separate resonator, whose input line doubles as a charge bias for the transmon. The inset shows the tunable SQuID of the transmon, as well as its flux bias above it. (c) Random access with multiplexed control. The quantum memory consists of the eigenmodes of the array, with each mode accessible to the transmon. This allows for quantum operations between two arbitrary memory modes (such as those highlighted in green) via the central processing transmon and its control lines.

Applying the B-V transformation introduced in section 2.3.1, we may write out the circuit Hamiltonian in the multimode normal mode basis, in a similar fashion to Eq. 2.50, as

$$\hat{\mathcal{H}}/\hbar = \omega_q \hat{a}^\dagger \hat{a} + \frac{\alpha}{2}\hat{a}^{\dagger 2}\hat{a}^2 + \sum_{k=1}^{n} g_k \left(\hat{a}^\dagger \hat{c}_k + \hat{a}\hat{c}_k^\dagger\right) + \sum_{k=1}^{n} \omega_k \hat{c}_k^\dagger \hat{c}_k, \tag{3.17}$$

with normal mode frequencies being

$$\omega_k = \omega_r - 2g_r \cos\left(\frac{k\pi}{n+1}\right). \tag{3.18}$$

The normal mode and bare multimode operators are connected to each other through

$$\hat{b}_k = \sum_{j=1}^{n} \sqrt{\frac{2}{n+1}} \sin\left(\frac{jk\pi}{n+1}\right) \hat{c}_j. \tag{3.19}$$

Substituting this into Eq. 3.16, we obtain the coupling strengths between the transmon and the normal modes as

$$g_k = g_q \sqrt{\frac{2}{n+1}} \sin\left(\frac{k\pi}{n+1}\right). \tag{3.20}$$

We see the important feature of the multimode circuit that every normal mode has non-zero participation at the edge site, allowing the transmon to couple to each mode. While this implementation is straightforward, the idea of a multimode memory also applies to related systems with many harmonic degrees of freedom, including long transmission-line [146] or 3D waveguide cavities [147]. It is also possible to use more of the oscillator Hilbert space, allowing logical encoding in terms of cat [148] and binomial code [149] states.

To achieve single-mode operation within the zero- and one-photon Fock states, we parametrically modulate the transmon frequency through an rf-flux tone. This results in a photon swapping operation (the "iSWAP gate") between the transmon and the normal mode when the modulation frequency is at the detuning between the two, which, along with qubit operations, can be utilized to perform arbitrary single-mode operations illustrated in Fig. 3.3a. Assuming the transmon is initially in the ground state, one simply needs to swap the state between the transmon and the normal mode, apply the desired quantum gate U to the transmon, then perform the swapping operation again, i.e.

$$|g\rangle\otimes(\alpha|0\rangle + \beta|1\rangle) \rightarrow i(\alpha|g\rangle + \beta|e\rangle)\otimes|0\rangle \rightarrow iU(\alpha|g\rangle + \beta|e\rangle)\otimes|0\rangle \rightarrow -|g\rangle\otimes U(\alpha|0\rangle + \beta|1\rangle). \tag{3.21}$$

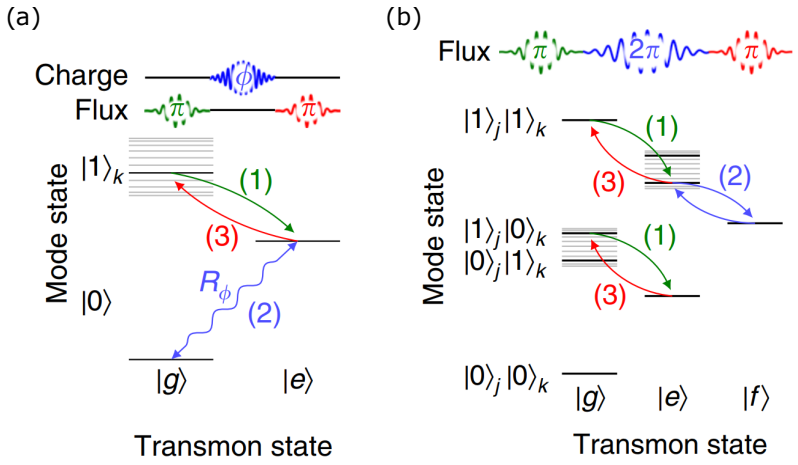

Figure 3.3: Single-mode gate and two-mode CZ gate pulse sequence for the multimode architecture. (a) The sequence for generating arbitrary single-qubit gates of a memory mode: (1) The mode's initial state, consisting of a superposition of 0 and 1 photon Fock states, is swapped to the transmon (initially in its ground state), using a transmon-mode iSWAP. (2) The transmon is rotated by the desired amount (R_ϕ) via its charge control line. (3) The rotated state is swapped back to the mode, by reversing the iSWAP gate in (1). Segments of this sequence are used to achieve state preparation [steps (2) and (3)] and measurement [steps (1) and (2)] of each mode. (b) Protocol for controlled-phase (CZ) gate between an arbitrary pair of modes, with j indicating the control mode and k indicating the target mode of the gate: (1) The state of mode j is swapped to the transmon via a transmon-mode iSWAP pulse at the frequency difference between the transmon $|g\rangle - |e\rangle$ transition and mode k. (2) A CZ gate is performed between mode k and the transmon, by applying two frequency-selective iSWAPs from energy level $|e1\rangle$ to level $|f0\rangle$ and back, mapping the state $|e1\rangle$ to $-|e1\rangle$. (3) The state of the transmon is swapped back to mode j, reversing the iSWAP in (1).

3.3.2 Universal quantum operations

To achieve universal control of the quantum memory, we extend our parametric protocols to realize two-mode gates. We perform conditional operations between the transmon and individual modes by utilizing the $|e\rangle - |f\rangle$ transition of the transmon. A controlled-phase (CZ) gate between the transmon and an individual mode consists of two sideband iSWAPs resonant to the $|e1\rangle - |f0\rangle$ transition, selectively mapping the state $|e1\rangle$ to -$|e1\rangle$, leaving all other states unchanged due to the anharmonicity of the transmon:

$$|g\rangle \otimes (\alpha\,|0\rangle + \beta\,|1\rangle) \rightarrow |g\rangle \otimes (\alpha\,|0\rangle + \beta\,|1\rangle)\,, \tag{3.22}$$

$$|e\rangle \otimes (\alpha |0\rangle + \beta |1\rangle) \rightarrow \alpha |e\rangle \otimes |0\rangle + i\beta |f\rangle \otimes |0\rangle \rightarrow |e\rangle \otimes (\alpha |0\rangle - \beta |1\rangle) . \tag{3.23}$$

To enact a CZ gate between two arbitrary modes, the control mode is swapped into the transmon, a transmon-mode CZ is performed, and the mode is swapped back as illustrated in Fig. 3.3b. In our device, gate speeds (250-400 ns) are primarily limited by crosstalk between iSWAP operations on the $|g\rangle - |e\rangle$ and $|e\rangle - |f\rangle$ transitions of modes with difference frequencies approaching the anharmonicity of the transmon. This crosstalk can be reduced by tailoring the frequency spacing of the memory modes and the anharmonicity of the transmon. In addition to the CZ gate, we obtain controlled-X and Y gates (CX, CY) between modes by swapping $|e\rangle$ and $|f\rangle$ transmon state populations in the middle of the pulse sequence for the CZ gate. These gate protocols can be extended to realize two-mode SWAP gates, as well as multi-qubit gates such as Toffoli and controlled-controlled-phase (CCZ) gates [150] between arbitrary modes.

3.4 Quantum Communication Between Remote Multimode Modules

On top of the multimode architecture that realizes high connectivity on the single chip level, another promising approach to scaling up superconducting quantum computing hardware is to adopt a modular architecture [151, 152, 153] in which modules are connected together via communication channels to form a quantum network. This reduces the number of qubits required on a single chip, and allows greater flexibility in reconfiguring and extending the resulting information processing system. In such an architecture, each module is capable of performing universal operations on multiple-bits, and neighboring modules are connected through photonic channels, allowing communication and entanglement generation between remote modules.

In light of this spirit, we show how to further push up the scalability of the multimode device by employing parametric flux control to perform quantum operations between remote multimode modules. Each module, as displayed in Fig. 3.4, is composed of a flux-tunable transmon (yellow), eight multimode cavities formed by two chains of identical lumped-element resonators (purple), a readout cavity (cyan) as well as a CPW "communication cavity" (green) that plays an important

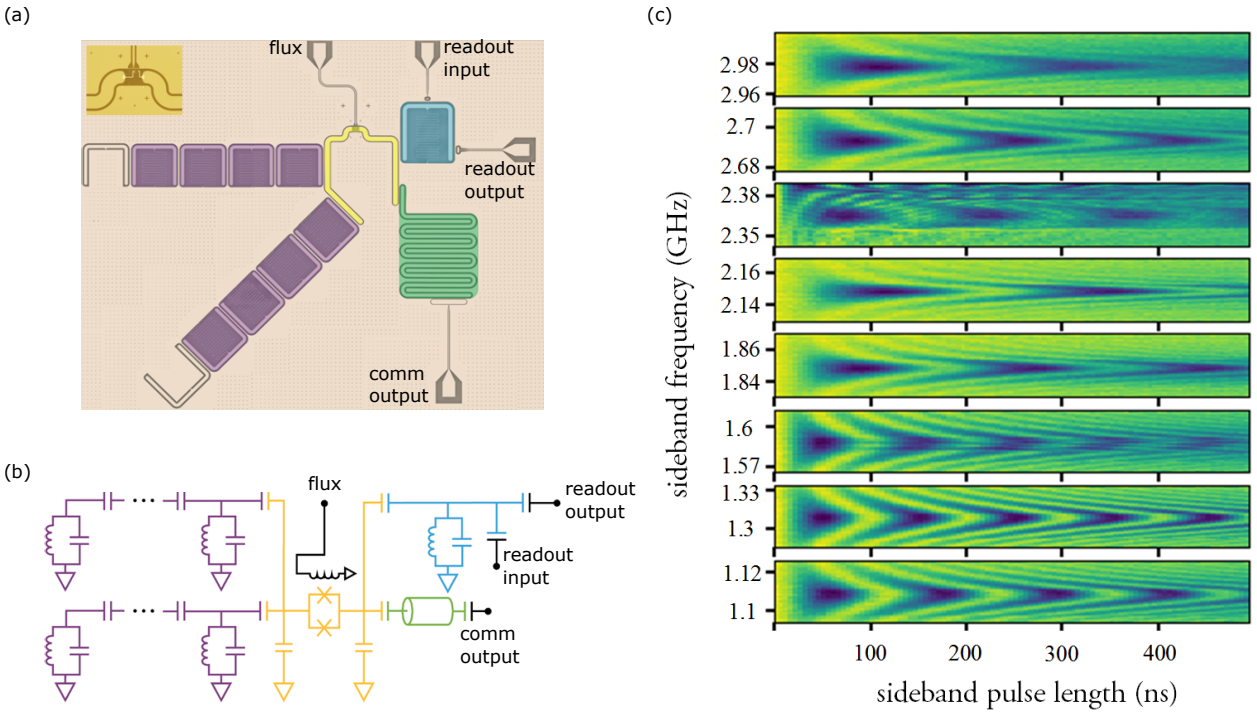

Figure 3.4: The remote multimode module. (a, b) False-colored photo and circuit diagram of a remote multimode module. Each chip consists of a frequency-tunable transmon and two chains of four identically designed, lumped-element resonators. In addition, a resonator is included for readout, and a second resonator is to be coupled to the coaxial cable that provides the communication link between the chips. (c) The chevron patterns generated by sweeping the length of the flux modulation pulse at each detuning frequency and measuring the excited state population of the transmon after the pulse ends. The local memory on each processor can be used for local processing and entanglement distillation in future work.

role in the communication experiment. The sideband modulation of the frequency-tunable transmon can access resonators in each chip by targeting their corresponding frequency detunings, as shown in Fig. 3.4c.

3.4.1 Connecting modules with communication channel

Remote entanglement between superconducting qubits has been realized probabilistically [154, 155, 156]. A deterministic quantum communication channel is advantageous over a probabilistic one because it lowers the threshold requirement for fault-tolerant quantum computation and can achieve higher entanglement rates [157]. Realizing deterministic photonic communication

requires releasing a single photon from one qubit and catching it with the remote qubit. In the long-distance limit, the photon emission and absorption are from a continuum density of states. In this limit, static coupling limits the maximum transfer fidelity to only 54% , as we have seen in section 2.4.3. This limit is exceeded by dynamically tailoring the emission and absorption profiles. These capabilities are presently being used to perform photonic communication between superconducting qubits connected by a transmission line within a cryostat [156, 158, 159, 160]. In these experiments, the use of a circulator enables the finite-length transmission line to be modeled as a long line with a continuum density of states, at the cost of added transmission loss.

Here, we establish bidirectional photonic communication between two superconducting qubits through a multimodal communication channel. Rather than inserting a circulator, the multimode nature of the finite length transmission line is made manifest and exploited [161]. For intra-cryostat communication, the required connection coaxial cable length of 1 m or less results in a free spectral range on the order of 100 MHz. Illustrated in Fig. 3.5, the coaxial cable is coupled to the communication cavities of the two modules. The communication cavities are designed to be CPW resonators with a large center pin and gap width to make the frequency insensitive to fabrication variations [162], resulting in their near-identical frequency ω_r as well as the coupling strength to the cable mode, g_c. Since the free spectral range of the coaxial cable is an order of magnitude larger than g_c, we consider the cable as a single mode at ω_c nearly resonant with the communication cavities. This leads to the Hamiltonian of the three modes as

$$\hat{\mathcal{H}}/\hbar = \sum_{i=1}^{2} \omega_i \hat{b}_i^\dagger \hat{b}_i + \omega_c \hat{b}_c^\dagger \hat{b}_c + g_c \sum_{i=1}^{2} \left(\hat{b}_i^\dagger \hat{b}_c + \hat{b}_i \hat{b}_c^\dagger \right). \tag{3.24}$$

Eq. 3.24 can be directly diagonalized by the B-V transformation, yielding three normal modes $\hat{B}_\pm$ and $\hat{D}$,

$$\hat{\mathcal{H}}/\hbar = \omega_+ \hat{B}_+^\dagger \hat{B}_+ + \omega_- \hat{B}_-^\dagger \hat{B}_- + \omega_D \hat{D}^\dagger \hat{D}. \tag{3.25}$$

In the ideal case where the two communication cavities are perfectly degenerate, $\omega_1, 2 = \omega_r$, we

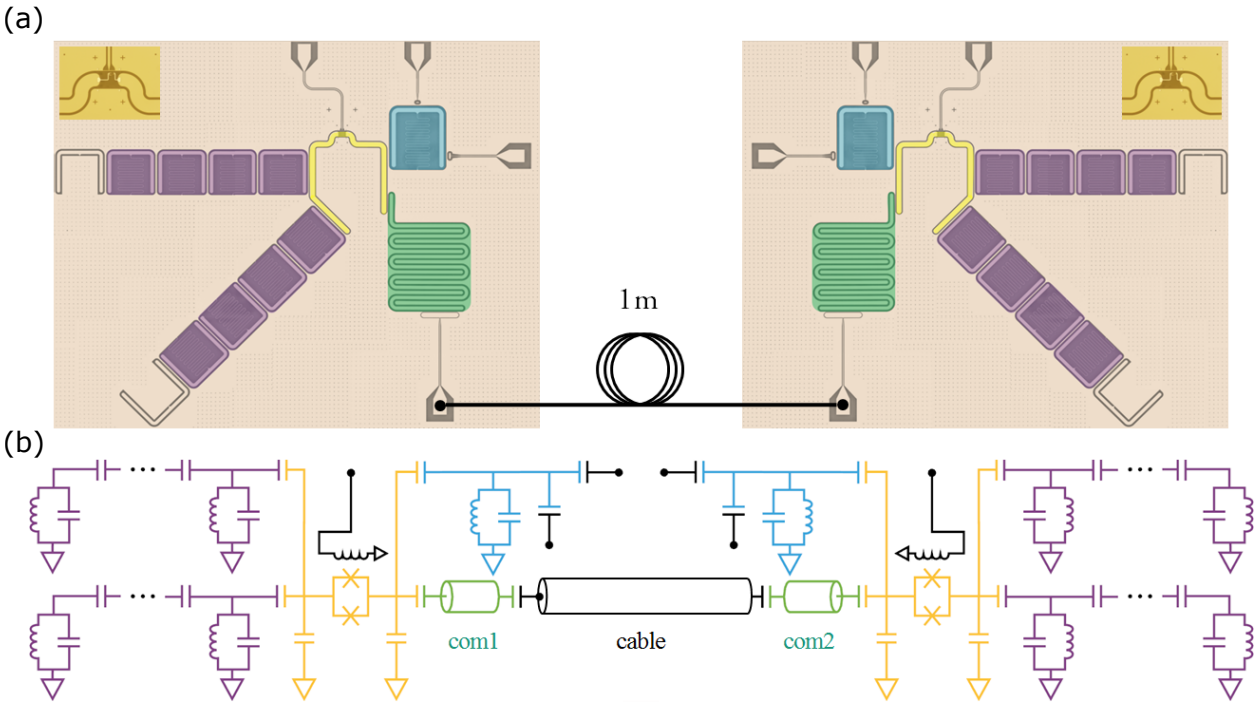

Figure 3.5: The remote multimode module. (a, b) False-colored photo and circuit diagram of a remote multimode module. Each chip consists of a frequency-tunable transmon and two chains of four identically designed, lumped-element resonators. In addition, a resonator is included for readout, and a second resonator is to be coupled to the coaxial cable that provides the communication link between the chips. (c) The chevron patterns generated by sweeping the length of the flux modulation pulse at each detuning frequency and measuring the excited state population of the transmon after the pulse ends. The local memory on each processor can be used for local processing and entanglement distillation in future work.

have

$$\omega_D = \omega_r, \quad \omega_\pm = \omega_r + \frac{1}{2}\left(\Delta \pm \sqrt{8g_c^2 + \Delta^2}\right), \tag{3.26}$$

and

$$\hat{D} = \frac{1}{\sqrt{2}}\left(\hat{b}_1 - \hat{b}_2\right), \quad \hat{B}_\pm = \frac{1}{\sqrt{2 + \left(r \pm \sqrt{2 + r^2}\right)^2}}\left[\hat{b}_1 + \hat{b}_2 + \left(r \pm \sqrt{2 + r^2}\right)\hat{b}_c\right]. \tag{3.27}$$

Here Δ stands for the deviation of the cable mode frequency from the communication resonator frequency, i.e. $\Delta = \omega_c - \omega_r$, and $r = \Delta/2g_c$. We refer to the $\hat{B}_\pm$ as the "bright" modes, and $\hat{D}$ the "dark" mode for the simple reason that the later has no cable mode participation, making it highly

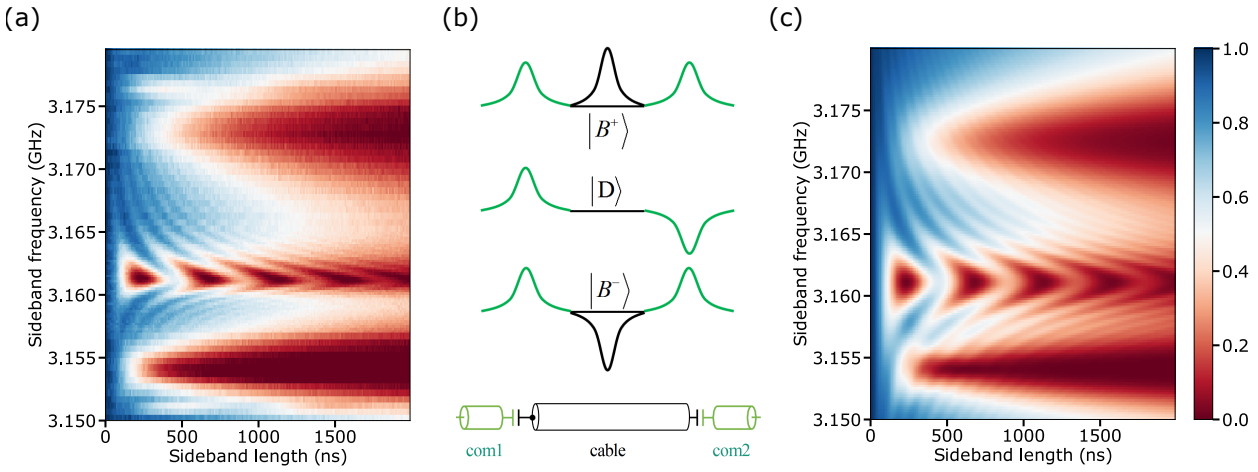

Figure 3.6: The communication normal modes and the stimulated vacuum Rabi oscillation between the qubit and normal modes. By fitting to the experimental data (a) using our analytical model, we extracted the deviation of the cable mode frequency from the two communication resonators to be 4.25 MHz, while the coupling between the cable mode and the communication resonator is 6.46 MHz. Plugging these along with other circuit parameters obtained from the experiment into a master equation, we can simulate the experimental result with decent agreement (c). (b) The schematic showing the wavefunctions of the coupled system involving the communication resonators and the coaxial cable. The three degenerate modes hybridize and form three normal modes with distinct signatures. The center dark mode has minimal participation in the lossy cable mode and has high quality factor.

immune to the photon loss of the cable. Suppose the bare coupling strength between the transmon and the communication cavity is g_0, the renormalized coupling strengths between the qubit and these normal modes are given by

$$g_D = \frac{g_0}{\sqrt{2}}, \quad g_\pm = \frac{g_0}{\sqrt{2 + \left(h \pm \sqrt{2+h^2}\right)^2}}. \tag{3.28}$$

We further see that the dark mode also couples more strongly to the qubit comparing to the other two bright modes, which will be helpful for a faster communication rate. These nice features of the dark mode are well confirmed in our experiment shown in Fig. 3.6, where parametric modulation of the transmon frequency leads to three stimulated vacuum Rabi oscillations at the normal mode frequencies, with the center chevron being the fastest and the most coherent of the three.

The above derivation is based on the ideal scenario where the two communication resonators

have the same resonant frequency. In reality, the imperfection of the circuit fabrication inevitably gives rise to a small detuning between the two resonators, with a typical value around a few MHz as observed from sample iterations. Also couplings between the two resonators and the rest of the cable modes need to be accounted for a more accurate calculation, as they lead to the an additional Purcell loss of the communication mode. Measure through our best fit of data with simulation, we find the detuning between the two communication cavities to be $\delta = 2\pi \times 5\,\text{MHz}$, the detuning and the coupling between the communication cavity and the cable mode to be $\Delta = 2\pi \times 4.25\,\text{MHz}$ and $g_c = 2\pi \times 6.46\,\text{MHz}$, the quality factors of the bare communication resonator and bare cable mode to be $Q_r = 2.65 \times 10^5$ and $Q_c = 2.1 \times 10^3$, and a free spectrum range of the cable of $\Delta\nu = 100\,\text{MHz}$, then the rotating frame Hamiltonian describing the communication cavities and the nearest three cable modes can be written as

$$\hat{\mathcal{H}}/\hbar = \sum_{k=1}^{2} \left[(k-1)\,\delta - \Delta\right] \hat{b}_k^\dagger \hat{b}_k + \sum_{n=-1}^{1} 2\pi n \Delta\nu \hat{b}_{c,n}^\dagger \hat{b}_{c,n} + g_c \sum_{k,n} \left(\hat{b}_k^\dagger \hat{b}_{c,n} + \hat{b}_k \hat{b}_{c,n}^\dagger\right). \quad (3.29)$$

Plugging the values for each parameter in the above Hamiltonian, and being cognizant of the alternating phase of neighboring cable mode wave functions, we numerically diagonalize the Hamiltonian and obtain a participation of the lossy cable in the communication mode to be 6.5%, and we find the quality factors of the "dark" communication mode and the "bright" normal modes to be $Q_c = 2.67 \times 10^4$, $Q_1 = 5.5 \times 10^3$ and $Q_2 = 3.8 \times 10^3$, which quantitatively agrees with their corresponding coherence times that are characterized by the combination of iSWAP operation plus transmon population measurement.

In order to calculate the communication processes between the remote modules, we write out the Hamiltonian of the driven network in the rotating frame, as

$$\hat{\mathcal{H}}/\hbar = \sum_{i=1}^{2} \sum_{l=\pm} \left\{ (\omega_l - \omega_D)\, \hat{B}_l^\dagger \hat{B}_l + J_1 \left(\frac{\epsilon_i}{\omega_{d,i}}\right) \left[g_l \left(\hat{B}_l \hat{\sigma}_i^+ + \hat{B}_l^\dagger \hat{\sigma}_i^-\right) + g_D \left(\hat{D}\hat{\sigma}_i^+ + \hat{D}^\dagger \hat{\sigma}_i^-\right)\right]\right\}, \quad (3.30)$$

Circuit parameters	1st	2nd	3rd
Transmon frequency (GHz)	4.7685	4.7420	N/A
Transmon T_1 (μs)	10.1	7.9	N/A
Transmon T_2^* (μs)	0.7	1.4	N/A
Bare comm frequency (GHz)	7.878 (comm1)	7.883 (cable)	7.883 (comm2)
Bare comm T_1 (μs)	5.35	0.043	5.35
Normal mode frequency (GHz)	7.872 (bright)	7.88 (dark)	7.891 (bright)
Normal mode T_1 (μs)	0.15	0.55	0.1

Table 3.1: Remote multimode module circuit parameters.

with ϵ_i and $\omega_{d,i}$ being the flux modulation amplitude and frequency of the i-th transmon. The corresponding master equation is

$$\dot{\rho} = -\frac{i}{\hbar}\left[\hat{\mathcal{H}}, \rho\right] + \sum_{l=\pm} \kappa_b \mathcal{D}[\hat{B}_l]\rho + \kappa_d \mathcal{D}[\hat{D}]\rho + \sum_{i=1}^{2} \gamma_i \mathcal{D}[\hat{\sigma}_i^-]\rho + \sum_{i=1}^{2} \gamma_{i,\phi} \mathcal{D}[\frac{\hat{\sigma}_{i,z}}{\sqrt{2}}]\rho, \tag{3.31}$$

where the decay and dephasing parameters can be directly obtained from Table. 3.1. With these, we are able to simulate the bidirectional photon transfer experiment and the remote entanglement experiment that will be discussed in the following sections.

3.4.2 Bidirectional single-photon transferring

To demonstrate photonic communication between the two chips, we send a single photon from one chip to the other using the dark mode (from this point on we will call it the "communication mode") as the transfer medium. As parametric modulation allows us to couple the transmons to the communication mode, the most obvious scheme would be to excite the sender qubit, swap its population into the communication mode by parametric flux modulation, followed by modulating the receiver qubit frequency to transfer the photon from the communication mode to the receiver qubit. In our experiment, we switch on sideband interactions simultaneously on both qubits. When the amplitudes of the flux modulations are carefully matched such that the two sideband couplings are equal, this effectively creates a non-adiabatic holonomic gate [121, 122] between the qubits that swaps the population from one to the other, allowing the photon transfer to be accomplished in

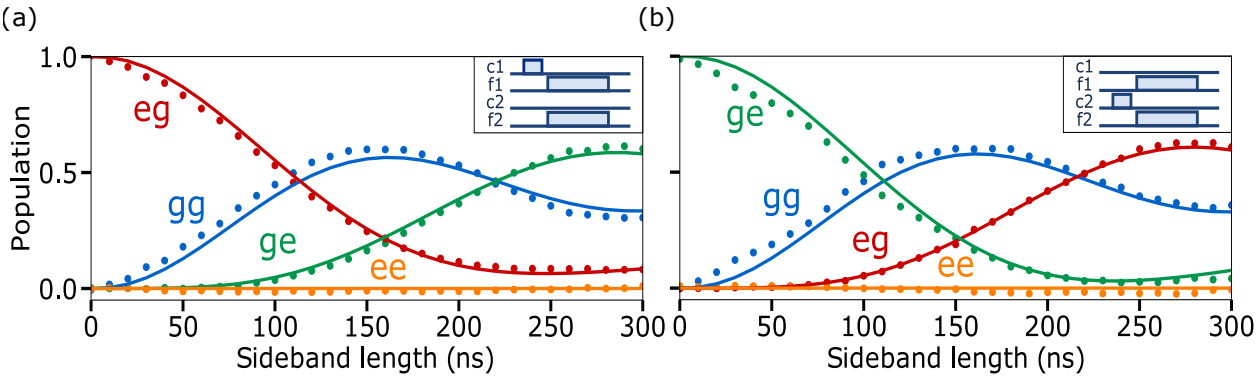

Figure 3.7: Bidirectional excitation transfer. The inset at top right shows the pulse sequence used to implement excitation transfer. The labels $c1$, $c2$ denote the charge drives on qubits 1 and 2, respectively, and $f1$, $f2$ the respective flux drives. We first apply a π pulse to excite one of the qubits, then simultaneously switch on the sideband flux pulse to drive the transfer process. Using the same sideband sequence, but instead applying the π pulse to the other qubit, we can send a single photon in the opposite direction. The transfer fidelity is limited by qubit dephasing and photon decay in the communication mode. Described in the following, the transfer process in different directions have slightly different loss mechanisms. (a) Excitation transfer from qubit 1 to qubit 2. Notice that in this transfer process the sender qubit is not able to fully receive its excitation (population of $|eg\rangle$ does not reach zero). As confirmed by the master equation simulation, this is due to the dephasing of qubit 1. The remaining errors arise from communication cavity loss and dephasing of qubit 2, which is less than that of qubit 1. (b) Excitation transfer from qubit 2 to qubit 1. In this process, while qubit 2 releases most of its excitations (population of $|ge\rangle$ comes close to zero), the dephasing of qubit 1 prevents it from capturing all the excitations in the communication mode, resulting in a slightly higher final population in $|gg\rangle$. The resulting fidelities for the transfer in the two directions are similar: $\{P_{|ge\rangle}, P_{|eg\rangle}\} \approx 61\%$, confirming the results from our numerical simulation.

a shorter time than two sequential sideband π pulses with less communication mode participation, which are both helpful for achieving a higher transfer fidelity. Sending a photon in the reverse direction simply takes the same sideband sequence but exciting the other qubit instead. Fig. 3.7 shows the transmon population plotted as a function of the sideband pulse length. The master equation simulation results (solid lines) are shown along with the experimental data (dots). We are able to obtain photon transfer with a success rate of $\{P_{|ge\rangle}, P_{|eg\rangle}\} \approx 61\%$. We use square pulses for the time-envelopes of the modulation which is the optimal choice under the current circuit parameters. Note that the achieved transfer fidelity exceeds 54%, the maximum fidelity for absorbing a naturally shaped emission into a continuum. This demonstrates a qualitative difference

in transferring via a multimode cable compared to that of releasing and catching flying photonic qubits through a continuum.

The transfer fidelity is limited by qubit dephasing and photon decay in the communication mode. Qubit 1 has a higher dephasing rate ($T_2^* \approx 700\,\text{ns}$) than qubit 2 ($T_2^* \approx 1.4\,\mu\text{s}$). The dephasing rate of qubit 1 is comparable to the sideband coupling rate, with the result that this qubit is not able to fully release its excitation during the transfer process. Conversely, for transfer in the other direction qubit 1 is not able to receive all of the excitations. This transfer infidelity can be largely mitigated by using a fixed-frequency qubit less susceptible to the flux noise, with its coupling strength to the communication mode parametrically controlled via a tunable coupler circuit [69, 68, 70, 71, 72]. The remaining loss of transfer fidelity comes from the loss in the communication mode. From our numerical simulations detailed in the appendix, we estimate that the overall photon loss in both the qubits and the communication mode contribute to an infidelity of 24%, while the dephasing error of the two qubits accounts for an infidelity of 15%. The sideband coupling rate of the transmon is limited by the range over which its frequency can be parametrically tuned, resulting in a maximum effective sideband coupling to the communication resonator of $\approx$ 2 MHz. With improved qubit coherence time, our simulation shows that more sophisticated transfer protocols such as STIRAP can be employed to boost transfer efficiency, see subsection 3.2.

3.4.3 Remote entanglement generation

We now entangle two qubits by creating a Bell state between the transmons on the respective chips. We can create such a state by first applying the $\sqrt{\text{iSWAP}}$ gate between the excited qubit 1 and the communication mode, which generates the Bell state $(|g1\rangle + |e0\rangle)/\sqrt{2}$ between them. We implement the $\sqrt{\text{iSWAP}}$ by applying a sideband modulation pulse to qubit 1 to perform a $\pi/2$ rotation. Subsequently, we transfer the state of the communication mode to qubit 2 through the iSWAP gate by applying a sideband modulation pulse to the latter to perform a π rotation. Ideally this sequence prepares the Bell state $|\Psi^+\rangle = (|ge\rangle + |eg\rangle)/\sqrt{2}$ shared between the two remote qubits. To minimize decoherence the sender and receiver pulses can be applied simultaneously, so

long as the lengths and amplitudes of the pulses are adjusted appropriately. Choosing qubit 1 as the sender and using square pulses, we found — both in our simulation and in the experiment — that maximal fidelity was obtained by setting both pulses at the same coupling rate and the length of the receiver pulse to be slightly longer than twice that of the sender, demonstrated by the pulse sequence diagram in Fig. 3.8b. The resulting Bell state has a fidelity of $\langle\Psi^+|\rho_{\text{exp}}|\Psi^+\rangle = 79.3 \pm 0.3\%$. We obtained the density matrix ρ_{exp} using quantum state tomography with an over-complete set of measurements complemented with the maximum likelihood method, and we corrected the measurement error by constructing a confusion matrix. To measure the two-qubit state, we record the homodyne voltage for each qubit from every run. For example, run i of the experiment would result in a 4D heterodyne voltage values ($V_{I1,i}$, $V_{Q1,i}$, $V_{I2,i}$, $V_{Q2,i}$). These voltages are random numbers generated from a specific distribution corresponding to state projection and experimental noise. To measure the population in the four two-qubit basis states: $|gg\rangle, |ge\rangle, |eg\rangle, |ee\rangle$ we construct the histograms for these states by applying π pulses to the qubits. These histograms approximate the probability distribution for measuring a given voltage pair when the system is in a given basis state. We employ logistic regression for classification of the two-qubit states. By setting decision thresholds for maximizing the classification accuracy for the two-qubit basis states according to the voltage distribution, we obtain a confusion matrix representing the correct and incorrect identification of basis state. For an unknown density matrix ρ we construct the classification distribution for ρ from N measurements, and project onto the basis states by applying the inverse of the calculated confusion matrix M (row: prepared state, column: measured state) for the states $\{|gg\rangle, |ge\rangle, |eg\rangle, |ee\rangle\}$, where

$$M = \begin{bmatrix} 0.8293 & 0.1053 & 0.0572 & 0.0082 \\ 0.1841 & 0.7514 & 0.0122 & 0.0523 \\ 0.101 & 0.0117 & 0.7923 & 0.095 \\ 0.0236 & 0.0979 & 0.1686 & 0.7099 \end{bmatrix}$$

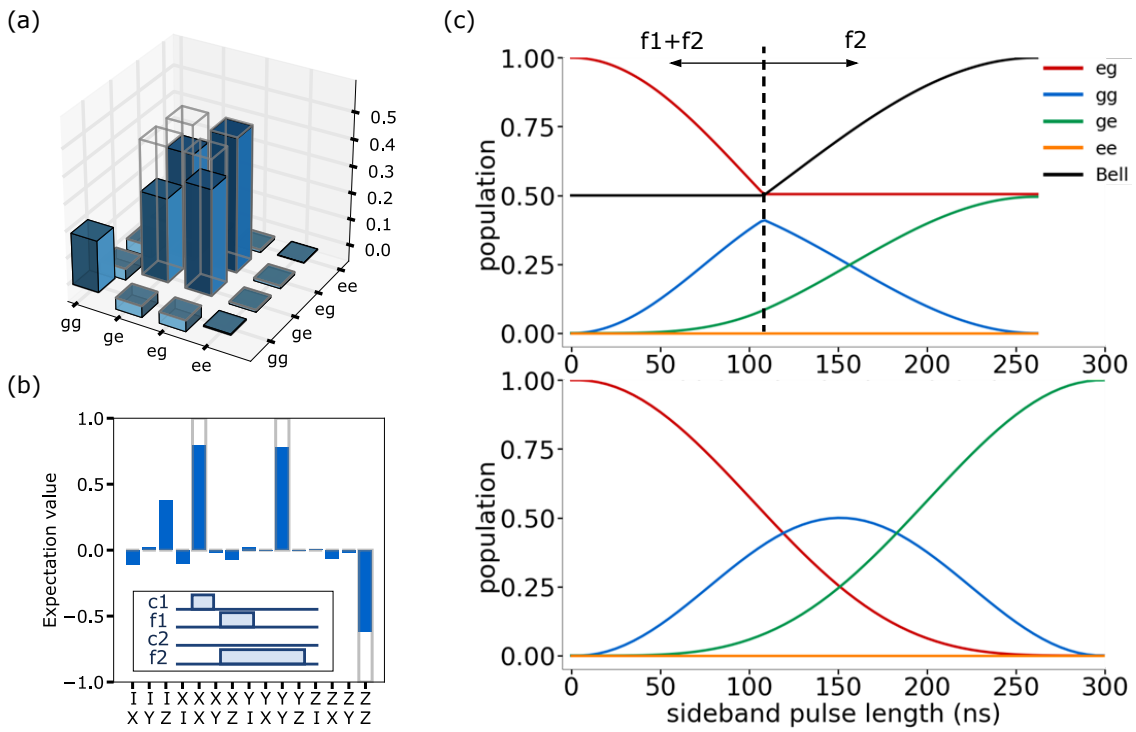

Figure 3.8: Bell pair creation. (a) Real component of the density matrix. (b) Expectation values of two-qubit Pauli operators. (c) Simulation of the evolution of the two-qubit states for the entanglement generation (up) and the single-photon transferring (down) under the same sideband coupling strength, in the lossless idea situation. The dashed line indicates the end of the sending flux pulse in the Bell pair creation, which is at the time point where the sender qubit drops to 50% population. Then the receiving pulses keeps transferring the "half photon" from the communication mode to the receiver qubit until the later also reaches 50% population, resulting in the creating of the Bell state.

We perform state tomography using the standard method by calculating the linear estimator,

$$\rho_{est} = \sum_{i,j} \frac{Tr[(\sigma_i \otimes \sigma_j)\rho](\sigma_i \otimes \sigma_j)}{4}. \tag{3.32}$$

To calculate the term $Tr[(\sigma_i \otimes \sigma_j)\rho$ we apply a unitary operator U to ρ prior to measurement. For two-qubits, there are nine required measurements corresponding to the following unitary operators, $(I, R_Y(\pi/2), R_X(\pi/2)) \otimes (I, R_Y(\pi/2), R_X(\pi/2))$. This simple linear estimator method can return unphysical results because it projects onto the space of all Hermitian matrices with Trace 1. However a physical density matrix must also be positive semi-definite. Following the maximum

likelihood protocol outlined in [84, 163], we estimate the most likely physical density matrix by minimizing the function,

$$F[\rho_{est}] = \sum_{i=1,j=1}^{N,4} (\langle j|U_i^\dagger \rho_{est} U_i|j\rangle - P_{i,j})^2 \tag{3.33}$$

, where U_i are the set of N applied tomography pulses, $|j\rangle$ is the j-th basis state, $P_{i,j}$ is the measured probability, and ρ_{est} is a physical density matrix satisfying the physical constraints. The starting guess for the minimization is the density matrix estimated from the linear estimator with all negative eigenvalues set to zero. To form a over-complete set for a total of 17 tomography measurements, we also measure the negative pulse set [164] $(I, R_Y(-\pi/2), R_X(-\pi/2)) \otimes (I, R_Y(-\pi/2), R_X(-\pi/2))$. It can be inferred from the data that the fidelity is almost equally limited by photon decay in the cable and the qubit dephasing errors. We also note that the Bell state fidelity is significantly higher than the success probability we achieved for photon transfer. The reason becomes more obvious by looking at the evolution of the states plotted in Fig. 3.8c. First of all, the entanglement scheme has shorter pulse length, and less channel mode participation which is the primary source of error. Moreover, in contrary to the photon swapping scheme, the entanglement pulse sequence is not time-reversal symmetric so that we can use the qubit with higher T2 as the sender qubit to minimize the infidelity due to the dephasing loss.

3.4.4 Suppression of 1/f noise in the communication process

In this subsection we study how quantum noises of realistic power spectrum affect the communication fidelity. We limit ourselves to single-excitation subspace where the relevant states are the dressed basis

$$|\mathcal{G}\rangle = |g0g\rangle\,, \quad |\mathcal{B}\rangle^{\pm} = \frac{1}{2}\left(|e0g\rangle + |g0e\rangle \pm \sqrt{2}\,|g1g\rangle\right), \quad |\mathcal{D}\rangle = \frac{1}{\sqrt{2}}\left(|e0g\rangle - |g0e\rangle\right). \tag{3.34}$$

$|\mathcal{D}\rangle$ and $|\mathcal{B}\rangle$ are not to be confused with the normal modes of the communication cavities and the cable, but should be understood as the dark and bright modes from the hybridization of the driven qubits and the communication mode in the rotating frame. Without loss of generality, we set the initial state to be

$$|\Phi(0)\rangle = |e0g\rangle = \frac{1}{\sqrt{2}}|\mathcal{D}\rangle + \frac{1}{2}\left(|\mathcal{B}\rangle^{+} + |\mathcal{B}\rangle^{-}\right). \tag{3.35}$$

Under coherent evolution, the state becomes

$$|\Phi(t)\rangle = \frac{1}{\sqrt{2}}|\mathcal{D}\rangle + \frac{1}{2}\left(e^{-i\sqrt{2}\Omega t}|\mathcal{B}\rangle^{+} + e^{i\sqrt{2}\Omega t}|\mathcal{B}\rangle^{-}\right). \tag{3.36}$$

Assuming the sideband interaction strength Ω to be far greater than the noise amplitudes, we make the following observations for relaxation and decoherence processes within the dressed basis:

1. The bright states $|B\rangle^{\pm}$ relax to each other at rates

$$\Gamma_{BB}^{\pm} = \frac{1}{8}\left(S_{zz}^{(1)}\left[\pm 2\sqrt{2}\Omega\right] + S_{zz}^{(2)}\left[\pm 2\sqrt{2}\Omega\right]\right), \tag{3.37}$$

while they relax to the dark state $|D\rangle$ at

$$\Gamma_{BD}^{\pm} = \frac{1}{4}\left(S_{zz}^{(1)}\left[\pm\sqrt{2}\Omega\right] + S_{zz}^{(2)}\left[\pm\sqrt{2}\Omega\right]\right). \tag{3.38}$$

The dark state also relax to the bright states at

$$\Gamma_{DB}^{\pm} = \frac{1}{4}\left(S_{zz}^{(1)}\left[\mp\sqrt{2}\Omega\right] + S_{zz}^{(2)}\left[\mp\sqrt{2}\Omega\right]\right). \tag{3.39}$$

Assuming symmetric PSD $S_{zz}[-\omega] = S_{zz}[\omega]$, we have

$$\Gamma_{BB}^{\pm} = \Gamma_{BB} = \frac{1}{8}\left(S_{zz}^{(1)}\left[2\sqrt{2}\Omega\right] + S_{zz}^{(2)}\left[2\sqrt{2}\Omega\right]\right), \tag{3.40}$$

$$\Gamma_{BD}^{\pm} = \Gamma_{DB}^{\pm} = \Gamma_{BD} = \frac{1}{4}\left(S_{zz}^{(1)}\left[\sqrt{2}\Omega\right] + S_{zz}^{(2)}\left[\sqrt{2}\Omega\right]\right). \tag{3.41}$$

2. $|B\rangle^{\pm}$ decay to the ground state $|G\rangle$ at

$$\Gamma_{BG}^{\pm} = \frac{1}{4}\left(S_{xy}^{(1)}\left[\omega_1 \pm \sqrt{2}\Omega\right] + S_{xy}^{(2)}\left[\omega_2 \pm \sqrt{2}\Omega\right] + 2S_{xy}^{(c)}\left[\omega_c \pm \sqrt{2}\Omega\right]\right), \tag{3.42}$$

while the dark state relax to the ground state at

$$\Gamma_{DG} = \frac{1}{2}\left(S_{xy}^{(1)}\left[\omega_1\right] + S_{xy}^{(2)}\left[\omega_2\right]\right). \tag{3.43}$$

Assuming $\Omega \ll \omega_1, \omega_2, \omega_c$, we have

$$\Gamma_{BG}^{\pm} = \Gamma_{BG} \approx \frac{\gamma_1 + \gamma_2 + 2\kappa_c}{4}, \quad \Gamma_{DG} \approx \frac{\gamma_1 + \gamma_2}{2}. \tag{3.44}$$

3. There is no intrinsic dephasing rate between the two bright states, but a relaxation-induced decoherence rate of

$$\Gamma_{B\phi} = \Gamma_{BB} + \Gamma_{BD} + \Gamma_{BG}. \tag{3.45}$$

In contrast, the dark state and the bright states have a pure dephasing rate of $\left(\gamma_{\phi,1} + \gamma_{\phi,2}\right)/16$, and the overall decoherence rate is

$$\Gamma_{D\phi} = \frac{1}{2}\left(\Gamma_{BB} + \Gamma_{BG} + \Gamma_{DG} + 3\Gamma_{BD} + \frac{\gamma_{\phi,1} + \gamma_{\phi,2}}{8}\right). \tag{3.46}$$

In above, γ_i and $\gamma_{\phi,i}$ stand for the lab-frame decay and dephasing rate of the i-th qubit, κ_c is the photon loss rate of the communication mode.

One can in principle construct the evolution of the density matrix based on the information above. Here we take a different approach by studying the effective Lindblad operators in the dressed basis. Within the single-excitation subspace, and in the rotating frame where the ground

state, dark state and bright states are isoenergetic, the Lindblad superoperators are given by

$$\widetilde{\mathcal{D}}\left[\hat{\sigma}_{1,2}^{-}\right]=\mathcal{D}\left[\frac{1}{2}\hat{\sigma}_{B+}^{-}\pm\frac{\sqrt{2}}{2}\hat{\sigma}_{D}^{-}+\frac{1}{2}\hat{\sigma}_{B-}^{-}\right],\quad\widetilde{\mathcal{D}}\left[\frac{\hat{\sigma}_{i,z}}{\sqrt{2}}\right]=\mathcal{D}\left[\frac{\hat{\Sigma}_{i,z}+\hat{\Sigma}_{i,x}}{\sqrt{2}}\right],\tag{3.47}$$

$$\widetilde{\mathcal{D}}\left[\hat{D}\right]=\mathcal{D}\left[\frac{1}{\sqrt{2}}\hat{\sigma}_{B+}^{-}-\frac{1}{\sqrt{2}}\hat{\sigma}_{B-}^{-}\right],\tag{3.48}$$

where

$$\Sigma_{i,z}=-\frac{\hat{\sigma}_{z,B+}+\sqrt{2}\hat{\sigma}_{z,D}+\hat{\sigma}_{z,B-}}{4},\tag{3.49}$$

$$\Sigma_{1,x}=-\sqrt{\frac{S_{zz}^{(1)}\left[2\sqrt{2}\Omega\right]}{S_{zz}^{(1)}\left[0\right]}}\hat{\sigma}_{BB}^{-}+\sqrt{\frac{S_{zz}^{(1)}\left[-\sqrt{2}\Omega\right]}{2S_{zz}^{(1)}\left[0\right]}}\hat{\sigma}_{DB+}^{-}+\sqrt{\frac{S_{zz}^{(1)}\left[\sqrt{2}\Omega\right]}{2S_{zz}^{(1)}\left[0\right]}}\hat{\sigma}_{DB-}^{-}+h.c.,\tag{3.50}$$

$$\Sigma_{2,x}=-\sqrt{\frac{S_{zz}^{(2)}\left[2\sqrt{2}\Omega\right]}{S_{zz}^{(2)}\left[0\right]}}\hat{\sigma}_{BB}^{-}-\sqrt{\frac{S_{zz}^{(2)}\left[\sqrt{2}\Omega\right]}{2S_{zz}^{(2)}\left[0\right]}}\left(\hat{\sigma}_{DB+}^{-}+\hat{\sigma}_{DB-}^{-}\right)+h.c.\tag{3.51}$$

Here we assume the relaxation noise to be white noise and the dephasing noise to be symmetric. Further,

$$\hat{\sigma}_{B\pm}^{-}=\left|\mathcal{G}\right\rangle\left\langle\mathcal{B}\right|^{\pm},\quad\hat{\sigma}_{D}^{-}=\left|\mathcal{G}\right\rangle\left\langle\mathcal{D}\right|\tag{3.52}$$

$$\hat{\sigma}_{z,B\pm}=\left|\mathcal{B}\right\rangle^{\pm}\left\langle\mathcal{B}\right|^{\pm}-\left|\mathcal{G}\right\rangle\left\langle\mathcal{G}\right|,\quad\hat{\sigma}_{z,D}=\left|\mathcal{D}\right\rangle\left\langle\mathcal{D}\right|-\left|\mathcal{G}\right\rangle\left\langle\mathcal{G}\right|,\tag{3.53}$$

$$\hat{\sigma}_{BB}^{-}=\left|\mathcal{B}\right\rangle^{-}\left\langle\mathcal{B}\right|^{+},\quad\hat{\sigma}_{DB+}^{-}=\left|\mathcal{B}\right\rangle^{+}\left\langle\mathcal{D}\right|,\quad\hat{\sigma}_{DB-}^{-}=\left|\mathcal{B}\right\rangle^{-}\left\langle\mathcal{D}\right|.\tag{3.54}$$

Plugging these into the effective master equation in the dressed basis

$$\dot{\widetilde{\rho}}=-\frac{i}{\hbar}\left[\widetilde{\hat{\mathcal{H}}},\widetilde{\rho}\right]+\kappa_{d}\widetilde{\mathcal{D}}[\hat{D}]\widetilde{\rho}+\sum_{i=1}^{2}\gamma_{i}\widetilde{\mathcal{D}}[\hat{\sigma}_{i}^{-}]\widetilde{\rho}+\sum_{i=1}^{2}\gamma_{i,\phi}\widetilde{\mathcal{D}}[\frac{\hat{\sigma}_{i,z}}{\sqrt{2}}]\widetilde{\rho},\tag{3.55}$$

we can numerically calculate the state evolution with noises under realistic PSD. The result is plotted in Fig. 3.9, which clearly manifests the suppression of the 1/f dephasing noise in the communication process, which can be understood as a spin-echo effect discussed in section 2.4.2. It needs to be pointed out that this approach is generally not equivalent to setting a weaker dephasing rate (one that corresponds to T_{ϕ} found from echo experiments) in the bare master equation, as the

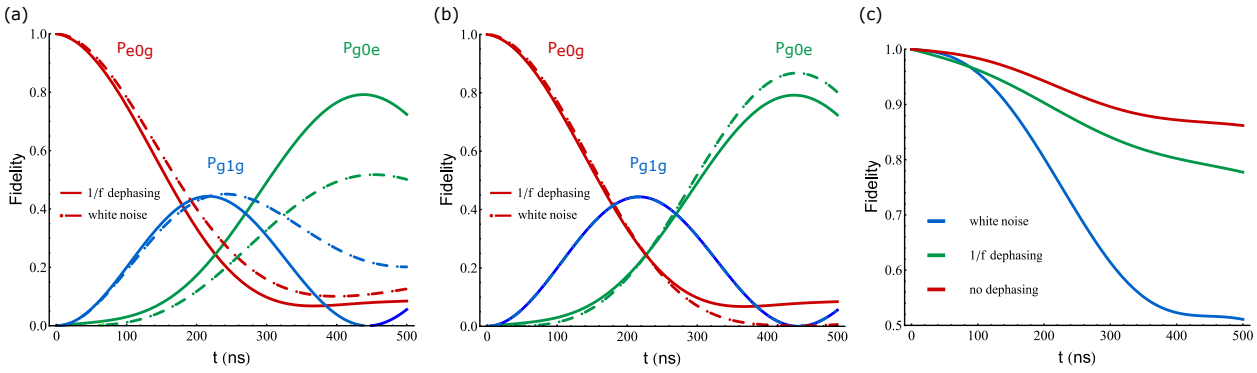

Figure 3.9: Calculation of the state evolution in the communication experiment with 1/f dephasing noise. In the simulation we set the parameters as follow: $\gamma_{1,2} = 0.1\,\text{MHz}$, $\gamma_{1,\phi} = 2\,\text{MHz}$, $\gamma_{2,\phi} = 5\,\text{MHz}$, $\kappa_d = 1\,\text{MHz}$, $\Omega = 5\,\text{MHz}$. (a) Comparison between white dephasing noise and 1/f dephasing noise. The swapping operation is dynamically decoupling the system from 1/f dephasing noise, leading to a much higher fidelity than the white noise model. (b) Comparison between 1/f dephasing noise and zero dephasing noise. This indicates that while some components of the 1/f noise term in the dressed basis is heavily suppressed, there remains other terms that are not completely cancelled out and will contribute to the transfer infidelity. (c) Simulation of the state fidelity for 1/f noise, white noise and no dephasing noise, showing again the suppression of the 1/f noise and intrinsic distinction between filtered 1/f noise and weaker white dephasing noise in the bare basis.

later fails to fully capture the time correlation between the noise terms: for example, in the dressed basis, the dephasing noise is transformed to a combination of dephasing noise as well as decay and excitation noise. As they are from the same noise source, these noise terms are correlated and strictly speaking should not be treated as separate Lindblad operators except for the strong coupling regime where their correlation gets integrated out.

3.4.5 "Dark" mode: is it really dark?

Simultaneous square sideband pulses are adopted in both the photon transfer and Bell state creation experiment to achieve the shortest pulse time possible. However, there is a possibility that better fidelities could be acquired through further minimizing the photon loss in the communication mode, by making use of adiabatic protocols in a manner akin to the stimulated Raman adiabatic passage (STIRAP) [165]. A typical STIRAP protocol has a pulse sequence shown in Fig. 3.11a, where after the excitation of the sender qubit, the receiving pulse turns on first, and slowly ramps down

together with the ramping up of the sending pulse. This creates instantaneous eigenstates of

$$|\mathcal{D}(t)\rangle = \cos\theta(t)\,|e0g\rangle - \sin\theta(t)\,|g0e\rangle\,, \tag{3.56}$$

$$|\mathcal{B}(t)\rangle^{+} = \frac{1}{\sqrt{2}}\left(\sin\theta(t)\,|e0g\rangle + |g1g\rangle + \cos\theta(t)\,|g0e\rangle\right), \tag{3.57}$$

$$|\mathcal{B}(t)\rangle^{-} = \frac{1}{\sqrt{2}}\left(\sin\theta(t)\,|e0g\rangle - |g1g\rangle + \cos\theta(t)\,|g0e\rangle\right), \tag{3.58}$$

where the mixing angle is determined by the ratio between the two drive strengths,

$$\theta(t) = \arctan\frac{\Omega_1(t)}{\Omega_2(t)}, \quad \theta(0) = 0, \quad \theta\left(t_f\right) = \frac{\pi}{2}. \tag{3.59}$$

This reduces back to the simultaneous square pulse scheme when $\Omega_1(t) = \Omega_2(t) = \Omega$, where the instantaneous eigenstates become the dark and the bright states in Eq. 3.34. When the ramping of the pulses is done adiabatically with respect to the gap between the dark and bright modes, the population is coherently trapped in $|\mathcal{D}(t)\rangle$ without exciting the communication mode, so that the transfer is immune to the photon loss of the communication mode.

Let us stop here for a moment and examine a paradox emerging from having a perfect dark mode as the communication mode, where the photon loss rate is only dependent on the decay rates of the communication cavities, $\kappa_{1,2}$, as we anticipated for the idea case in subsection 3.4.1. This is saying that the dark mode should be able to mediate the perfect sending of photons as long as the neighboring bright modes are not excited, regardless of how lossy the cable is. On the other hand, it is an obvious fact that any photon passing through a cable must be subject to the cable loss for at least a single-passage time T_s. This paradox can be resolved by understanding that the dark mode is actually not completely dark. Illustrated in Fig. 3.10, the communication cavities are in fact coupled to an infinite number of cable modes with strength g_c and free spectral range Δ. The relative phases between their couplings having alternating signs, as the result of the wave functions

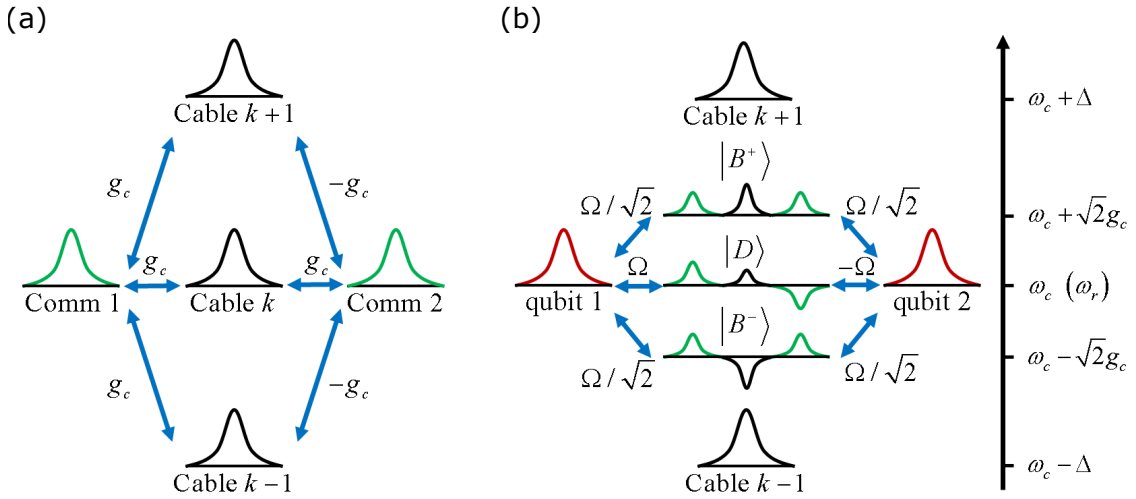

Figure 3.10: The communication mode is not completely dark to the cable loss even when the communication cavities are perfectly resonant to the cable mode. (a) The communication cavities are coupled to all the cable modes. Because the standing waves of different harmonics have alternating phases at the boundary, the couplings between one of the communication cavities and cable modes have alternating signs. (b) The hybridization of the communication cavities and the cable modes gives rise to the dark and bright modes, with the dark mode wavefunction acquiring a small component of the cable mode. The transferring of a single photon will be simultaneously susceptible to photon losses in both the dark mode and bright modes, with the minimum possible loss set by the single-passage loss of the cable.

of cable modes having alternating phases at the end of the cable,

$$\hat{\mathcal{H}}/\hbar = \sum_{k=1}^{2} \omega_r \hat{b}_k^\dagger \hat{b}_k + \sum_{n=1}^{\infty} n\Delta \hat{b}_{c,n}^\dagger \hat{b}_{c,n} + g_c \sum_{n=1}^{\infty} \left(\hat{b}_1^\dagger \hat{b}_{c,n} + (-1)^n \hat{b}_2^\dagger \hat{b}_{c,n} + h.c. \right). \tag{3.60}$$

This gives rise to a finite cable mode participation in the dark mode wavefunction, making it no longer immune to the photon loss of the cable. The total decay rate of the communication mode is calculated to be

$$\kappa_{\text{tot}} = \frac{\Delta^2}{\pi^2 g_c^2 + 2\Delta^2} (\kappa_1 + \kappa_2) + \frac{\pi^2 g_c^2}{\pi^2 g_c^2 + 2\Delta^2} \kappa_c. \tag{3.61}$$

The cable loss term diminishes when $\Delta \to \infty$, which represents a short cable with no physical length. To better demonstrate how the single-pass loss is fundamentally limiting the transfer fidelity, we consider the STIRAP session described in Eq. 3.56 to 3.59. Considering the cable loss

only, the Purcell loss to the bright states due to non-adiabaticity is

$$\epsilon_1 \approx \left(\frac{\dot{\theta}\left(t\right)}{\Omega}\right)^2 \kappa_d t_f \approx \frac{\pi^2 g_c^2 \kappa_c}{\left(\pi^2 g_c^2 + 2\Delta^2\right)\Omega^2 t_f} \approx \frac{\pi^2 g_c^2 \kappa_c}{2\Delta^2 \Omega^2 t_f}, \tag{3.62}$$

while the Purcell loss to the bright modes is

$$\epsilon_2 \approx \left(\frac{\frac{1}{\sqrt{2}}\Omega}{\sqrt{2}g_c}\right)^2 \kappa_b t_f \approx \frac{1}{8}\left(\frac{\Omega}{g_c}\right)^2 \kappa_c t_f. \tag{3.63}$$

In above we have assumed $\dot{\theta}\left(t\right) \ll \kappa_d \ll \Omega \ll \kappa_b \approx \frac{\kappa_c}{2} \ll g_c$. Minimizing over $\epsilon_1 + \epsilon_2$, we find the optimal value for the transfer time and the total loss to be

$$t_f = \frac{2\pi g_c^2}{\Delta \Omega^2}, \quad \epsilon_{\text{tot}} \approx \frac{\kappa_c}{2\Delta} = \kappa_c T_s, \tag{3.64}$$

which is indeed the single-pass loss. This also leads to an interesting proposition that the complete swapping of a single photon between the remote qubits can never be achieved in a shorter time than the single-passage time, however fast we try to operate, which agrees well with the theory of special relativity.

In reality, the finite coherence time of the transmons poses another important constraint to the transfer fidelity. While the STIRAP protocol significantly suppresses the cable loss, it comes at the cost of much longer transfer time, making qubit decoherence the dominant source of error. For simplicity, we model the sender and receiver pulses as two Gaussian pulses with the same maximum amplitude as the square pulse scheme used in our experiment. In the time domain, the two pulses are set to be

$$f_s(t) = \begin{cases} Ae^{-\frac{(t-t_0)^2}{2\sigma^2}}, & |t-t_0| \leqslant 5\sigma \\ 0, & |t-t_0| > 5\sigma \end{cases}, \quad f_r(t) = \begin{cases} Ae^{-\frac{(t-t_0-\Delta t)^2}{2\sigma^2}}, & |t-t_0-\Delta t| \leqslant 5\sigma \\ 0, & |t-t_0-\Delta t| > 5\sigma \end{cases}. \tag{3.65}$$

The fidelity yielded by this protocol is calculated as a function of both the pulse width σ and

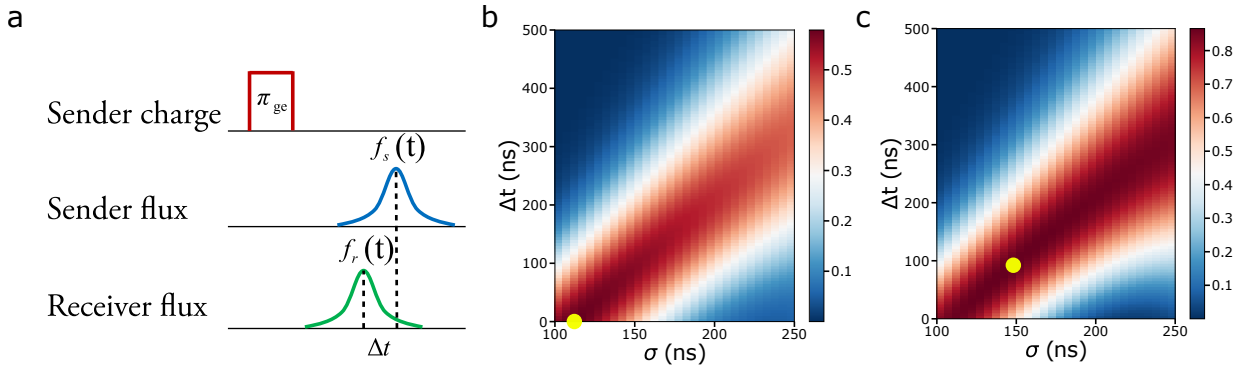

Figure 3.11: STIRAP-like protocol. (a) Pulse sequence of the STIRAP protocol for photon transfer. After initializing of the sender qubit state in the excited state, two Gaussian pulses with same duration and amplitude (set to be the maximum amplitude achievable in the experiment) are applied to the flux channels of the two qubits, with the receiver pulse turned on ahead of the sending pulse by a time of Δt. (b) Calculation of the transfer fidelity as a function of the Gaussian RMS width, σ, as well as the delay time Δt. A maximum fidelity of 56% occurs at $\{\sigma = 120\ ns, \Delta t = 0\ ns\}$ (labeled by the yellow dot), which is worse than the 60% fidelity achieved by the simultaneous square pulse scheme. This indicates that, in our current parameter regime, the fidelity is optimal with simultaneous square pulse scheme which has the shortest pulse length. (c) With better qubit coherence properties of $T1, T2 = 20$ us, the STIRAP protocol promises 85% maximum fidelity at $\{\sigma = 145\ ns, \Delta t = 95\ ns\}$ (labeled by the yellow dot), which is higher than the maximum fidelity of 82% yielded by the simultaneous square pulse scheme under the same parameters.

the delay time Δt, via master equation simulation with real circuit parameters. Fig. 3.11b shows that a maximum fidelity of 56% is achieved when two Gaussian pulses with $\sigma = 120$ ns overlap each other, which indicates that non-adiabatic transfer with the shortest time is favorable in our current parameter regime. This also justifies our choice of the simultaneous square pulse scheme which is the fastest in all non-adiabatic schemes. In contrast, if the coherence of the qubit is improved to $T_1 = 20$ us and $T_2 = 20$ us, the same simulation results in a maximum fidelity of 85% at delay time $\Delta t =$ (Fig. 3.11c) that is higher than the simultaneous square pulse fidelity of 82%, proving the usefulness of the adiabatic protocol for future improvements. Here we have only considered the simple Gaussian pulse scheme as a proof of principle demonstration. There are more sophisticated protocols that can further improve the transfer fidelity [166]. With better qualities of qubits, the fidelity can potentially be improved through protocols with a small detuning between the parametric drive frequency and the frequency difference between the qubit and the

communication mode. This virtual process mitigates the loss in the cables by avoiding excitation in the communication mode.

3.4.6 Purcell effect and the stepped impedance Purcell filter

It is worth emphasizing again the importance of the communication cavities in our experiment. In principle, one can always minimize the cable loss down to the single-pass loss through adiabatic protocols, even by coupling the qubits directly to the cable. However, as the bare cable modes are much more weakly coupled to the qubits due to their lower density of states, the transfer time will have to be substantially longer in order to reach the single-pass limit. As we have argued, this significantly compromises the qubit coherence and causes the overall communication fidelity to drop. Besides, without the protection from the communication cavities as Purcell filters, the lifetime of the idling qubit will be heavily Purcell-limited by the lossy cable modes, which we have illustrated in Fig. 2.11. These nice properties the communication cavities bring about could be further enhanced, by upgrading the communication cavities to more dedicated Purcell filters, such as the stepped impedance Purcell filter (SIPF) [167]. The SIPF is composed of N sections of alternating high and low impedance CPW cavities, which form periodic stop and passbands with broad ranges. The impedance mismatch at the boundaries of the high and low impedance sections causes standing waves to form at the $\left(n+\frac{1}{2}\right)\lambda$ resonances of all the sections, which hybridize into N "normal modes" for each n that constructively interfere with the transmission signal and give rise to the passbands. Outside the passbands the signal is reflected off the boundary, leading to the stopbands with a range set by the high and low impedance ratio $Z_{\text{hi}}/Z_{\text{lo}}$. Obviously, at $Z_{\text{hi}} = Z_{\text{lo}}$, the SIPF reduces to a regular transmission line, where the passband normal modes fall back to the transmission line multimodes.

Like we did in Chapter 2, here we apply the ABCD matrix formalism and the black-box quantization to calculate the Purcell limit of the qubit as well as their couplings to the communication mode. We use the SIPFs in the same way as the communication cavities, where they are capacitively coupled to the transmon as well as to the cable, as opposed to directly connected to the cable

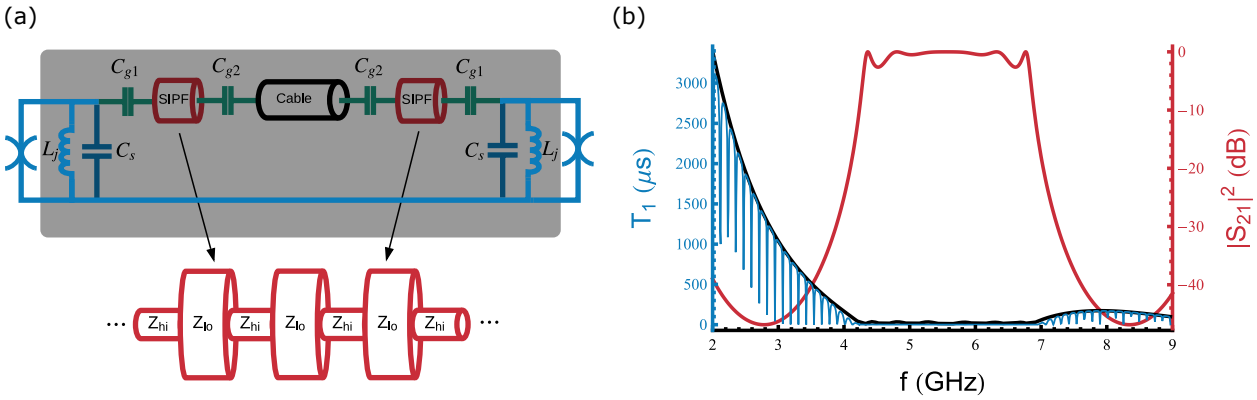

Figure 3.12: Black-box quantization (BBQ) Calculation of the communication network with stepped impedance Purcell filters (SIPFs). (a) The new communication network is composed of two transmons capacitively coupled to communication SIPFs, which are made of alternating sections of high and low impedance lines. The SIPFs are also capacitively coupled to the 1-meter-long cable at their other ends. The black box is the part of the circuit that has been included in the BBQ calculation. (b) BBQ calculation with ABCD matrix showing the Purcell-limited lifetime of the transmon, overlaid on top of the transmission spectrum of the SIPF (red curve). In the calculation, we neglect transmon decay and set the lifetimes of the cable and the SIPF to be 0.5 μs and 6 μs respectively. The SIPF have seven sections of $Z_{hi} = 150\,\Omega$ and $Z_{lo} = 25\,\Omega$, and the coupling capacitors have values of $C_{g1} = 40$ fF and $C_{g2} = 40$ fF. To mimic the frequency sweep of a tunable transmon, we vary Lj with fixed shunting capacitance, $C_s = 100$ fF. The cyan curve represents the circuit where the SIPF is directly connected to the cable. In this situation, the transmon mode, while being protected by the stopband of the SIPF, is still affected by the lossy cable modes which manifest themselves as the periodic dips on the T1 curve. In comparison, the black line corresponds to the capacitive coupling scheme in (a) and does not have these sudden jumps in the transmon lifetime. The T1 limit in this case is due to the finite lifetime of the SIPF in the simulation.

(see Fig. 3.12). In the stopband, this capacitive coupling scheme further reduces the Purcell loss when the qubit mode hits one of the cable modes. In the passband, parametric modulation brings both qubits into resonance with the same SIPF normal mode(s) with strong coupling strengths, allowing the communication tasks to be accomplished in a similar manner to the previous experiment. Using the numerical method outlined in section 2.4.1 we may also calculate the coupling strength between the transmon and the SIPF normal modes. Under realistic circuit parameters where the asymmetry of the SIPFs due to fabrication imperfections are taken into account, we find a coupling strength of ~ 70 MHz well achievable between the transmons and the SIPF normal mode, while this number drops to ~ 20 MHz when the capacitor between the SIPF and the cable

is removed.

Incorporating the SIPF into the remote modular architecture to a large extent lifts the Purcell limit of the cable loss and allows the accommodation of larger couplings between the qubit and the communication mode. This promises the strong coupling regime, where the coupling strength becomes comparable to the free spectral range of the cable. This regime is also reached for much longer cables, although it is unclear what the benefits would be for long-distance communications with microwave photons whose energies are well below the room temperature thermal noise. In this regime, the photon no longer interacts with one or several cable modes only, but an ensemble of modes altogether. In section 2.4.3, we have showcased how the quantum input-output theory can be used for the calculation of the transfer fidelity in the strong coupling regime. This approach can be easily integrated with the BBQ simulation, where the SIPF could be modeled as a collection of N normal modes capacitively coupled to the qubit in the passband, with the evolution of the n-th normal mode operator coupled to the m-th transmon governed by quantum Langevin equations,

$$\dot{\hat{a}}_{mn}(t) = -\frac{\kappa^c_{mn} + \kappa^i_{mn}}{2}\hat{a}_{mn}(t) - ig_{mn}(t)\,\hat{\sigma}^-_m(t) + \sqrt{\kappa^c_{mn}}\hat{b}_{\text{in},mn}(t)\,, \tag{3.66}$$

$$\dot{\hat{\sigma}}^-_m(t) = -\frac{\gamma_m}{2}\hat{\sigma}^-_m(t) - i\sum_n^N g_{mn}(t)\,\hat{a}_{mn}(t)\,, \tag{3.67}$$

$$\hat{b}_{\text{in},\bar{m}n}(t) = e^{-\kappa_0 T_s}\left[\sqrt{\kappa^c_{mn}}\hat{a}_{mn}(t - T_s) - \hat{b}_{\text{in},mn}(t - T_s)\right], \tag{3.68}$$

where T_s is the single-passage time and κ_0 is the damping rate of the photon amplitude.

The concern about minimizing the Purcell effect while remaining fully operational can also be resolved if we can implement a controllable coupling strength between the qubit and the cable, which can be turned on to perform communication tasks, and turned off to protect the qubit coherence. This brings up the next topic of this thesis, about tunable coupling circuits and the parametric control of the coupling strength.

CHAPTER 4

PARAMETRIC MODULATION OF COUPLING STRENGTH

As we mentioned earlier, one of the most distinctive advantages of circuit QED is that stronger couplings can be very easily attained. However, this sometimes comes at the cost of stronger undesired couplings as well, which can lead to reduced qubit lifetime or gate errors. The previous frequency modulation scheme allows for the generation of sideband interaction strength with tunable strength, at the cost of an increased sensitivity of the qubit to flux noise, compromising the qubit coherence time. To address these issues, we invent a flux tunable coupler with controllable coupling strength that can be switched on and off on demand. Tunable coupling elements are not new to circuit QED: they have been used for frequency conversion [67, 70], quantum logic gates [68, 71, 168], and a variety of other tasks in quantum information processing and quantum simulation. While sharing various compatibilities with these previous works, our tunable coupling circuit has a particularly simple circuit architecture with high scalability, strong tunable coupling strength and decent coherence properties. Moreover, it allows the parametric control of the coupling strength to be harnessed for exploring interesting physics or as a useful resource for practical applications.

In this chapter, we will first demonstrate how the coupling modulation is achieved with the tunable coupling design, in which the qubit and the resonator are connected in parallel to a superconducting quantum interference device, allowing for the quasi-static flux tuning of the qubit-cavity coupling strength from 12 MHz to more than 300 MHz. Qubit coherence times exceeding 20 μs are maintained over the majority of the range of tuning, limited primarily by the Purcell effect. By parametric modulation of the coupling, we realize both photon conserving red-sideband interactions to transfer single photons [132, 133, 168], as well as photon non-conserving blue-sideband interactions [168, 169, 170, 171] necessary for qubit bath engineering and qubit state stabilization. Finally We present the experimental protocol to parametrically stabilize arbitrary single-qubit states by using the blue-sideband interaction in conjunction with a regular qubit Rabi drive, which is an important step towards autonomous quantum error correction.

4.1 Tunable Coupling Circuit

The tunable coupling circuit, shown in Fig. 4.1, consists of a transmon qubit and a lumped-element resonator, both grounded at the same node through a dc-SQuID. The dc-SQuID acts as a tunable inductor shared between the qubit and the resonator, creating a coupling strength between the two systems proportional to its inductance $L_g = L_{g0}/\left|\cos(\pi\Phi_{\text{ext}}/\Phi_0)\right|$, which is controlled by the external flux Φ_{ext} threading the loop. Previous tunable coupler designs [68, 71] utilized series coupling schemes which are convenient for chains and lattices of qubits or resonators. By contrast, the topology of our circuit enables many resonators or qubits to share the same coupler, rendering it highly scalable as a superconducting circuit device.

To obtain the circuit Hamiltonian, we perform circuit quantization introduced in section 2.1. We begin our analysis by linearizing the circuit, where the non-linear inductive components including the transmon qubit junction and the SQuID, are simplified as linear inductors L_q and L_g. We denote the node flux variables Φ_1, Φ_2 and Φ_3, and the circuit Lagrangian is given by

$$\mathcal{L} = -\frac{(\Phi_1-\Phi_3)^2}{2L_q} - \frac{(\Phi_2-\Phi_3)^2}{2L_r} - \frac{\Phi_3^2}{2L_g} + \frac{C_q\dot{\Phi}_1^2}{2} + \frac{C_r\dot{\Phi}_2^2}{2} + \frac{C_g\left(\dot{\Phi}_1-\dot{\Phi}_2\right)^2}{2}. \tag{4.1}$$

Charge variables conjugate to the flux can be found from a Legendre transformation

$$Q_i = \frac{\partial\mathcal{L}}{\partial\dot{\Phi}_i}, \tag{4.2}$$

and the circuit Hamiltonian can be obtained via

$$\mathcal{H} = \dot{\Phi}_i Q_i - \mathcal{L} \tag{4.3}$$

$$= \frac{(\Phi_1-\Phi_3)^2}{2L_q} + \frac{(\Phi_2-\Phi_3)^2}{2L_r} + \frac{\Phi_3^2}{2L_g} + \frac{1}{2C_*^2}\left[\left(C_r+C_g\right)Q_1^2 + \left(C_q+C_g\right)Q_2^2 + 2C_gQ_1Q_2\right], \tag{4.4}$$

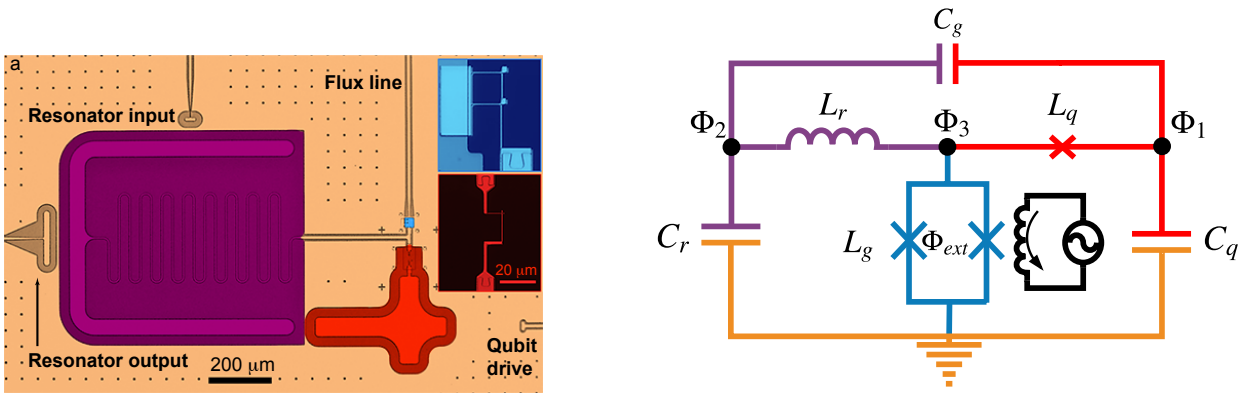

Figure 4.1: (a) Optical image and (b) circuit diagram of our device. The lumped-element resonator is formed by a "C" shaped capacitor pad and an isolated meander line inductor. The inductor line protrudes to the common node where both the qubit Josephson junction and the coupler SQuID loop are connected. Two voltage ports are placed at the two sides of the resonator's capacitor pad enabling transmission measurements. The qubit-cavity coupling strength is tuned with the SQuID-loop flux by modulating the current that flows through the flux line. The qubit can be probed via a separate qubit driveline that is weakly coupled to the qubit's shunting capacitor. Insets show the details of the qubit Josephson junction and the dc-SQuID loop.

where

$$C_*^2 = C_r C_q + C_r C_g + C_q C_g. \tag{4.5}$$

Φ_3 is a non-dynamical degree of freedom that can be eliminated from minimizing the Hamiltonian,

$$\frac{\partial \mathcal{H}}{\partial \Phi_3} = 0, \tag{4.6}$$

which gives

$$\Phi_3 = \frac{L_g}{L_*^2}\left(L_r \Phi_1 + L_q \Phi_2\right), \tag{4.7}$$

where

$$L_*^2 = L_r L_q + L_r L_g + L_q L_g. \tag{4.8}$$

We note that the elimination of the coupler mode can also be understood from the constraint of current conservation at node 3, which is equivalent to Eq. 4.7 and 4.8. This circuit is then described

by the following two-body Hamiltonian that has both capacitive and inductive coupling terms,

$$\begin{aligned}\mathcal{H} &= \frac{1}{2L_*^2}\left[\left(L_r+L_g\right)\Phi_1^2+\left(L_q+L_g\right)\Phi_2^2-2L_g\Phi_1\Phi_2\right] \\ &+ \frac{1}{2C_*^2}\left[\left(C_r+C_g\right)Q_1^2+\left(C_q+C_g\right)Q_2^2+2C_gQ_1Q_2\right]. \end{aligned} \tag{4.9}$$

With the flux and charge operators expressed in terms of creation and annihilation operators

$$\Phi_i = \sqrt{\frac{\hbar Z_i}{2}}\left(\hat{a}_i^\dagger+\hat{a}_i\right), \tag{4.10}$$

$$Q_i = i\sqrt{\frac{\hbar}{2Z_i}}\left(\hat{a}_i^\dagger-\hat{a}_i\right) \tag{4.11}$$

where

$$Z_1 = \frac{L_*}{C_*}\sqrt{\frac{C_r+C_g}{L_r+L_g}}, \tag{4.12}$$

$$Z_2 = \frac{L_*}{C_*}\sqrt{\frac{C_q+C_g}{L_q+L_g}}, \tag{4.13}$$

the Hamiltonian is rewritten as

$$\hat{\mathcal{H}}/\hbar = \omega_q\hat{a}_1^\dagger\hat{a}_1+\omega_r\hat{a}_2^\dagger\hat{a}_2+g_L\left(\hat{a}_1^\dagger+\hat{a}_1\right)\left(\hat{a}_2^\dagger+\hat{a}_2\right)+g_C\left(\hat{a}_1^\dagger-\hat{a}_1\right)\left(\hat{a}_2^\dagger-\hat{a}_2\right), \tag{4.14}$$

where

$$\omega_q = \frac{\sqrt{\left(L_r+L_g\right)\left(C_r+C_g\right)}}{L_*C_*}, \tag{4.15}$$

$$\omega_r = \frac{\sqrt{\left(L_q+L_g\right)\left(C_q+C_g\right)}}{L_*C_*}, \tag{4.16}$$

$$g_L = -\frac{\hbar L_g}{2L_*^2}\sqrt{Z_1Z_2}, \tag{4.17}$$

$$g_C = -\frac{\hbar C_g}{2C_*^2}\sqrt{\frac{1}{Z_1Z_2}}. \tag{4.18}$$

Strictly speaking, the finite capacitance of the dc-SQuID leads to a high-frequency nonlinear

mode that is strongly coupled to both the transmon and the cavity. The strong couplings arise from the fact that the shunting capacitors of the transmon and the cavity are also playing the role of coupling capacitors as well, which corresponds to a unit voltage division $\beta = 1$ that maximizes the coupling strength. The size of the coupler junctions is designed to be 100 times larger than the qubit junction, which guarantees that $L_{g0} \ll L_{r,} L_q$ and allows the adiabatic elimination of the coupler mode in the same way as in subsection 2.3.2, resulting in an effective qubit-cavity coupling similar to the one in Eq. 2.70. We make sure the SQuID loop size is small enough so that the geometric inductance of the loop itself does not become comparable to the Josephson inductance of the SQuID junctions, in order to avoid undesired hysteresis [172]. In the high frequency limit, this coupling is well approximated by Eq. 4.17.

Within the two-level approximation of the transmon, the circuit is described by the effective Hamiltonian,

$$\hat{\mathcal{H}}/\hbar = \omega_r \hat{a}^\dagger \hat{a} + \frac{\omega_q}{2}\hat{\sigma}_z - g_R(\hat{a}^\dagger \hat{\sigma}^- + \hat{a}\hat{\sigma}^+) - g_B(\hat{a}^\dagger \hat{\sigma}^+ + \hat{a}\hat{\sigma}^-),$$

where

$$g_{R,B} = \frac{L_{g0}}{2\left|\cos(\pi\Phi_{\text{ext}}/\Phi_0)\right|}\sqrt{\frac{\omega_r\omega_q}{L_r L_q}} \mp \frac{C_g}{2}\sqrt{\frac{\omega_r\omega_q}{C_r C_q}} \tag{4.19}$$

are the coupling strengths associated with the red and blue-sidebands [169]. When the coupler is not being driven, the counter-rotating g_B term can usually be dropped from Eq. 4.19, but by dynamically modulating the inductance via the external flux Φ_{ext}, both red- and blue-sideband interactions can be utilized. Additionally, by balancing the inductive and capacitive terms in Eq. (4.19), one can achieve a higher on to off ratio[1].

We perform flux spectroscopy of the qubit (Fig. 4.2a) to determine the static coupling strength $g_R(\Phi_{\text{ext}})$, finding it to range from 12 MHz to 300 MHz. To calibrate the static coupling strength of g_R as a function of the flux, two methods have been employed in the experiment. The first one is to make use of the photon number splitting of the qubit peak that can be observed from the two-tone

1. Here we naively ignore their nonlinear interactions inherited from the coupler mode.

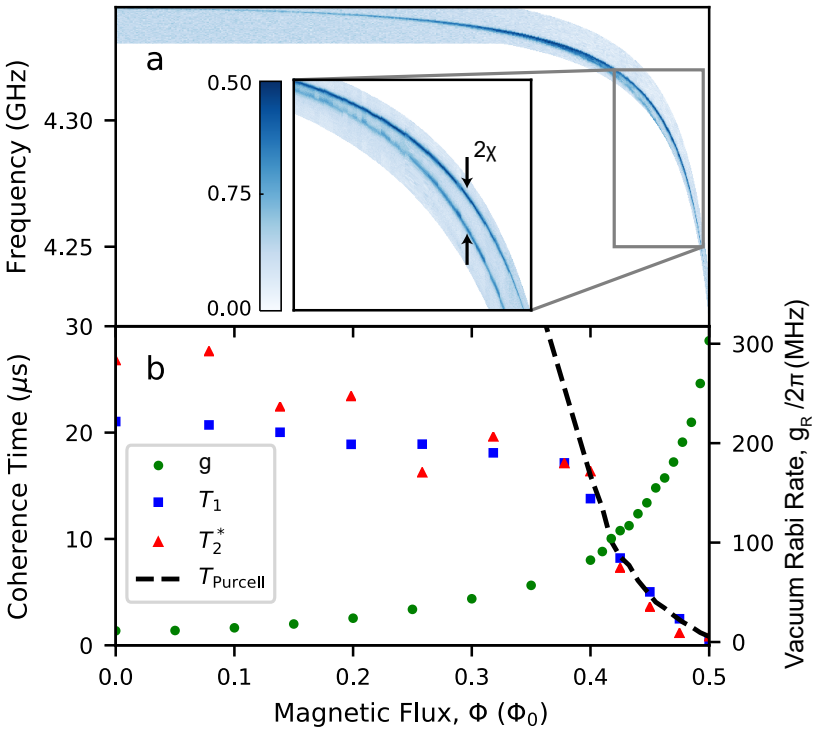

Figure 4.2: (a) Spectroscopy showing the qubit excited state population as a function of flux through the coupler. The qubit frequency is insensitive over nearly the entire flux range. (Inset) Number splitting of the qubit peak due to photons in the resonator, used to calibrate the static coupling between the qubit and the resonator. (b) Qubit coherence and qubit-cavity coupling strength as a function of the flux through the coupler. The dephasing time (T_2^*) is comparable to the energy relaxation time (T_1) over the entire tuning range. The coherence times drop near $\Phi = 0.5\Phi_0$ as a result of the Purcell effect due to the strong coupling to the readout resonator, as indicated by the black dashed line.

measurement of the qubit spectrum, shown in Fig. 4.2. g_R can thus be directly calculated using the formula [173]

$$|g_R| = \sqrt{\frac{2\chi\Delta(\Delta+\alpha)}{\alpha}}, \tag{4.20}$$

where both the anharmonicity α and the qubit-cavity detuning Δ are easily obtained from spectroscopy measurements.

At flux values where the coupling strength is not strong enough to resolve the number splitting, we take a different approach by applying a voltage drive with strength ϵ_d on the cavity at the qubit

frequency, and measuring the Rabi rate of the qubit,

$$\Omega_R = 2\epsilon_d \left|\frac{g_R}{\Delta}\right| + \Omega_0, \tag{4.21}$$

where the first term represents the perturbative strength of the cavity drive on the qubit, and the second term, which is a constant rate, is due to the spurious coupling between the cavity driveline to the qubit capacitor pad. ϵ_d and Ω_0 can be calibrated by fitting Eq. (4.21) with g_R/Δ and Ω_R measurement values (taken in the same flux range where the number-splitting is still well resolved). With calibrated ϵ_d and Ω_0, Eq. (4.21) is capable of providing g_R across the entire flux range.

As the qubit itself does not have a SQuID loop, its frequency is only indirectly affected by the modulation of the coupler. $L_{g0} \ll L_{r,}\, L_q$ also ensures that the tuning of the qubit and resonator frequencies from the change in the coupler inductance is small. As seen in Fig. 4.2, the qubit frequency varies by less than 15 MHz over 80% of the tuning range, making the qubit nearly immune to flux noise. Both the energy relaxation time T_1 and the dephasing time T_2^* remain above 20 μs over most of the flux period ($|\Phi_{\text{ext}}| < 0.4\Phi_0$). Only when the flux approaches half a flux quantum do coherence times start to drop significantly. There the Purcell effect from coupling to the readout resonator, as well as an increased frequency-flux sensitivity, limit the coherence.

4.2 Red- and Blue-Sideband Interactions

The usefulness of parametric coupling becomes most evident when the qubit-cavity coupling strength is modulated at the qubit-cavity difference or sum frequency. Modulation of Φ_{ext} in Eq. (4.19) at frequency ω_d turns $g_{R,B}$ into $g_{R,B}(t) = \sum_n g_{R,B}^{(n)} \cos \omega_d^{(n)} t$, where $\omega_d^{(n)} = n\omega_d$ is the effective modulation frequency of the n-th harmonic with Fourier coefficient $g_{R,B}^{(n)}$. Substituting this into Eq. 4.19, we obtain the red- and blue-sideband Hamiltonians in rotating frames as

$$\hat{H}_{rot}^{R,B} = (\omega_r' \mp \omega_q' - \chi'\hat{\sigma}_z)\hat{a}^\dagger\hat{a} \pm \frac{\omega_d}{2}\hat{\sigma}_z - g_{R,B}'(\hat{a}^\dagger\hat{\sigma}^\mp + \hat{a}\hat{\sigma}^\pm), \tag{4.22}$$

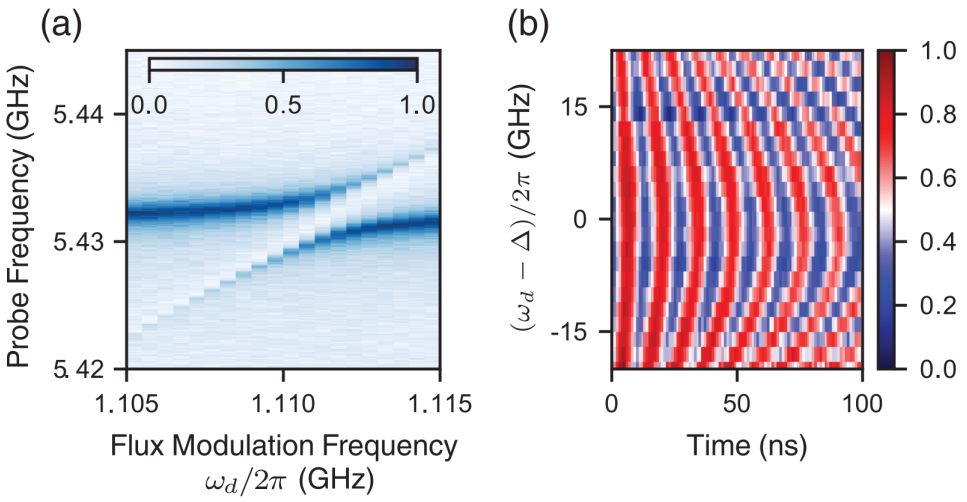

Figure 4.3: Red-sideband interactions probed by applying an rf flux tone to the tunable coupler to generate sidebands. (a) Spectroscopy of the (normalized) resonator transmission as a function of sideband and resonator probe frequency, showing the stimulated vacuum Rabi spitting. (b) Stimulated vacuum Rabi oscillations between the qubit and resonator, measured as an oscillation of the qubit excited state population. A single photon is loaded into the qubit before the flux pulse.

valid for effective modulation frequencies, $\omega_d^{(n)} \approx \omega_r' \pm (\omega_q' + \chi')$, respectively, with fast-oscillating terms abandoned. Here, the primes stand for the dressed basis after diagonalizing the static component of the driven Hamiltonian. At $\omega_d^{(n)} = \omega_r' - \omega_q' + \chi'$, energy pumped into the circuit through the parametric flux drive bridges the gap between the first excited state of the qubit $|e0\rangle$ and the single-photon Fock state of the cavity $|g1\rangle$, causing a splitting of $2g_R'$ due to the red-sideband coupling between the two levels. This is seen as an avoided crossing in the cavity transmission spectrum when the modulation frequency matches the detuning (Fig. 4.3a). In the time domain, the red-sideband coupling mediates stimulated vacuum Rabi oscillations which coherently swap a single photon between qubit and resonator. The oscillation rate, $2g_R'/2\pi \approx 80\,\text{MHz}$, can be directly seen from Fig. 4.3b and determines how fast qubit-photon gates can be performed.

While the red-sideband coupling enables photon-conserving processes, the blue-sideband coupling, which takes place at $\omega_d^{(n)} = \omega_r' + \omega_q' - \chi'$, generates two-photon oscillations between states $|g0\rangle$ and $|e1\rangle$. This interaction, created in our experiment through the second harmonic term by flux modulating at $\omega_d = (\omega_r' + \omega_q' - \chi')/2$, produces a much richer resonance structure in transmis-

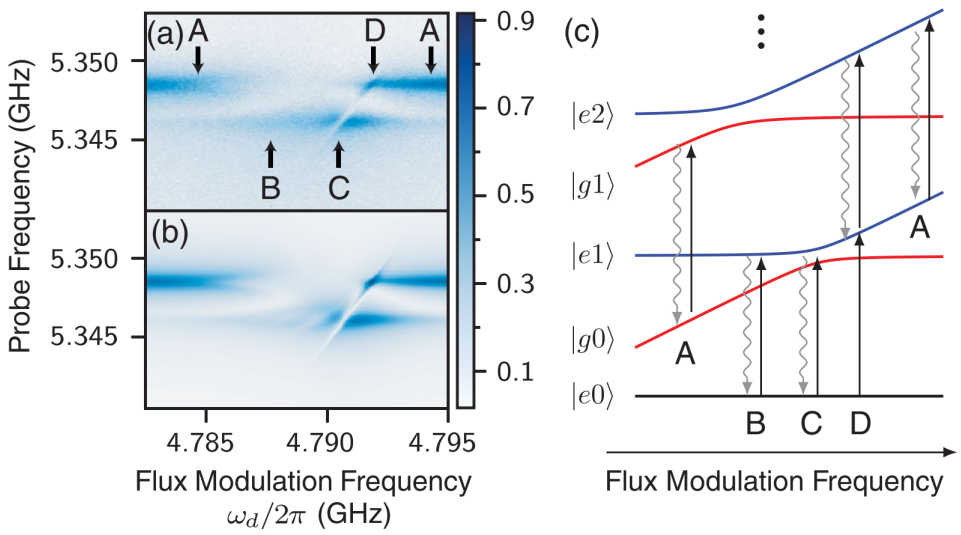

Figure 4.4: Resonator spectroscopy showing (normalized) transmission near the blue-sideband resonance condition. Experimental data (a) and master equation simulations (b) show excellent agreement. (c) Energy level diagram corresponding to Eq. (4.22) provides a map to the spectroscopic features A, B, C and D at different modulation frequencies, indicated by arrows in (a). A: When the modulation frequency is far-detuned from the blue-sideband resonance, the qubit stays in its ground state. B: The excited state of the qubit is stabilized, causing the cavity to be shifted down by 2χ. C: The crossing of $|e1\rangle$ and $|g0\rangle$, manifest as an avoided crossing. The qubit excited state is also maximally stabilized at this frequency due to the resonance of $|e1\rangle$ and $|g0\rangle$. D: Enhanced cavity transmission appears when $|e0\rangle \rightarrow |g0\rangle$ and $|g0\rangle \rightarrow |g1\rangle$ transition energies are equal. The asymmetry of the unshifted cavity peak line centered at the blue-sideband resonance is likely due to interactions between higher levels $|g, n\rangle \rightarrow |e, n+1\rangle$.

sion (Fig. 4.4a), which can be accurately reproduced numerically (Fig. 4.4b) with master equation simulation. The observed features can be understood conceptually by considering the Floquet quasienergy levels within the first Brillouin zone (Fig. 4.4c). The blue-sideband interaction acts as a coherent two-photon pump that drives the circuit to $|e1\rangle$, causing an avoided crossing between $|g0\rangle$ and $|e1\rangle$ in the level diagram. As the cavity photon loss rate is faster than the qubit decay rate by two orders of magnitude in the experiment ($1/\kappa \approx 100\,\text{ns}$ and $T_1 > 20\,\mu\text{s}$), $|e1\rangle \rightarrow |e0\rangle$ is the dominant decay process and traps most of the population in the single-photon subspace in state $|e0\rangle$. When both photons are eventually lost from the circuit, the state immediately transitions to $|e1\rangle$, beginning the cycle again. In this sense, the blue-sideband flux drive stabilizes the qubit in the excited state. This, in turn, shifts the cavity frequency down by $2\chi'$ (B in Fig. 4.4a).

Furthermore, as the blue-sideband interaction splits the degenerate levels of $|e1\rangle$ and $|g0\rangle$ in the rotating frame, the cavity transmission measurement actually probes the transitions between $|e0\rangle$ and $(|e1\rangle \pm |g0\rangle)/\sqrt{2}$ so that the avoided crossing is visible within the shifted cavity peak (C in Fig. 4.4a). Enhanced cavity transmission is observed at the crossing between the unshifted cavity peak and the avoided crossing (D in Fig. 4.4a). Here the transition energy between $|e0\rangle$ and $|g0\rangle$ in the rotating frame coincides with the energy between $|g0\rangle$ and $|g1\rangle$, resulting in an enhanced transmission due to the $|g0\rangle$ population being weakly replenished by the cavity probe.

4.2.1 Tunable coupling circuit as a non-reciprocal device

The sideband interactions the tunable coupling circuit generates also allow it to be manipulated as various non-reciprocal elements [174]. For example, the blue-sideband interaction under parametric modulation at the sum frequency is shown to be the key component of the non-degenerate parametric amplifier in subsection 2.4.3. While in our experiment we did not intend to exploit this feature of the tunable coupling circuit, we were able to witness its paramp nature by observing an amplified transmission peak at the cavity frequency, when performing cavity spectroscopy under a strong blue-sideband tone. This was also seen on a vector network analyzer with a connected output port and a disconnected input port, where a sharp peaks appears at the cavity frequency, which can be understood as the amplification of the vacuum as the idler (transmon) input field.

In addition, the red-sideband interaction also allows the tunable coupling circuit to be operated as a frequency converter as well as a circulator. The basic idea is to connect the transmon, the cavity and the coupler mode into a closed loop through sideband interactions with different phases. As a result of the path interference, the field propagation becomes directional akin to the chiral ground state of a synthetic magnetic field [175]. Similarly, directional amplification can also be achieved through a combination of the red- and blue-sideband interactions with different phases.

4.3 Universal Stabilization of Single Qubit State

Previously, we have seen that the blue-sideband resonance features can be largely attributed to the stabilization of the qubit excited state. Coming back to look at the red-sideband interaction from a similar prospective, we find that it also creates a stabilization process, but with the qubit ground state being stabilized instead. This is known as the sideband cooling [176, 177, 178, 179], useful for quickly resetting the qubit to a lower effective temperature. The natural next step to make would be to stabilize arbitrary qubit states on demand, which constitutes important building blocks for future error-tolerant circuit QED networks. In the past, several schemes have been explored using active feedback [180, 181] or autonomous stabilization [182, 183, 184, 185, 186, 187, 188]. Here we demonstrate our experimental scheme that employs engineered dissipation processes to stabilize arbitrary single-qubit states, which is an important step towards implementing error-correction code. On the theory side, we further explore the possibilities of achieving the stabilization effect with different combinations of sideband interactions.

4.3.1 The weak and the strong coupling regime

We first present a theoretical proposal for stabilizing arbitrary single-qubit state, through a qubit-cavity Hamiltonian of the form

$$\hat{\mathcal{H}} = \hat{\mathcal{H}}_q + \hat{\mathcal{H}}_{\text{int}} + \hat{\mathcal{H}}_c, \tag{4.23}$$

where the qubit term $\hat{\mathcal{H}}_q/\hbar = \frac{\Omega_R}{2}\vec{r}\cdot\vec{\hat{\sigma}}$ is a spin-$\frac{1}{2}$ Hamiltonian subject to a magnetic field $\vec{B} = \Omega_R\vec{r}$, and $\hat{\mathcal{H}}_c/\hbar = \Omega_c\hat{a}^\dagger\hat{a}$ represents a lossy cavity that is coupled via some interaction H_{int} to the qubit. We assume this is a rotating frame Hamiltonian resulted by some external drives, without worrying for now about its realization.

For simplicity and without loss of generality, we choose $\vec{B}$ to have only $\vec{z}$ and $\vec{x}$ components, which lets us write

$$\hat{\mathcal{H}}_q = \frac{1}{2}(\Omega_x\hat{\sigma}_x + \Omega_z\hat{\sigma}_z) = \frac{\Omega_R}{2}(\hat{\sigma}_x\sin\theta + \hat{\sigma}_z\cos\theta), \tag{4.24}$$

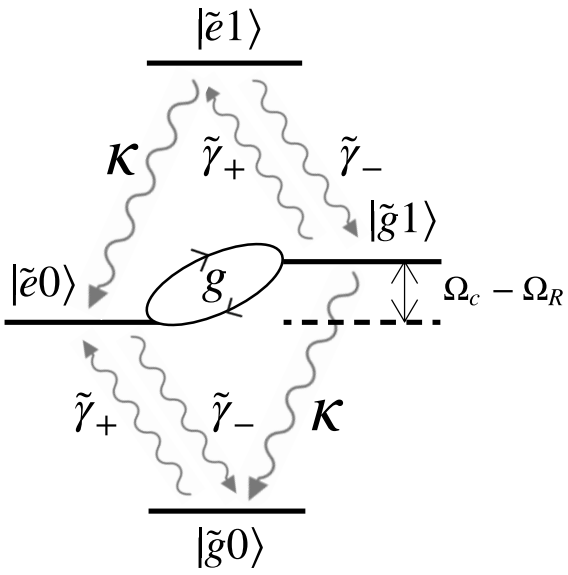

Figure 4.5: The decay diagram consisting the lowest four Floquet levels. The lab frame decay rates translate to these rotating frame decay rates via a unitary transformation acting on the lab frame dissipators. $|\widetilde{e}0\rangle$ and $|\widetilde{g}1\rangle$ coupled with strength g can be brought to resonance by tuning the qubit or cavity frequency, while all other levels are far detuned.

where $\Omega_R = \sqrt{\Omega_x^2 + \Omega_z^2}$ is the qubit's total Rabi frequency, and $\theta = \arccos(\Omega_z/\Omega_R)$. The rotation matrix U

$$U = \begin{pmatrix} \cos\frac{\theta}{2} & \sin\frac{\theta}{2} \\ -\sin\frac{\theta}{2} & \cos\frac{\theta}{2} \end{pmatrix} \tag{4.25}$$

connects the rotating frame eigenstates of the qubit to its lab frame basis,

$$|\widetilde{g}\rangle = U\,|g\rangle = \cos\frac{\theta}{2}\,|g\rangle - \sin\frac{\theta}{2}\,|e\rangle\,, \tag{4.26}$$

$$|\widetilde{e}\rangle = U\,|e\rangle = \sin\frac{\theta}{2}\,|g\rangle + \cos\frac{\theta}{2}\,|e\rangle\,. \tag{4.27}$$

Here and throughout the text, objects with tilde stand for those in the rotating frame. The decay and excitation rate between $|\widetilde{g}\rangle$ and $|\widetilde{e}\rangle$ can be easily calculated by rewriting the lab frame dissipators (at zero temperature) in the new basis,

$$\gamma\mathcal{D}[\hat{\sigma}^-]\rho = \gamma\mathcal{D}[U^\dagger\widetilde{\hat{\sigma}}^- U]\rho = \gamma\mathcal{D}\left[\frac{\widetilde{\hat{\sigma}}_z}{2}\sin\theta - \widetilde{\hat{\sigma}}^+\sin^2\frac{\theta}{2} + \widetilde{\hat{\sigma}}^-\cos^2\frac{\theta}{2}\right]\rho, \tag{4.28}$$

$$\gamma_\phi\mathcal{D}[\hat{\sigma}_z]\rho = \gamma_\phi\mathcal{D}[U^\dagger\widetilde{\hat{\sigma}}_z U]\rho = \gamma_\phi\mathcal{D}\left[\widetilde{\hat{\sigma}}_z\cos\theta - (\widetilde{\hat{\sigma}}^+ + \widetilde{\hat{\sigma}}^-)\sin\theta\right]\rho, \tag{4.29}$$

where γ and γ_ϕ are the decay and dephasing rate of the qubit in the lab frame. Therefore, by regrouping the above dissipators and dropping out the fast oscillating terms (assuming $\Omega_R \gg \gamma, \gamma_\phi$), such as $\widetilde{\hat{\sigma}}^+\rho\widetilde{\hat{\sigma}}^+$ and $\widetilde{\hat{\sigma}}^-\rho\widetilde{\hat{\sigma}}^-$ etc., we obtain the effective decay rate $\widetilde{\gamma}_-$, excitation rate $\widetilde{\gamma}_+$ and dephasing rate $\widetilde{\gamma}_\phi$ in the rotating frame as

$$\widetilde{\gamma}_- = \gamma\cos^4\frac{\theta}{2} + \frac{\gamma_\phi}{2}\sin^2\theta, \tag{4.30}$$

$$\widetilde{\gamma}_+ = \gamma\sin^4\frac{\theta}{2} + \frac{\gamma_\phi}{2}\sin^2\theta, \tag{4.31}$$

$$\widetilde{\gamma}_\phi = \frac{\gamma}{2}\sin^2\theta + \gamma_\phi\cos^2\theta. \tag{4.32}$$

Note that here we have assumed the spectrums of all noises to be white. The more general form of the dressed decay and dephasing rate, with noise PSD incorporated, can be found in Eq. 2.125.

Now we can write down the master equation in the rotating frame basis,

$$\dot{\rho} = -i[\hat{\mathcal{H}}, \rho] + \kappa\mathcal{D}[\hat{a}]\rho + \widetilde{\gamma}_-\mathcal{D}[\widetilde{\hat{\sigma}}_-]\rho + \widetilde{\gamma}_+\mathcal{D}[\widetilde{\hat{\sigma}}_+]\rho + \widetilde{\gamma}_\phi\mathcal{D}[\frac{\widetilde{\hat{\sigma}}_z}{\sqrt{2}}]\rho, \tag{4.33}$$

where κ is the cavity's photon loss rate. Our goal is to stabilize the qubit in its rotating frame ground state $|\widetilde{g}\rangle$. To gain more insight into the stabilization process, we focus on the dynamics of the lowest four energy levels of Eq. (4.23) (which is well justified when the energy scale of the rotating frame Hamiltonian is small compared to the anharmonicity of the qubit), illustrated by Fig. 4.5. Without coupling to the cavity, the ratio of the excitation rate and the decay rate sets the "rotating frame temperature" $\widetilde{T}$ of the qubit

$$\frac{\widetilde{\gamma}_+}{\widetilde{\gamma}_-} = e^{-\frac{\hbar\Omega}{k_B\widetilde{T}}}, \tag{4.34}$$

which further sets the qubit's population distribution. However, when $|\widetilde{e}0\rangle$ and $|\widetilde{g}1\rangle$ are coupled together through H_{int} with strength g,

$$g = \langle\widetilde{e}0|\,\hat{\mathcal{H}}_{\text{int}}\,|\widetilde{g}1\rangle\,, \tag{4.35}$$

the qubit can lose its excitation and scatter a Raman photon in the cavity mode, which is again lost through the cavity decay channel that brings $|\widetilde{g}1\rangle$ back to $|\widetilde{g}0\rangle$, and autonomously completes the stabilization process. The $|\widetilde{e}0\rangle \rightarrow |\widetilde{g}1\rangle \rightarrow |\widetilde{g}0\rangle$ transition can be thought of as a cavity assisted qubit decay channel, which is sometimes referred to as the "refilling" process [189]. Intuitively, the success of the scheme with high stabilization fidelity lies upon $\kappa \gg \widetilde{\gamma}_+$ as well as a decent $|\widetilde{e}0\rangle \rightarrow |\widetilde{g}1\rangle$ transition rate Γ.

To begin our treatment with a more quantitative analysis, under the assumption that the cavity decay rate is dominant among all dissipation rates, we divide the parameter space into two different regimes in terms of the ratio g/κ, namely the weak coupling regime ($g/\kappa \ll 1$) and the strong coupling regime ($g/\kappa \gg 1$), as shown in Fig. 4.6. In the weak coupling regime, the $|\widetilde{g}1\rangle$ state can not build up any population as the photon is very quickly drained. Therefore $|\widetilde{e}0\rangle$ exponentially decays at the transition rate Γ given by Fermi's golden rule [99]

$$\Gamma = \frac{g^2\kappa}{(\kappa/2)^2 + (\Omega_c - \Omega_R)^2}, \tag{4.36}$$

where the transition rate is maximized at $\Omega_c = \Omega_R$ and reduces simply to

$$\Gamma = \frac{4g^2}{\kappa}. \tag{4.37}$$

In the weak coupling regime, the population of $|\widetilde{e}0\rangle$ varies at a rate much slower than κ. Thus the qubit dissipation terms associated with $\widetilde{\gamma}_\pm$ can be linearly added into the optical Bloch equations.

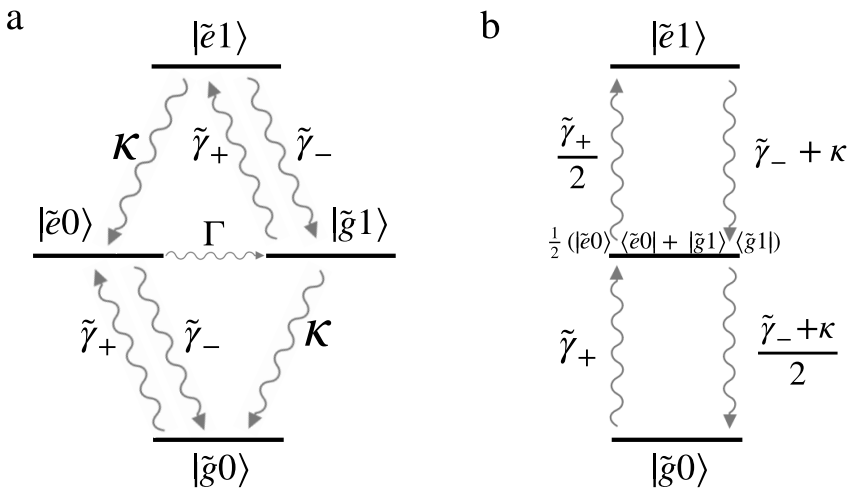

Figure 4.6: Decay diagrams for (a) weak and (b) strong coupling regimes, depending on g/κ. We set $\Omega_c = \Omega_R$ for both cases for optimal performance. (a) When $g/\kappa \ll 1$, the $|\widetilde{e}0\rangle$ state can decay back to the ground state $|\widetilde{g}0\rangle$ through a two-step process $|\widetilde{e}0\rangle \rightarrow |\widetilde{g}1\rangle \rightarrow |\widetilde{g}0\rangle$, which is limited by the slower rate of the two. Γ is calculated from Fermi's golden rule as $4g^2/\kappa$. (b) When $g/\kappa \gg 1$, the transition rate is strong enough to build up population in $|\widetilde{g}1\rangle$ and even allow the photon to tunnel back to $|\widetilde{e}0\rangle$ before it is lost, giving rise to a coherent oscillation between the two levels fast enough to be viewed as a equally weighted mixture. As the photon spends half of its time in each mode, its decay rate to $|\widetilde{g}0\rangle$ is effectively the average of κ and γ, and it jumps to $|\widetilde{e}1\rangle$ at half of the excitation rate $\widetilde{\gamma}_+$, as this transition is only allowed when the photon lives in the qubit mode. Similarly, we can find the rest of the decay rates for this approximate three level system. Finally, by solving the optical Bloch equations we arrive to the analytical expressions of the stabilization fidelity, given by Eq. (4.38) and Eq. (4.39).

Those can be straightforwardly solved for the qubit ground state population as,

$$P_{\widetilde{g}} = P_{\widetilde{g}0} + P_{\widetilde{g}1} = \frac{\widetilde{\gamma}_-(\widetilde{\gamma}_- + \widetilde{\gamma}_+ + \kappa)\kappa^2 + 4g^2(\widetilde{\gamma}_- + \kappa)(\widetilde{\gamma}_+ + \kappa)}{(\widetilde{\gamma}_- + \widetilde{\gamma}_+)(\widetilde{\gamma}_- + \widetilde{\gamma}_+ + \kappa)\kappa^2 + 4g^2[(\widetilde{\gamma}_- + \widetilde{\gamma}_+)(\widetilde{\gamma}_+ + \kappa) + \kappa^2]}. \tag{4.38}$$

As for the strong coupling regime, the system first undergoes coherent oscillations between the $|\widetilde{e}0\rangle$ and $|\widetilde{g}1\rangle$ states which eventually are driven into a statistical mixture with (almost) equal population of the two levels. Therefore, at long times we can approximate the two levels as one, with a decay rate to $|\widetilde{g}0\rangle$ corresponding to the mean value of the cavity decay and the qubit decay $(\widetilde{\gamma}_- + \kappa)/2$, as it can decay through both the qubit and the cavity channels. We can find the decay rates shown between other levels shown in Fig. 4.6 in a similar fashion. Solving the corresponding

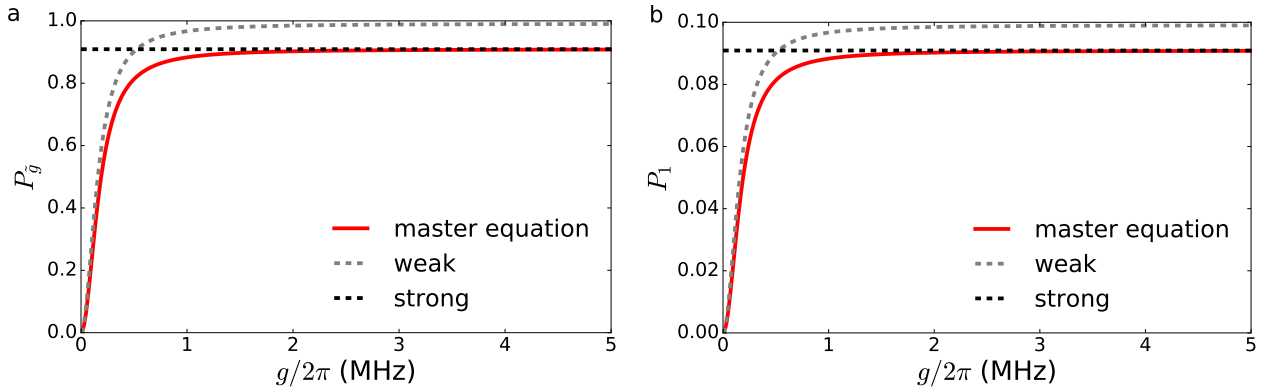

Figure 4.7: (a) The stabilized state population and (b) mean cavity photon number for stabilization angle $\theta = \pi$, as a function of the coupling strength $g = \langle \widetilde{e}0 | \hat{\mathcal{H}}_{int} | \widetilde{g}1 \rangle$, calculated with $\kappa/2\pi$= 1 MHz, $\gamma/2\pi$ = 0.1 MHz, $\gamma_\phi/2\pi$ = 0.1 MHz. Parameters are exaggerated for enhancing visual contrast and do not reflect experimental values. At $\theta = \pi$, the rotating frame ground state overlaps with the lab frame excited state, i.e. $|\widetilde{g}\rangle = |e\rangle$. The exact solution from the master equation coincides with the weak coupling formula when g is small, whereas it falls into its asymptote predicted by the strong coupling formula when g is big, showing an good agreement between the theory and the numerical calculation.

optical Bloch equations again gives the stabilization fidelity as (with $\Omega_c = \Omega_R$)

$$P_{\widetilde{g}} = P_{\widetilde{g}0} + P_{\widetilde{g}1} = \frac{\widetilde{\gamma}_- + \kappa}{\widetilde{\gamma}_- + \widetilde{\gamma}_+ + \kappa}. \tag{4.39}$$

The interaction $\hat{\mathcal{H}}_{\text{int}}$ may also induce finite coupling between other levels, through $\langle i | \hat{\mathcal{H}}_{\text{int}} | j \rangle$. However, unlike Γ between (near-)resonant levels $|\widetilde{e}0\rangle$ and $|\widetilde{g}1\rangle$, these transition probabilities are strongly suppressed by the detuning and can be safely dropped out as long as $\langle i | \hat{\mathcal{H}}_{\text{int}} | j \rangle \ll \Omega_R, \Omega_c$.

Eq. (4.38) and (4.39) are shown in Fig. 4.7 as the two asymptotes of the fidelity versus coupling strength g calculated from master equation, which shows quantitative agreements between the analytical formulas and the numerical simulations.

In the analysis above we have ignored the effect of the dressed dephasing in Eq. 4.32. While it has no explicit contribution to $\widetilde{\gamma}_\pm$, we need to point out that dephasing indeed weakens the stabilization along the z axis, especially when in the weak coupling regime. The reason is a little subtle

but can be understood as follow: in the derivation of the weak coupling regime, we have made the assumption that in the subspace spanned by $|\widetilde{e}0\rangle$ and $|\widetilde{g}1\rangle$, they evolve as a pure superposition state. However, this assumption becomes invalid when qubit dephasing causes their superposition to lose pureness over time. This impedes the swapping of population between $|\widetilde{e}0\rangle$ and $|\widetilde{g}1\rangle$ and reduces the effective decay rate from $|\widetilde{e}0\rangle$ to $|\widetilde{g}0\rangle$, and ultimately results in a lower stabilization fidelity.

4.3.2 Universal stabilization with blue-sideband interaction and Rabi drive

In the previous subsection, we have proved that the success of universal stabilization critically relies on the implementation of the coupling strength, $g = \langle\widetilde{e}0|\,\hat{\mathcal{H}}_{int}\,|\widetilde{g}1\rangle$. In other words, we need to find an interaction Hamiltonian $\hat{\mathcal{H}}_{int}$ that universally provides decent coupling strength for all possible $|\widetilde{e}0\rangle$ and $|\widetilde{g}1\rangle$. To gain more insights on what the detailed form of this interaction term should be, we rewrite it as

$$\hat{\mathcal{H}}_{\text{int}}/\hbar = \Omega\left(|\widetilde{e}0\rangle\,\langle\widetilde{g}1| + |\widetilde{g}1\rangle\,\langle\widetilde{e}0|\right). \tag{4.40}$$

The components of this Hamiltonian immediately become clear by plugging in Eq. 4.26 and 4.27,

$$\hat{\mathcal{H}}_{\text{int}}/\hbar = \Omega\left[\cos^2\frac{\theta}{2}\left(\hat{a}^\dagger\hat{\sigma}^- + \hat{a}\hat{\sigma}^+\right) - \sin^2\frac{\theta}{2}\left(\hat{a}^\dagger\hat{\sigma}^+ + \hat{a}\hat{\sigma}^-\right) + \frac{1}{2}\sin\theta\left(\hat{a}^\dagger + \hat{a}\right)\hat{\sigma}_z\right], \tag{4.41}$$

where the first two terms are the familiar red- and blue-sideband interactions, while the last term represents the longitudinal coupling that can be achieved in a similar way to the cross-resonance gate [190, 191], i.e. by Rabi driving through qubit's charge port at the cavity frequency[2]. The amplitudes of the three components vary according to the stabilization angle: the blue-sideband terms maximizes at $\theta = 0$ where the stabilization target state is the qubit excited state, the red-sideband interaction at $\theta = \pi$ which optimally stabilizes the ground state, and the longitudinal coupling at

2. This is typically accompanied by a quite significant direct cavity drive tone that needs to be compensated by another cavity drive of the opposite phase.

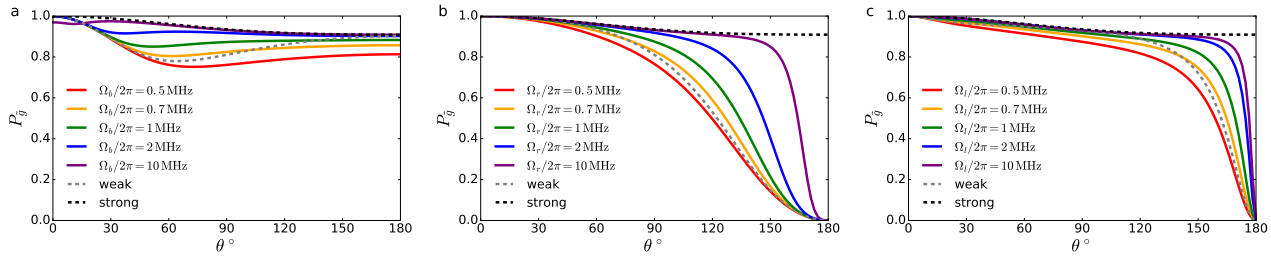

Figure 4.8: Comparison of stabilization fidelity with respect to $P_{|\tilde{g}\rangle}$ at different polar angles θ, between schemes using (a) blue-sideband interaction $\Omega_b(\hat{a}^\dagger\hat{\sigma}^+ + \hat{a}\hat{\sigma}^-)$, (b) red-sideband interaction $\Omega_r(\hat{a}^\dagger\hat{\sigma}^- + \hat{a}\hat{\sigma}^+)$ and (c) longitudinal interaction $\Omega_l(\hat{a}^\dagger + \hat{a})\hat{\sigma}_z$. All three interactions can be realized with the tunable coupling circuit, by using flux modulations and charge drives. Each scheme is calculated with its coupling strength varying from the weak coupling regime to the strong coupling regime. The grey and black dashed lines are theoretical limitations in the weak ($\Omega_{b,r,l}/2\pi = 0.5\,\mathrm{MHz}$) and the stronger coupling regime ($\Omega_{b,r,l}/2\pi = 10\,\mathrm{MHz}$), respectively. Other parameters are $\Omega_R/2\pi = 100\,\mathrm{MHz}$, $\kappa/2\pi$= 1 MHz, $\gamma/2\pi$ = 0.1 MHz, $\gamma_\phi/2\pi$ = 0.1 MHz. For all three schemes, the increase of the interaction strength results in higher overall fidelity levels, gradually approaching the upper limit set by Eq. (4.39). However only the blue-sideband interaction allows for universal stabilization throughout all θ values, as it uniquely remains highly efficient up to $\theta = \pi$ when the other two rapidly lose fidelity.

$\theta = \pi/2$ that stabilizes the xy superposition state. Conversely, they all have their "weak points" on the Bloch sphere that they fail to stabilize: the ground state for the blue-sideband, excited state for the red-sideband and both ground and excited states for the longitudinal coupling. However, the spontaneous decay of the qubit makes the stabilization of the ground state a trivial task, as it can always be accomplished under low enough temperatures. The specialty of the blue-sideband interaction is clearly displayed in Fig. 4.8, which shows the comparison of the stabilization fidelity under the three coupling schemes. While all three schemes could achieve stabilization with high efficiency at small θ, only the blue-sideband interaction is able to couple $|g0\rangle$ and $|e1\rangle$, which is critical for achieving a truly universal stabilization.

Now we will show how the universal stabilization is experimentally realized with only the blue-sideband interaction plus the qubit-dressing Rabi drive. We begin by writing down the lab-frame

Hamiltonian of the tunable coupling circuit under simultaneous charge and flux modulation,

$$\hat{\mathcal{H}}/\hbar = \frac{\omega_q}{2}\hat{\sigma}_z + \omega_c \hat{a}^\dagger \hat{a} + \chi \hat{a}^\dagger \hat{a}\hat{\sigma}_z + \Omega_x \hat{\sigma}_x \cos\omega_1 t + 2\Omega_b(\hat{a}^\dagger + \hat{a})\hat{\sigma}_x \cos\omega_2 t, \tag{4.42}$$

where the first three terms are the static energy of the device, and the last two represent the Rabi drive and the flux modulation. When the flux is modulated in the vicinity of the blue-sideband frequency, this Hamiltonian can be transformed to the rotating frame by the operator,

$$U = e^{i[\frac{\omega_1}{2}\hat{\sigma}_z + (\omega_2 - \omega_1)\hat{a}^\dagger \hat{a}]t}, \tag{4.43}$$

which is given by (under RWA)

$$\hat{\mathcal{H}}_{\text{rot}}/\hbar = \frac{\Omega_x}{2}\hat{\sigma}_x + \frac{\omega_q - \omega_1}{2}\hat{\sigma}_z + \chi \hat{a}^\dagger \hat{a}\hat{\sigma}_z + \Omega_b(\hat{a}^\dagger \hat{\sigma}^+ + \hat{a}\hat{\sigma}^-) + (\omega_c + \omega_1 - \omega_2)\hat{a}^\dagger \hat{a}. \tag{4.44}$$

Denoting $\Omega_z = \omega_q - \omega_1$ and $\Omega_c = \omega_c + \omega_1 - \omega_2$, the Hamiltonian is rewritten as

$$\hat{\mathcal{H}}_{\text{rot}}/\hbar = \frac{1}{2}\Omega_x \hat{\sigma}_x + \frac{1}{2}(\Omega_z + 2\chi \hat{a}^\dagger \hat{a})\hat{\sigma}_z + \Omega_b(\hat{a}^\dagger \hat{\sigma}^+ + \hat{a}\hat{\sigma}^-) + \Omega_c \hat{a}^\dagger \hat{a}. \tag{4.45}$$

We can approximate the above Hamiltonian as

$$\hat{\mathcal{H}}_{\text{rot}}/\hbar = \frac{1}{2}\Omega_x \hat{\sigma}_x + \frac{1}{2}(\Omega_z + 2\chi \bar{n})\hat{\sigma}_z + \Omega_b(\hat{a}^\dagger \hat{\sigma}^+ + \hat{a}\hat{\sigma}^-) + \Omega_c \hat{a}^\dagger \hat{a} \tag{4.46}$$

as long as $2\chi\bar{n} \ll \Omega_R$ is satisfied, where $\bar{n}$ is the mean cavity photon number. This requirement guarantees that the dispersive shift term can be safely counted in as only a small perturbation to the stabilization angle

$$\theta' = \arccos \frac{\Omega_z + 2\chi\bar{n}}{\sqrt{\Omega_x^2 + (\Omega_z + 2\chi\bar{n})^2}}. \tag{4.47}$$

Fig. 4.7b plots the mean cavity photon number versus the coupling strength. Similar to Fig. 4.7a,

in the strong coupling regime the mean cavity photon number saturates at the upper limit given by

$$\bar{n}_{\text{max}} = \frac{\widetilde{\gamma}_+}{\widetilde{\gamma}_- + \widetilde{\gamma}_+ + \kappa}, \tag{4.48}$$

which is small under $\kappa \gg \widetilde{\gamma}_\pm$. In our experiment, the Rabi drive strength is $2\pi\times 9$ MHz while the dispersive shift is less than $2\pi\times 1$ MHz at zero dc flux, so the requirement $2\chi\bar{n} \ll \Omega_R$ is well met.

The dispersive shift term can also be viewed as a qubit state dependent frequency shift to the cavity, in which sense Eq. 4.45 becomes

$$\hat{\mathcal{H}}_{\text{rot}}/\hbar = \frac{1}{2}\Omega_x\hat{\sigma}_x + \frac{1}{2}\Omega_z\hat{\sigma}_z + \Omega_b(\hat{a}^\dagger\hat{\sigma}^+ + \hat{a}\hat{\sigma}^-) + (\Omega_c + 2\chi\hat{\sigma}_z)\hat{a}^\dagger\hat{a}. \tag{4.49}$$

As stated previously, the optimized fidelity is reached when $|\widetilde{e}0\rangle$ and $|\widetilde{g}1\rangle$ become degenerate, which happens at

$$\Omega_c = \Omega_R - 2\chi\,\langle\hat{\sigma}_z\rangle \approx \Omega_R + 2\chi\cos\theta \tag{4.50}$$

that corresponds to the qubit Rabi drive frequency ω_1 and blue-sideband drive frequency ω_2 being

$$\omega_1 = \omega_q - \Omega_z, \quad \omega_2 = \omega_q + \omega_c - \Omega_R - \Omega_z, \tag{4.51}$$

see Fig. 4.11a.

In our experiment, the static flux in the coupler SQuID loop is biased to zero via the dc flux line. This tunes the coupling strength $g_{R,B}$ to its minimum where the first order term $g^{(1)}_{R,B}$ in the Fourier series of $g_B(t)$ vanishes by symmetry in the expansion of the Josephson potential [192], allowing the blue-sideband interaction to be created through the second harmonic term $g^{(2)}_B$ by flux modulation at half of the qubit-cavity sum frequency Σ. This avoids the need to drive at the sum frequency directly, and requires lower bandwidth control. The blue-sideband frequency is calibrated by finding the modulation frequency that corresponds to the maximum value of the qubit excited state population, which is measured after the flux pulse is turned on for sufficiently long time. The strength of the blue-sideband interaction, Ω_b, can be directly obtained from the oscil-

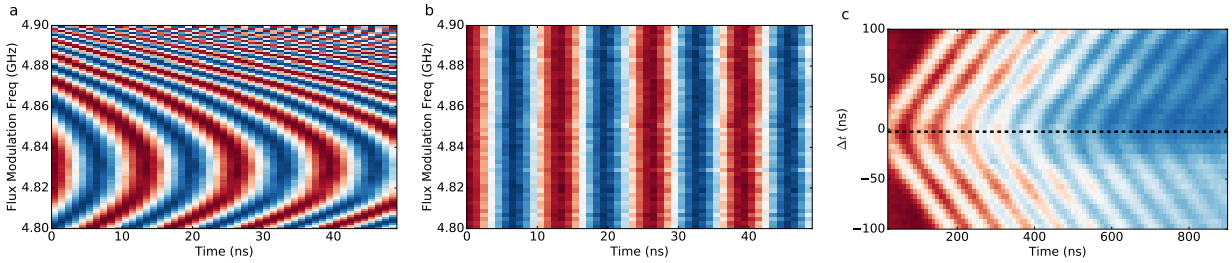

Figure 4.9: (a) Ramsey experiment done with flux modulation applied between the two qubit $\pi/2$ operations. The flux signal is created by an AWG of fixed output power. From the curved fringes qubit dc-offset/effective flux-modulation strength can be measured. (b) Output power of the awg is compensated using the calibration result obtained from (a), showing vertical lines which indicates that the effective flux-modulation strength is kept constant over the modulation frequency range. (c) calibration of the mismatch time Δt between the flux pulse and Rabi drive pulse of the same length, using $\theta = 3\pi/4$ scheme shown in Fig. 4.10. Qubit excited state population is measured as a function of pulse durations as well as the delay time between the two pulses, shown as a chevron pattern. At times when the two pulses are not overlapping, they do not affect the qubit state as both are far-detuned from resonance. Therefore, the red regions (where qubit is in the ground state) in the upper and lower left corners indicate the mismatch between the two pulses. They only precisely overlap each other at the axis of symmetry of the pattern, indicated by the dashed line.

lation rate of the qubit excited state population. It is a necessity for the stabilization protocol to drive the blue-sideband modulation at different frequencies depending on the stabilization target state (4.51). However, the effective amplitude of the flux modulation will change at different frequencies, due to the frequency-dependent power loss along the rf flux line. On the other hand, the flux modulation also gives rise to a shift of the qubit frequency known as the "dc-offset", which is uniquely dependent on the modulation amplitude. As shown in Fig. 4.9a, Ramsey fringes can be used to directly measure the dc-offset at different flux modulation frequencies. By adjusting the output power of the arbitrary wave form generator (AWG) which is used to provide the rf flux signal, we produce a constant qubit dc-offset across the flux modulation frequency of interest (Fig. 4.9b), equivalent to realizing a constant blue-sideband interaction strength for all these frequencies. The strength of the Rabi drive Ω_x, which is also kept fixed throughout the stabilization protocol, can be directly measured from the Rabi experiment. The Rabi drive pulse and the blue-sideband flux pulse are simultaneously sent to the circuit sample, with detunings Ω_z and $\Omega_z + \Omega_R$,

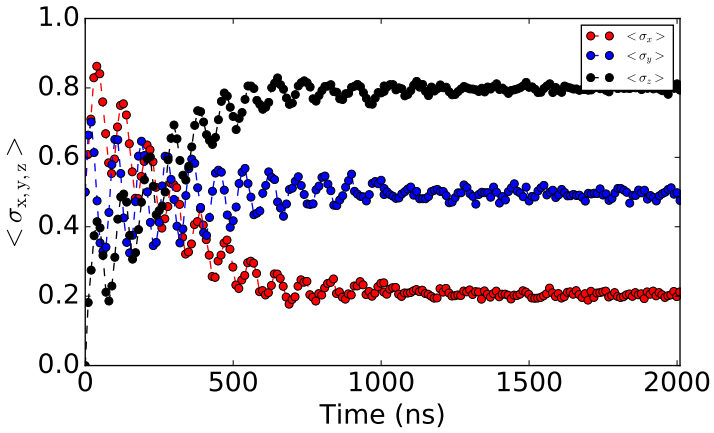

Figure 4.10: Stabilization of the qubit state at polar angle $\theta = 3\pi/4$, illustrated by the evolution of its projections to the x (red), y (blue), and z (black) axis.

respectively. Synchronization of the two pulses is guaranteed by calibrating their mismatch time Δt (see Fig. 4.9c). Qubit tomography, with phase synchronized to the Rabi drive, is performed at different pulse times. As is displayed in Fig. 4.10, a coherent oscillation of the qubit state is observed at the beginning of time, with a rate close to the total Rabi rate Ω_R. We set the initial phase of the Rabi drive to zero (for Fig. 4.10 it is set to π), so that in the long-time limit the qubit state will be stabilized with $\langle\sigma_y\rangle \approx 0$, while the polar angle and the purity are measured as

$$\theta_{\text{measured}} = \arccos \frac{\langle\sigma_z\rangle}{\sqrt{\langle\sigma_x\rangle^2 + \langle\sigma_y\rangle^2 + \langle\sigma_z\rangle^2}}, \tag{4.52}$$

$$|\langle\vec{\sigma}\rangle| = \sqrt{\langle\sigma_x\rangle^2 + \langle\sigma_y\rangle^2 + \langle\sigma_z\rangle^2}. \tag{4.53}$$

We apply this protocol to demonstrate stabilization of arbitrary states on the Bloch sphere. The polar angle was varied by changing the Rabi drive detuning Ω_z while keeping its strength $\Omega_x/2\pi$ fixed at 9 MHz. As can be seen from Eq. (4.38), the azimuthal angle has no effect on the stabilization fidelity and was thus set to zero. The amplitude of the flux modulation is calibrated to create a constant blue-sideband coupling strength $\Omega_b/2\pi = 0.5$ MHz for all stabilization angles,

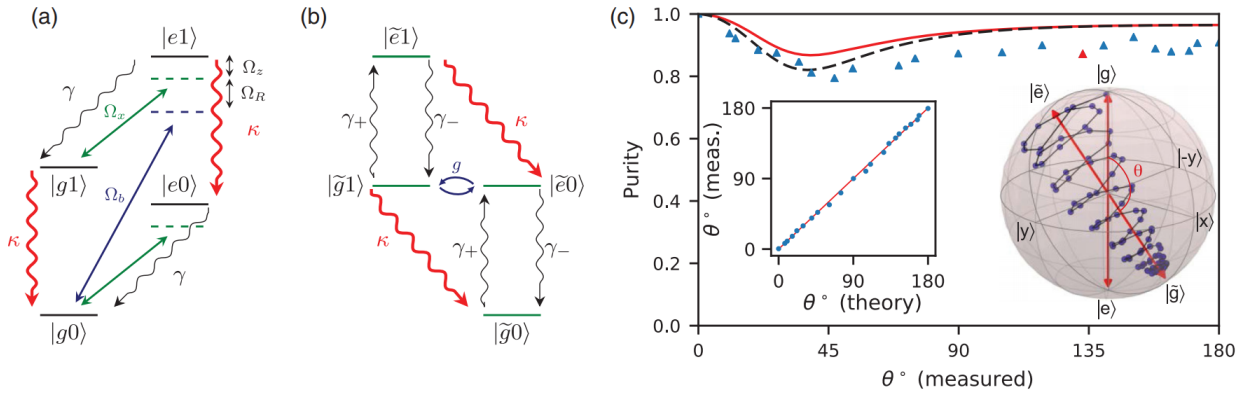

Figure 4.11: Illustration of the universal stabilization scheme for single-qubit states. In the lab frame (a), qubit Rabi drive and blue-sideband modulation are applied with appropriately chosen detuning and strength. In the rotating frame (b), these two drives result in the dressing of the qubit state into arbitrary superpositions $|\widetilde{g}\rangle$, $|\widetilde{e}\rangle$, with resonant coupling between $|\widetilde{e}0\rangle$ to $|\widetilde{g}1\rangle$. Together with the aid of the fast cavity decay, these finally lead to the stabilization of the $|\widetilde{g}0\rangle$ state. (c) The stabilization purity $|\langle\vec{\sigma}\rangle|$, plotted against the polar angle θ of the stabilization axis, both obtained from qubit tomography. Purities exceeding 80% are achieved over the entire Bloch sphere, while purities >90% and $> 99\%$ are reached for stabilizing the $|e\rangle$ ($\theta = 180°$) and $|g\rangle$ ($\theta = 0°$) states, respectively. Experimental data qualitatively agrees with the analytical calculation from Eq. 4.38 (red line) and numerical master equation simulation (black dashed line). The stabilization experiment was performed at zero flux, where qubit and cavity frequencies are $\omega_q/2\pi = 4.343\,\text{GHz}$ and $\omega_r/2\pi = 5.439\,\text{GHz}$, with the linewidths being $\gamma/2\pi \approx 7.6\,\text{KHz}$, $\gamma_\phi/2\pi \approx 3\,\text{KHz}$ and $\kappa/2\pi \approx 1.6\,\text{MHz}$. Left inset: stabilization angles predicted by theory closely match the experimental values. Right inset: trajectory of the qubit state in the dynamic process of stabilization, for the specific case of $\theta = 135°$ (red triangle) with measured purity of 87%. Starting from $|g\rangle$, the qubit state moves in a helical path along the stabilization axis, until it saturates around the rotating frame ground state, $|\widetilde{g}\rangle$.

with the detuning chosen in each case to be $\Omega_z + \Omega_R$. The measured stabilization purity $|\langle\vec{\sigma}\rangle| = \sqrt{\langle\sigma_x\rangle^2 + \langle\sigma_y\rangle^2 + \langle\sigma_z\rangle^2}$ is plotted as a function of the stabilization polar angle θ in Fig. 4.11c, which closely follow the theory prediction made by Eq. 4.38. The excited state $|e\rangle$ is stabilized with 93% purity at $\theta = 180°$, where only the blue-sideband process is required. Purity starts to reduce as θ is lowered, which can be understood by the blue-sideband interaction losing efficiency in coupling the $|\widetilde{g}1\rangle$ and $|\widetilde{e}0\rangle$ states when the rotating-frame ground state $|\widetilde{g}\rangle$ has less overlap with the bare excited state, $|e\rangle$. This, however, does not invalidate the scheme's performance for small angles. According to Eq. 4.30 and Eq. 4.31, the qubit's natural decay guarantees $\widetilde{\gamma}_- \gg \widetilde{\gamma}_+$ as $\theta \to 0$, resulting in good stabilization fidelity in Eq. 4.38, irrespective of how small Γ is. This

is reflected in Fig. 4.11c as a revival of the purity from a minimum value of $\sim 80\%$ to near unity (limited by lab-frame qubit temperature) at $\theta = 0$, where the lab-frame ground state $|g\rangle$ is "stabilized" through the natural decay of the qubit. The high fidelity at all stabilization angles therefore relies upon the mixed contribution of the active stabilization process induced by the blue-sideband interaction (Γ), and the passive process from natural qubit decay ($\widetilde{\gamma}_-$).

4.3.3 Universal stabilization with "purple" sideband interaction

While the blue-sideband interaction is capable of universally stabilizing all qubit states with the aid of the qubit's natural decay, the stabilization rate significantly drops down as $\theta \to 0$ and is ultimately limited by the spontaneous emission rate. On the other hand, the optimal interaction obtained in Eq. 4.41 poses stringent experimental requirement as it calls for all three parametric drives of different amplitude and frequencies. Here we demonstrate how the optimal scheme can be further simplified while maintaining the same stabilization performance. An alternative to Eq. 4.40, the optimal interaction term that is universally efficient for all stabilization angles can be written as

$$H_{\text{int}} = \Omega_p(a^\dagger + a)(e^{i\phi}\widetilde{\sigma}^+ + e^{-i\phi}\widetilde{\sigma}^-) \tag{4.54}$$

where ϕ is an arbitrary phase, and $\widetilde{\sigma}^+$ is defined as

$$\widetilde{\sigma}^+ = |\widetilde{e}\rangle \langle\widetilde{g}| \,. \tag{4.55}$$

Comparing to Eq. 4.40, Eq. 4.54 contains "counter-rotating terms" that lead to off-resonant stray coupling between $|\widetilde{g}0\rangle$ and $|\widetilde{e}1\rangle$. Nevertheless, as long as the Rabi drive energy far exceeds this interaction energy, this undesired coupling is fast oscillating and can be averaged out. Transforming it back to the lab basis through the unitary operator from Eq. (4.25),

$$\widetilde{\sigma}^+ = \frac{1}{2}\begin{pmatrix} \sin\theta & -1+\cos\theta \\ 1+\cos\theta & -\sin\theta \end{pmatrix}, \tag{4.56}$$

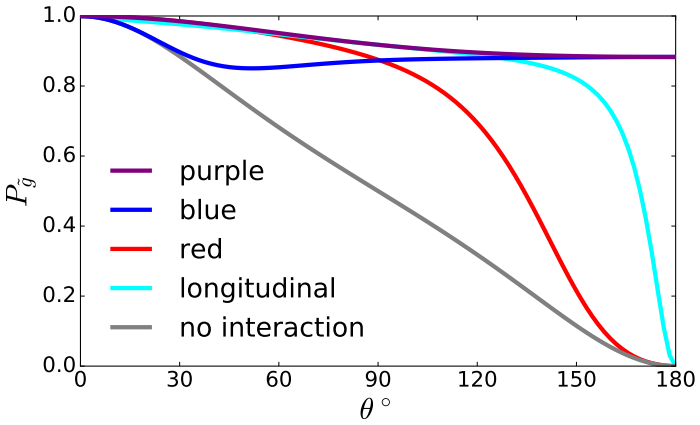

Figure 4.12: Comparison of stabilization schemes with different interactions, by plotting their stabilization state population $P_{\tilde{g}}$ as a function of the stabilization angle θ. The grey curve represents "stabilization" from qubit's natural decay without interactions at play. All interaction terms have the same coupling strength of $2\pi \times 1\,\text{MHz}$. Other parameters are $\Omega_R/2\pi = 100\,\text{MHz}$, $\kappa/2\pi = 1\,\text{MHz}$, $\gamma/2\pi = 0.1\,\text{MHz}$ and $\gamma_\phi/2\pi = 0.1\,\text{MHz}$. The purple interaction outperforms all of the other interactions by providing highest stabilization population for all angles.

so

$$e^{i\phi}\tilde{\sigma}^{+} + e^{-i\phi}\tilde{\sigma}^{-} = \begin{pmatrix} \cos\phi\sin\theta & -i\sin\phi + \cos\phi\cos\theta \\ i\sin\phi + \cos\phi\cos\theta & -\cos\phi\sin\theta \end{pmatrix}. \tag{4.57}$$

By setting $\phi = \pi/2$ here, we arrive to the "purple" sideband interaction

$$H_{\text{int}} = \Omega_p(a^\dagger + a)\sigma_y \tag{4.58}$$

which is a balanced mixture of the red- and blue-sideband interactions completely independent of θ. Fig. 4.12 displays the comparison between the purple-sideband stabilization and the other three schemes, which shows that under the same coupling strength, the purple-sideband interaction provides the highest stabilization fidelity at all angles. The mixing of the red-and blue-sideband interactions, which might be hard to achieve via conventional schemes using the qubit's nonlinearity, can be directly realized by driving the tunable coupling device at the red- and blue-sideband frequency simultaneously with equal drive strength.

4.3.4 *Dark state picture of qubit state stabilization*

This subsection aims to provide a slightly different perspective to look at the cavity-assisted qubit stabilization process. Assuming we have a qubit-cavity system whose Hamiltonian is given as follows,

$$\hat{\mathcal{H}}/\hbar = \frac{\Omega_q}{2}\widetilde{\hat{\sigma}}_z + \Omega_c \hat{a}^\dagger \hat{a} + g(\hat{a}^\dagger \widetilde{\hat{\sigma}}^- + H.c.), \tag{4.59}$$

where $\widetilde{\sigma}_z = -|\widetilde{g}\rangle\langle\widetilde{g}| + |\widetilde{e}\rangle\langle\widetilde{e}|$, and $\widetilde{\sigma}^- = |\widetilde{g}\rangle\langle\widetilde{e}|$ is some arbitrary qubit operator. This Hamiltonian can be defined in the lab frame, or is transformed from the lab frame Hamiltonian through unitary operators. The tilde signs indicate dressed basis that can be different from natural bare basis.

The master equation that describes the evolution of this open system is given by

$$\dot{\rho} = -i[\hat{\mathcal{H}}, \rho] + \kappa\mathcal{D}[\hat{a}]\rho + \widetilde{\gamma}_-\mathcal{D}[\widetilde{\hat{\sigma}}_-]\rho + \widetilde{\gamma}_+\mathcal{D}[\widetilde{\hat{\sigma}}_+]\rho + \widetilde{\gamma}_\phi\mathcal{D}[\frac{\widetilde{\hat{\sigma}}_z}{\sqrt{2}}]\rho, \tag{4.60}$$

Note that here the qubit dissipators are defined in the same dress basis as Eq. 4.59. In the weak coupling limit where $\kappa \gg g, \widetilde{\gamma}, \widetilde{\gamma}_\phi$, the cavity terms can be adiabatically eliminated [193], yielding the effective qubit master equation,

$$\dot{\rho} = (\Gamma + \widetilde{\gamma}_-)\,\mathcal{D}[\widetilde{\hat{\sigma}}_-]\rho + \widetilde{\gamma}_+\mathcal{D}[\widetilde{\hat{\sigma}}_+]\rho + \frac{\widetilde{\gamma}_\phi}{2}\mathcal{D}[\widetilde{\hat{\sigma}}_z]\rho, \tag{4.61}$$

where

$$\Gamma = \frac{g^2\kappa}{(\kappa/2)^2 + (\Omega_q - \Omega_c)^2}. \tag{4.62}$$

From here we can easily recover the main result in subsection 4.3.1 where the stabilized qubit state is

$$\rho_q = \frac{\Gamma + \widetilde{\gamma}_-}{\Gamma + \widetilde{\gamma}_- + \widetilde{\gamma}_+}\widetilde{\rho}_g + \frac{\widetilde{\gamma}_+}{\Gamma + \widetilde{\gamma}_- + \widetilde{\gamma}_+}\widetilde{\rho}_e. \tag{4.63}$$

Now we take a dark state point of view [194], where we note the fact that each jump operator in the master equation has its corresponding dark state (or degenerate dark subspace) and the global steady state is usually an incoherent mixture of these darks states. When one of the dissipators is

dominant while others can be treated as perturbations, its dark state becomes approximately equal to the steady state. This observation, along with the adiabatic elimination method, can be useful for providing a quick and convenient way to intuitively discover the steady state of qubit(s) under cavity-assisted dissipation processes. We now give an example of its application.

Imagine we have two qubits parametrically coupled to a lossy quantum bus mode via blue-sideband interactions, and we now want to find the steady state of the qubits. Assuming the blue-sideband drives are on resonance, we write out the Hamiltonian as,

$$\hat{\mathcal{H}} = g\left(\hat{a}^\dagger(\widetilde{\hat{\sigma}}_1^- + \widetilde{\hat{\sigma}}_2^-) + H.c.\right), \tag{4.64}$$

where we have moved to the rotating frame and $\widetilde{\hat{\sigma}}_i^- = \hat{\sigma}_i^+$. After adiabatic elimination of the bus mode, we have

$$\dot{\rho} = \frac{4g^2}{\kappa}\mathcal{D}[\hat{\sigma}_1^+ + \hat{\sigma}_2^+]\rho + \gamma_1\mathcal{D}[\hat{\sigma}_1^-]\rho + \gamma_2\mathcal{D}[\hat{\sigma}_2^-]\rho + \gamma_{1,\phi}\mathcal{D}[\frac{\hat{\sigma}_{1,z}}{\sqrt{2}}]\rho + \gamma_{2,\phi}\mathcal{D}[\frac{\hat{\sigma}_{2,z}}{\sqrt{2}}]\rho. \tag{4.65}$$

Assuming $4g^2/\kappa \gg \gamma_i, \gamma_{i,\phi}$, we estimate the qubit steady state to be the dark state of the leading dissipator, $\hat{\sigma}_1^+ + \hat{\sigma}_2^+$, which can be easily found as

$$\begin{aligned}(\hat{\sigma}_1^+ + \hat{\sigma}_2^+)\left|ee\right\rangle &= 0,\\ (\hat{\sigma}_1^+ + \hat{\sigma}_2^+)\left|\psi^-\right\rangle &= 0,\end{aligned} \tag{4.66}$$

where $\left|\psi^-\right\rangle = |ge\rangle - |eg\rangle$ is a Bell state. This means that, assuming weak qubit decoherence, the two-qubit steady state is a superposition or mixture of the Bell state $\left|\psi^-\right\rangle$ and $|ee\rangle$ state, depending on the initial condition. This is further verified by numerical simulations, proving this quick estimation method to be valid.

4.4 Stabilization of Bell states

As a natural extension of the stabilization of single-qubit state, in this section we showcase the stabilization of an arbitrary Bell state via parametric flux modulation of the tunable coupling circuit, in a hardware-efficient way analogues to the "VSLQ" error correction scheme [187] that will be the subject of discussion in Chapter 5. We scale up the tunable coupling circuit to a 4-mode system consisting of two qubits and two lossy cavities, sharing a dc-SQuID to ground. The circuit Hamiltonian then becomes

$$\hat{\mathcal{H}}/\hbar = \sum_{i,j=1}^{2}\left[\frac{\omega_{qi}}{2}\hat{\sigma}_{zi} + \omega_{rj}\hat{a}_j^{\dagger}\hat{a}_j + g_{ij}\left(t\right)\left(\hat{a}_j^{\dagger}+\hat{a}_j\right)\hat{\sigma}_{xi}\right] + g_q\left(t\right)\hat{\sigma}_{x1}\hat{\sigma}_{x1} + g_c\left(t\right)\left(\hat{a}_1^{\dagger}+\hat{a}_1\right)\left(\hat{a}_2^{\dagger}+\hat{a}_2\right). \tag{4.67}$$

In order to stabilize an even-parity Bell state of $|\phi\left(\theta\right)\rangle = \left(|gg\rangle + e^{i\theta}|ee\rangle\right)/\sqrt{2}$, we simply need to modulate the circuit with a flux tone of (assuming modulating at a linear flux point)

$$f\left(t\right) = \epsilon_0 \sin\left(\omega_{q1}+\omega_{q2}\right)t + \epsilon_1 \sin\left|\omega_{q1}-\left(\omega_{c1}+\Omega\right)\right|t + \epsilon_2 \sin\left|\omega_{q2}-\left(\omega_{c2}+\Omega\right)\right|t. \tag{4.68}$$

Properly adjusting the drive amplitudes and phases, we may obtain the rotating frame Hamiltonian as

$$\hat{\mathcal{H}}/\hbar = \Omega\left(e^{i\theta}\hat{\sigma}_1^{+}\hat{\sigma}_2^{+} + e^{-i\theta}\hat{\sigma}_1^{-}\hat{\sigma}_2^{-}\right) + \sum_{i=1}^{2}\left[g_i\left(\hat{a}_i^{\dagger}\hat{\sigma}_i^{-}+\hat{a}_i\hat{\sigma}_i^{+}\right) - \Omega\hat{a}_i^{\dagger}\hat{a}_i\right]. \tag{4.69}$$

As displayed in Fig. 4.13, when the energy scale of $\Omega \gg g_i \sim \kappa_i \gg \gamma_i$ is fulfilled, the stabilization of $|\phi\left(\theta\right)\rangle$ will take place. Comparing to the single-qubit stabilization Hamiltonian Eq. 4.49, we see that the first term of Eq. 4.69 is essentially playing the same role as defining the "principle-axis" in the stabilization subspace, which determines the effective ground state to be its lowest eigenstate, in this case $|\phi\left(\theta\right)\rangle$. The second term couples the two-qubit state to the quantum bath made of two lossy resonators, while the last term guarantees a resonant Raman process that optimizes the stabilization fidelity. In the weak coupling regime where $\sqrt{\kappa\gamma} \ll g \ll \kappa$, this gives rise to an effective decay and excitation rate between $\left|\varphi^{+}\right\rangle$ and $|ge\rangle$ as

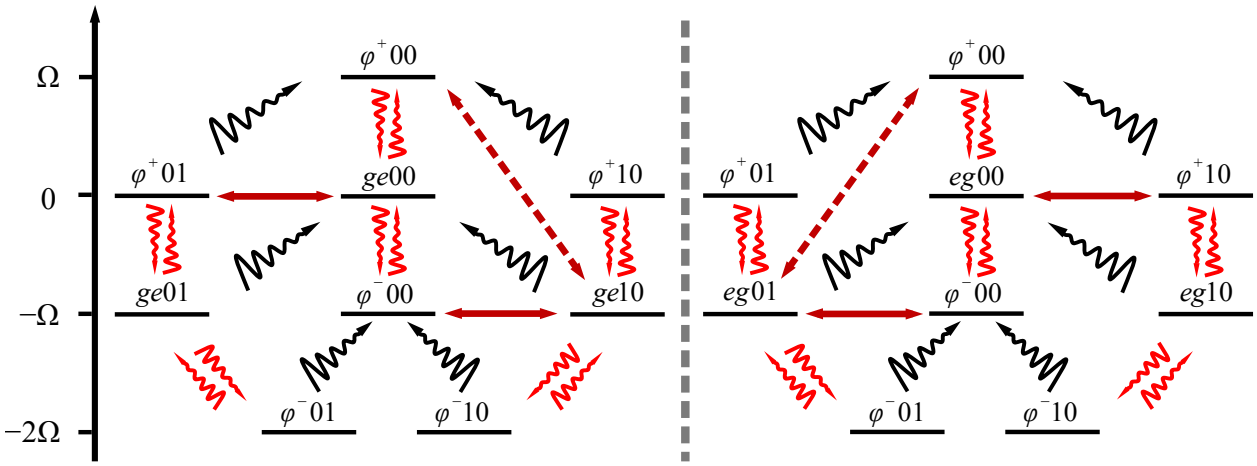

Figure 4.13: Stabilization of the $\left|\varphi^{+}\right\rangle = \left(|gg\rangle + |ee\rangle\right)/\sqrt{2}$ illustrated with the rotating frame Hamiltonian energy levels. The blue-sideband interaction between the two-qubits gives rise to the energy level structure where $\left|\varphi^{+}\right\rangle$ and $\left|\varphi^{-}\right\rangle$ are gapped by 2Ω. The red and black waved-arrows represent qubit and cavity decay respectively. The solid red double-headed arrows stand for the red-sideband interactions between the qubit and the cavity, and the dashed red arrow is the off-resonant interaction that transfers the population from the stabilization target state to other states. Single-photon loss can result in (a) $|ge00\rangle$ or (b) $|eg00\rangle$ depending on from which qubit the photon is lost. For both cases, the "error state" will be mapped to the parent Bell state while adding a photon to the lossy cavity through the resonant red-sideband coupling, which quickly decays to the stabilization target state due to fast cavity photon loss rate. Like the single-qubit's case, the stabilization of the Bell state works well when the engineered dissipation rate is far greater than the qubit spontaneous emission rate, i.e. $g \geq \kappa \gg \gamma$. The off-resonant sideband couplings are suppressed by the gap of 2Ω, further requiring $\Omega \gg g$. The levels with two cavity photons are not displayed here as they should have minimum population.

$$\Gamma_{\uparrow}^{\mathrm{ge}} = \frac{\gamma_2}{2} + \frac{2g_2^2}{\kappa_2}, \quad \Gamma_{\downarrow}^{\mathrm{ge}} = \frac{\gamma_1}{2} + \frac{2g_1^2\kappa_1}{16\Omega^2 + \kappa_1^2}, \tag{4.70}$$

similarly the relaxation rates between $\left|\varphi^{+}\right\rangle$ and $|eg\rangle$ are

$$\Gamma_{\uparrow}^{\mathrm{eg}} = \frac{\gamma_1}{2} + \frac{2g_1^2}{\kappa_1}, \quad \Gamma_{\downarrow}^{\mathrm{eg}} = \frac{\gamma_2}{2} + \frac{2g_2^2\kappa_2}{16\Omega^2 + \kappa_2^2}. \tag{4.71}$$

To the leading order in $\kappa\gamma/g^2$ and in κ/Ω, the fidelity of the $\left|\varphi^{+}00\right\rangle$ is given by

$$P_{\varphi^{+}} = 1 - \frac{\kappa\gamma}{2g^2} - \frac{\kappa^2}{8\Omega^2}, \tag{4.72}$$

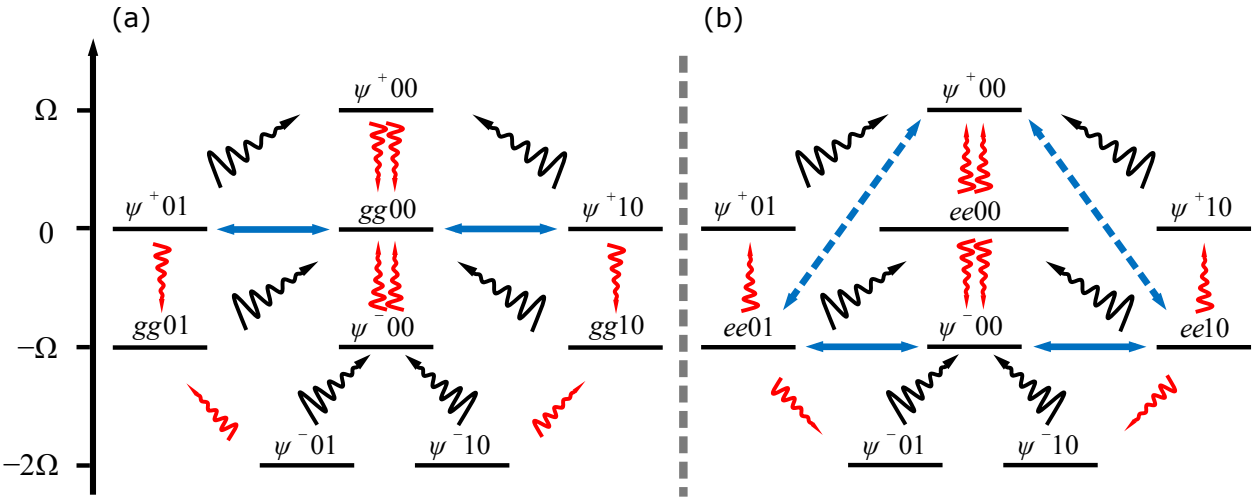

Figure 4.14: Illustration of the $\left|\psi^{+}\right\rangle = \left(|ge\rangle + |eg\rangle\right)/\sqrt{2}$ stabilization in the rotating frame. As the dominant term, the qubit-qubit red-sideband interaction defines the rotating frame levels while the qubit-cavity sideband interactions, labeled by the blue double-headed arrows, can be viewed as perturbations between these levels. The red and black waved-arrows represent qubit and cavity decay respectively. (a) In this case, single-photon loss on either qubit brings the Bell state into the zero-photon state $|gg00\rangle$, which is simultaneously coupled to $\left|\psi^{+}01\right\rangle$ and $\left|\psi^{+}10\right\rangle$. Fast cavity decay then ensures the trapping of the population in $\left|\psi^{+}00\right\rangle$. (b) Unlike in the stabilization of $\left|\varphi^{+}\right\rangle$, this stabilization scheme creates a "metastable state" of $|ee00\rangle$ from the off-resonant blue-sideband coupling between the $\left|\psi^{+}00\right\rangle$ and $|ee01\rangle$ or $|ee10\rangle$, leading to a lower stabilization fidelity for $\left|\psi^{+}00\right\rangle$. This infidelity can be suppressed by increasing the energy gap of 2Ω.

assuming $g_1 \approx g_2, \kappa_1 \approx \kappa_2, \gamma_1 \approx \gamma_2$. It is worth noting that the specific choice of the red-sideband coupling between the qubit and the cavity can also be replaced by blue-sideband coupling as well.

Similarly, under the trichromatic flux drive of

$$f\left(t\right) = \epsilon_0 \sin\left|\omega_{q1} - \omega_{q2}\right| t + \epsilon_1 \sin\left(\omega_{q1} + \omega_{c1} + \Omega\right) t + \epsilon_2 \sin\left(\omega_{q2} + \omega_{c2} + \Omega\right) t, \tag{4.73}$$

another rotating frame Hamiltonian could be generated as follows,

$$\hat{\mathcal{H}}/\hbar = \Omega\left(e^{i\theta}\hat{\sigma}_1^{-}\hat{\sigma}_2^{+} + e^{-i\theta}\hat{\sigma}_1^{+}\hat{\sigma}_2^{-}\right) + \sum_{i=1}^{2}\left[g_i\left(\hat{a}_i^{\dagger}\hat{\sigma}_i^{+} + \hat{a}_i\hat{\sigma}_i^{-}\right) - \Omega\hat{a}_i^{\dagger}\hat{a}_i\right], \tag{4.74}$$

which is capable of stabilizing an arbitrary odd-parity Bell state of $\left|\psi\left(\theta\right)\right\rangle = \left(|ge\rangle + e^{i\theta}\left|eg\right\rangle\right)/\sqrt{2}$, with the same requirement of the energy scale. As depicted in Fig. 4.14b, this scheme also creates

a metastable state of $|ee00\rangle$. Again we can find out the effective decay rates from $\left|\psi^{+}00\right\rangle$ to $|gg00\rangle$ and $|ee00\rangle$,

$$\Gamma^{\mathrm{gg}}_{+\downarrow} = \frac{\gamma_1+\gamma_2}{2}, \quad \Gamma^{\mathrm{ee}}_{+\downarrow} = \frac{2g_1^2\kappa_1}{16\Omega^2+\kappa_1^2} + \frac{2g_2^2\kappa_2}{16\Omega^2+\kappa_2^2}, \tag{4.75}$$

and the excitation rates as well,

$$\Gamma^{\mathrm{gg}}_{-\uparrow} = \frac{2g_1^2}{\kappa_1} + \frac{2g_2^2}{\kappa_2}, \quad \Gamma^{\mathrm{ee}}_{-\uparrow} = \frac{\gamma_1+\gamma_2}{2}. \tag{4.76}$$

Likewise, we can write out the relaxation rates between $|gg\rangle$, $|ee\rangle$ and $\left|\psi^{-}\right\rangle$,

$$\Gamma^{\mathrm{gg}}_{-\downarrow} = \frac{\gamma_1+\gamma_2}{2}, \quad \Gamma^{\mathrm{ee}}_{-\downarrow} = \frac{2g_1^2}{\kappa_1} + \frac{2g_2^2}{\kappa_2}, \tag{4.77}$$

$$\Gamma^{\mathrm{gg}}_{-\uparrow} = 0, \quad \Gamma^{\mathrm{ee}}_{-\uparrow} = \frac{\gamma_1+\gamma_2}{2}. \tag{4.78}$$

From Eq. 4.75 to Eq. 4.78 we may obtain the fidelity of $\left|\psi^{+}00\right\rangle$, to the leading order of $s=\kappa\gamma/g^2$ and $t=\kappa/\Omega$, as

$$P_{\psi^+} = 1 - \frac{s}{4} + \left(\frac{1}{8} - \frac{1}{4s}\right)t^2 + O\left[s^2\right] + O\left[t^4\right] + O\left[\left(\frac{t^2}{s}\right)^2\right], \tag{4.79}$$

where we immediately find an extra constraint on the energy scale,

$$\Omega \gg \sqrt{\frac{\kappa}{\gamma}}g, \tag{4.80}$$

which agrees with the intuitive observation that the energy gap needs to be far larger than the blue-sideband interaction strength in order to suppress the population leakage to $|ee\rangle$. This leakage can be also remedied by by introducing a qubit-qubit dispersive shift term, $\chi\,|ee\rangle\,\langle ee|$ that detunes $|ee\rangle$ without affecting other levels. When χ is small, to the lowest order in s, t and $r=\chi/\kappa$ we have

$$P_{\psi^+} = 1 - \frac{s}{4} + \left(\frac{1}{8} - \frac{1}{4s}\right)t^2 + \left(\frac{1}{4s} - \frac{1}{8}\right)t^3 r, \tag{4.81}$$

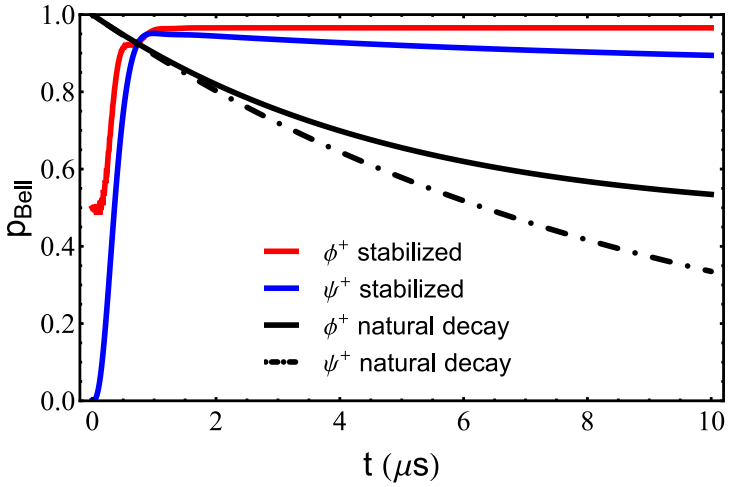

Figure 4.15: Master equation simulation of the Bell state stabilization fidelity. In the simulation, we set the qubit lifetime to be $10\,\mu$s, while the cavity is $0.1\,\mu$s. With fixed $\Omega = 2\pi \times 20\,$MHz, we sweep qubit-cavity coupling strength g for fidelity optimization. For odd-parity Bell state stabilization, optimal g happens at $2\pi \times 0.6\,$MHz, with stabilization fidelity ≈ 0.9. The gradual descending of the $|\psi^+\rangle$ fidelity indicates the population trapping in the $|ee00\rangle$ level. For even-parity Bell states, a maximum stabilization fidelity of 0.97 is reached at $g = 2\pi \times 1.3\,$MHz. The black curves are the natural decay of the Bell states for reference.

which reduces back to Eq. 4.79 as $\chi \to 0$. Eq. 4.81 shows that the fidelity improves when χ goes negative, which is a natural result of the increased gap between $|\psi^+\rangle$ and $|ee\rangle$. When χ becomes much larger, $\chi \gg \Omega$, we can similarly obtain the stabilization fidelity to be

$$P_{\psi^+} = 1 - \frac{s}{4} + \left(\frac{3}{8} - \frac{1}{s}\right) r^{-2} - \frac{4}{st} r^{-3}, \tag{4.82}$$

and when $\chi \to \infty$, the fidelity asymptotes to $1 - s/4$.

We can further calculate the stabilization fidelity for the two cases from the master equation simulation, shown in Fig. 4.15. We choose the ground state to be the initial state and plot the fidelity of the $|\phi^+\rangle$ and $|\psi^+\rangle$ as a function of time. The lifetime of the stabilized Bell state is shown to be substantially prolonged, comparing to the bare T_1 of the Bell state with no parametric modulation.

Finally, when the modes in the tunable coupling circuits are made inherently fixed-frequency (i.e. single-junction transmon and linear resonator), their dephasing noises mostly (neglecting ther-

mal noise) originate from the frequency fluctuation of the coupler mode, and therefore are strongly correlated to each other. This cross-correlation has some interesting effects on the dephasing of the Bell states. According to the quantum noise theory [99], under zero correlation, the decoherence rate from pure qubit dephasing of any Bell state is $\left(\gamma_{\phi,1}+\gamma_{\phi,2}\right)/2$, where $\gamma_{\phi,i}$ is the i-th qubit dephasing rate. With maximum correlation (identical dephasing noise), the decoherence rate of $|\psi\rangle$ drops to $\left(\sqrt{\gamma_{\phi,1}}-\sqrt{\gamma_{\phi,2}}\right)^2/2$, while that of $|\varphi\rangle$ rises to $\left(\sqrt{\gamma_{\phi,1}}+\sqrt{\gamma_{\phi,2}}\right)^2/2$, which suggests that $|\psi\rangle$ could be the preferable entanglement resource for quantum computation with the tunable coupling circuit.

CHAPTER 5

TOWARDS AUTONOMOUS QUANTUM ERROR CORRECTION

In this chapter, we take another step forward and put parametric flux modulation to even greater use. While we had a lot of fun playing with qubit stabilization in previous chapters, we have yet to see any particularly useful applications except for perhaps sideband cooling. Here, with the concrete example of the Very Small Logial Qubit (VSLQ) superconducting device, we will demonstrate stabilization and other driven dissipation processes as a valuable resource for quantum computation.

Quantum error correction (QEC) is vital for the ultimate goal of quantum computing - constructing a useful quantum computer. Traditionally, quantum error correction scheme [195, 196, 197, 198] are based on feedback processes, which places formidable overhead requirements on both quantum circuitry and classical control hardware. An alternative approach is the autonomous quantum error correction [199, 189, 186, 187, 200, 201, 202, 203, 204], which can be loosely thought of as the stabilization of any unknown logical state. Stabilization of any particular state requires to know the state beforehand which is clearly not QEC, but if we can somehow stabilize a manifold of logical bases, in a coherent way without destroying the embedded quantum information, then we can stabilize any unknown superposition of the logical bases, which is equivalent to AQEC. Thanks to its passive nature, AQEC protocol neither requires feedback control that poses stringent experimental requirements, nor is it limited by the cycle time that tends to be long enough to become the bottleneck for higher QEC fidelities. Even more remarkable is the VSLQ circuit [187, 203], which, albeit its simple physical form consisting only two transmon qubits coupled by dc-SQuID, and two lossy resonators, is capable of protecting against all realistic single-qubit quantum error channels with orders of magnitude improvement. In this chapter we will first introduce the theory of VSLQ, then present our experimental effort towards its realization in circuit-QED.

5.1 Theory of the Very Small Logical Qubit

This section is structured as follows: We first introduce the VSLQ as a digital error correction code, and define its logical states and error correction operators. We then construct a driven dissipation protocol with a rotating frame Hamiltonian that governs the interaction between the logical qubit and the bath modes. Finally, we verify its capability of correcting photon losses and suppressing phase noise errors from rigorous numerical simulations.

5.1.1 Codewords of VSLQ

Most quantum error correction codes rely on a repetitive codeword, where the logical bases inherently possess some degree of redundancy to protect against certain types of errors, in a way that quantum information is not deterministically lost, but can be recovered after error events. The two logical bases of the VSLQ are product states of the 0- and 2-photon superposition of two qutrits, with different phases,

$$|0\rangle_L = \frac{|0\rangle_1 + |2\rangle_1}{\sqrt{2}} \otimes \frac{|0\rangle_2 + |2\rangle_2}{\sqrt{2}}, \quad |1\rangle_L = \frac{|0\rangle_1 - |2\rangle_1}{\sqrt{2}} \otimes \frac{|0\rangle_2 - |2\rangle_2}{\sqrt{2}}. \tag{5.1}$$

It can be interpreted as a two-qutrit binomial codeword [149] with a mean photon number of 2, with invariant superposition weights under single-photon loss error on either side,

$$\begin{aligned} \hat{a}_1 \left(\alpha |0\rangle_L + \beta |1\rangle_L\right) &= \alpha |1\rangle_1 \otimes \widetilde{|+\rangle}_2 - \beta |1\rangle_1 \otimes \widetilde{|-\rangle}_2, \\ \hat{a}_2 \left(\alpha |0\rangle_L + \beta |1\rangle_L\right) &= \alpha \widetilde{|+\rangle}_1 \otimes |1\rangle_2 - \beta \widetilde{|-\rangle}_1 \otimes |1\rangle_2 , \end{aligned} \tag{5.2}$$

where $|\alpha|^2 + |\beta|^2 = 1$, and $\widetilde{|\pm\rangle}$ stand for the 0- and 2-photon equal superposition state with opposite phases. In principle, with the VSLQ codeword, we can already perform quantum error correction against single-photon loss in the measurement-based fashion. We simply need to simultaneously monitor the single-photon state population on both sides, which heralds the error events while being quantum non-demolition to the logical state (of course, we need to make very sure that the

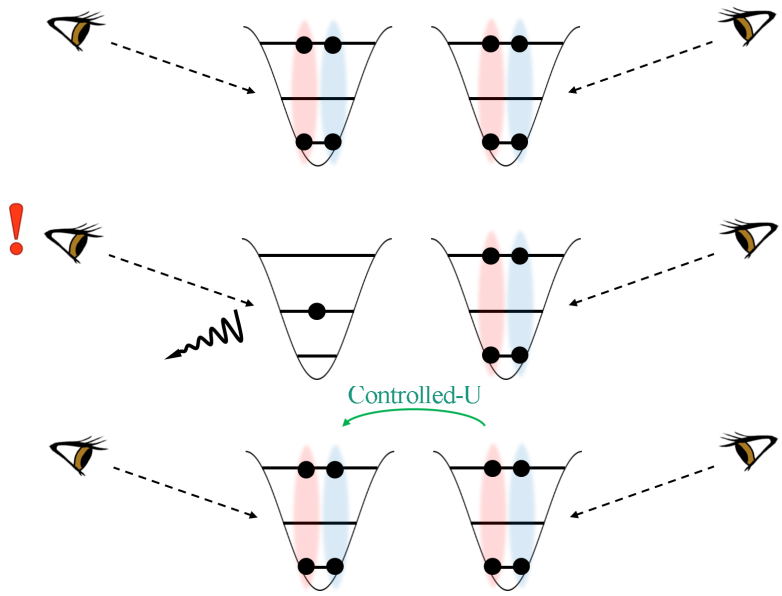

Figure 5.1: A measurement-based QEC protocol using the VSLQ codeword. The single-photon population is being monitored for both qutrits in real time, which should be zero under arbitrary logical states. Thus the detection of the population heralds the single-photon loss error event, which can be corrected by applying a controlled gate on the error bit with the other transmon being the control bit.

detector does not distinguish between the $|0\rangle$ and $|2\rangle$ states). Shown in Fig. 5.1, when a photon is lost from either the left or the right qutrit, population in the single-photon level will be detected on the same side, followed by unitary operations conditioned on the other qutrit state, which map the error state back to its parent logical state. These unitary operators must satisfy

$$\begin{aligned} U_{2\to 1}\left(|1\rangle_1 \otimes \widetilde{|\pm\rangle}_2\right) &= \pm\left(\widetilde{|\pm\rangle}_2 \otimes \widetilde{|\pm\rangle}_2\right), \\ U_{1\to 2}\left(\widetilde{|\pm\rangle}_2 \otimes |1\rangle\right)_1 &= \pm\left(\widetilde{|\pm\rangle}_2 \otimes \widetilde{|\pm\rangle}_2\right). \end{aligned} \tag{5.3}$$

Like bosonic codes, the VSLQ codeword does not protect against two-photon lost, either happening together on the same qutrit or separately on both. Luckily, two-photon loss is typically rare to happen and can thus be safely ignored.

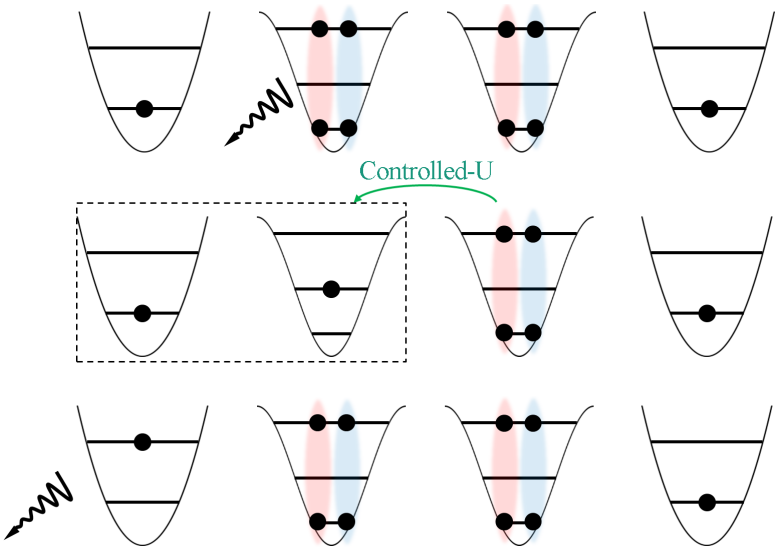

Figure 5.2: An ancilla-assisted autonomous VSLQ scheme. In principle, we can always find a unitary operation that does not affect the logical state, but can map the single-photon-loss error state back to its parent logical state while adding a photon to the ancillary mode. This photon is then quickly lost through the fast dissipation of the ancilla. Autonomous error correction is simply achieved by applying the unitary operation over and over again.

5.1.2 From measurement-based protocol to autonomous implementation

While the measurement-based VSLQ can be used for error correction, it suffers from the overhead requirements that most measurement-based QEC protocols do, such as high fidelity QND measurement, real-time data acquisition and fast feedback control. Recall that in a prototypical 3 qubit bit-flip error correction, ancillary qubits are employed to store the error syndrome, followed by stabilizer measurement that instructs the subsequent error correction operation. While the stabilizer measurement and error correction operation can be formally combined into a controlled gate conditioned on the ancillary state, it should not be thought of as autonomous error correction, as there is no way of dumping the entropy from such a closed system. Indeed, the no-deleting theorem [205] states that there is no way to delete an unknown state, making the error correction impossible to last for more than one cycle as long as the uncertainty still lives within the ancillary space - unless its state can be reset, say, from dissipation to environment. This “upside of noise” [200] enables error correction to be passively accomplished.

VSLQ error correction can also be autonomously implemented by coupling the qutrits to one or more ancillae. There, the entropy of error is removed not by measurements, but by the dissipative ancillae. The ancillae remain in their ground state through dissipation, and do not disturb the logical qubit state until photon loss happens. Then, the interaction between the ancillae and the qutrit must map the error state back to its parent logical state, at the cost of exciting the ancillary states. Finally, dissipation resets the ancillae back to the ground state, ready for the next round of error correction.

Making the most intuitive choice of coupling the two qutrits each to a low-Q cavity mode, it is not hard to formulate a unitary transformation that carries out the error correction effect (see Fig. 5.2), following the recipe in subsection 5.2.6. Such a unitary transformation can then be decomposed into quantum gate sequence and implemented in a digital manner. However, the gate time may outgrow the time scale of the error, rendering this digital error correction scheme ineffective. Naturally one may wonder, following the digital-analog quantum computing correspondence, if this unitary transformation can be instead enforced in an analog way, by a Hamiltonian whose energy scale far exceeds the spectral density of the error. Remarkably, such a Hamiltonian does exist for the VSLQ qutrit-ancilla model, which reads

$$\hat{\mathcal{H}}/\hbar = W\hat{X}_1\hat{X}_2 + \sum_{i=1}^{2}\frac{\delta_i}{2}\hat{P}_i^1 + \sum_{i=1}^{2}\Omega_i\left(\hat{a}_{qi}^\dagger\hat{a}_{ri}^\dagger + \hat{a}_{qi}\hat{a}_{ri}\right) + \sum_{i=1}^{2}\left(W+\frac{\delta}{2}\right)\hat{a}_{ri}^\dagger\hat{a}_{ri}, \tag{5.4}$$

where $\hat{X}$ is the Pauli-x operator defined in the 0- and 2-photon subspace, $\hat{P}^1$ is the projection operator to the single-photon subspace, $\hat{a}_q$ and $\hat{a}_r$ are the annihilation operator for the qutrit and the lossy cavity. In this Hamiltonian, the first term contains the two-photon-swapping and four-photon-pumping interactions between the qutrits, the second term modifies the energy of the qutrits' single-photon subspace, the third term represents the blue-sideband interactions between the qutrits and their ancillae, while the last term describes the ancillary energy.

More insights can be gained by looking at the rotating frame levels of the VSLQ Hamiltonian in Fig. 5.3. For simplicity here we only consider the photon loss and recovery processes in qutrit

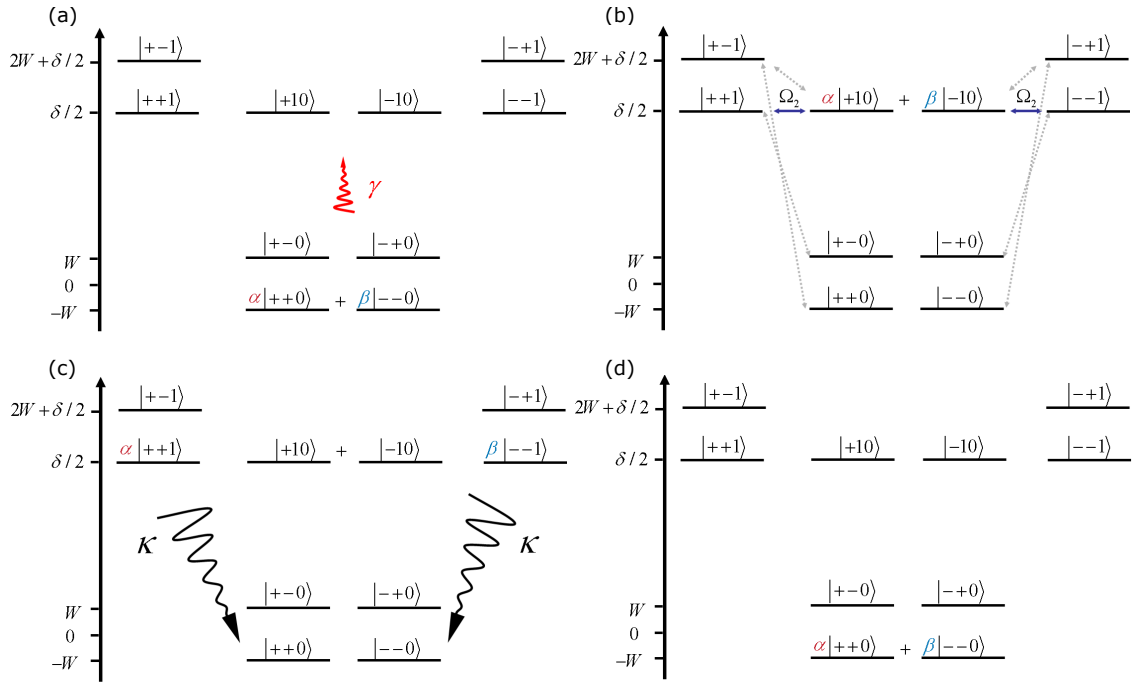

Figure 5.3: The error correction cycle of the VSLQ in the rotating frame. For simplicity we only show the photon loss and correction for the second qutrit. (a) Initial logical state jumps to the error state manifold at photon loss rate γ. (b) The blue-sideband interaction couples each basis of the error state to the logical basis in the excited-ancilla subspace. The pale dashed arrows represent error passages where phase-flips happen to the logical superposition. (c) and (d) The fast dissipation of the ancillary states brings the system back to the initial logical state.

2. Similar to Rabi term that defines the principal axis in the universal stabilization scheme, the XX and the P term of the VSLQ Hamiltonian are playing the role of a stabilizer that defines the logical and error basis as two separated manifolds of degenerate eigenstates. The blue-sideband terms couple the error state manifold to the logical state subspace with a single photon in the ancilla, which are further brought into resonance by the ancillary energy term. For arbitrary superposition of logical bases, when a single photon is lost, the system will be placed in the same superposition of the error basis. Then, due to the resonant blue-sideband interaction, the error state will be mapped back to the logical state subspace at the cost of adding one photon to the ancilla. Finally, the fast decay of the ancilla brings the state back to its initial logical state, completing the error correction. Throughout the whole process, the state remains in a coherent superposition with the same amplitude.

The blue-sideband interaction inevitably creates systematic error channels by linking logical bases with different parities to each other, showing in Fig. 5.3b by the dashed arrows. To avoid infidelity due to these harmful transitions, along with the stabilization requirement, the following hierarchy of energy scale must be met,

$$\delta_i - W, W \gg \Omega_i \sim \kappa_i \gg \gamma_i. \tag{5.5}$$

5.1.3 Suppression of 1/f dephasing noise

Aside from the photon loss error, dephasing noise acting on the physical qutrits also creates an error channel where $|\pm\pm\rangle$ relaxes to $|\pm\mp\rangle$ and vice versa. While such dephasing noise is not actively corrected by the VSLQ design (though in principle it could be corrected in a larger three-qubit ring implementation [189]), it is energetically suppressed by the gap of $2W$ between the two manifold of degenerate logical bases of even and odd parities. Upon further examination of this relaxation process using quantum noise theory, one finds that it is only sensitive to dephase noise near the transition frequency $2W$,

$$\Gamma^i_{\text{rel}} = 2S^{(i)}_{zz}\left[2W\right], \tag{5.6}$$

where $\Gamma^{1,2}_{\text{rel}}$ are the relaxation rates between $|\pm\pm\rangle$ and $|\mp\pm\rangle$, and between $|\pm\pm\rangle$ and $|\pm\mp\rangle$. If the qutrit dephasing noise has a low-frequency dominated power spectrum like 1/f spectrum, the relaxation effect will be dramatically weakened when $1/W$ is far smaller than the noise correlation time, just in the same way as we have demonstrated in subsection 3.4.4. This additional benefit of phase noise suppression is intrinsic to this "analog" VSLQ scheme with continuously applied Hamiltonian.

It is also interesting to note that *single* qutrit dephasing noise alone does not dephase VSLQ logical states in same-parity manifolds, i.e. photon number measurement does not distinguish between the basis,

$$\langle +\pm|\,\hat{n}_{qi}\,|+\pm\rangle = \langle -\mp|\,\hat{n}_{qi}\,|-\mp\rangle\,,\ \langle +\pm|\,\hat{n}_{qi}\,|-\mp\rangle = 0, \tag{5.7}$$

where $\hat{n}_{qi} = \hat{a}_{qi}^{\dagger}\hat{a}_{qi}$. However, things can become a little different under two-qutrit dephasing noise of the form $\hat{n}_{q1}\hat{n}_{q2}$. While such two-qutrit dephasing noise does not contribute to the pure dephasing rate between any VSLQ levels, it does lead to relaxation between logical bases with the same parity (flipping both phases at the same time). Unfortunately the W term has no suppression to this relaxation rate, as there is no energy gap between the two bases involved. However, a remedy can be found by introducing extra terms into the VSLQ Hamiltonian [187].

5.1.4 Can the VSLQ be any smaller?

A natural question arises from the name of VSLQ, that if it could be made any smaller without compromising its error correction performance. The answer is unclear, but at least it will be very difficult. One may be tempted to further reduce the number of transmons, by encoding quantum information in the superposition of higher levels of an artificial atom, much like the bosonic codes do. However, one does so at ones own peril which can be seen from the following example. The logical qubit states in this case are made of the first four levels of a transmon,

$$\begin{aligned} |L_0\rangle &= \frac{|0\rangle + |4\rangle}{\sqrt{2}} \otimes |0\rangle\,, \\ |L_1\rangle &= |2\rangle \otimes |0\rangle\,. \end{aligned} \tag{5.8}$$

Mimicking the VSLQ Hamiltonian, we may even formally write out the "Smallest Logical Qubit" Hamiltonian, as

$$H = -W\hat{X}_{04} - W\sigma_{22} + \Omega\left[(\sigma_{21} + \sigma_{43})\, a_r^{\dagger} + H.c.\right] + W a_r^{\dagger} a_r, \tag{5.9}$$

where $\sigma_{ij} = |i\rangle\langle j|$, $\hat{X}_{ij} = \sigma_{ij} + \sigma_{ji}$ are defined in the transmon space while $a_r^{\dagger}$ is the cavity ladder operator. Enforcing the energy scale hierarchy of $W \gg \Omega \approx \kappa \gg \gamma$, where γ and κ are the lifetimes of the qubit and the cavity, we may arrive at the rotating frame energy level diagram in Fig. 5.4 that clearly shows the "error correction" process. At first glance this protocal looks

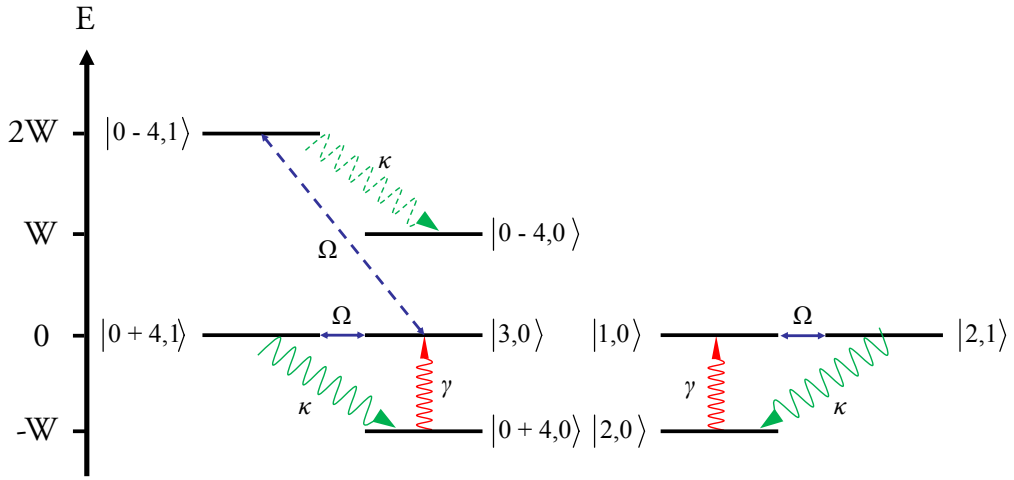

Figure 5.4: Rotating frame energy level diagram for the error correction protocol encoding the bosonic code with the lowest four levels of an atom. We plot the Floquet levels of the Hamiltonian in Eq. 5.9 (the splitting by the Ω term not displayed here). The red and blue waved-arrows stand for the photon loss processes in the qubit and the cavity space, while the double-headed arrows represent couplings from the Ω term. Single-photon loss error brings the state from the logical space $\{|0+4,0\rangle, |2,0\rangle\}$ to the error space $\{|3,0\rangle, |1,0\rangle\}$, which then coherently transits to $\{|0+4,1\rangle, |2,1\rangle\}$, accompanied by rapid cavity photon loss that sends the state back to $\{|0+4,0\rangle, |2,0\rangle\}$, completing the error correction cycle. The dashed arrows represent the leakage path from $|L_0\rangle$ to the error state $|0-4,0\rangle$. However, this process is suppressed by the energy gap of $2W$ at a rate of $\Gamma_E = 4\Omega^2/(16W^2+\kappa^2)$, which is much slower comparing to the refilling rate of $\Gamma_R = 4\Omega^2/\kappa^2$. The hierarchy of energy scales can also be intuitively inferred from this diagram, which imposes the requirement of $W \gg \kappa \approx \Omega \gg \gamma$.

very promising: suppose an arbitrary initial state of $|\psi\rangle = (\alpha|L_0\rangle + \beta|L_1\rangle)\otimes|0\rangle$ suffers a single-photon loss that turns the state into

$$a|\psi\rangle = (\alpha|3\rangle + \beta|1\rangle)\otimes|0\rangle\,. \tag{5.10}$$

In the rotating frame Hamiltonian, states $|3\rangle|0\rangle$ and $|L_0\rangle|1\rangle$ are degenerate and coupled through the Ω term. $|3\rangle|0\rangle$ can further decay into $|2\rangle|0\rangle$, yet $|L_0\rangle|1\rangle$ decays to $|L_0\rangle|0\rangle$ at a much faster rate and results in its correction back to $|L_0\rangle$. Likewise, the error state $|1\rangle|0\rangle$ is corrected back to $|L_1\rangle$ via the process $|1\rangle|0\rangle \to |2\rangle|1\rangle \to |2\rangle|0\rangle$. The same correction rate of $4\Omega^2/\kappa$ for these two processes guarantees that the corrected state remains in the same superposition as the initial state $|\psi\rangle = (\alpha|L_0\rangle + \beta|L_1\rangle)\otimes|0\rangle$.

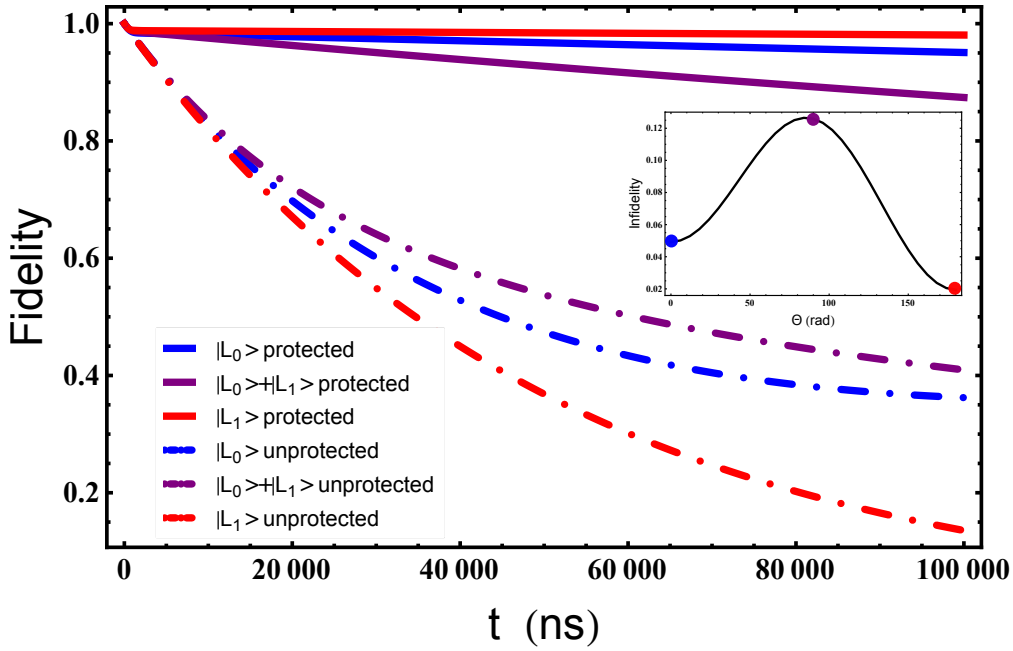

Figure 5.5: Strong enhancement of the effective logical state lifetimes against photon losses through engineered dissipation. We calculate the state fidelity as a function of time from master equation simulations, with the initial state being $|L_0\rangle$ (Blue), $|L_1\rangle$ (red) and $(|L_0\rangle + |L_1\rangle)/\sqrt{2}$ (purple). In comparison, the dash-dotted curves are unprotected fidelities of corresponding initial states. The inset shows the infidelity at $t = 100\mu$s as a function of the mixing angle θ of the logical state superposition, with colored dots representing the three initial states in the main graph. The infidelity is higher for the superposition state because it is susceptible to dephasing loss, which arises from the decay and refilling process between the logical states and the error states.

However this scheme has one fatal drawback: for transmon qubits, the unequal energy difference between $|2\rangle$ and $|1\rangle$, and $|4\rangle$ and $|3\rangle$ dephases the error state of $\alpha\,|3\rangle + \beta\,|1\rangle$ in Eq. 5.10. A more intuitive way to look at this dephasing is that the photons emitted from the $|2\rangle \rightarrow |1\rangle$ decay and $|4\rangle \rightarrow |3\rangle$ decay are at different frequencies, allowing for the distinction of the final states and thus dephasing their superposition. From the quantum trajectory point of view, the decay process is equivalent to applying the jump operator with some probability at all time points for a single trajectory, and then averaging up all trajectories. Because the jump operator is randomly applied at different time points between different trajectory, and the phase advance of the initial superposition is different from the final state, averaging over trajectories will destroy the phase information of the final superposition, in a similar way to the regular dephasing of a qubit. We want to point out that

in above, the error correction effect of the Hamiltonian in Eq. 5.9 is completely valid as proved by the master equation simulation result in Fig. 5.5. It is the nonlinearity of the physical system that will prevent such an ideal rotating frame Hamiltonian to take place. This is an important reason why bosonic codes are designed for linear cavity modes, where the emitted photons are identical and do not destroy the phase information of logical states.

5.2 Experimental Realization of the VSLQ

As discussed in the above sections, the most remarkable feature of the VSLQ is that it can be realized in a fully autonomous way with the ability to correct errors in continuous time. Comparing with measurement-based QEC protocols, it neither needs fast feed-back control that poses stringent experimental requirements, nor is it limited by the cycle time that tends to be long enough to become the bottleneck for higher QEC fidelities. These nice features of the VSLQ critically rely on the VSLQ Hamiltonian in Eq. 5.4. However, realizing the VSLQ Hamiltonian is no simple task, because it requires the generation of multi-photon interactions terms, such as the 2-photon-swapping and 4-photon-pumping terms between the logical qubits, as well as the 2-photon-pumping term (the blue-sideband interaction), between the logical qubit and the ancillary qubit. Moreover, the VSLQ scheme requires rather strong interaction strengths for these terms, which are difficult to realize through charge drive schemes, such as 4-wave mixing, without inducing other undesired interactions.

Motivated by this, we have invented a novel flux-tunable circuit that nicely accommodates the VSLQ Hamiltonian, through parametric flux modulation. In this section, we will demonstrate the working mechanism of the VSLQ circuit along with its experimental characterization, and the preliminary realization of the VSLQ Hamiltonian.

5.2.1 VSLQ circuit device

The circuit device of the VSLQ is shown in Fig. 5.6. The primary qutrits, which are colored in red, are made of two transmons with bridged grounds, coupled by a flux-driven SQuID colored purple. Aside from the relative placement of the capacitances and values of the junctions, this architecture is identical to a four-junction flux qubit [206], which has been shown to possess coherence times similar to those of the best planar transmon qubits [207]. The dc-SQuID loop and the big flux loop beneath are controlled by the two fluxes Φ_2 and Φ_1, which results in a nonlinear interaction between the transmon modes,

$$\hat{\mathcal{H}}_{\text{int}} = -E_{Jc}\cos\left(\hat{\delta\theta} + \theta_1\right) - E_{Jc}\cos\left(\hat{\delta\theta} + \theta_1 + \theta_2\right) = -2E_{Jc}\cos\frac{\theta_2}{2}\cos\left(\hat{\delta\theta} + \theta_1 + \frac{\theta_2}{2}\right), \tag{5.11}$$

where $\hat{\delta\theta} = \hat{\theta}_{q1} - \hat{\theta}_{q2}$ is the phase difference between the transmons, and $\theta_i = \Phi_i/\Phi_0$ is the external phase. At $\theta_2 = 2n\pi \pm \pi$, it is easy to see that the transmons are decoupled from each other, corresponding to a SQuID inductance of infinity.

We may further trig-expand Eq. 5.11 and find out how it perturbs the transmon energies. Under dc-flux tuning, we can always gauge away the phase offsets of the phase variables like we did in subsection 1.2.3, equivalent to recentering the 2D potential to its local minimums. To this end, we group the Josephson energy of the two transmons with Eq. 5.11 to obtain the 2D potential energy as

$$U_q = -E_{J1}\cos\left(\hat{\theta}_1 + \bar{\hat{\theta}}_1\right) - E_{J2}\cos\left(\hat{\theta}_2 + \bar{\hat{\theta}}_2\right) - 2E_{Jc}\cos\frac{\theta_2}{2}\cos\left(\hat{\delta\theta} + \bar{\hat{\delta\theta}} + \theta_1 + \frac{\theta_2}{2}\right), \tag{5.12}$$

where $\bar{\hat{\theta}}_{1,2}$ and $\bar{\hat{\delta\theta}} = \bar{\hat{\theta}}_1 - \bar{\hat{\theta}}_2$ are classical equilibriums that can be found by solving

$$\left.\frac{\partial\widetilde{U}_q}{\partial\hat{\theta}_{1,2}}\right|_{\hat{\theta}_1=\bar{\hat{\theta}}_1,\hat{\theta}_2=\bar{\hat{\theta}}_2} = 0, \tag{5.13}$$

with $\widetilde{U}_q$ being the uncentered 2D potential. Trig-expanding Eq. 5.12 and keeping the leading order

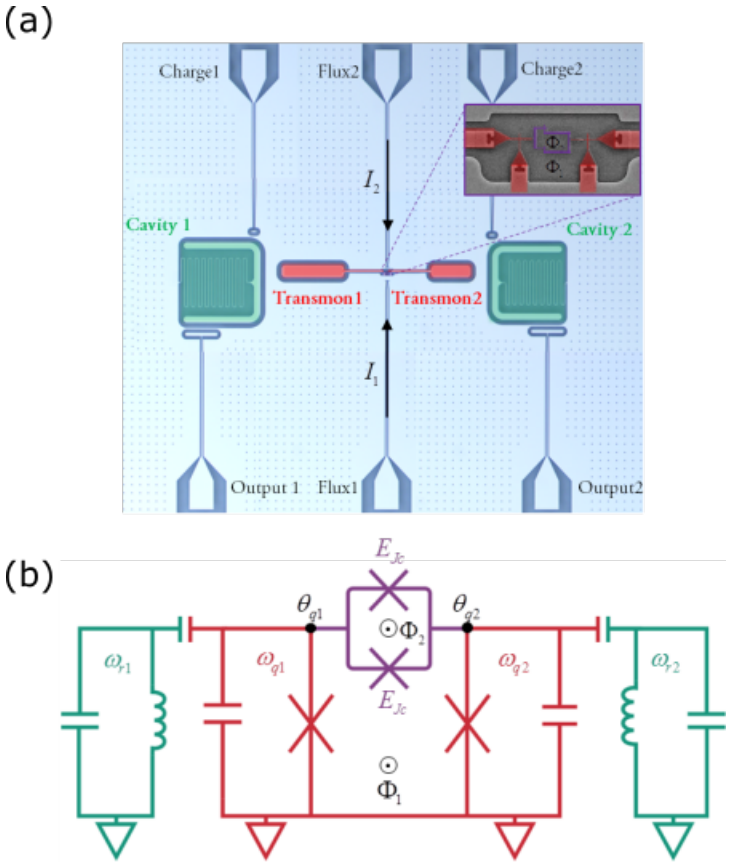

Figure 5.6: (a) False-colored circuit micrograph and (b) circuit diagram showing the VSLQ circuit components. The two transmons are plotted in red and will be used as logical qubits. In green are the two lumped-element resonators designed to be low-Q as the ancillary qubits, which are capacitively coupled to the transmons with fixed coupling strengths. At the heart of the device lies the dc-SQuID in purple, which, along with the transmon junctions, forms two superconducting loops controlled by tunable fluxes Φ_1 and Φ_2, giving rise to the tunable nonlinear coupling term in Eq. 5.11, which is crucial for the generation of the VSLQ Hamiltonian.

terms, we obtain

$$U_q \approx -E_{J1}^{\text{eff}} \cos\hat{\theta}_1 - E_{J2}^{\text{eff}} \cos\hat{\theta}_2 + E_{g1}\hat{\theta}_1\hat{\theta}_2 + E_{g2}\hat{\theta}_1\hat{\theta}_2^2 + E_{g3}\hat{\theta}_1^2\hat{\theta}_2 + E_{g4}\hat{\theta}_1^2\hat{\theta}_2^2. \tag{5.14}$$

with all the coefficients being 2D functions of the fluxes. We see that the primary circuit is essentially two flux-tunable transmons coupled through flux-tunable nonlinear interactions, promising the generations of multi-photon parametric interactions through flux modulation.

In practice, Eq. 5.13 and 5.14 can be numerically calculated, then the whole VSLQ circuit

Circuit parameters (GHz)	1st	2nd
Transmon Josephson energy	10.7	13.4
SQuID Josephson energy	7.9	7.7
Transmon charging energy	0.17	0.21
SQuID charging energy	0.009	
Resonator frequency	6.9	8
Transmon-resonator coupling	0.048	0.055

Table 5.1: Circuit parameters of the VSLQ device.

can be canonically quantized in the same way as in section 2.1. This of course assumes that the coupling terms in Eq. 5.14 can be treated as perturbations, otherwise the calculation of the full 2D wavefunction is required.

In the actual circuit design, the capacitances and junction energies are chosen such that the energies of the two transmons are $\sim$1 GHz apart (when decoupled), to minimize any stray interactions between them. We also work in the deep transmon limit with $E_J/E_C \simeq 65$.

To enable passive quantum error correction, the transmons are each coupled to a low-Q resonator, with fixed capacitive coupling strength. These resonators are made lossy by overcoupling to the readout lines, enabling them to be used as dissipative ancillae as well as fast readout cavities. The circuit parameters of the VSLQ circuit can be found in Table. 5.1

5.2.2 Parametric modulation of the VSLQ circuit

To operate the VSLQ, we need to apply rf flux tones through the coupler elements. Operating the fluxes at the "VSLQ operating point"

$$\{\theta_1(t), \theta_2(t)\} = \left\{0.25 - \frac{\epsilon_d}{2}\sin\omega_d t, -0.5 + \epsilon\sin\omega_d t\right\}, \tag{5.15}$$

the interaction in Eq. 5.11 is reduced to a much simpler form as a cosine function of the transmon phase difference, with a linearly modulated amplitude:

$$\hat{\mathcal{H}}_{\text{int}} = -2\epsilon_d E_{Jc}\sin\omega_d t\cos\hat{\delta\theta}. \tag{5.16}$$

To understand how this term can provide all the necessary parametric interactions for the VSLQ Hamiltonian in Eq. 5.4, we first go to the dressed basis where the transmon and the cavity modes are decoupled. Under the leading order S-W transformation, and in the rotating frame where the dressed transmon $|f\rangle$ levels and cavity single-photon states are isoenergetic, the interaction term becomes[1]

$$\hat{\mathcal{H}}_{\text{int}} = -2\epsilon_d E_{Jc} \sin\omega_d t \cos\left[\sqrt[4]{\frac{2E_c}{E_J}}\left(\hat{a}_{q1}^\dagger e^{i\omega_{q1}t} - \hat{a}_{q2}^\dagger e^{i\omega_{q2}t} + \frac{g_1}{\Delta_1}\hat{a}_{r1}^\dagger e^{i\omega_{r1}t} - \frac{g_2}{\Delta_2}\hat{a}_{r2}^\dagger e^{i\omega_{r2}t} + h.c.\right)\right]. \tag{5.17}$$

From the interference between the rotating terms and the sine modulation term, different parametric interactions can be created. For example, the so-called 3-wave mixing processes can be obtained from the quadratic component of the cosine interaction, when the modulation frequency is at the detuning or the sum between any two of the four modes. At the sum frequency of the transmon and the resonator $\omega_d = \omega_{qi} + \omega_{ri}$, the blue-sideband interaction is created,

$$\hat{\mathcal{H}}_{\text{int}} = \frac{\epsilon_d E_{Jc} g_i}{\Delta_i}\sqrt{\frac{2E_c}{E_J}}\left(\hat{a}_{qi}^\dagger \hat{a}_{ri}^\dagger + \hat{a}_{qi}\hat{a}_{ri}\right). \tag{5.18}$$

Similarly, from the quartic term we can achieve 5-wave mixing, useful for the generation of the VSLQ Hamiltonian. It is easy to check that when the modulating is at twice the transmon detuning frequency $\omega_d = 2\left(\omega_{q1} - \omega_{q2}\right)$, we will obtain the 2-photon-swapping interaction,

$$\hat{\mathcal{H}}_{\text{int}} = -\frac{\epsilon_d E_c E_{Jc}}{2E_J}\left(\hat{a}_{q1}^{\dagger 2}\hat{a}_{q2}^2 + \hat{a}_{q1}^2\hat{a}_{q2}^{\dagger 2}\right), \tag{5.19}$$

while modulating at twice the sum frequency $\omega_d = 2\left(\omega_{q1} + \omega_{q2}\right)$ gives rise to the 4-photon-pumping term,

$$\hat{\mathcal{H}}_{\text{int}} = -\frac{\epsilon_d E_c E_{Jc}}{2E_J}\left(\hat{a}_{q1}^{\dagger 2}\hat{a}_{q2}^{\dagger 2} + \hat{a}_{q1}^2\hat{a}_{q2}^2\right). \tag{5.20}$$

1. Here we have ignored the phase dependence of the cavity operator on the transmon state, which reduces the transmon-cavity blue-sideband rate.

Finally, by driving at all four frequencies together with appropriate strengths and phases, we can combine the four terms in Eq. 5.18-5.20 to become the desired stabilizer term (the W term) that distinguishes the VSLQ logical and error basis, as well as the error correction term (the Ω term) that maps the error state back to the logical state manifold. The single-photon projection term $\hat{P}^1$ is simply a residue of the rotating frame transformation, with its coefficient related to the transmon anharmonicity, $\delta_i = -\alpha_i$. Likewise, the last term in the VSLQ Hamiltonian, the ancillary energy of $W+\delta/2$, can be similarly achieved as a rotating frame residue term, by shifting the four modulation frequencies to

$$\omega_{b1,2} = \omega_{qi}+\omega_{ri}-\alpha_i-W, \quad \omega_{2p} = 2\left(\omega_{q1}-\omega_{q2}\right)-\alpha_1+\alpha_2, \quad \omega_{4p} = 2\left(\omega_{q1}+\omega_{q2}\right)-\alpha_1+\alpha_2, \tag{5.21}$$

where ω_{bi} is the i-th blue-sideband tone, and ω_{2p}, ω_{4p} are the two-photon-swapping and the four-photon pumping tone. The parametric modulation of the VSLQ circuit is thus shown to be a highly hardware-efficient control scheme for versatile quantum operations, including autonomous quantum error correction.

5.2.3 Flux calibration and coherence measurement

In order to access the VSLQ operating point, we need to calibrate the two fluxes through cavity spectroscopy measurement. In the numerical simulation (Fig. 5.7), we find that the periodic avoided-crossings between the cavity and the transmon levels can be useful for determining the flux scale. However, in the experiment, we find that the cavity spectrum is distorted and becomes non-periodic when the flux is biased away from zero. This is because the current that we use to tune one flux will also affect the other flux due to inevitable flux crosstalks. This can be better illustrated by plotting the 2D cavity spectroscopy against both fluxes (see Fig. 5.8), where the avoided-crossings appear as a 2D lattice of elliptical contours, whose principal axes are tilted by the flux crosstalks. Now it becomes obvious that, as a vertical slice of the 2D spectrum, the 1D flux spectroscopy is deformed and non-periodic.

In the vector form, we can connect the fluxes $\Phi_{1,2}$ in the two loops represented by flux vector $\mathbf{\Phi}$, with the two control currents $I_{1,2}$ represented by the current vector $\mathbf{I}$, through the mutual inductance matrix $\mathbf{L}$,

$$\mathbf{\Phi} = \mathbf{LI} + \mathbf{\Phi^0}, \tag{5.22}$$

where the diagonal entry L_{ii} of the $\mathbf{L}$ is the mutual inductance between the i-th flux line and its corresponding loop, while the off-diagonal element L_{ij} represents that between the flux line and the other loop as flux crosstalk, and $\mathbf{\Phi}^0$ stands for flux offsets due to stray fluxes trapped in the loops.

To cancel out the flux crosstalk as well as the flux offset, we simply need to apply the following transformation to $\mathbf{I}$:

$$\mathbf{I} \rightarrow \mathbf{L}^{-1}\left(\mathbf{L'I} - \mathbf{\Phi^0}\right), \tag{5.23}$$

where $\mathbf{L'}$ is an arbitrary diagonal matrix. This is directly verified by plugging it back to Eq. 5.22, which gives

$$\mathbf{\Phi} = \mathbf{L'I}, \tag{5.24}$$

showing that $\mathbf{L'}$ sets the new mutual inductance for the transformed currents. In order to perform this transformation, we first need to find out the entries of $\mathbf{L}$ and $\mathbf{\Phi^0}$. This can be achieved by reading the flux vectors $\mathbf{\Phi}_{1,2,3}$ and current vectors $\mathbf{I}_{1,2,3}$ of the three ellipse centers (red dots) off Fig. 5.8a, then feeding them into Eq. 5.22,

$$\mathbf{\Phi}_{1,2,3} = \mathbf{LI}_{1,2,3} + \mathbf{\Phi^0}. \tag{5.25}$$

This gives rise to a set of six independent equations, which is exactly equal to the number of unknown variables.

To show the effectiveness of the transformation, we retake the 1D cavity spectroscopy over multiple flux periods shown in Fig. 5.7(c), and this time we observe a perfectly periodic flux response. This is further verified from the 2D spectroscopy measurement in Fig. 5.8, where the

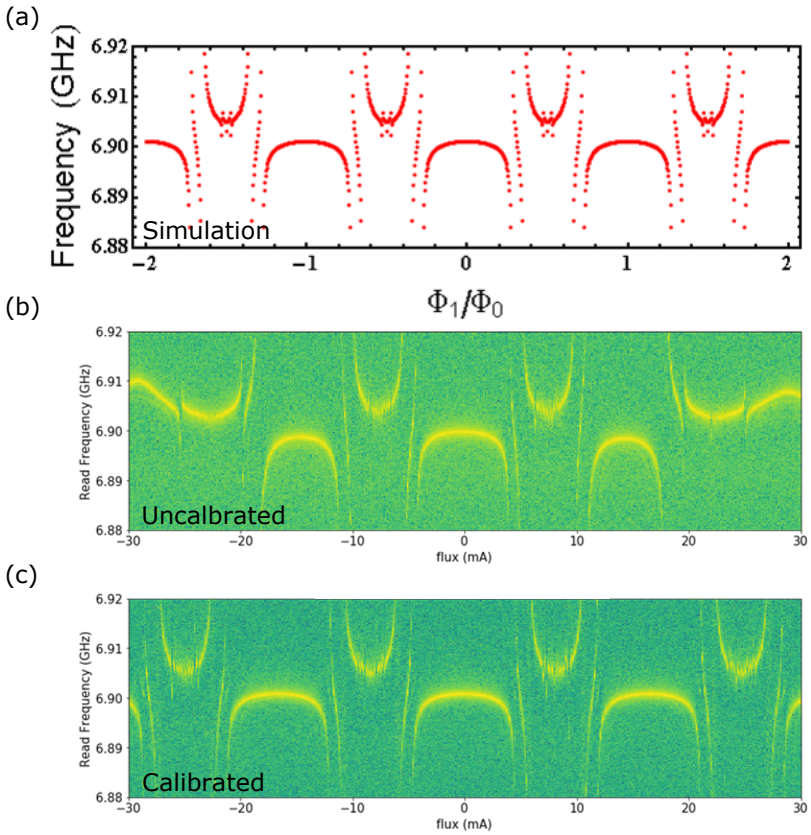

Figure 5.7: Cavity spectroscopy of the VSLQ. (a) Numerical simulation of the cavity frequency as a function of Φ_1 with $\Phi_2 = 0$. The avoided crossings are from the interaction with the cavity single-photon level and the f level of transmon 2. (b) Cavity spectroscopy against flux 1. Distortions are obvious to notice at large flux values, a signature of the flux crosstalk between the two SQuID loops. (c) With calibrated control currents taking the flux crosstalk into account, the cavity spectroscopy possess periodic avoided crossing features that agree well with the numerical simulation.

transformation maps the tilted principal axes back to the orthogonal axes. Qubit spectroscopy is also obtained by measuring the two qubit frequencies as a function of the two fluxes. This enables the fine characterization of circuit parameters, which is reflected as an excellent agreement between the measurement and the numerical simulation.

At the VSLQ operating point, coherence measurements are performed for the two qubits. and decent lifetimes are observed (see Table. 5.2), which build a solid foundation for the logical qubit lifetime. Cavity lifetimes are also measured, and are found to be shorter than the transmons by two orders of magnitude, which satisfies the requirement for dissipative error correction. These,

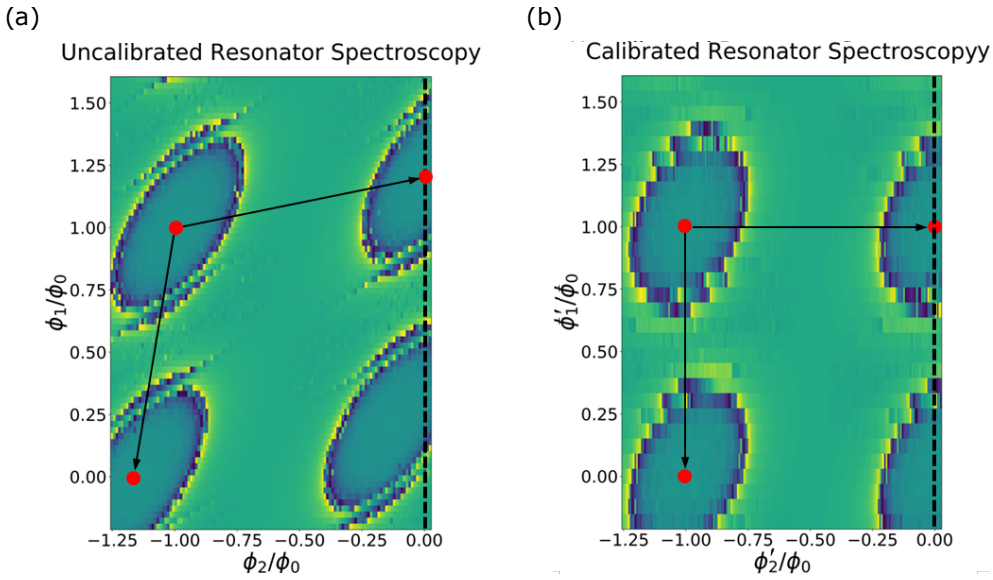

Figure 5.8: 2D flux spectroscopy of the VSLQ cavity mode for flux calibration. Cavity frequency is measured at each point (Φ_1, Φ_2), and the avoided crossings between the cavity and qubit levels appear to be a 2D lattice of ellipses. (a) Without flux calibration, the principal axes of the lattice are skewed, manifesting the effect of flux crosstalk that acts as the off-diagonal elements in Eq. 5.22. The dashed line indicated where the 1D flux spectroscopy in Fig. 5.7b is taken. (b) Plugging the coordinates of the ellipse centers into Eq. 5.22 and being cognizant of the actual flux values they should correspond to, we solve for the mutual inductance matrix and use it for the flux calibration. The principal axes become orthogonal after the calibration, and retaking the 1D flux spectroscopy (Fig. 5.7c) results in an excellent agreement with the theory.

along with other designed circuit parameters, contribute to a significant enhancement of the VSLQ lifetime, which is predicted to be around 400 us by the master equation simulation.

Coherence time	Transmon 1	Transmon 2	Cavity 1	Cavity 2
T1 (μs)	43	22	0.4	0.18
T2* (μs)	17	12	N/A	N/A

Table 5.2: Coherence times of the transmon and the cavity at the VSLQ operating point.

5.2.4 Experimental observation of the VSLQ Hamiltonian

As the first step of realizing the VSLQ Hamiltonian, we demonstrate the generation of its individual interaction terms by parametric flux modulation. For simplicity we park the dc fluxes at zero and

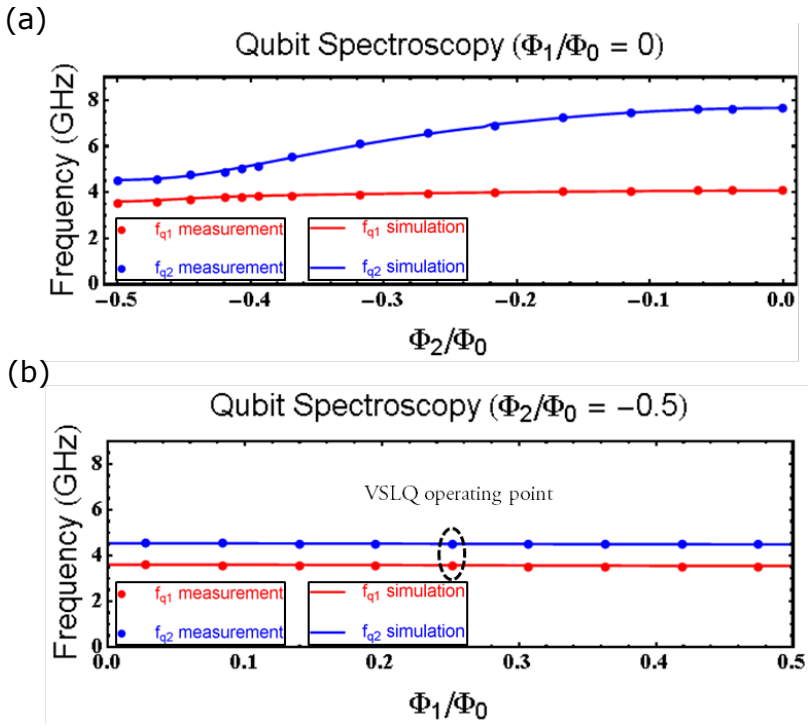

Figure 5.9: Qubit spectroscopy of the VSLQ, (a) as a function of Φ_2 with $\Phi_1 = 0$, and (b) against Φ_1 at $\Phi_2 = 0.5$. The calibration of flux crosstalk corrects the flux scale, making the spectroscopy measurement closely follow the numerical simulation.

modulate Φ_2 only. There, the modulation term becomes a cosine function, which naturally serves as a frequency doubler that allows us to drive at only half of the transition frequency.

For example, when we drive at half of the transmon sum frequency, the two-photon pumping interaction is created, which manifests itself as a coherent oscillation between the $|gg\rangle$ and $|ee\rangle$ state in the time domain. Similarly, if we initialize the first transmon in the excited state by a π pulse, then turn on flux modulation at half of the transmon detuning frequency, the single-photon swapping interaction is generated, which is observed as a coherent exchange of excitation between the two qubits. While these two interactions are not needed for the VSLQ scheme, they can be very useful for implementing the iSWAP and bSWAP gates, which enables the hardware-efficient universal operation of two-qubit states.

Taking another step forward, if we initialize the first transmon in the $|f\rangle$ state by consecutive π pulses, then drive the flux at half of the transmon $|f\rangle$ level detuning frequency, we create

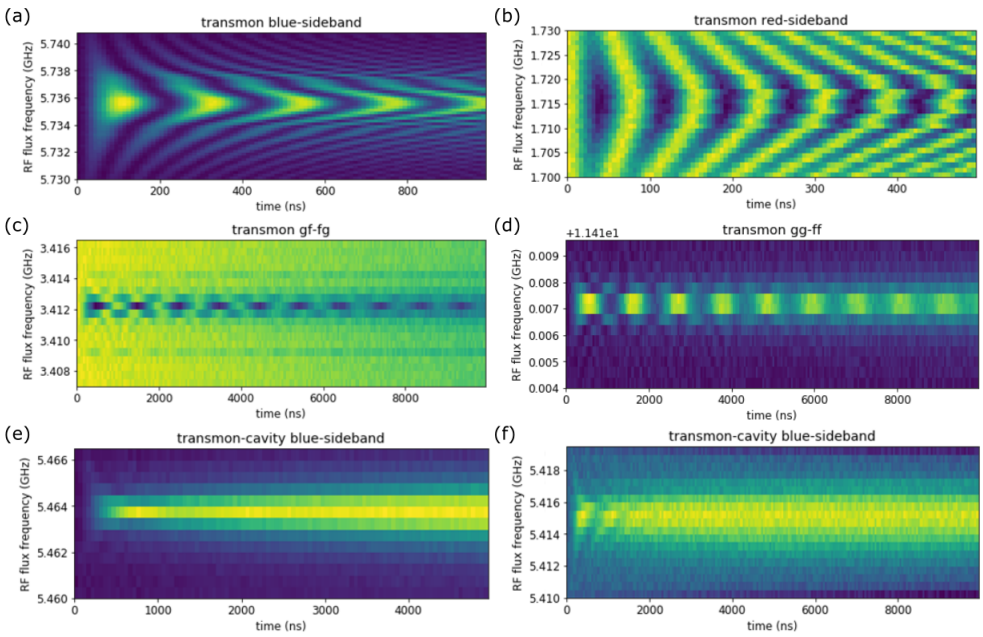

Figure 5.10: Observation of individual VSLQ Hamiltonian terms in the form of time-domain coherent oscillations. We bias the dc fluxes to zero and dynamically modulate Φ_2 at half transition frequencies corresponding to these dynamic processes. (a) and (b): Blue- and red-sideband interactions between the two transmons. (c) and (d): Two-photon-swapping and four-photon-pumping interactions. (e) and (f): Blue-sideband interaction between the transmon and the cavity, in the transmon $\{|g\rangle, |e\rangle\}$ and $\{|e\rangle, |f\rangle\}$ manifolds.

the 2-photon-swapping term needed for the VSLQ, and observe it as a coherent oscillation of the transmon $|f\rangle$ level population in real time. The 4-photon-pumping term, which is perhaps the most formidable part of the VSLQ Hamiltonian, can be achieved by driving at half of the transmon $|f\rangle$ level sum frequency. Without frequency doubling from the cosine term, we will have to drive at the $|gg\rangle$ to $|ff\rangle$ transition frequency around 23 GHz, which can be experimentally challenging for parametric modulation. With frequency doubling, we are able to observe this parametric interaction around 11 GHz.

Finally, we need to create the blue-sideband interaction between the transmon and the low-q cavity for the dissipative error correction process. Driven at half of their sum frequency, the transmon and the cavity will first undergo a coherent oscillation process, but not for very long because the cavity will quickly lose its population due to its large photon loss rate, which traps the qubit population in the excited state. In the experiment, this is observed as the stabilization of

the qubit excited state in the long time scale. The VSLQ protocol relies on a similar stabilization process, but with the blue-sideband interaction defined for the transmon $\{|e\rangle, |f\rangle\}$ manifold as opposed to the $\{|e\rangle, |f\rangle\}$ manifold. In our experiment, we first initialize the transmon in the excited state by a π pulse, then turn on flux modulation to couple the $|0e\rangle$ and $|1f\rangle$ states together. Similarly, after the initial coherent oscillations, the fast decay of the cavity will trap the transmon population in the $|f\rangle$ level. However, this is not a true stabilization of the $|f\rangle$ level, as two-photon loss events can bring the transmon population out of the $\{|e\rangle, |f\rangle\}$ manifold into the ground state, which is a dark state to this driven dissipation process. Nonetheless, as the two-photon loss rate is much slower than the stabilization rate, the transmon $|f\rangle$ level lifetime is greatly prolonged. In the experiment, this is observed as a 10-fold enhancement of the $|f\rangle$ level lifetime, comparing to the case where the flux modulation is off. While not being a true error correction, this gives us a taste of how the VSLQ works, because likewise, the VSLQ is not protected against two-photon losses, but is nevertheless capable of dramatically enhancing the lifetime of its logical states.

In summary, we have created and calibrated the VSLQ circuit device, and we have observed all the key ingredients of the VSLQ Hamiltonian, by parametrically modulating the control fluxes at appropriate frequencies. With the well-calibrated VSLQ circuit and the individual parametric interactions at hand, the next fun thing to try can be the stabilization of arbitrary 2-qubit states, such as the Bell states. The parametric interaction rates we have achieved need to be further increased, and spurious interaction terms emerging from larger modulation amplitudes need to be canceled. Finally, autonomous error correction can be accomplished by putting all the pieces together to create and stabilize the VSLQ logical states, which is an extremely important step towards the ultimate realization of universal quantum computation.

5.2.5 "Digital" AQEC with VSLQ codeword and others

In this subsection, we propose a "digital" quantum error correction protocol based on the codeword of VSLQ. This protocol does not require feedback control, but only relies on performing universal quantum gates and resetting the ancillary qubit. Comparing to VSLQ, it offers weaker

protections to the logical state as error correction is only done in a time-segregated sense, and it doesn't suppress dephasing error. On the other hand, this protocol doesn't require special circuit design and operation scheme, and be can run on any superconducting circuit device that is capable of performing universal operations between two physical qubit and ancillary qubits, and resetting the ancilla. We further generalize this gate-based protocol for correcting other types of errors.

The VSLQ has logical qubit state of

$$|L\rangle = \alpha\,|L_0\rangle + \beta\,|L_1\rangle = \alpha\,|{+}{+}\rangle + \beta\,|{-}{-}\rangle \tag{5.26}$$

where $|+\rangle$ and $|-\rangle$ are defined in the 0 and 2 photon subspace. Single-photon loss error brings the logical state into error states of

$$\left|E^l\right\rangle = \alpha\left|E_0^l\right\rangle + \beta\left|E_1^l\right\rangle = \alpha\,|1{+}\rangle - \beta\,|1{-}\rangle\,, \tag{5.27}$$

$$|E^r\rangle = \alpha\,|E_0^r\rangle + \beta\,|E_1^r\rangle = \alpha\,|{+}1\rangle - \beta\,|{-}1\rangle\,. \tag{5.28}$$

Coupling the logical qubit to an ancillary qubit with some initial state $|A\rangle$, the task of correcting the single-photon loss error is simply achieved by performing a unitary operation U_{ec} that satisfies

$$\begin{aligned} U_{ec}\left|L_{0,1}\right\rangle|A\rangle &= \left|L_{0,1}\right\rangle\left|A_{0,1}^0\right\rangle, \\ U_{ec}\left|E_{0,1}^{l,r}\right\rangle|A\rangle &= \left|L_{0,1}\right\rangle\left|A_{0,1}^{l,r}\right\rangle, \end{aligned} \tag{5.29}$$

here $\left|A_{0,1}^{0,l,r}\right\rangle$ are six unknown states, the detailed knowledge of which are not of importance, as they will be reset to the initial state $|A\rangle$ at the end of the error correction sequence, thus completing the cycle.

Eq. (5.29) forms incomplete constraints on the solution of U_{ec}, that is, there is an infinite number of U_{ec} that satisfy this requirement, making further optimization of U_{ec}'s fidelity possible, which depends on the actual number and fidelities of the gates U_{ec} is decomposed into.

It is interesting to note that the original VSLQ Hamiltonian itself conveniently offers one pos-

sible U_{ec} that meets Eq. (5.29),

$$U_{ec} = e^{-\frac{i}{\hbar}\hat{\mathcal{H}}_{\text{VSLQ}}t_\pi}, \tag{5.30}$$

where $t_\pi = 1/4\Omega$ is the π-pulse time between $|e0\rangle$ and $|f1\rangle$. This U_{ec} is then directly decomposed into the desired universal gate set.

Next, we show how the gate-based protocol can be applied to not only the VSLQ but also other error correction codes with codewords being $|L_0\rangle$ and $|L_1\rangle$. Suppose there are N independent error channels that introduce $2N$ different error basis $\left|E^i_{0,1}\right\rangle, i \in [1, N]$, orthogonal to each other and to the logical state. In addition, the error operators and the logical state basis must satisfy

$$O^i_E \left|L_{0,1}\right\rangle = k \left|E^i_{0,1}\right\rangle, i \in [1, N] \tag{5.31}$$

with k being an arbitrary complex number independent of the indexes, so that errors may not alter the coefficients of the logical state superposition,

$$O^i_e(\alpha \left|L_0\right\rangle + \beta \left|L_1\right\rangle) = \alpha \left|E^i_0\right\rangle + \beta \left|E^i_1\right\rangle, i \in [1, N]. \tag{5.32}$$

In a manner akin to Eq. 5.29, we write down the criteria for the desired error-correcting unitary

$$\begin{aligned} U_{ec} \left|L_{0,1}\right\rangle |A\rangle &= \left|L_{0,1}\right\rangle \left|A^0_{0,1}\right\rangle, \\ U_{ec} \left|E^i_{0,1}\right\rangle |A\rangle &= \left|L_{0,1}\right\rangle \left|A^i_{0,1}\right\rangle, i \in [1, N]. \end{aligned} \tag{5.33}$$

Eq. 5.33 also implies that

$$\left\langle A^i_0 | A^j_0 \right\rangle = 0, \left\langle A^i_1 | A^j_1 \right\rangle = 0, \forall i \neq j \in [0, N], \tag{5.34}$$

which poses a lower bound of $N + 1$ on the dimension of the ancilla space. We further assume that the dimension of the ancilla space is K with $K \geqslant N + 1$, and the dimension of the qubit Fock space is M with $M \geqslant 2(N + 1)$.

Now we demonstrate the general approach to construct the unitary U_{ec}. We first write it as

$$U_{ec} = U_1 + U_2, \tag{5.35}$$

with U_1 containing the elements given by Eq. 5.33,

$$U_1 = \left[\sum_{i=0,1} \left(|L_i\rangle \left|A_i^0\right\rangle \langle L_i| + \sum_{j=1}^{N} |L_i\rangle \left|A_i^j\right\rangle \left\langle E_i^j\right| \right) \right] \langle A| \,, \tag{5.36}$$

and U_2 being rest of the elements that make U_{ec} unitary,

$$U_2 = \sum_{i=0,1} \sum_{j=N+1}^{K-1} |L_i\rangle \left|A_i^j\right\rangle \langle W_{i,j}| + \sum_{i=1}^{M-2} \sum_{j=0}^{K-1} |l_i\rangle \left|a_i^j\right\rangle \langle w_{i,j}| \,. \tag{5.37}$$

Here, $|l_i\rangle$ stands for an arbitrary set of $M-2$ orthogonal states in the qubit Fock space outside the logical qubit state subspace, $\left|A_i^j\right\rangle$ with $j \in [N+1, K-1]$ are $K-N-1$ ancillary states that, along with Eq. 5.34, forms a complete orthogonal basis of the the ancillary space

$$\left\langle A_0^i | A_0^j \right\rangle = 0, \left\langle A_1^i | A_1^j \right\rangle = 0, \forall i \neq j \in [0, K-1]. \tag{5.38}$$

$\left|a_i^j\right\rangle$ is a set of ancillary states that satisfies

$$\left\langle a_i^j | a_i^{j'} \right\rangle = \delta(j-j'), \forall i \in [1, M-2], \forall j, j' \in [0, K-1], \tag{5.39}$$

and $\left|W_{i,j}\right\rangle$ and $\left|w_{i,j}\right\rangle$ together stand for any $MK-2N-2$ orthogonal states in the following set of states,

$$\begin{aligned} &\left\{ \left|l_i'\right\rangle |A\rangle \,, \left|F_j\right\rangle \left|A_\perp^k\right\rangle \right\}, \\ &i \in [1, M-2(N+1)], j \in [1, M], k \in [1, K-1], \end{aligned} \tag{5.40}$$

where $\left|l_i'\right\rangle$ are orthogonal qubit states not belonging to either the logical or the error qubit subspace, $\left|F_j\right\rangle$ are M complete orthogonal basis of the full qubit space, and $\left|A_\perp^k\right\rangle$ are $K-1$ ancillary state orthogonal to each other and $|A\rangle$.

Plugging Eq. 5.36 and Eq. 5.37 back to Eq. 5.35, it is straightforward to verify that

$$U_{ec}U_{ec}^\dagger = I. \tag{5.41}$$

CHAPTER 6

APPENDIX

6.1 Transformation between charge and phase basis

Here we demonstrate how to transform the phase basis CPB Hamiltonian in Eq. 1.38 to the charge basis. Note that $\cos\hat{\theta} = \left(e^{i\hat{\theta}} + e^{-i\hat{\theta}}\right)/2$, we simply need to find out the charge basis representation for the unitary operator $U = e^{i\hat{\theta}}$. We first show that $U_{n_g} = e^{in_g\hat{\theta}}$ is a displacement operator to the charge operator $\hat{n}$,

$$U_{n_g}^{\dagger}\hat{n}U_{n_g} = \hat{n} + n_g. \tag{6.1}$$

This can be easily proved by expanding the LHS into a series using the Baker-Campbell-Hausdorff formula,

$$U_{n_g}^{\dagger}\hat{n}U_{n_g} = \hat{n} + in_g\left[\hat{n},\hat{\theta}\right] + \frac{\left(in_g\right)^2}{2!}\left[\left[\hat{n},\hat{\theta}\right],\hat{\theta}\right] + \cdots = \hat{n} + n_g, \tag{6.2}$$

where the second equation is from the commutation relationship $\left[\hat{n},\hat{\theta}\right] = -i$. In the same way, we can prove that $U_{\theta_0} = e^{i\theta_0\hat{n}}$ is a displacement operator to the phase operator $\hat{\theta}$,

$$U_{\theta_0}^{\dagger}\hat{\theta}U_{\theta_0} = \hat{\theta} - \theta_0, \tag{6.3}$$

which has been used to gauge away the phase offset in section 1.2.3. This result can be generalized for any two operators whose commutator is a c-number, including the ladder operator $\hat{a}^{\dagger}$ (or $\hat{a}$) and the generator of the Glauber displacement operator, $\alpha\hat{a}^{\dagger} - \alpha^{*}\hat{a}$.

For the special case of $U = e^{i\hat{\theta}}$, we have

$$e^{i\hat{\theta}}\left(\hat{n}+1\right) = \hat{n}e^{i\hat{\theta}}, \tag{6.4}$$

$$\left\langle m\right| e^{i\hat{\theta}}\left|n\right\rangle\left(n+1\right) = m\left\langle m\right| e^{i\hat{\theta}}\left|n\right\rangle. \tag{6.5}$$

Obviously when $m \neq n+1$, $\langle m| e^{i\hat{\theta}} |n\rangle = 0$. The unitarity of $e^{i\hat{\theta}}$ further enforces it to be

$$e^{i\hat{\theta}} = \sum_{n=-\infty}^{\infty} e^{i\phi_n} |n+1\rangle \langle n| , \tag{6.6}$$

where ϕ_n is an arbitrary phase. The charge-basis CPB Hamiltonian in Eq. 1.38 is immediately recovered by setting $\phi_n = 0$.

6.2 Charging Energy of a Cooper-Pair Box under gate voltage

In this section we derive for the charging energy of $4E_c \left(\hat{n} - n_g\right)^2$. Assume that in the initial of time there is a net charge of $\hat{Q} = 2e\hat{n}$ on the Josephson island (labeled red in Fig. 6.1). The junction capacitance is C_s and the voltage source connects to the junction via the gate capacitor C_g, with $C_g \ll C_s$.

Once the bias voltage of V_g is turned on, it begins to charge both capacitors, and the work done by it is

$$W = \int_0^q \left(V_g - \frac{Q+q'}{C_s} - \frac{q'}{C_g} \right) dq' = qV_g - \frac{2qQ+q^2}{2C_s} - \frac{q^2}{2C_g}, \tag{6.7}$$

where q is the charge on the gate capacitor. Also note that

$$V_g = \frac{q}{C_g} + \frac{q+Q}{C_s}, \tag{6.8}$$

so

$$W = \frac{q^2}{2}\left(C_g^{-1} + C_s^{-1}\right) = \frac{C_g\left(Q^2 - 2C_sV_gQ + C_s^2V_g^2\right)}{2C_s\left(C_s+C_g\right)}. \tag{6.9}$$

The total energy of the system after the charging process is given by

$$E = W + \frac{Q^2}{2C_s} = \frac{C_g\left(Q^2 - 2C_sV_gQ + C_s^2V_g^2\right) + \left(C_s+C_g\right)Q^2}{2C_s\left(C_s+C_g\right)}, \tag{6.10}$$

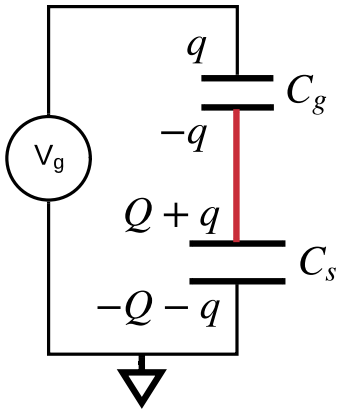

Figure 6.1: Sketch of a Cooper-pair box connected to a voltage source.

and under $C_g \ll C_s$, this charging energy is simplified to

$$E = \frac{Q^2 - 2C_g V_g Q + C_g C_s V_g^2}{2\left(C_s + C_g\right)} = 4\frac{e^2}{2C_\Sigma}\left(\hat{n} - n_g\right)^2 + \frac{1}{2}C_g V_g^2, \tag{6.11}$$

where $n_g = \frac{C_g V_g}{2e}$. The last term can be abandoned as a classical offset.

6.3 Quantization Procedure of RF-Flux Driven Circuits

We use the typical circuit consisting of a flux-tunable transmon coupled to a linear resonator (Fig. 6.2) to demonstrate how to incorporate time-dependent flux tone into circuit quantization. We assume that the external flux only penetrates the SQuID loop. The circuit Lagrangian is given by

$$\begin{aligned}
\mathcal{L} &= T - V \\
&= \frac{1}{2}\left[C_1\left(\dot{\Phi}_1 - \dot{\Phi}_{\text{ext}}\right)^2 + C_2\dot{\Phi}_2^2 + C_g\left(\dot{\Phi}_2 - \dot{\Phi}_1\right)^2 + C_r\dot{\Phi}_2^2\right] \\
&+ E_{J1}\cos\frac{\Phi_1 - \Phi_{\text{ext}}}{\Phi_0} + E_{J2}\cos\frac{\Phi_1}{\Phi_0} - \frac{\Phi_2^2}{2L_r}.
\end{aligned} \tag{6.12}$$

Finding the correct phase allocation among the circuit modes is equivalent to minimizing the kinetic energy that eliminates the cross terms of the form $\dot{\Phi}_i\dot{\Phi}_{\text{ext}}$, with classical equilibrium of the

flux variable determined by

$$\left.\frac{\partial T}{\partial \dot{\Phi}_i}\right|_{\dot{\Phi}_i=\bar{\dot{\Phi}}_i} = 0, \tag{6.13}$$

which are solved to be

$$\bar{\Phi}_1 = \frac{C_1\left(C_g+C_r\right)\Phi_{\text{ext}}}{\left(C_1+C_2+C_g\right)\left(C_g+C_r\right)-C_g^2}, \quad \bar{\Phi}_2 = \frac{C_1 C_g \Phi_{\text{ext}}}{\left(C_1+C_2+C_g\right)\left(C_g+C_r\right)-C_g^2}. \tag{6.14}$$

Recentering the Lagrangian with respect to the classical equilibriums, we have

$$\begin{aligned}\mathcal{L} &= \frac{1}{2}\left[\left(C_1+C_2+C_g\right)\dot{\Phi}_1^2 - 2C_g\dot{\Phi}_1\dot{\Phi}_2 + \left(C_g+C_r\right)\dot{\Phi}_2^2\right] \\ &+ E_{J1}\cos\frac{\Phi_1 - r_1\Phi_{\text{ext}}}{\Phi_0} + E_{J2}\cos\frac{\Phi_1+\left(r_1-1\right)\Phi_{\text{ext}}}{\Phi_0} - \frac{\left(\Phi_2+r_2\Phi_{\text{ext}}\right)^2}{2L_r},\end{aligned} \tag{6.15}$$

where

$$r_1 = \frac{C_2C_g + C_2C_r + C_gC_r}{\left(C_1+C_2+C_g\right)\left(C_g+C_r\right)-C_g^2}, \quad r_2 = \frac{C_1C_g}{\left(C_1+C_2+C_g\right)\left(C_g+C_r\right)-C_g^2}. \tag{6.16}$$

From here we may follow the standard Legendre transformation and obtain the circuit Hamiltonian as

$$\begin{aligned}\hat{\mathcal{H}} &= \frac{\hat{Q}_q^2}{2C_q^{\text{eff}}} + \frac{\hat{Q}_r^2}{2C_r^{\text{eff}}} + \frac{\hat{Q}_q\hat{Q}_r}{2C_g^{\text{eff}}} \\ &- E_{J1}\cos\frac{\Phi_1 - r_1\Phi_{\text{ext}}}{\Phi_0} - E_{J2}\cos\frac{\Phi_1+\left(r_1-1\right)\Phi_{\text{ext}}}{\Phi_0} + \frac{\left(\Phi_2+r_2\Phi_{\text{ext}}\right)^2}{2L_r},\end{aligned} \tag{6.17}$$

where

$$C_q^{\text{eff}} = \frac{C_qC_r + C_g\left(C_q+C_r\right)}{C_g+C_r}, \quad C_r^{\text{eff}} = \frac{C_qC_r + C_g\left(C_q+C_r\right)}{C_g+C_q}, \quad C_g^{\text{eff}} = \frac{C_qC_r + C_g\left(C_q+C_r\right)}{2C_g}. \tag{6.18}$$

Interestingly, Eq. 6.17 suggests that the parametric flux modulation of the transmon also creates a cavity drive term. It is easy to check that when $C_g = 0$ i.e. when the transmon and the resonator

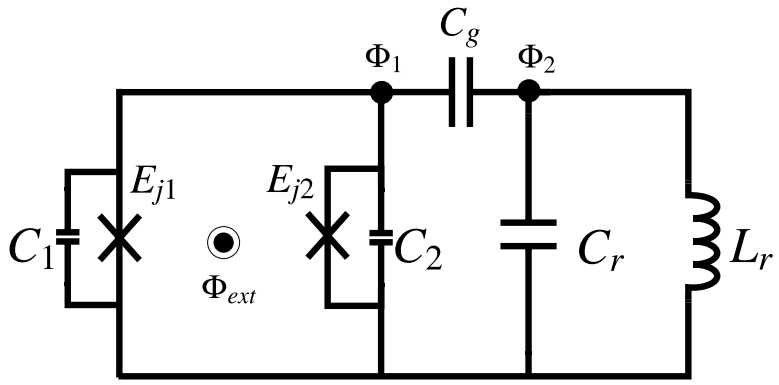

Figure 6.2: Circuit quantization of the flux-tunable transmon capacitively coupled to a linear resonator, assuming the flux threading the SQuID loop is time-dependent.

are decoupled, Eq. 6.17 reduces to Eq. 2.26 plus a harmonic oscillator Hamiltonian.

6.4 Commutation relations

Following commutation relations hold for bosonic ladder operators:

$$\left[\hat{a}, \hat{a}^\dagger\right] = 1, \tag{6.19}$$

$$\left[\hat{a}, \hat{a}^\dagger \hat{a}\right] = \hat{a}, \tag{6.20}$$

$$\left[\hat{a}^\dagger, \hat{a}^\dagger \hat{a}\right] = -\hat{a}^\dagger, \tag{6.21}$$

$$\left[\hat{a}, \left(\hat{a}^\dagger \hat{a}\right)^2\right] = \left(1 + 2\hat{a}^\dagger \hat{a}\right) \hat{a}, \tag{6.22}$$

$$\left[\hat{a}^\dagger, \left(\hat{a}^\dagger \hat{a}\right)^2\right] = \left(1 - 2\hat{a}^\dagger \hat{a}\right) \hat{a}^\dagger, \tag{6.23}$$

and for spin-$\frac{1}{2}$ operators (**by atomic convention** $\hat{\sigma}_z = \left(\begin{smallmatrix} -1 & 0 \\ 0 & 1 \end{smallmatrix}\right)$),

$$\left[\hat{\sigma}_x, \hat{\sigma}_y\right] = -2i\hat{\sigma}_z, \quad \left[\hat{\sigma}_y, \hat{\sigma}_z\right] = -2i\hat{\sigma}_x, \quad \left[\hat{\sigma}_z, \hat{\sigma}_x\right] = -2i\hat{\sigma}_y, \tag{6.24}$$

$$\left[\hat{\sigma}_x, \hat{\sigma}^\pm\right] = \mp\hat{\sigma}_z, \quad \left[\hat{\sigma}_y, \hat{\sigma}^\pm\right] = i\hat{\sigma}_z, \quad \left[\hat{\sigma}_z, \hat{\sigma}^\pm\right] = \pm 2\hat{\sigma}^\pm, \quad \left[\hat{\sigma}^+, \hat{\sigma}^-\right] = \hat{\sigma}_z. \tag{6.25}$$

For Jaynes-Cummings type of interaction operators such as

$$\hat{\Delta}^{\pm} = \hat{a}^{\dagger}\hat{\sigma}^{-} \pm \hat{a}\hat{\sigma}^{+}, \quad \hat{\Sigma}^{\pm} = \hat{a}^{\dagger}\hat{\sigma}^{+} \pm \hat{a}\hat{\sigma}^{-}, \tag{6.26}$$

we have the following commutation relations:

$$\left[\hat{\Delta}^{+}, \hat{\Delta}^{-}\right] = \hat{I} + \left(2\hat{a}^{\dagger}\hat{a} + 1\right)\hat{\sigma}_z, \tag{6.27}$$

$$\left[\hat{\Sigma}^{+}, \hat{\Sigma}^{-}\right] = \hat{I} - \left(2\hat{a}^{\dagger}\hat{a} + 1\right)\hat{\sigma}_z, \tag{6.28}$$

$$\left[\hat{\Sigma}^{-}, \hat{\Delta}^{+}\right] = \left[\hat{\Sigma}^{+}, \hat{\Delta}^{-}\right] = \left(\hat{a}^{\dagger 2} + \hat{a}^{2}\right)\hat{\sigma}_z, \tag{6.29}$$

$$\left[\hat{\Sigma}^{-}, \hat{\Delta}^{-}\right] = \left[\hat{\Sigma}^{+}, \hat{\Delta}^{+}\right] = \left(\hat{a}^{\dagger 2} - \hat{a}^{2}\right)\hat{\sigma}_z, \tag{6.30}$$

$$\left[\hat{\Delta}^{\pm}, \hat{\sigma}_z\right] = 2\hat{\Delta}^{\mp}, \quad \left[\hat{\Sigma}^{\pm}, \hat{\sigma}_z\right] = -2\hat{\Sigma}^{\mp}. \tag{6.31}$$

6.5 ABCD matrix

The ABCD matrix is a 2×2 matrix that describes the transmission of a two-port network,

$$\begin{bmatrix} V_1 \\ I_1 \end{bmatrix} = \begin{bmatrix} A & B \\ C & D \end{bmatrix} \begin{bmatrix} V_2 \\ I_2 \end{bmatrix}. \tag{6.32}$$

Here, V_1 and V_2 are the voltage of port 1 and port 2, and I_1 and I_2 are the currents flowing into port 1 and out of port 2. The four entries of the ABCD matrix can be found through finding the ratio of the voltages and currents at different boundary conditions,

$$A = \left.\frac{V_1}{V_2}\right|_{I_2=0}, \quad B = \left.\frac{V_1}{I_2}\right|_{V_2=0}, \quad C = \left.\frac{I_1}{V_2}\right|_{I_2=0}, \quad D = \left.\frac{I_1}{I_2}\right|_{V_2=0}. \tag{6.33}$$

From this one can easily find the ABCD matrix for a series impedance of Z to be

$$\begin{bmatrix} A & B \\ C & D \end{bmatrix} = \begin{bmatrix} 1 & Z \\ 0 & 1 \end{bmatrix}, \tag{6.34}$$

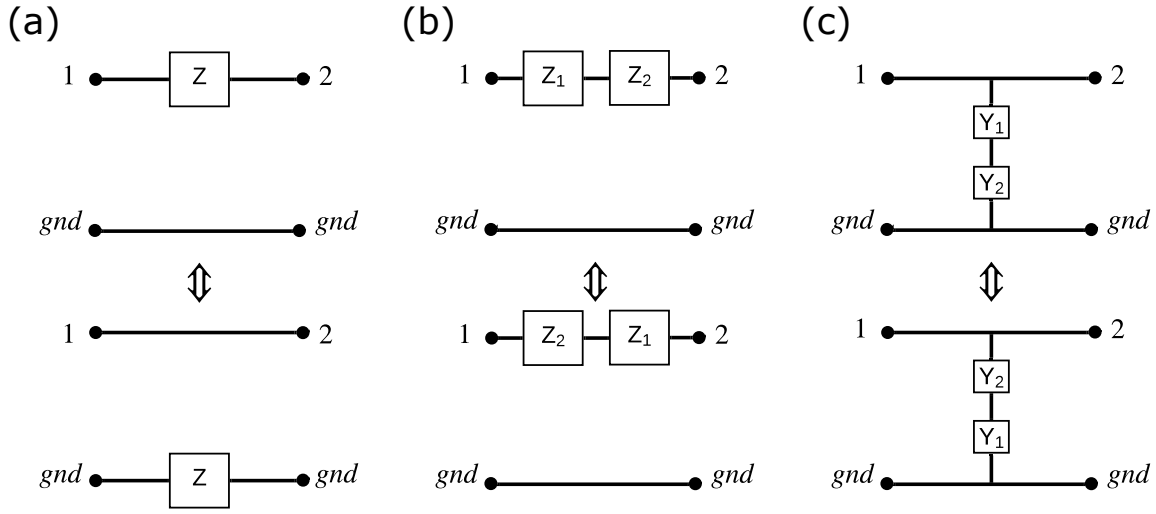

Figure 6.3: Some equivalent circuits in the prospective of transmission. The ABCD matrix and hence the transmission of a network is invariant under (a) moving the impedance element from the signal line to the ground line, (b) swapping the impedance elements in series and (c) swapping the admittance impedance between the signal and ground line.

while that of a shunt admittance of Y is

$$\begin{bmatrix} A & B \\ C & D \end{bmatrix} = \begin{bmatrix} 1 & 0 \\ Y & 1 \end{bmatrix}. \tag{6.35}$$

These suggest the equivalences (on the transmission level) between the circuit shown in Fig. 6.3, which is helpful for simplifying superconducting circuit design.

The beauty of the ABCD matrix is that for large network cascaded by N smaller blocks, one can readily find out the total ABCD matrix as the product of the ABCD matrices of all blocks,

$$\begin{bmatrix} V_1 \\ I_1 \end{bmatrix} = \begin{bmatrix} A_1 & B_1 \\ C_1 & D_1 \end{bmatrix} \begin{bmatrix} A_2 & B_2 \\ C_2 & D_2 \end{bmatrix} \cdots \begin{bmatrix} A_N & B_N \\ C_N & D_N \end{bmatrix} \begin{bmatrix} V_2 \\ I_2 \end{bmatrix}, \tag{6.36}$$

where the order of the matrix multiplication is from port 1 to port 2. For the lossy transmission

line that has been used in the communication experiment, its ABCD matrix is given by

$$\begin{bmatrix} A & B \\ C & D \end{bmatrix} = \begin{bmatrix} \cosh\gamma l & Z_0 \sinh\gamma l \\ Y_0 \sinh\gamma l & \cosh\gamma l \end{bmatrix}, \tag{6.37}$$

where

$$\gamma = \sqrt{(R + j\omega L)\,(G + j\omega C)}, \quad Z_0 = \sqrt{\frac{R + j\omega L}{G + j\omega C}} \tag{6.38}$$

are the propagation coefficient and the characteristic impedance of the transmission line, with R, G, L and C its the resistance, conductance, inductance and capacitance per unit length.

With ABCD matrix we can easily calculate other properties of the network, including the scattering matrix $\mathcal{S}$, the impedance matrix $\mathcal{Z}$ and the admittance matrix $\mathcal{Y}$,

$$\mathcal{S} = \begin{bmatrix} \frac{A+B/Z_0-CZ_0-D}{A+B/Z_0+CZ_0+D} & \frac{2(AD-BC)}{A+B/Z_0+CZ_0+D} \\ \frac{2}{A+B/Z_0+CZ_0+D} & \frac{-A+B/Z_0-CZ_0+D}{A+B/Z_0+CZ_0+D} \end{bmatrix}, \tag{6.39}$$

$$\mathcal{Z} = \begin{bmatrix} \frac{A}{C} & \frac{AD-BC}{C} \\ \frac{1}{C} & \frac{D}{C} \end{bmatrix}, \tag{6.40}$$

$$\mathcal{Y} = \begin{bmatrix} \frac{D}{B} & -\frac{AD-BC}{B} \\ -\frac{1}{B} & \frac{A}{B} \end{bmatrix}, \tag{6.41}$$

useful for the black-box quantization calculation outlined in subsection 2.4.1 and 3.4.6.

6.6 Coupling between transmon and linear network

The equivalent circuit of a transmon capacitively coupled to a linear network is shown in Fig. 6.4. In this section we explain why, under certain regime, it is possible to calculate the coupling strength between the qubit and an individual mode by ignoring all the other modes (see Fig. 2.12c). The

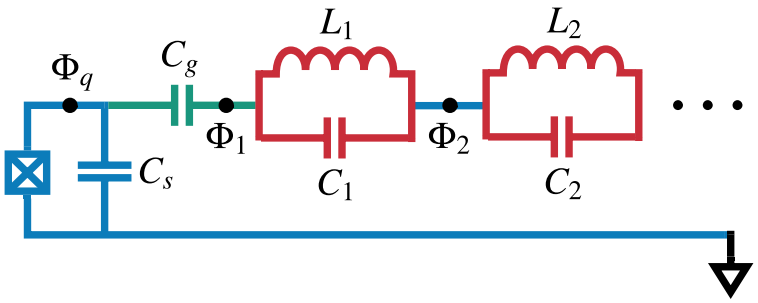

Figure 6.4: Circuit diagram of transmon capacitively coupled to a linear network. The network has been transformed into a series of LC oscillators according to the Foster theorem.

kinetic energy of the circuit is

$$K = \frac{1}{2}C_s\dot{\Phi}_q^2 + \frac{1}{2}C_g\left(\dot{\Phi}_q - \dot{\Phi}_1\right)^2 + \frac{1}{2}\sum_{i=1}^{N} C_i\left(\dot{\Phi}_i - \dot{\Phi}_{i+1}\right)^2. \tag{6.42}$$

Denote $V_i = \dot{\Phi}_i - \dot{\Phi}_{i+1}$ which stands for the voltage drop on the i-th oscillator, Eq. 6.42 can be rewritten as

$$K = \frac{1}{2}C_sV_q^2 + \frac{1}{2}C_g\left(V_q - \sum_{i=1}^{N} V_i\right)^2 + \frac{1}{2}\sum_{i=1}^{N} C_iV_i^2. \tag{6.43}$$

From the expansion of the center term, we immediately see that the coupling capacitance between any two modes is C_g. Therefore, when the mode capacitances are much larger than C_g as in the case of a coaxial cable, the capacitive coupling strength between the modes becomes very weak. When the gaps between the modes are far larger than the coupling strengths, the normal modes are effectively decoupled from each other, but are all coupled to the transmon with capacitance C_g.

6.7 Cryogenic setup and Wiring Diagram

For the tunable coupling circuit device, the base layer is made of 150 nm of niobium sputtered on 430 μm thick C-plane sapphire substrate, and patterned by optical lithography and reactive ion etching (RIE) to define the optical part of the circuit (excluding the qubit and the coupler part). The circuit is surrounded by an array of 5 μm wide square holes spaced by 50 μm for flux

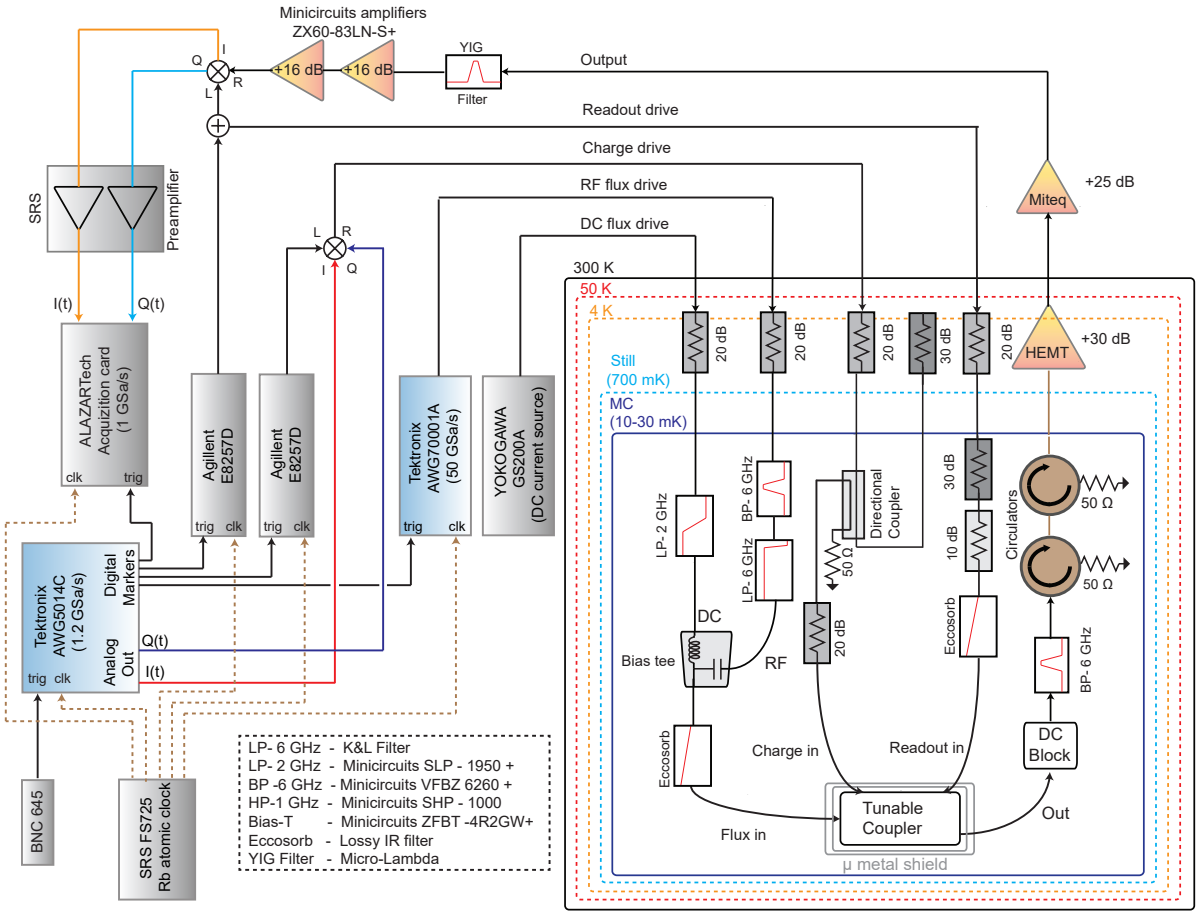

Figure 6.5: Schematic of the experimental setup for the tunable coupling circuit, including the cryogenic and room-temperature control instrumentation.

vortex pinning [208]. The qubit and the coupler junctions are both fabricated in the Manhattan pattern [209], with the bottom (80 nm) and the top (150 nm) aluminum layers deposited via dual-angle electron-beam evaporation. The two layers are gapped by an Al_xO_y insulating layer grown in an oxidation process under 20 mBar of high-purity O_2 for 12 minutes.

The schematic of the instrumentation and cryogenic setup can be seen in Fig. 6.5. The device is mounted and wirebonded to a customized multilayer copper PCB (similar to that used in [210]) with microwave-launchers, which is then heat sunk to the base stage of a Bluefors dilution refrigerator (10-30 mK) via an OFHC copper post. The sample is surrounded by a can containing two layers of μ-metal shielding, thermally anchored using an inner close fit copper shim sheet, attached to the copper can lid. The device is connected to the rest of the setup through four ports:

a charge port that applies qubit drive tones, an input and an output port for readout drive tones, a flux port for shifting the qubit frequency using a dc-flux bias current and for applying rf sideband flux pulses. The charge pulses are generated by mixing a local oscillator tone (generated from an Agilent 8257D rf signal generator), with pulses generated by a Tektronix AWG5014C arbitrary waveform generator (TEK) with a sampling rate of 1.2 GSa/s, using an IQ-Mixer (MARQI MLIQ0218). The readout drive pulse is generated from a second Agilent 8257D rf signal generator, which is also controlled by digital trigger pulses from the TEK. The flux-modulation pulses are directly synthesized by a Tektronix AWG70001A arbitrary waveform generator (50 GSa/s) and attenuated by 20 dB at the 4K stage. Filters on the rf flux line are configured to create a pass band between 4.8 GHz - 6 GHz, which allows blue-sideband modulation while cutting off noise at the qubit frequency. For red-sideband flux modulation, a low pass filter (Minicircuits VLF - 1800+) at 2 GHz is used instead. A better filtering option for the simultaneous implementation of both sidebands could be using a notch (band stop) filter, with a rejection band covering only the qubit frequency and allowing both the red and blue frequency to pass through. The dc flux bias current is generated by a YOKOGAWA GS200 low-noise current source, attenuated by 20 dB at the 4K stage, and low-pass filtered down to a bandwidth of 2 MHz. The dc flux bias current is combined with the flux-modulation pulses at a bias tee thermalized at the base stage. The state of the transmon is measured using the transmission of the readout resonator, through the dispersive circuit QED readout scheme [211]. The transmitted signal from the readout resonator is passed through a set of cryogenic circulators (thermalized at the base stage) and amplified using a HEMT amplifier (thermalized at the 4K stage). Once out of the fridge, the signal is filtered (tunable narrow band YIG filter with a bandwidth of 80 MHz) and further amplified. The amplitude and phase of the resonator transmission signal are obtained through a homodyne measurement, with the transmitted signal demodulated using an IQ mixer and a local oscillator at the readout resonator frequency. The homodyne signal is amplified (SRS preamplifier) and recorded using a fast ADC card (ALAZARtech).

The communication device is heat sunk via an OFHC copper post to the base stage of a Blue-

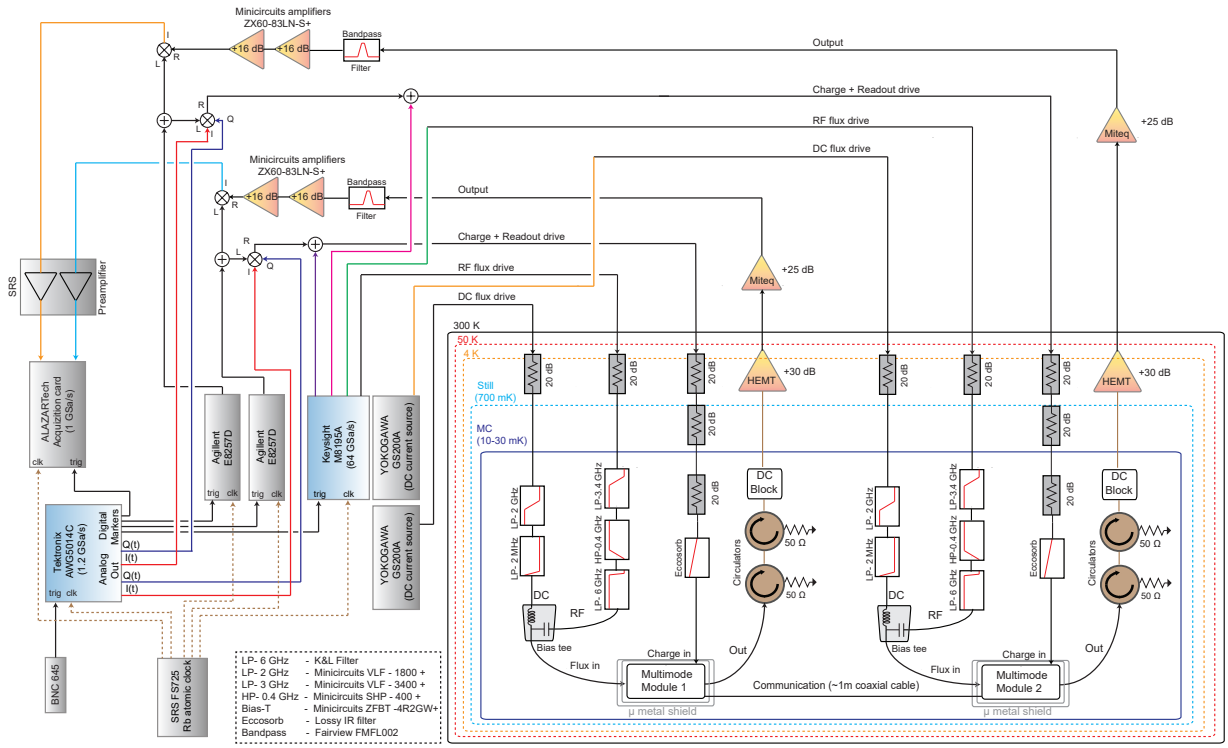

Figure 6.6: Detailed schematic of the cryogenic setup, control instrumentation, and the wiring of microwave and DC connections to the remote quantum modules.

fors dilution refrigerator (10-30 mK). The sample is surrounded by a can containing two layers of μ-metal shielding and a layer of lead shielding, thermally anchored using an inner close fit copper shim sheet, attached to the copper can lid. The schematic of the cryogenic setup, control instrumentation, and the wiring of the device is shown if Supplementary Figure 6.6. Each device is connected to the rest of the setup through three ports: a charge port that applies qubit and readout drive tones, a flux port for shifting the qubit frequency using a DC-flux bias current and for applying RF sideband flux pulses, and an output port for measuring the transmission from the readout resonator. The readout pulses are generated by mixing a local oscillator tone (generated from an Agilent 8257D RF signal generator), with pulses generated by a Tektronix AWG5014C arbitrary waveform generator (TEK) with a sampling rate of 1.2 GSa/s, using an IQ-Mixer (MARQI MLIQ0218). The charge drive pulses are generated with Keysight M8195A arbitrary waveform generator by direct synthesis, and subsequently combined with the readout drive pulse. The combined signals are

sent to the device, after being attenuated a total of 60 dB in the dilution fridge, using attenuators thermalized to the 4K (20 dB), still (20 dB) and base stages (20 dB). The charge driveline also includes a lossy ECCOSORB CR-117 filter to block IR radiation, and a low-pass filter with a sharp roll-off at 6 GHz, both thermalized to the base stage. The flux-modulation pulses are also directly synthesized by the Keysight M8195A arbitrary waveform generator and attenuated by 20 dB at the 4 K stage, and bandpass filtered to within a band of 400 MHz - 3.4 GHz at the base stage, using the filters indicated in the schematic. The DC flux bias current is generated by a YOKOGAWA GS200 low-noise current source, attenuated by 20 dB at the 4K stage, and low-pass filtered down to a bandwidth of 1.9 MHz. The DC flux bias current is combined with the flux-modulation pulses at a bias tee thermalized at the base stage. The state of the transmon is measured using the transmission of the readout resonator, through the dispersive circuit QED readout scheme [211]. The transmitted signal from the readout resonator is passed through a set of cryogenic circulators (thermalized at the base stage) and amplified using a HEMT amplifier (thermalized at the 4K stage). Once out of the fridge, the signal is filtered (narrow bandpass filter around the readout frequency) and further amplified. The amplitude and phase of the resonator transmission signal are obtained through a heterodyne measurement, with the transmitted signal demodulated using an IQ mixer and a local oscillator at the readout resonator frequency. The heterodyne signal is amplified (SRS preamplifier) and recorded using a fast ADC card (ALAZARtech).

6.8 Fabrication Recipe

1. Wafer pretreatment:

   (a) Sapphire wafer annealing: (a) RT-700°C, 350°C/hr; (b) 700°C-1000°C, 250°C/hr; (c) 1000°C-1200°C, 100°C/hr; (d) Wait 1.5hr, 1200°C-RT, 100°C/hr.

   (b) "TAMI" Clean: Sonication in toluene, acetone, methanol and IPA for 3min each, then rinse under DI water for 3min and blow dry.

      i. Alternatively: Sonicate wafer in warm NMP, IPA, acetone and IPA for 5min each,

rinse for 3min and blow dry.

2. Base-layer deposition:

   (a) Bake wafer on hotplate @ 200°C for 10min (optional if baking in Plassys @ 200°C for 30min).

   (b) Immediately transfer wafer to AJA ATC-Orion 8E ebeam evaporation system or Plassays evaporator (for Nb or Al evaporation), or AJA Orion 5 UHV sputtering system (for Nb sputtering).

3. Photo lithography:

   (a) Bake cleaned wafer on hotplate at 120°C for 2 min.

   (b) With mask-aligner: Spin coat S1811 (4000RPM for 40s) then bake wafer at 90°C for 90s. Let cool and expose with Karl Suss MA6 mask aligner for 1.5s (in hard contact or vacuum contact mode). Develop in MF-351/water 1:4 mixture for 45s with slight agitation. Thoroughly rinse in DI water, then blow dry.

   (c) With Heidelberg MLA 150 Direct Write: Spin AZ 703 @ 3500rpm (Ramp @ 1000rpm) for 45s. Bake for 1min @ 95C. Convert design file, select laser 405 or 375 (high dose) and set defocus, load wafer in and start exposure. Develop in AZ MIF 300 (for Nb) for 1min or in AZ 1:1 (for Al) for 1min30s. Rinse and blow dry.

4. Base-layer etching:

   (a) Al etching:

      i. Dry etching: Pre-condition plasma etcher(RIE Oxford PlasmaLab 100). The etching process has two steps: the break-through of the alumina on top first and then the etch-through of 100nm Al. Al2O3 break-through: 30 sccm. Cl2, 100W RF forward power, 0W ICP forward power, 5s. Al etch-through: 18 sccm. HBr, 100W RF forward power, 0W ICP forward power, 80s.

ii. Wet etching: Soak developed wafer in Aluminum Etchant Type A for 2min50s (100nm) with slight agitation, then quickly dip into IPA and agitate for 30s, then rinse in DI water and blow dry. Note: The isotropic nature of wet etching will cause natural undercut to happen along the edge of your pattern and tend to make the gap size slightly bigger.

(b) Nb etching: O2 clean and pre-condition PlasmaTherm ICP Fluorine Etch. Etch for 6min @ ICP run power = 100 W, Bias run power = 100 W, Table temperature = 10°C. Gases: 15 sccm. SF6, 40 sccm. CHF3, 10 sccm. Ar.

5. Resist strip-off: NMP @ 80°C bath for >4hrs, then sonicate for 6mins. Rinse with and sonicate in IPA (1mins), Acetone (5mins) and IPA (1min), rinse in DI and blow dry.

6. Ebeam session starts here. One can either dice the wafer here and ebeam write on single chips, or write on the wafer scale and then dice into chips. The later is practiced much more often now with the advanced Raith tool.

7. Ebeam resist spin-coating:

   (a) Bake wafer @ 200°C for 5min. Let cool.

   (b) Spin MMA EL11: 4000rpm, ramp=500, time=45s

   (c) Bake @ 180°C for 5min.

   (d) Spin PMMA 950 A7: 4000rpm, ramp=500, time=45s

   (e) Bake @ 180°C for 5min.

8. Evaporate 10nm gold conducting layer in Angstrom Nexdep Thermal E-Beam Evaporator.

9. Ebeam lithography:

   (a) Prepare pattern file, import to beamer, generate Raith file, load sample and start writing.

   (b) Gold layer etching: submerge wafer in iodine gold etchant for 45s. Rinse in DI and thoroughly blow dry.

(c) Develop ebeam resist: submerge wafer in 3:1 IPA:Water @ 6°C (make sure it is pre-thermalized) for 1min30s.

(d) Rinse in DI water (optional) and blow dry promptly and thoroughly.

10. Junction evaporation: load sample in Plassys in appropriate orientation, pump down, run mild O2 plasma cleaning before running junction recipe:

    (a) Chamber purging with Ti

    (b) Ar ion milling

    (c) Chamber purging with Ti

    (d) First junction layer, 0.1nm/s, 60nm

    (e) Oxidizing with O2-Ar mixture (15/85) for 12 minutes at 20mBar

    (f) Chamber purging with Ti

    (g) Second layer, 0.1nm/s, 150nm

    (h) Oxidizing for 5min

11. Take out the sample from Plassys and leave it under Ionizing fan for >1hr.

12. From here there are two paths to the qubit sample: lift off the Al layers then dice the wafer, or dice first and do lift-off for chips. While the former has been used more often, it requires coating the bare junctions with another resist layer which is potentially a contaminant that may degrade the qubit quality. Moreover, the Al layer before lift-off may provide extra protection to the junctions against ESD issues, especially during the dicing session. Finally, lift-off on the whole wafer level typically takes much longer time to finish than individual chips. For these benefits we adopt the later approach.

13. Pre-dicing resist-coating:

    (a) AZ1518 1500 RPM for 40s.

(b) Bake @ 90°C for 1min.

14. Dice wafer in Disco DAD3240 automatic dicing saw.

15. Al layer lift-off for chips (have ionizing fan on and wear anti-static equipment):

    (a) Clamp the chips of interest to the specially design stage.

    (b) NMP hot bath @ 80°C for >4hrs.

    (c) When the Al layer is noticeably peeling off, transfer the stage to a new beaker of warm NMP, sonicate for 1min.

    (d) Transfer to IPA, idle for 20min, sonicate for 30s.

    (e) Transfer to wide beaker of IPA, remove sample from stage, agitate in clean IPA, DI water and blow dry.

    (f) Idle sample under ionizer for >10min then inspect under microscope.

Always remember to inspect the sample (with microscope) between steps.

REFERENCES

[1] Richard P. Feynman. Simulating physics with computers. *International Journal of Theoretical Physics*, 21(6-7):467–488, 6 1982.

[2] Andrew Steane. Quantum computing. *Reports on Progress in Physics*, 61(2):117–173, 2 1998.

[3] T. D. Ladd, F. Jelezko, R. Laflamme, Y. Nakamura, C. Monroe, and J. L. OBrien. Quantum computers. *Nature*, 464(7285):45–53, 3 2010.

[4] John Preskill. Quantum Computing in the NISQ era and beyond. *Quantum*, 2:79, 1 2018.

[5] Samuel L. Braunstein, A. Mann, and M. Revzen. Maximal violation of Bell inequalities for mixed states. *Physical Review Letters*, 68(22):3259–3261, 6 1992.

[6] G. C Ghirardi, R Grassi, A Rimini, and T Weber. Experiments of the EPR Type Involving CP -Violation Do not Allow Faster-than-Light Communication between Distant Observers. *Europhysics Letters (EPL)*, 6(2):95–100, 5 1988.

[7] Phillippe H. Eberhard and Ronald R. Ross. Quantum field theory cannot provide faster-than-light communication. *Foundations of Physics Letters*, 2(2):127–149, 3 1989.

[8] A Acín, A Andrianov, L Costa, E Jané, J I Latorre, and R Tarrach. Generalized Schmidt Decomposition and Classification of Three-Quantum-Bit States. Technical report, 2000.

[9] Otfried Gühne and Gza Tóth. Entanglement detection. *Physics Reports*, 474(1-6):1–75, 4 2009.

[10] Shuhao Wang, Yao Lu, Ming Gao, Jianlian Cui, and Junlin Li. Classification of arbitrary-dimensional multipartite pure states under stochastic local operations and classical communication using the rank of coefficient matrix. *Journal of Physics A: Mathematical and Theoretical*, 46(10):105303, 3 2013.

[11] Shuhao Wang, Yao Lu, and Gui-Lu Long. Entanglement classification of 2 2 2 d quantum systems via the ranks of the multiple coefficient matrices. *Physical Review A*, 87(6):062305, 6 2013.

[12] Yao Lu, Gui Lu Long, and Ting Gao. Stronger Criteria for Nonseparability in n-Partite Quantum States. *International Journal of Theoretical Physics*, 52(3):699–705, 3 2013.

[13] Ting Gao, Yan Hong, Yao Lu, and Fengli Yan. Efficient k-separability criteria for mixed multipartite quantum states. *EPL (Europhysics Letters)*, 104(2):20007, 10 2013.

[14] Tomi H Johnson, Stephen R Clark, and Dieter Jaksch. What is a quantum simulator? *EPJ Quantum Technology*, 1(1):10, 12 2014.

[15] I.M. Georgescu, S. Ashhab, and Franco Nori. Quantum simulation. *Reviews of Modern Physics*, 86(1):153–185, 3 2014.

[16] Andrew A. Houck, Hakan E. Türeci, and Jens Koch. On-chip quantum simulation with superconducting circuits. *Nature Physics*, 8(4):292–299, 4 2012.

[17] R. Blatt and C. F. Roos. Quantum simulations with trapped ions. *Nature Physics*, 8(4):277–284, 4 2012.

[18] J. Orenstein and A. J. Millis. Advances in the physics of high-temperature superconductivity. *Science (New York, N.Y.)*, 288(5465):468–75, 4 2000.

[19] E. Manousakis. A Quantum-Dot Array as Model for Copper-Oxide Superconductors: A Dedicated Quantum Simulator for the Many-Fermion Problem. *Journal of Low Temperature Physics*, 126(5/6):1501–1513, 2002.

[20] Markus Greiner, Olaf Mandel, Tilman Esslinger, Theodor W. Hänsch, and Immanuel Bloch. Quantum phase transition from a superfluid to a Mott insulator in a gas of ultracold atoms. *Nature*, 415(6867):39–44, 1 2002.

[21] A. Friedenauer, H. Schmitz, J. T. Glueckert, D. Porras, and T. Schaetz. Simulating a quantum magnet with trappedions. *Nature Physics*, 4(10):757–761, 10 2008.

[22] R. Islam, E.E. Edwards, K. Kim, S. Korenblit, C. Noh, H. Carmichael, G.-D. Lin, L.-M. Duan, C.-C. Joseph Wang, J.K. Freericks, and C. Monroe. Onset of a quantum phase transition with a trapped ion quantum simulator. *Nature Communications*, 2(1):377, 9 2011.

[23] Jonathan Simon, Waseem S. Bakr, Ruichao Ma, M. Eric Tai, Philipp M. Preiss, and Markus Greiner. Quantum simulation of antiferromagnetic spin chains in an optical lattice. *Nature*, 472(7343):307–312, 4 2011.

[24] Aln Aspuru-Guzik, Anthony D Dutoi, Peter J Love, and Martin Head-Gordon. Simulated quantum computation of molecular energies. *Science (New York, N.Y.)*, 309(5741):1704–7, 9 2005.

[25] Ivan Kassal, Stephen P Jordan, Peter J Love, Masoud Mohseni, and Aln Aspuru-Guzik. Polynomial-time quantum algorithm for the simulation of chemical dynamics. *Proceedings of the National Academy of Sciences of the United States of America*, 105(48):18681–6, 12 2008.

[26] Abhinav Kandala, Antonio Mezzacapo, Kristan Temme, Maika Takita, Markus Brink, Jerry M. Chow, and Jay M. Gambetta. Hardware-efficient variational quantum eigensolver for small molecules and quantum magnets. *Nature*, 549(7671):242–246, 9 2017.

[27] B P Lanyon, C Hempel, D Nigg, M Müller, R Gerritsma, F Zähringer, P Schindler, J T Barreiro, M Rambach, G Kirchmair, M Hennrich, P Zoller, R Blatt, and C F Roos. Universal digital quantum simulation with trapped ions. *Science (New York, N.Y.)*, 334(6052):57–61, 10 2011.

[28] Guan-Ru Feng, Yao Lu, Liang Hao, Fei-Hao Zhang, and Gui-Lu Long. Experimental simulation of quantum tunneling in small systems. *Scientific Reports*, 3(1):2232, 12 2013.

[29] Y. Salathé, M. Mondal, M. Oppliger, J. Heinsoo, P. Kurpiers, A. Potočnik, A. Mezzacapo, U. Las Heras, L. Lamata, E. Solano, S. Filipp, and A. Wallraff. Digital Quantum Simulation of Spin Models with Circuit Quantum Electrodynamics. *Physical Review X*, 5(2):021027, 6 2015.

[30] R. Barends, L. Lamata, J. Kelly, L. García-Álvarez, A. G. Fowler, A Megrant, E Jeffrey, T. C. White, D. Sank, J. Y. Mutus, B. Campbell, Yu Chen, Z. Chen, B. Chiaro, A. Dunsworth, I.-C. Hoi, C. Neill, P. J. J. OMalley, C. Quintana, P. Roushan, A. Vainsencher, J. Wenner, E. Solano, and John M. Martinis. Digital quantum simulation of fermionic models with a superconducting circuit. *Nature Communications*, 6(1):7654, 11 2015.

[31] Yao Lu, Guan-Ru Feng, Yan-Song Li, and Gui-Lu Long. Experimental digital quantum simulation of temporalspatial dynamics of interacting fermion system. *Science Bulletin*, 60(2):241–248, 1 2015.

[32] H. F. Trotter. On the product of semi-groups of operators. *Proceedings of the American Mathematical Society*, 10(4):545–545, 4 1959.

[33] Ruichao Ma, Brendan Saxberg, Clai Owens, Nelson Leung, Yao Lu, Jonathan Simon, and David I. Schuster. A dissipatively stabilized Mott insulator of photons. *Nature*, 566(7742):51–57, 2 2019.

[34] Q. A. Turchette, C. J. Hood, W. Lange, H. Mabuchi, and H. J. Kimble. Measurement of Conditional Phase Shifts for Quantum Logic. *Physical Review Letters*, 75(25):4710–4713, 12 1995.

[35] D. Jaksch, H.-J. Briegel, J. I. Cirac, C. W. Gardiner, and P. Zoller. Entanglement of Atoms via Cold Controlled Collisions. *Physical Review Letters*, 82(9):1975–1978, 3 1999.

[36] Gavin K. Brennen, Carlton M. Caves, Poul S. Jessen, and Ivan H. Deutsch. Quantum Logic Gates in Optical Lattices. *Physical Review Letters*, 82(5):1060–1063, 2 1999.

[37] Daniel Barredo, Sylvain de Léséleuc, Vincent Lienhard, Thierry Lahaye, and Antoine Browaeys. An atom-by-atom assembler of defect-free arbitrary two-dimensional atomic arrays. *Science (New York, N.Y.)*, 354(6315):1021–1023, 11 2016.

[38] J. I. Cirac and P. Zoller. Quantum Computations with Cold Trapped Ions. *Physical Review Letters*, 74(20):4091–4094, 5 1995.

[39] C. Monroe, D. M. Meekhof, B. E. King, W. M. Itano, and D. J. Wineland. Demonstration of a Fundamental Quantum Logic Gate. *Physical Review Letters*, 75(25):4714–4717, 12 1995.

[40] Jan Benhelm, Gerhard Kirchmair, Christian F. Roos, and Rainer Blatt. Towards fault-tolerant quantum computing with trapped ions. *Nature Physics*, 4(6):463–466, 6 2008.

[41] K. R. Brown, A. C. Wilson, Y. Colombe, C. Ospelkaus, A. M. Meier, E. Knill, D. Leibfried, and D. J. Wineland. Single-qubit-gate error below 10 4 in a trapped ion. *Physical Review A*, 84(3):030303, 9 2011.

[42] N. A. Gershenfeld, I. L. Chuang, L. Levitov, Lin Tian, Caspar H. van der Wal, and Seth Lloyd. Bulk Spin-Resonance Quantum Computation. *Science*, 275(5298):350–356, 1 1997.

[43] L. M. K. Vandersypen and I. L. Chuang. NMR techniques for quantum control and computation. *Reviews of Modern Physics*, 76(4):1037–1069, 1 2005.

[44] B. E. Kane. A silicon-based nuclear spin quantum computer. *Nature*, 393(6681):133–137, 5 1998.

[45] G. Koolstra, Ge Yang, and D. I. Schuster. Spectroscopy of Wigner molecules on superfluid helium using a superconducting resonator. 2 2019.

[46] I Chiorescu, Y Nakamura, C J P M Harmans, and J E Mooij. Coherent quantum dynamics of a superconducting flux qubit. *Science (New York, N.Y.)*, 299(5614):1869–71, 3 2003.

[47] T. Yamamoto, Yu. A. Pashkin, O. Astafiev, Y. Nakamura, and J. S. Tsai. Demonstration of conditional gate operation using superconducting charge qubits. *Nature*, 425(6961):941–944, 10 2003.

[48] Jens Koch, Terri M. Yu, Jay Gambetta, A. A. Houck, D. I. Schuster, J. Majer, Alexandre Blais, M. H. Devoret, S. M. Girvin, and R. J. Schoelkopf. Charge-insensitive qubit design derived from the Cooper pair box. *Physical Review A*, 76(4):042319, 10 2007.

[49] Vladimir E Manucharyan, Jens Koch, Leonid I Glazman, and Michel H Devoret. Fluxonium: single cooper-pair circuit free of charge offsets. *Science (New York, N.Y.)*, 326(5949):113–6, 10 2009.

[50] Yuriy Makhlin, Gerd Schön, and Alexander Shnirman. Quantum-state engineering with Josephson-junction devices. *Reviews of Modern Physics*, 73(2):357–400, 5 2001.

[51] J. D. Teufel, Dale Li, M. S. Allman, K. Cicak, A. J. Sirois, J. D. Whittaker, and R. W. Simmonds. Circuit cavity electromechanics in the strong-coupling regime. *Nature*, 471(7337):204–208, 3 2011.

[52] B.D. Josephson. Possible new effects in superconductive tunnelling. *Physics Letters*, 1(7):251–253, 7 1962.

[53] P. W. Anderson and J. M. Rowell. Probable Observation of the Josephson Superconducting Tunneling Effect. *Physical Review Letters*, 10(6):230–232, 3 1963.

[54] Audrey Cottet. Implémentation d'un bit quantique dans un circuit supraconducteur / Implementation of a quantum bit in a superconducting circuit. 9 2002.

[55] R. C. Jaklevic, John Lambe, A. H. Silver, and J. E. Mercereau. Quantum Interference Effects in Josephson Tunneling. *Physical Review Letters*, 12(7):159–160, 2 1964.

[56] Juhani Kurkijärvi. Intrinsic Fluctuations in a Superconducting Ring Closed with a Josephson Junction. *Physical Review B*, 6(3):832–835, 8 1972.

[57] Siyuan Han, R. Rouse, and J. E. Lukens. Observation of Cascaded Two-Photon-Induced Transitions between Fluxoid States of a SQUID. *Physical Review Letters*, 84(6):1300–1303, 2 2000.

[58] Jonathan R. Friedman, Vijay Patel, W. Chen, S. K. Tolpygo, and J. E. Lukens. Quantum superposition of distinct macroscopic states. *Nature*, 406(6791):43–46, 7 2000.

[59] R. Vijay, M. H. Devoret, and I. Siddiqi. Invited Review Article: The Josephson bifurcation amplifier. *Review of Scientific Instruments*, 80(11):111101, 11 2009.

[60] Y. Nakamura, Yu. A. Pashkin, and J. S. Tsai. Coherent control of macroscopic quantum states in a single-Cooper-pair box. *Nature*, 398(6730):786–788, 4 1999.

[61] Jay Gambetta and Sarah Sheldon. Cramming More Power Into a Quantum Device — IBM Research blog, 2019.

[62] N. Earnest, S. Chakram, Y. Lu, N. Irons, R.K. Naik, N. Leung, L. Ocola, D.A. Czaplewski, B. Baker, J. Lawrence, J. Koch, and D.I. Schuster. Realization of a Λ System with Metastable States of a Capacitively Shunted Fluxonium. *Physical Review Letters*, 120(15), 2018.

[63] D Vion, A Aassime, A Cottet, P Joyez, H Pothier, C Urbina, D Esteve, and M H Devoret. Manipulating the quantum state of an electrical circuit. *Science (New York, N.Y.)*, 296(5569):886–9, 5 2002.

[64] John M. Martinis, S. Nam, J. Aumentado, and C. Urbina. Rabi Oscillations in a Large Josephson-Junction Qubit. *Physical Review Letters*, 89(11):117901, 8 2002.

[65] A O Niskanen, K Harrabi, F Yoshihara, Y Nakamura, S Lloyd, and J S Tsai. Quantum coherent tunable coupling of superconducting qubits. *Science (New York, N.Y.)*, 316(5825):723–6, 5 2007.

[66] S. J. Srinivasan, A. J. Hoffman, J. M. Gambetta, and A. A. Houck. Tunable Coupling in Circuit Quantum Electrodynamics Using a Superconducting Charge Qubit with a V -Shaped Energy Level Diagram. *Physical Review Letters*, 106(8):083601, 2 2011.

[67] Eva Zakka-Bajjani, Francois Nguyen, Minhyea Lee, Leila R. Vale, Raymond W. Simmonds, and Jose Aumentado. Quantum superposition of a single microwave photon in two different colour states. *Nature Physics*, 7(8):599–603, 7 2011.

[68] Yu Chen, C. Neill, P. Roushan, N. Leung, M. Fang, R. Barends, J. Kelly, B. Campbell, Z. Chen, B. Chiaro, A. Dunsworth, E. Jeffrey, A. Megrant, J.Y. Mutus, P.J.J. OMalley, C.M. Quintana, D. Sank, A. Vainsencher, J. Wenner, T.C. White, Michael R. Geller, A.N. Cleland, and John M. Martinis. Qubit Architecture with High Coherence and Fast Tunable Coupling. *Physical Review Letters*, 113(22):220502, 11 2014.

[69] M.S. Allman, J.D. Whittaker, M. Castellanos-Beltran, K. Cicak, F. da Silva, M.P. DeFeo, F. Lecocq, A. Sirois, J.D. Teufel, J. Aumentado, and R.W. Simmonds. Tunable Resonant and Nonresonant Interactions between a Phase Qubit and L C Resonator. *Physical Review Letters*, 112(12):123601, 3 2014.

[70] A. J. Sirois, M. A. Castellanos-Beltran, M. P. DeFeo, L. Ranzani, F. Lecocq, R. W. Simmonds, J. D. Teufel, and J. Aumentado. Coherent-state storage and retrieval between superconducting cavities using parametric frequency conversion. *Applied Physics Letters*, 106(17):172603, 4 2015.

[71] David C. McKay, Stefan Filipp, Antonio Mezzacapo, Easwar Magesan, Jerry M. Chow, and Jay M. Gambetta. Universal Gate for Fixed-Frequency Qubits via a Tunable Bus. *Physical Review Applied*, 6(6):064007, 12 2016.

[72] Yao Lu, S. Chakram, N. Leung, N. Earnest, R.K. Naik, Ziwen Huang, Peter Groszkowski, Eliot Kapit, Jens Koch, and David I. Schuster. Universal Stabilization of a Parametrically Coupled Qubit. *Physical Review Letters*, 119(15):150502, 10 2017.

[73] Christine Vu. IBM Announces Advances to IBM Quantum Systems and Ecosystem. Technical report, IBM Q, 2017.

[74] Hsu Jeremy. CES 2018: Intels 49-Qubit Chip Shoots for Quantum Supremacy - IEEE Spectrum, 2018.

[75] Julian Kelly. A Preview of Bristlecone, Googles New Quantum Processor, 2018.

[76] Michel H. Devoret. Quantum Fluctuations in Electrical Circuits. In E. Giacobino S. Reynaud and J. Zinn-Justin, editors, *Fluctuations Quantiques/Quantum Fluctuations*, chapter 10, page 351. Elsevier Science, Les Houches, 1997.

[77] Guido Burkard, Roger H. Koch, and David P. DiVincenzo. Multilevel quantum description of decoherence in superconducting qubits. *Physical Review B*, 69(6):064503, 2 2004.

[78] Uri Vool and Michel Devoret. Introduction to quantum electromagnetic circuits. *International Journal of Circuit Theory and Applications*, 45(7):897–934, 7 2017.

[79] A. Wallraff, D. I. Schuster, A. Blais, L. Frunzio, R.-S. Huang, J. Majer, S. Kumar, S. M. Girvin, and R. J. Schoelkopf. Strong coupling of a single photon to a superconducting qubit using circuit quantum electrodynamics. *Nature*, 431(7005):162–167, 9 2004.

[80] Xinyuan You, J. A. Sauls, and Jens Koch. Circuit quantization in the presence of time-dependent external flux. 2 2019.

[81] N.N. Bogolyubov. On the theory of superfluidity. *Izv.Akad.Nauk Ser.Fiz.*, 11:23–32, 1947.

[82] Ming-wen Xiao. Theory of transformation for the diagonalization of quadratic Hamiltonians. 8 2009.

[83] Phan Thnh Nam, Marcin Napiórkowski, and Jan Philip Solovej. Diagonalization of bosonic quadratic Hamiltonians by Bogoliubov transformations. *Journal of Functional Analysis*, 270(11):4340–4368, 6 2016.

[84] David C. McKay, Ravi Naik, Philip Reinhold, Lev S. Bishop, and David I. Schuster. High-Contrast Qubit Interactions Using Multimode Cavity QED. *Physical Review Letters*, 114(8):080501, 2 2015.

[85] R. K. Naik, N. Leung, S. Chakram, P. Groszkowski, Y. Lu, N. Earnest, D. C. McKay, Jens Koch, and D. I. Schuster. Random access quantum information processors. 5 2017.

[86] N. Leung, Y. Lu, S. Chakram, R. K. Naik, N. Earnest, R. Ma, K. Jacobs, A. N. Cleland, and D. I. Schuster. Deterministic bidirectional communication and remote entanglement generation between superconducting qubits. *npj Quantum Information*, 5(1):18, 12 2019.

[87] J. R. Schrieffer and P. A. Wolff. Relation between the Anderson and Kondo Hamiltonians. *Physical Review*, 149(2):491–492, 9 1966.

[88] Susanne Richer, Barbara M Terhal, and David P Divincenzo. Perturbative analysis of two-qubit gates on transmon qubits Naturwissenschaften der RWTH Aachen im September 2013 angefertigt im Institut für Quanteninformation. Technical report.

[89] S. Poletto, Jay M. Gambetta, Seth T. Merkel, John A. Smolin, Jerry M. Chow, A. D. Córcoles, George A. Keefe, Mary B. Rothwell, J. R. Rozen, D. W. Abraham, Chad Rigetti, and M. Steffen. Entanglement of Two Superconducting Qubits in a Waveguide Cavity via Monochromatic Two-Photon Excitation. *Physical Review Letters*, 109(24):240505, 12 2012.

[90] Brian Baker, Andy C. Y. Li, Nicholas Irons, Nathan Earnest, and Jens Koch. Adaptive rotating-wave approximation for driven open quantum systems. *Physical Review A*, 98(5):052111, 11 2018.

[91] Roy J. Glauber. Coherent and Incoherent States of the Radiation Field. *Physical Review*, 131(6):2766–2788, 9 1963.

[92] Thomas Schneider. Four-Wave-Mixing (FWM). In Thomas Schneider, editor, *Nonlinear Optics in Telecommunications*, pages 167–200. Springer Berlin Heidelberg, Berlin, Heidelberg, 2004.

[93] Wolfgang Pfaff, Christopher J. Axline, Luke D. Burkhart, Uri Vool, Philip Reinhold, Luigi Frunzio, Liang Jiang, Michel H. Devoret, and Robert J. Schoelkopf. Controlled release of multiphoton quantum states from a microwave cavity memory. *Nature Physics*, 6 2017.

[94] Simon E. Nigg, Hanhee Paik, Brian Vlastakis, Gerhard Kirchmair, S. Shankar, Luigi Frunzio, M. H. Devoret, R. J. Schoelkopf, and S. M. Girvin. Black-Box Superconducting Circuit Quantization. *Physical Review Letters*, 108(24):240502, 6 2012.

[95] Heinz-Peter Breuer and Francesco Petruccione. *The Theory of Open Quantum Systems*. Oxford University Press, Oxford/New York, 2002.

[96] Klaus Hornberger. *Introduction to Decoherence Theory, in Entanglement and decoherence : foundations and modern trends*. Springer, 2009.

[97] Lev S. Bishop, J. M. Chow, Jens Koch, A. A. Houck, M. H. Devoret, E. Thuneberg, S. M. Girvin, and R. J. Schoelkopf. Nonlinear response of the vacuum Rabi resonance. *Nature Physics*, 5(2):105–109, 2 2009.

[98] C. W. Gardiner and P. Zoller. *Quantum noise : a handbook of Markovian and non-Markovian quantum stochastic methods with applications to quantum optics*. Springer, 2000.

[99] A. A. Clerk, M. H. Devoret, S. M. Girvin, Florian Marquardt, and R. J. Schoelkopf. Introduction to quantum noise, measurement, and amplification. *Reviews of Modern Physics*, 82(2):1155–1208, 4 2010.

[100] Fei Yan, Simon Gustavsson, Jonas Bylander, Xiaoyue Jin, Fumiki Yoshihara, David G. Cory, Yasunobu Nakamura, Terry P. Orlando, and William D. Oliver. Rotating-frame relax-

ation as a noise spectrum analyser of a superconducting qubit undergoing driven evolution. *Nature Communications*, 4(1):2337, 12 2013.

[101] R. Dum, P. Zoller, and H. Ritsch. Monte Carlo simulation of the atomic master equation for spontaneous emission. *Physical Review A*, 45(7):4879–4887, 4 1992.

[102] Jean Dalibard, Yvan Castin, and Klaus Mølmer. Wave-function approach to dissipative processes in quantum optics. *Physical Review Letters*, 68(5):580–583, 2 1992.

[103] Howard Carmichael. *An Open Systems Approach to Quantum Optics*, volume 18 of *Lecture Notes in Physics Monographs*. Springer Berlin Heidelberg, Berlin, Heidelberg, 1993.

[104] M. B. Plenio and P. L. Knight. The quantum-jump approach to dissipative dynamics in quantum optics. *Reviews of Modern Physics*, 70(1):101–144, 1 1998.

[105] Klaus Mølmer, Yvan Castin, and Jean Dalibard. Monte Carlo wave-function method in quantum optics. *Journal of the Optical Society of America B*, 10(3):524, 3 1993.

[106] K. W. Murch, S. J. Weber, C. Macklin, and I. Siddiqi. Observing single quantum trajectories of a superconducting quantum bit. *Nature*, 502(7470):211–214, 10 2013.

[107] D. Ristè, M. Dukalski, C. A. Watson, G. de Lange, M. J. Tiggelman, Ya. M. Blanter, K. W. Lehnert, R. N. Schouten, and L. DiCarlo. Deterministic entanglement of superconducting qubits by parity measurement and feedback. *Nature*, 502(7471):350–354, 10 2013.

[108] L. Sun, A. Petrenko, Z. Leghtas, B. Vlastakis, G. Kirchmair, K. M. Sliwa, A. Narla, M. Hatridge, S. Shankar, J. Blumoff, L. Frunzio, M. Mirrahimi, M. H. Devoret, and R. J. Schoelkopf. Tracking photon jumps with repeated quantum non-demolition parity measurements. *Nature*, 511(7510):444–448, 7 2014.

[109] Z.K. Minev, S.O. Mundhada, S. Shankar, P. Reinhold, R. Gutiérrez-Jáuregui, R.J. Schoelkopf, M. Mirrahimi, H.J. Carmichael, and M.H. Devoret. To catch and reverse a quantum jump mid-flight. *Nature*, 570(7760):200–204, 6 2019.

[110] Bernard Yurke. Use of cavities in squeezed-state generation. *Physical Review A*, 29(1):408–410, 1 1984.

[111] C.W. Gardiner and C.M. Savage. A multimode quantum theory of a degenerate parametric amplifier in a cavity. *Optics Communications*, 50(3):173–178, 6 1984.

[112] M. J. Collett and C. W. Gardiner. Squeezing of intracavity and traveling-wave light fields produced in parametric amplification. *Physical Review A*, 30(3):1386–1391, 9 1984.

[113] C. W. Gardiner and M. J. Collett. Input and output in damped quantum systems: Quantum stochastic differential equations and the master equation. *Physical Review A*, 31(6):3761–3774, 6 1985.

[114] Benjamin A. Mazin. Microwave kinetic inductance detectors. 2005.

[115] M. S. Khalil, M. J. A. Stoutimore, F. C. Wellstood, and K. D. Osborn. An analysis method for asymmetric resonator transmission applied to superconducting devices. *Journal of Applied Physics*, 111(5):054510, 3 2012.

[116] Omid Noroozian. Superconducting Microwave Resonator Arrays for Submillimeter/Far-infrared Imaging. 2012.

[117] Baleegh Abdo, Katrina Sliwa, Flavius Schackert, Nicolas Bergeal, Michael Hatridge, Luigi Frunzio, A. Douglas Stone, and Michel Devoret. Full Coherent Frequency Conversion between Two Propagating Microwave Modes. *Physical Review Letters*, 110(17):173902, 4 2013.

[118] Ananda Roy and Michel Devoret. Introduction to parametric amplification of quantum signals with Josephson circuits. *Comptes Rendus Physique*, 17(7):740–755, 8 2016.

[119] J. I. Cirac, P. Zoller, H. J. Kimble, and H. Mabuchi. Quantum State Transfer and Entanglement Distribution among Distant Nodes in a Quantum Network. *Physical Review Letters*, 78(16):3221–3224, 4 1997.

[120] L.-M. Duan and H. J. Kimble. Scalable Photonic Quantum Computation through Cavity-Assisted Interactions. *Physical Review Letters*, 92(12):127902, 3 2004.

[121] Erik Sjöqvist, D M Tong, L Mauritz Andersson, Bjrn Hessmo, Markus Johansson, and Kuldip Singh. Non-adiabatic holonomic quantum computation. *New Journal of Physics*, 14(10):103035, 10 2012.

[122] Guanru Feng, Guofu Xu, and Guilu Long. Experimental Realization of Nonadiabatic Holonomic Quantum Computation. *Physical Review Letters*, 110(19):190501, 5 2013.

[123] M. Stobińska, G. Alber, and G. Leuchs. Perfect excitation of a matter qubit by a single photon in free space. *EPL (Europhysics Letters)*, 86(1):14007, 4 2009.

[124] Yimin Wang, Ji Minář, Lana Sheridan, and Valerio Scarani. Efficient excitation of a two-level atom by a single photon in a propagating mode. *Physical Review A*, 83(6):063842, 6 2011.

[125] Yi Yin, Yu Chen, Daniel Sank, P. J. J. OMalley, T. C. White, R. Barends, J. Kelly, Erik Lucero, Matteo Mariantoni, A. Megrant, C. Neill, A. Vainsencher, J. Wenner, Alexander N. Korotkov, A. N. Cleland, and John M. Martinis. Catch and Release of Microwave Photon States. *Physical Review Letters*, 110(10):107001, 3 2013.

[126] J. Wenner, Yi Yin, Yu Chen, R. Barends, B. Chiaro, E. Jeffrey, J. Kelly, A. Megrant, J.Y. Mutus, C. Neill, P.J.J. OMalley, P. Roushan, D. Sank, A. Vainsencher, T.C. White, Alexander N. Korotkov, A.N. Cleland, and John M. Martinis. Catching Time-Reversed Microwave Coherent State Photons with 99.4% Absorption Efficiency. *Physical Review Letters*, 112(21):210501, 5 2014.

[127] Srikanth J. Srinivasan, Neereja M. Sundaresan, Darius Sadri, Yanbing Liu, Jay M. Gambetta, Terri Yu, S. M. Girvin, and Andrew A. Houck. Time-reversal symmetrization of spontaneous emission for quantum state transfer. *Physical Review A*, 89(3):033857, 3 2014.

[128] G. Floquet. Sur les équations différentielles linéaires à coefficients périodiques. *Annales scientifiques de l'École normale supérieure*, 12:47–88, 1883.

[129] Jon H. Shirley. Solution of the Schrödinger Equation with a Hamiltonian Periodic in Time. *Physical Review*, 138(4B):B979–B987, 5 1965.

[130] Milena Grifoni and Peter Hänggi. Driven quantum tunneling. *Physics Reports*, 304(5-6):229–354, 10 1998.

[131] Matti Silveri, Jani Tuorila, Mika Kemppainen, and Erkki Thuneberg. Probe spectroscopy of quasienergy states. *Physical Review B*, 87(13):134505, 4 2013.

[132] Flix Beaudoin, Marcus P. da Silva, Zachary Dutton, and Alexandre Blais. First-order sidebands in circuit QED using qubit frequency modulation. *Physical Review A*, 86(2):022305, 8 2012.

[133] J. D. Strand, Matthew Ware, Flix Beaudoin, T. A. Ohki, B. R. Johnson, Alexandre Blais, and B. L. T. Plourde. First-order sideband transitions with flux-driven asymmetric transmon qubits. *Physical Review B*, 87(22):220505, 6 2013.

[134] Omid Noroozian, Peter K. Day, Byeong Ho Eom, Henry G. Leduc, and Jonas Zmuidzinas. Crosstalk Reduction for Superconducting Microwave Resonator Arrays. *IEEE Transactions on Microwave Theory and Techniques*, 60(5):1235–1243, 5 2012.

[135] J Wenner, M Neeley, Radoslaw C Bialczak, M Lenander, Erik Lucero, A D OConnell, D Sank, H Wang, M Weides, A N Cleland, and John M Martinis. Wirebond crosstalk and cavity modes in large chip mounts for superconducting qubits. *Superconductor Science and Technology*, 24(6):065001, 6 2011.

[136] Zijun Chen, A. Megrant, J. Kelly, R. Barends, J. Bochmann, Yu Chen, B. Chiaro, A. Dunsworth, E. Jeffrey, J. Y. Mutus, P. J. J. O'Malley, C. Neill, P. Roushan, D. Sank,

A. Vainsencher, J. Wenner, T. C. White, A. N. Cleland, and John M. Martinis. Fabrication and characterization of aluminum airbridges for superconducting microwave circuits. *Applied Physics Letters*, 104(5):052602, 2 2014.

[137] V. Vesterinen, O. P. Saira, A. Bruno, and L. DiCarlo. Mitigating information leakage in a crowded spectrum of weakly anharmonic qubits. 5 2014.

[138] B. Foxen, J. Y. Mutus, E. Lucero, R. Graff, A. Megrant, Yu Chen, C. Quintana, B. Burkett, J. Kelly, E. Jeffrey, Yan Yang, Anthony Yu, K. Arya, R. Barends, Zijun Chen, B. Chiaro, A. Dunsworth, A. Fowler, C. Gidney, M. Giustina, T. Huang, P. Klimov, M. Neeley, C. Neill, P. Roushan, D. Sank, A. Vainsencher, J. Wenner, T. C. White, and John M. Martinis. Qubit compatible superconducting interconnects. 8 2017.

[139] A. Dunsworth, R. Barends, Yu Chen, Zijun Chen, B. Chiaro, A. Fowler, B. Foxen, E. Jeffrey, J. Kelly, P. V. Klimov, E. Lucero, J. Y. Mutus, M. Neeley, C. Neill, C. Quintana, P. Roushan, D. Sank, A. Vainsencher, J. Wenner, T. C. White, H. Neven, John M. Martinis, and A. Megrant. A method for building low loss multi-layer wiring for superconducting microwave devices. *Applied Physics Letters*, 112(6):063502, 2 2018.

[140] D. Rosenberg, D. Kim, R. Das, D. Yost, S. Gustavsson, D. Hover, P. Krantz, A. Melville, L. Racz, G. O. Samach, S. J. Weber, F. Yan, J. L. Yoder, A. J. Kerman, and W. D. Oliver. 3D integrated superconducting qubits. *npj Quantum Information*, 3(1):42, 12 2017.

[141] D. Hucul, I. V. Inlek, G. Vittorini, C. Crocker, S. Debnath, S. M. Clark, and C. Monroe. Modular entanglement of atomic qubits using photons and phonons. *Nature Physics*, 11(1):37–42, 1 2015.

[142] S. Debnath, N. M. Linke, C. Figgatt, K. A. Landsman, K. Wright, and C. Monroe. Demonstration of a small programmable quantum computer with atomic qubits. *Nature*, 536(7614):63–66, 8 2016.

[143] Norbert M Linke, Dmitri Maslov, Martin Roetteler, Shantanu Debnath, Caroline Figgatt, Kevin A Landsman, Kenneth Wright, and Christopher Monroe. Experimental comparison of two quantum computing architectures. *Proceedings of the National Academy of Sciences of the United States of America*, 114(13):3305–3310, 3 2017.

[144] Matthew Reagor, Wolfgang Pfaff, Christopher Axline, Reinier W. Heeres, Nissim Ofek, Katrina Sliwa, Eric Holland, Chen Wang, Jacob Blumoff, Kevin Chou, Michael J. Hatridge, Luigi Frunzio, Michel H. Devoret, Liang Jiang, and Robert J. Schoelkopf. Quantum memory with millisecond coherence in circuit QED. *Physical Review B*, 94(1):014506, 7 2016.

[145] Nissim Ofek, Andrei Petrenko, Reinier Heeres, Philip Reinhold, Zaki Leghtas, Brian Vlastakis, Yehan Liu, Luigi Frunzio, S. M. Girvin, L. Jiang, Mazyar Mirrahimi, M. H. Devoret, and R. J. Schoelkopf. Extending the lifetime of a quantum bit with error correction in superconducting circuits. *Nature*, 536(7617):441–445, 8 2016.

[146] Neereja M. Sundaresan, Yanbing Liu, Darius Sadri, Lszl J. Szőcs, Devin L. Underwood, Moein Malekakhlagh, Hakan E. Türeci, and Andrew A. Houck. Beyond Strong Coupling in a Multimode Cavity. *Physical Review X*, 5(2):021035, 6 2015.

[147] Srivatsan Chakram, Ravi Naik, Akash Dixit, Yao Lu, Alexander Anferov, Nelson Leung, Andrew Oriani, and David Schuster. Quantum information processing using 3D multimode circuit QED. *Bulletin of the American Physical Society*, Volume 64, Number 2, 2019.

[148] Mazyar Mirrahimi, Zaki Leghtas, Victor V Albert, Steven Touzard, Robert J Schoelkopf, Liang Jiang, and Michel H Devoret. Dynamically protected cat-qubits: a new paradigm for universal quantum computation. *New Journal of Physics*, 16(4):045014, 4 2014.

[149] Marios H. Michael, Matti Silveri, R.T. Brierley, Victor V. Albert, Juha Salmilehto, Liang Jiang, and S.M. Girvin. New Class of Quantum Error-Correcting Codes for a Bosonic Mode. *Physical Review X*, 6(3):031006, 7 2016.

[150] Ming Hua, Ming-Jie Tao, and Fu-Guo Deng. Fast universal quantum gates on microwave photons with all-resonance operations in circuit QED. *Scientific Reports*, 5(1):9274, 8 2015.

[151] C. Monroe, R. Raussendorf, A. Ruthven, K. R. Brown, P. Maunz, L.-M. Duan, and J. Kim. Large-scale modular quantum-computer architecture with atomic memory and photonic interconnects. *Physical Review A*, 89(2):022317, 2 2014.

[152] Teresa Brecht, Wolfgang Pfaff, Chen Wang, Yiwen Chu, Luigi Frunzio, Michel H Devoret, and Robert J Schoelkopf. Multilayer microwave integrated quantum circuits for scalable quantum computing. *npj Quantum Information*, 2(1):16002, 11 2016.

[153] Kevin S. Chou, Jacob Z. Blumoff, Christopher S. Wang, Philip C. Reinhold, Christopher J. Axline, Yvonne Y. Gao, L. Frunzio, M. H. Devoret, Liang Jiang, and R. J. Schoelkopf. Deterministic teleportation of a quantum gate between two logical qubits. *Nature*, 561(7723):368–373, 9 2018.

[154] N. Roch, M.E. Schwartz, F. Motzoi, C. Macklin, R. Vijay, A.W. Eddins, A.N. Korotkov, K.B. Whaley, M. Sarovar, and I. Siddiqi. Observation of Measurement-Induced Entanglement and Quantum Trajectories of Remote Superconducting Qubits. *Physical Review Letters*, 112(17):170501, 4 2014.

[155] A. Narla, S. Shankar, M. Hatridge, Z. Leghtas, K.M. Sliwa, E. Zalys-Geller, S.O. Mundhada, W. Pfaff, L. Frunzio, R.J. Schoelkopf, and M.H. Devoret. Robust Concurrent Remote Entanglement Between Two Superconducting Qubits. *Physical Review X*, 6(3):031036, 9 2016.

[156] C. Dickel, J. J. Wesdorp, N. K. Langford, S. Peiter, R. Sagastizabal, A. Bruno, B. Criger, F. Motzoi, and L. DiCarlo. Chip-to-chip entanglement of transmon qubits using engineered measurement fields. *Physical Review B*, 97(6):064508, 2 2018.

[157] Liang Jiang, Jacob M. Taylor, Anders S. Sørensen, and Mikhail D. Lukin. Distributed

quantum computation based on small quantum registers. *Physical Review A*, 76(6):062323, 12 2007.

[158] Christopher J. Axline, Luke D. Burkhart, Wolfgang Pfaff, Mengzhen Zhang, Kevin Chou, Philippe Campagne-Ibarcq, Philip Reinhold, Luigi Frunzio, S. M. Girvin, Liang Jiang, M. H. Devoret, and R. J. Schoelkopf. On-demand quantum state transfer and entanglement between remote microwave cavity memories. *Nature Physics*, 14(7):705–710, 7 2018.

[159] P. Campagne-Ibarcq, E. Zalys-Geller, A. Narla, S. Shankar, P. Reinhold, L. Burkhart, C. Axline, W. Pfaff, L. Frunzio, R.J. Schoelkopf, and M.H. Devoret. Deterministic Remote Entanglement of Superconducting Circuits through Microwave Two-Photon Transitions. *Physical Review Letters*, 120(20):200501, 5 2018.

[160] P. Kurpiers, P. Magnard, T. Walter, B. Royer, M. Pechal, J. Heinsoo, Y. Salathé, A. Akin, S. Storz, J.-C. Besse, S. Gasparinetti, A. Blais, and A. Wallraff. Deterministic quantum state transfer and remote entanglement using microwave photons. *Nature*, 558(7709):264–267, 6 2018.

[161] Kurt Jacobs, Rebing Wu, Xiaoting Wang, Sahel Ashhab, Qi-Ming Chen, and Herschel Rabitz. Fast quantum communication in linear networks. *EPL (Europhysics Letters)*, 114(4):40007, 5 2016.

[162] D L Underwood, W E Shanks, Jens Koch, and A A Houck. Low-disorder microwave cavity lattices for quantum simulation with photons. *PHYSICAL REVIEW A*, 86, 2012.

[163] Daniel F. V. James, Paul G. Kwiat, William J. Munro, and Andrew G. White. Measurement of qubits. *Physical Review A*, 64(5):052312, 10 2001.

[164] J. M. Chow, L. DiCarlo, J. M. Gambetta, A. Nunnenkamp, Lev S. Bishop, L. Frunzio, M. H. Devoret, S. M. Girvin, and R. J. Schoelkopf. Detecting highly entangled states with a joint qubit readout. *Physical Review A*, 81(6):062325, 6 2010.

[165] Nikolay V. Vitanov, Andon A. Rangelov, Bruce W. Shore, and Klaas Bergmann. Stimulated Raman adiabatic passage in physics, chemistry, and beyond. *Reviews of Modern Physics*, 89(1):015006, 3 2017.

[166] N V Vitanov, K-A Suominen, and B W Shore. Creation of coherent atomic superpositions by fractional stimulated Raman adiabatic passage. *Journal of Physics B: Atomic, Molecular and Optical Physics*, 32(18):4535–4546, 9 1999.

[167] Nicholas T. Bronn, Yanbing Liu, Jared B. Hertzberg, Antonio D. Córcoles, Andrew A. Houck, Jay M. Gambetta, and Jerry M. Chow. Broadband filters for abatement of spontaneous emission in circuit quantum electrodynamics. *Applied Physics Letters*, 107(17):172601, 10 2015.

[168] Marco Roth, Marc Ganzhorn, Nikolaj Moll, Stefan Filipp, Gian Salis, and Sebastian Schmidt. Analysis of parametrically driven exchange-type (iSWAP) and two-photon (bSWAP) interactions between superconducting qubits. 8 2017.

[169] A Wallraff, D I Schuster, A Blais, J M Gambetta, J Schreier, L Frunzio, M H Devoret, S M Girvin, and R J Schoelkopf. Sideband Transitions and Two-Tone Spectroscopy of a Superconducting Qubit Strongly Coupled to an On-Chip Cavity. 2007.

[170] P. J. Leek, S. Filipp, P. Maurer, M. Baur, R. Bianchetti, J. M. Fink, M. Goppl, L. Steffen, and A. Wallraff. Using sideband transitions for two-qubit operations in superconducting circuits. *Physical Review B*, 79(18):180511, 5 2009.

[171] S. Novikov, T. Sweeney, J. E. Robinson, S. P. Premaratne, B. Suri, F. C. Wellstood, and B. S. Palmer. Raman coherence in a circuit quantum electrodynamics lambda system. *Nature Physics*, 12(1):75–79, 11 2015.

[172] K Fossheim and A Sudbø. *Superconductivity: physics and applications*. 2005.

[173] D. I. Schuster, A. A. Houck, J. A. Schreier, A. Wallraff, J. M. Gambetta, A. Blais, L. Frunzio, J. Majer, B. Johnson, M. H. Devoret, S. M. Girvin, and R. J. Schoelkopf. Resolving photon number states in a superconducting circuit. *Nature*, 445(7127):515–518, 2 2007.

[174] F. Lecocq, L. Ranzani, G.A. Peterson, K. Cicak, R.W. Simmonds, J.D. Teufel, and J. Aumentado. Nonreciprocal Microwave Signal Processing with a Field-Programmable Josephson Amplifier. *Physical Review Applied*, 7(2):024028, 2 2017.

[175] P. Roushan, C. Neill, A. Megrant, Y. Chen, R. Babbush, R. Barends, B. Campbell, Z. Chen, B. Chiaro, A. Dunsworth, A. Fowler, E. Jeffrey, J. Kelly, E. Lucero, J. Mutus, P. J. J. O'Malley, M. Neeley, C. Quintana, D. Sank, A. Vainsencher, J. Wenner, T. White, E. Kapit, H. Neven, and J. Martinis. Chiral ground-state currents of interacting photons in a synthetic magnetic field. *Nature Physics*, 13(2):146–151, 10 2016.

[176] Sergio O Valenzuela, William D Oliver, David M Berns, Karl K Berggren, Leonid S Levitov, and Terry P Orlando. Microwave-induced cooling of a superconducting qubit. *Science (New York, N.Y.)*, 314(5805):1589–92, 12 2006.

[177] A Schliesser, O Arcizet, R Rivière, G Anetsberger, and T J Kippenberg. Resolved-sideband cooling and position measurement of a micromechanical oscillator close to the Heisenberg uncertainty limit. *Nature Physics*, 5, 2009.

[178] J. D. Teufel, T. Donner, Dale Li, J. W. Harlow, M. S. Allman, K. Cicak, A. J. Sirois, J. D. Whittaker, K. W. Lehnert, and R. W. Simmonds. Sideband cooling of micromechanical motion to the quantum ground state. *Nature*, 475(7356):359–363, 7 2011.

[179] A. M. Kaufman, B. J. Lester, and C. A. Regal. Cooling a Single Atom in an Optical Tweezer to Its Quantum Ground State. *Physical Review X*, 2(4):041014, 11 2012.

[180] R. Vijay, C. Macklin, D. H. Slichter, S. J. Weber, K. W. Murch, R. Naik, A. N. Korotkov, and I. Siddiqi. Stabilizing Rabi oscillations in a superconducting qubit using quantum feedback. *Nature*, 490(7418):77–80, 10 2012.

[181] P. Campagne-Ibarcq, E. Flurin, N. Roch, D. Darson, P. Morfin, M. Mirrahimi, M. H. Devoret, F. Mallet, and B. Huard. Persistent Control of a Superconducting Qubit by Stroboscopic Measurement Feedback. *Physical Review X*, 3(2):021008, 5 2013.

[182] K. W. Murch, U. Vool, D. Zhou, S. J. Weber, S. M. Girvin, and I. Siddiqi. Cavity-Assisted Quantum Bath Engineering. *Physical Review Letters*, 109(18):183602, 10 2012.

[183] S. Shankar, M. Hatridge, Z. Leghtas, K. M. Sliwa, A. Narla, U. Vool, S. M. Girvin, L. Frunzio, M. Mirrahimi, and M. H. Devoret. Autonomously stabilized entanglement between two superconducting quantum bits. *Nature*, 504(7480):419–422, 11 2013.

[184] K. Geerlings, Z. Leghtas, I. M. Pop, S. Shankar, L. Frunzio, R. J. Schoelkopf, M. Mirrahimi, and M. H. Devoret. Demonstrating a Driven Reset Protocol for a Superconducting Qubit. *Physical Review Letters*, 110(12):120501, 3 2013.

[185] Zaki Leghtas, Gerhard Kirchmair, Brian Vlastakis, Robert J. Schoelkopf, Michel H. Devoret, and Mazyar Mirrahimi. Hardware-Efficient Autonomous Quantum Memory Protection. *Physical Review Letters*, 111(12):120501, 9 2013.

[186] Eliot Kapit, John T. Chalker, and Steven H. Simon. Passive correction of quantum logical errors in a driven, dissipative system: A blueprint for an analog quantum code fabric. *Physical Review A*, 91(6):062324, 6 2015.

[187] Eliot Kapit. Hardware-Efficient and Fully Autonomous Quantum Error Correction in Superconducting Circuits. *Physical Review Letters*, 116(15):150501, 4 2016.

[188] Ziwen Huang, Yao Lu, Eliot Kapit, David I. Schuster, and Jens Koch. Universal stabilization of single-qubit states using a tunable coupler. *Physical Review A*, 97(6):062345, 6 2018.

[189] Eliot Kapit, Mohammad Hafezi, and Steven H. Simon. Induced Self-Stabilization in Fractional Quantum Hall States of Light. *Physical Review X*, 4(3):031039, 9 2014.

[190] Chad Rigetti and Michel Devoret. Fully microwave-tunable universal gates in superconducting qubits with linear couplings and fixed transition frequencies. *Physical Review B*, 81(13):134507, 4 2010.

[191] Jerry M. Chow, A. D. Córcoles, Jay M. Gambetta, Chad Rigetti, B. R. Johnson, John A. Smolin, J. R. Rozen, George A. Keefe, Mary B. Rothwell, Mark B. Ketchen, and M. Steffen. Simple All-Microwave Entangling Gate for Fixed-Frequency Superconducting Qubits. *Physical Review Letters*, 107(8):080502, 8 2011.

[192] Eliot Kapit. Universal two-qubit interactions, measurement, and cooling for quantum simulation and computing. *Physical Review A*, 92(1):012302, 7 2015.

[193] M. Mamaev, L. C. G. Govia, and A. A. Clerk. Dissipative stabilization of entangled cat states using a driven Bose-Hubbard dimer. 11 2017.

[194] B. Kraus, H. P. Büchler, S. Diehl, A. Kantian, A. Micheli, and P. Zoller. Preparation of entangled states by quantum Markov processes. *Physical Review A*, 78(4):042307, 10 2008.

[195] A.Yu. Kitaev. Fault-tolerant quantum computation by anyons. *Annals of Physics*, 303(1):2–30, 1 2003.

[196] H. Bombin. Topological subsystem codes. *Physical Review A*, 81(3):032301, 3 2010.

[197] Austin G. Fowler, Matteo Mariantoni, John M. Martinis, and Andrew N. Cleland. Surface codes: Towards practical large-scale quantum computation. *Physical Review A*, 86(3):032324, 9 2012.

[198] Barbara M. Terhal. Quantum error correction for quantum memories. *Reviews of Modern Physics*, 87(2):307–346, 4 2015.

[199] Joseph Kerckhoff, Hendra I. Nurdin, Dmitri S. Pavlichin, and Hideo Mabuchi. Designing Quantum Memories with Embedded Control: Photonic Circuits for Autonomous Quantum Error Correction. *Physical Review Letters*, 105(4):040502, 7 2010.

[200] Eliot Kapit. The upside of noise: engineered dissipation as a resource in superconducting circuits. *Quantum Science and Technology*, 2(3):033002, 9 2017.

[201] C. Daniel Freeman, C. M. Herdman, and K. B. Whaley. Engineering autonomous error correction in stabilizer codes at finite temperature. *Physical Review A*, 96(1):012311, 7 2017.

[202] F. Reiter, A. S. Sørensen, P. Zoller, and C. A. Muschik. Dissipative quantum error correction and application to quantum sensing with trapped ions. *Nature Communications*, 8(1):1822, 12 2017.

[203] Eliot Kapit. Error-Transparent Quantum Gates for Small Logical Qubit Architectures. *Physical Review Letters*, 120(5):050503, 2 2018.

[204] Victor V Albert, Shantanu O Mundhada, Alexander Grimm, Steven Touzard, Michel H Devoret, and Liang Jiang. Pair-cat codes: autonomous error-correction with low-order nonlinearity. *Quantum Science and Technology*, 4(3):035007, 6 2019.

[205] Arun Kumar Pati and Samuel L. Braunstein. Impossibility of deleting an unknown quantum state. *Nature*, 404(6774):164–165, 3 2000.

[206] J. E. Mooij, T. P. Orlando, L. Levitov, Lin Tian, Caspar H. van der van der Wal CH, and Seth Lloyd. Josephson persistent-current qubit. *Science (New York, N.Y.)*, 285(5430):1036–9, 8 1999.

[207] Fei Yan, Simon Gustavsson, Archana Kamal, Jeffrey Birenbaum, Adam P Sears, David Hover, Ted J. Gudmundsen, Danna Rosenberg, Gabriel Samach, S Weber, Jonilyn L. Yoder, Terry P. Orlando, John Clarke, Andrew J. Kerman, and William D. Oliver. The flux qubit revisited to enhance coherence and reproducibility. *Nature Communications*, 7(1):12964, 12 2016.

[208] C. Song, M. P. DeFeo, K. Yu, and B. L. T. Plourde. Reducing microwave loss in superconducting resonators due to trapped vortices. *Applied Physics Letters*, 95(23):232501, 12 2009.

[209] Sergey Gladchenko, David Olaya, Eva Dupont-Ferrier, Benoit Douçot, Lev B. Ioffe, and Michael E. Gershenson. Superconducting nanocircuits for topologically protected qubits. *Nature Physics*, 5(1):48–53, 1 2009.

[210] Antonio D. Córcoles, Jerry M. Chow, Jay M. Gambetta, Chad Rigetti, J. R. Rozen, George A. Keefe, Mary Beth Rothwell, Mark B. Ketchen, and M. Steffen. Protecting superconducting qubits from radiation. *Applied Physics Letters*, 99(18):181906, 10 2011.

[211] A. Wallraff, D. I. Schuster, A. Blais, L. Frunzio, J. Majer, M. H. Devoret, S. M. Girvin, and R. J. Schoelkopf. Approaching Unit Visibility for Control of a Superconducting Qubit with Dispersive Readout. *Physical Review Letters*, 95(6):060501, 8 2005.